

***Effect of Fabrication Methods on the Porosity,  
Microstructure, Strength and In-Vitro Bioactivity of  
Porous Hydroxyapatite Scaffolds***

**A Thesis Submitted in Partial Fulfillment of the  
Requirements for the Degree of**

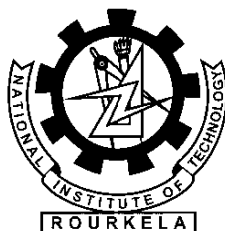
**Doctor of Philosophy**

**By**

**Smruti Rekha Dash  
(Roll No: 509CR103)**

**Under the Supervision of**

**Prof. Santanu Bhattacharyya  
and  
Prof. Ritwik Sarkar**



**Department of Ceramic Engineering  
National Institute of Technology  
Rourkela-769008, Odisha, India  
August, 2015**

## **DECLARATION**

Date:

I hereby declare that the work presented in the thesis entitled “**Effect of Fabrication Methods on the Porosity, Microstructure, Strength and In-Vitro Bioactivity of Porous Hydroxyapatite Scaffolds**” submitted for Ph. D. Degree to the National Institute of Technology, Rourkela has been carried out by me at Department of Ceramic Engineering, National Institute of Technology, Rourkela under the supervision of Dr. Santanu Bhattacharyya and Dr. Ritwik Sarkar. The work is original and has not been submitted in part or full by me for any degree or diploma to this or any other University/Institute.

**Smruti Rekha Dash**

Department of Ceramic Engineering  
National Institute of Technology, Rourkela  
Rourkela – 769008, Odisha, India



**DEPARTMENT OF CERAMIC ENGINEERING  
NATIONAL INSTITUTE OF TECHNOLOGY,  
ROURKELA-769008**

CERTIFICATE

This is to certify that the thesis entitled “**Effect of Fabrication Methods on the Porosity, Microstructure, Strength and In-Vitro Bioactivity of Porous Hydroxyapatite Scaffolds**” submitted by **Smruti Rekha Dash**, for the degree of **Doctor of Philosophy in Ceramic Engineering** to the National Institute of Technology, Rourkela, is a record of bonafide research work carried out by her under our supervision and guidance. Her thesis, in our opinion, is worthy of consideration for the award of the degree of Doctor of Philosophy in Ceramic Engineering in accordance with the regulations of the Institute.

The results embodied in this thesis have not been submitted to any other university or institute for the award of a Degree.

**Prof. Ritwik Sarkar**  
Co-Supervisor  
Department of Ceramic Engineering  
National Institute of Technology  
Rourkela

**Prof. Santanu Bhattacharyya**  
Supervisor  
Department of Ceramic Engineering  
National Institute of Technology  
Rourkela

## ACKNOWLEDGMENTS

I am deeply indebted to my supervisor Prof. Santanu Bhattacharyya who has supported, encouraged, guided and also taught me the value of hard work through my Ph.D. I would also like to thank my co-supervisor Prof. Ritwik Sarkar for his constructive suggestions on this project.

I am again grateful to Prof. B. B Nayak, Head of the Department of Ceramic Engineering for his encouragement and help to carry out the thesis work. I would also take this opportunity to express my gratitude and sincere thanks to Prof. S.K Pratihara and other faculty members of Ceramic Engineering Department, NIT Rourkela for their constructive suggestions and encouragement at various stages of the work.

I would like to express my gratitude to all technicians and staff who have helped with a number of aspects of my Ph.D. Especially, thanks to Mr Prasant Kumar Mohanty and Mr. Subhobrata Chakraborty. All the support they have provided me through my Ph.D years was the greatest gift anyone has ever given me.

I would also like to thank all my friends and colleagues, especially Geetanjali, Nadiya, Ganesh, Sarat, Subrat, Ezhil Venuswaram, Anantha, Abhishek, Jayarao, Prativa, Satyananda, Kanchan, Raju, Rupita, Soumini, Pinki, Sowjanya, Pallavi, Aiswarya, Srinivas, Sangeeta, Soumya and Pranati for their good wishes and support over the last few years, which will always be remembered with deep gratitude.

Last but definitely not least, some of the important people in my life, my parents, my grandparents, my in-laws, my sister, my cousins and all my family members are so lovingly acknowledged for their continual emotional support and encouragement. And especially to my grand-mother Smt. Kamalini Kar, my mother Smt Pramila Kar and my father-in-law Mr. Bighnaraj Panda for all your encouragement and prayers are so much appreciated. Most importantly, I would like to thank my husband Er. Satya Narayan Panda, for always believing in me, even in the times when I did not! I just want to thank you for being with me through the good times and the bad times.

Smruti Rekha Dash



2.1.4 Sol-gel Synthesis	24
2.1.5 Hydrothermal Synthesis Route	25
2.1.6 Hydrolysis Method	27
2.1.7 Emulsion Method	28
2.1.8 Combustion Synthesis	29
2.1.9 Spray Pyrolysis	30
2.1.10 Biomimetic Synthesis	31
2.1.11 Synthesis of HA from bio wastes	32
2.2 Part-B-Porous Scaffold Fabrication Routes	35
2.2.1 Sacrificial fugitive method	35
2.2.2 Gel Casting	40
2.2.3 Freeze Casting	42
2.2.4 Replica Technique	44
2.2.5 Protein Coagulation Casting	46
2.2.6 Foaming agents other than starch or albumin	50
2.3 Part-C-In-vitro Bioactivity – Process and Mechanism	52
<b>Chapter 3 Motivation and Plan for the Present work</b>	
3.1 Summary of the Literature and Motivation for Work	55
3.2 Plan of Work	57
<b>Chapter 4 A review of the Characterization Techniques used in this Study</b>	
4.1 Background	60
4.2 Thermal decomposition behavior of precipitated powder	60
4.3 Particle size analysis of HA by Dynamic Light Scattering Technique (DLS)	61
4.4 Specific surface area of HA powder	62
4.5 Phase evolution and phase stability of HA	63
4.6 Study of Functional groups of prepared HA by Fourier Transform Infrared Spectroscopy	64
4.7 Densification study of HA particle by Dilatometer	64
4.8 Bulk Density and Apparent Porosity Measurement	65
4.9 Cold Compressive Strength (CCS)	65

4.10	Microstructure study by Scanning Electron Microscope (SEM)	66
4.11	Slurry Rheology	66
4.12	Mercury Intrusion Porosimeter	67
4.13	In vitro Bioactivity	67
4.15	Preparation of Simulated Body Fluid (SBF)	68
4.14	Cytotoxicity evaluation through MTT Test	69
<b>Chapter 5 Hydroxyapatite powder processing</b>		
5.1	Background	71
5.2	Raw materials and Powder synthesis	72
5.3	Characterization of the as precipitated and calcined powder	73
	5.3.1 Thermal analysis of HA precipitates	73
	5.3.2 Study of phase evolution in calcined HA	74
	5.3.2.1 Phase Analysis by X-Ray Diffraction	74
	5.3.2.2 Phase purity study by FTIR spectroscopy	78
	5.3.3 Particle size distribution and specific surface area of calcined powder	79
	5.3.4 Study of HA particle size by SEM	80
5.4	Study of the densification behavior and sintering behaviour of HA	81
5.5	Study of HA Phases in the sintered HA	82
5.6	Effect of sintering schedule on Bulk Density and Apparent Porosity and Compressive Strength of sintered HA	85
	5.6.1 Bulk Density and Apparent porosity of sintered HA	85
	5.6.2 Effect of Sintering Temperature on compressive strength	86
	5.6.3 Effect of soaking Time on Apparent Porosity, Bulk Density and Compressive Strength of the sintered HA	88
5.7	Conclusions	89
<b>Chapter 6 Porous Hydroxyapatite by Solid State Route</b>		
6.1	Background	90
6.2	Raw materials and processing of pellets	90
	6.2.1 Raw materials	90
	6.2.2 Mixing and Compaction of HA-NA mixed powder	90

6.3	Results and Discussion	91
6.3.1	Removal of Pore former and Binder	91
6.3.2	Bulk density and Apparent porosity of the Sintered HA-NA Scaffold	92
6.3.3	Pore Size Distribution of HA-NA Scaffold	92
6.3.4	Microstructure of Sintered HA-NA Scaffold	94
6.4	Porosity and Strength of Sintered HA-NA Scaffold	97
6.5	In-vitro aging behavior of Porous HA Scaffolds	99
6.5.1	Microstructure of the SBF aged porous HA Scaffold	99
6.5.2	Weight loss behavior of the scaffolds during aging in SBF	102
6.5.3	Change in the Ca <sup>+2</sup> and P <sup>+5</sup> concentrations due to the dissolution behaviour of Porous HA in SBF aging	105
6.6	Conclusions	106
<b>Chapter 7</b>	<b>Porous Hydroxyapatite by Gel casting Route</b>	
7.1	Background	107
7.2	Raw Materials and Processing	108
7.3	Thermal behavior of the dried Gel	111
7.4	Slurry Rheology	112
7.5	Effect of Naphthalene content on Strength and Apparent Porosity of porous HA	115
7.6	Porosity and pore size distribution of Gel Cast Porous HA scaffold	118
7.7	Microstructural Analysis of HA scaffold prepared by gel casting	120
7.8	In-vitro bioactivity and the formation of apatite layer	122
7.8.1	Effect of aging days on the morphology of apatite layer	122
7.8.2	Effect of porosity on the apatite layer formation	123
7.9	Dissolution Behaviour of Gel Cast HA scaffolds on aging in SBF	125
7.10	Cytotoxicity Behaviour	128
7.11	Conclusions	130
<b>Chapter 8</b>	<b>Porous Hydroxyapatite by Protein Coagulation Casting (PCC) Route</b>	
8.1	Background	131



8.2	Raw Materials and Processing	132
8.3	Results and Discussion	134
	8.3.1 Thermal Decomposition Behavior of EW	134
	8.3.2 Foaming Behavior and Foam stability	134
	8.3.3 Properties of dried and sintered Cast bodies	135
	8.3.4 Bulk Density, Apparent Porosity and Compressive strength of Scaffolds	138
	8.3.5 Pore size distribution	142
	8.3.6 Microstructural characterization of HA scaffold prepared by PCC	144
	8.3.7 In-vitro bioactivity	146
	8.3.7.1 Effect of aging days on the apatite layer formation	146
	8.3.7.2 In vitro bioactivity and the formation of apatite layer	148
	8.3.7.3 Dissolution behaviour of porous HA in SBF	149
	8.3.7.4 Changes in Ca <sup>+2</sup> and P <sup>+5</sup> ion concentration of SBF	149
	8.3.7.5 Effect of SBF aging of HA Scaffold on the pH of SBF	151
	8.3.7.6 Cytotoxicity behaviour of Porous HA Scaffolds	151
8.4	Conclusions	153
<b>Chapter 9</b>	<b>Conclusions and Scope for Future Work</b>	155-159
	<b>References</b>	160
	Curriculum Vitae	186

## **LIST OF FIGURES**

Page no.

### **Chapter 1**

Fig. 1.1	(a) Monoclinic (P21/b) (b) Hexagonal (P63)	2
Fig.1.2	Phase Diagram of CaO-P <sub>2</sub> O <sub>5</sub> System in presence of 500 mm Hg Water Vapour pressure	3
Fig. 1.3	Classification of porous materials by pore size and application areas	5
Fig. 1.4	Representative Fabrication processes of Macro-Porous Ceramics	6
Fig. 1.5	Different Stages of Foaming of an Aqueous Suspension	11
Fig. 1.6	Changes in the interfacial energy of foam on the absorption of colloidal particles at the gas-liquid interface	11
Fig. 1.7	(a) and (b) Stabilization of gas bubbles by colloidal particle, (c) adsorption of partially lyophobic particles at the gas-liquid interface	12
Fig. 1.8	Different Stages of Freeze Casting	14
Fig. 1.9	Microstructure of Porous HAP Samples Prepared by Freeze Casting	15
Fig.1.10	Porous Scaffold Fabricated by Stereolithography (SLA).	16

### **Chapter 2**

Fig.2.1	Synthesis of HA nanoparticles by two-step Hydrothermal route	26
Fig. 2.2	Effect of temperature, pH and hydrothermal duration on morphology, particle size and phase of CaP powder	27
Fig. 2.3	Schematic representation of the three important emulsion synthesis of HA nanoparticles	29
Fig.2.4	Spherical and Rod like morphology of HA nanoparticles by Reverse micelle system	29
Fig. 2.5	Synthesis of HA from Bio Wastes: (a) Mineral Extraction, (b) Egg Shells, (c) Skeleton of Marine organism, (d) Naturally derived Biomolecules, (e) Bio- Membrane	33

### **Chapter 5**

Fig. 5.1	Process flow chart for HA powder using Ca (NO <sub>3</sub> ) <sub>2</sub> .4H <sub>2</sub> O and (NH <sub>4</sub> ) <sub>2</sub> HPO <sub>4</sub>	73
Fig. 5.2	DSC-TG of amorphous calcium phosphate precipitates	73

Fig. 5.3	(a) XRD plots for powder calcined between 200 and 900°C	75
	(b) XRD pattern of HA calcined at different temperatures (200-900 °C) showing the triplet peak of HA in the 2θ range 30-40°.	76
	(c) XRD pattern of HA calcined at 750°C, 850°C, 900°C showing the triplet peak of HA, in the 2θ range 30°-40°	77
Fig. 5.4	FTIR spectrum of HA powder calcined at 850 °C	79
Fig. 5.5	Particle Size distribution of calcined HA	79
Fig. 5.6	FESEM image of HA particles calcined at 850, 900 and 1000 °C respectively	81
Fig. 5.7	Densification behavior of HA	82
Fig. 5.8	XRD pattern of HA sintered between (1000-1300 °C)	83
Fig. 5.9	FTIR spectra of HA at (a) 1250 and (b) 1300 °C	85
Fig. 5.10	Effect of sintering temperature on bulk density and porosity	86
Fig. 5.11	Effect of sintering temperature on compressive strength	87
Fig. 5.1.12	Microstructure of Fractured surface of HA sintered at (a) 1250 and (b, c) 1300 °C	88
Fig. 5.13	Effect of soaking time on the porosity and bulk density of sintered HA.	89
Fig. 5.14	Effect of soaking time on compressive strength of sintered HA	89
<b>Chapter 6</b>		
Fig. 6.1	DSC-TG of as pressed HA- 50NA pellet	91
Fig. 6.2	Variation of Apparent Porosity (AP) and Bulk Density (BD) of Sintered Scaffolds with NA content	92
Fig. 6.3	Pore Size distribution of HA-NA scaffold in different HA-NA Composition (a) HA-30NA, (b) HA-40 NA, (c) HA-50NA and (d) HA-60NA	93
Fig. 6.4	(a-e) Microstructures of different (a) HA-30 NA, (b) HA-40 NA, (c) HA-50 NA, (d) HA-60 NA, ( e) HA-70 NA	96
Fig. 6.5	(a) Strength vs. Apparent Porosity Plot of Porous HA-NA Scaffold	98
	(b) A plot $\ln \sigma$ vs. vol Percent Porosity	98

Fig. 6.6	Microstructure of different HA-NA scaffold (a) HA-30 NA, (b) HA-40 NA, (c) HA-50 NA, (d) HA-60 NA, (e) HA-70 NA	100
Fig. 6.7	Microstructure of HA-30NA scaffold for different aging time (a) After 3 days (b) Higher magnification of (a)(c) After 5 days (d) After 35 days.	101
Fig: 6.8	(a) Mechanism of Apatite formation in SBF	103
	(b) Weight loss behavior of HA scaffold as function of aging period	103
Fig. 6.9	Change in pH of SBF with aging time of HA-NA	104
Fig.6.10	Change in $\text{Ca}^{+2}$ concentration of SBF with aging time	105
Fig. 6.11	Change in $\text{P}^{+5}$ concentration of SBF with aging time	106

## Chapter 7

Fig. 7.1	Flowchart for Porous HA fabrication combining Gel Casting and NA addition	110
Fig. 7.2	Physical appearance of sintered HA scaffolds prepared by gel casting (HA-15NA, HA25NA, C-35NA and HA-45NA)	110
Fig. 7.3	DSC-TG of as dried gel of HA	112
Fig. 7.4	(a) Shear stress versus shear rate plot as a function of HA slurry as a function of solid loading	113
	(b) Viscosity-Shear rate plot of HA slurry as a function of HA solid loading	114
	(c) Shear stress – Shear rate plot for 55 vol% solid loading	114
	(d) Variation of $\tau_{\text{gel}}$ of HA slurry with variation of HA solid loading	115
	(e) Variation of steady state viscosity as a function of HA solid loading	115
Fig. 7.5	(a)Variation of Apparent Porosity of Gel Cast HA Scaffold as a function of Naphthalene content	116
	(b)Variation of Compressive Strength as a function of Porosity.	117
	(c) A plot $\ln\sigma$ vs Porosity for HA Scaffold	117

Fig. 7.6	(a-e) Pore size distribution of Sintered HA scaffolds prepared by Gel Casting (a) HA-0 NA, (b) HA-15NA, (c) HA-25NA, (d) HA-35NA, (e) HA-45NA	119
Fig. 7.7	FESEM microstructure of Gel Cast sintered HA scaffolds prepared by combination of Gel Casting and NA addition (a) HA-0NA, (b) HA-15NA, (c) HA-25NA, (d) HA-35NA and (e) HA-45NA.	121
Fig. 7.8	(a-g) Effect of Aging time on the growth of apatite layer of HA-35 NA as a function of (a) 3 days (b) 5 days (c) 7 days (d) 14 days (e) 17 days (f) 21 days and (g) 28 days	122-123
Fig.7.9	(a), (b), (c), (d), (e) represent FESEM of aged HA-0NA, HA-15NA, HA-25NA, HA-35NA, HA-45NA after 21days.	124-125
Fig.7.10	Change in the $Ca^{+2}$ concentration of SBF with increase in the Aging Time of HA	126
Fig. 7.11	Change in the $P^{+5}$ concentrations of SBF with the increase in Aging Time of HA	126
Fig. 7.12	Dissolution of Porous HA as function of Aging Time	127
Fig. 7.13	Effect of Aging time on the pH change of SBF solution	128
Fig. 7.14	Fluorescence microscopy images of mouse osteoblasts cultured in HA scaffolds after 24h incubation in cell culture medium. (a) Control, (b) HA-25NA, (c) HA-45NA.	129
Fig. 7.15	Cell viability index of HA scaffolds. Proliferation is shown relative to control	130

## Chapter 8

Fig. 8.1	Processing of Porous HA using Protein Coagulation Casting (PCC) method	133
Fig. 8.2	Thermal Decomposition Behaviour of pure Egg White	134
Fig. 8.3	Viscosity of the pure egg white with temperature	137
Fig. 8.4	Effect of porosity on compressive strength for different solid loading	140
Fig. 8.5	Microstructure of 35% solid loading samples prepared from different EWH ratio, (a) EWH 1:4, (b) EWH 1:3, (c) EWH 1:1	141

Fig. 8.6	Microstructure of 30% solid loading samples prepared from different EWH ratio, (a) EWH 1:4, (b) EWH 1:3	142
Fig. 8.7	Microstructure of 25% solid loading samples prepared from different EWH ratio, (a) EWH 1:4, (b) EWH 1:3	142
Fig. 8.8	Pore size distribution for HA scaffolds prepared from varying EWH ratio and different solid loading.	143
Fig. 8.9	Microstructure of porous HA prepared with EWH ratio 1: 1 and varying solid loading (a) 15 vol% (b) 25 vol% (c) 30 vol % and (d) 35 vol%	145
Fig. 8.10	Microstructure of Porous Hydroxyapatite prepared with EWH ratio 1:2 (a) 25 vol% Solid loading (b) 30 vol% Solid loading	146
Fig. 8.11	Microstructure of Porous HA at 25 vol% Solid loading at EWH ratio 1:3	146
Fig. 8.12	Effect of aging time on the apatite layer formation of porous HA Scaffold prepared from 1:3 EWH and 30 vol% Solid loading. Fig (a-e) represents 3, 14, 17, 21 and 28 aging days respectively.	147
Fig. 8.13	FESEM images of EWH scaffolds after 21 days aging in SBF (a) 25 vol%, (b) 30 vol%, (c) 35 vol%	148
Fig. 8.14	Weight loss behavior of porous HA on SBF aging for different time	149
Fig. 8.15	Change of $\text{Ca}^{+2}$ concentration of SBF after aging of HA for different times	150
Fig. 8.16	Change of $\text{P}^{+5}$ concentration of SBF after aging of HA for different times	150
Fig. 8.17	Effect of SBF aging of HA on pH of SBF solution	151
Fig.8.18	Cell viability index of two HA scaffold samples prepared from different EWH ratio at two different solid loading (25 and 30 vol %). The cell proliferation is shown relative to the control sample.	152
Fig.8.19	Fluorescence microscopy images of mouse osteoblasts cultured in HA scaffolds after 24 h incubation in cell culture medium. (a) Control, (b) 25 vol% (1:3) [b], (c) 30 vol% (1:4)	153

## LIST OF TABLES

### Chapter -1

- 1.1 A summary of the Porous Hydroxyapatite Scaffold Fabrication Method used in Literature 17

### Chapter-2

- 2.1 A Comparison of Various Synthesis Method used in the literature for HA powder preparation 34
- 2.2 Different Shape Forming Methods and the Factors affecting the Processing 47

### Chapter 4

- 4.1 Batch Composition for SBF preparation 69

### Chapter 5

- 5.1 Change in the d-spacing of the three prominent HA peaks as a function of calcination temperature 78
- 5.2 Change in the d-spacing value of HA as a function of HA sintering temperature 83

### Chapter 6

- 6.1 Bulk Density, Apparent Porosity, Closed Porosity and Strength of porous scaffolds prepared by solid state route 99

### Chapter 7

- 7.1 Components of Gel casting slurries 109
- 7.2 Slurry composition for scaffold preparation 111
- 7.3 Bulk Density, Apparent Porosity and Compressive Strength of Porous HA scaffolds prepared by Gel Casting. 118

### Chapter 8

- 8.1 Raw materials and their Functions 133
- 8.2 Foaming behavior of pure EW as well as different EWH compositions 135
- 8.3 Defects in the as dried bodies made from different EWH ratio and different solid loading 138
- 8.4 Bulk Density, Apparent Porosity and Compressive strength of Scaffolds 139

### Chapter 9

- 9.1 Summary of the major characteristics of the scaffolds prepared by three different routes used for this study 158

## **ABSTRACT**

Porous Hydroxyapatite (HA) scaffold has been prepared from stoichiometric HA powder. The HA powder has been prepared in the laboratory by the wet chemical method. The as-prepared powder was amorphous. On calcination at 850°C, stoichiometric HA powder crystallized. The HA phase was stable till 1250°C and Tricalcium phosphate (TCP) formed at 1300°C.

The HA scaffolds were prepared by three different routes. In the Solid State Fugitive route, porous HA scaffolds were prepared by mixing HA powder and Naphthalene (NA) granules. Five different volume percent (30, 40, 50, 60 and 70) NA was used. At a lower NA content, mostly isolated open pore were observed. Large and interconnected pores were seen at 50 and 60 vol% NA addition. The strength - porosity variation showed an inverse relation and the strength was low at 60 vol% NA. At 70vol%, NA strength could not be measured due to the fragile nature of the sample. The microstructures of Simulated body Fluid (SBF) aged porous HA scaffold show that apatite formation starts from the surface of large grains.

The scaffolds prepared by Gel Casting Route had only 22% porosity. When NA was additionally added, the porosity and interconnectivity increased. At 45vol% NA addition, the pores were mostly open pores. The interconnectivity increases with the increase in NA content. At 45 vol% NA, the compressive strength was 0.96 MPa. In-vitro bioactivity showed that the apatite growth was more in higher porosity samples. With the increase in aging time, the morphology of the deposited apatite changed from granular to flower like. After 21 days aging, petal-like apatite crystals were observed.

Porous scaffolds were also prepared by Protein Coagulation Casting method using Egg white as the foaming and binding agent. The foaming behavior was modified by varying the Egg White: Water (EWH) ratio (1:1, 1:2, 1:3, and 1:4). The foaming was less at higher water contents. The foaming was also less in pure Egg white sample. It was also noted that at a higher Egg White: Water ratio, foaming was more. At any EWH ratio, the minimum solid loading that could be cast without cracking was nearly ten times the foam height. The cracking of the samples at a lower solid loading was related to the fast foam drainage rate. Use of Poly-vinyl alcohol (PVA) and Nitric acid (HNO<sub>3</sub>) reduced the drainage rate and



reduced the cracking tendency. The in-vitro bioactivity tests showed that the apatite crystals were globular shaped. The porosity development was non-uniform in the Protein Coagulation Casting method.

In the summary, it can be said that the three different methods of scaffold preparation produced different microstructures and pore sizes. The different microstructures resulted in varying compressive strength and bioactivity.

**Key Words:** Hydroxyapatite (HA); Scaffolds; Porosity; Gel-Casting; Protein Coagulation Casting; In-vitro bioactivity;

## **Organization of the Thesis**

The present thesis is the outcome of the research work on Processing of Porous Hydroxyapatite by different Methods and their characterizations. For this purpose, the HA powder was synthesized in the laboratory. For systematic description and discussion of entire work, the thesis has been divided into 9 Chapters. The brief contents of different Chapters has been described below:

### **Chapter-1**

Chapter-1 starts with a brief general introduction to HA, its phase stability and the need for making a porous HA. A general description of the fabrication of porous ceramics follows this section. Finally, a consolidated list has been provided detailing the methods that have been used in the literature for porous HA fabrication.

### **Chapter-2**

This Chapter describes the available literature in the area of Porous Ceramics. Since, the porous HA scaffolds were prepared from HA powder prepared in-house, the first part of the Chapter has discussed the literature on HA powder synthesis. The second part of the Introduction has discussed the literature on scaffold preparation, and the third part has summarized the literature on in-vitro bioactivity.

### **Chapter-3**

Chapter 3 has summarized the principles of scaffold fabrication and literature on powder synthesis and scaffold fabrication that has been elaborated in Chapter 1 and 2 respectively. The Chapter has also identified the area on which research can be done. This is followed a work plan to be executed in the present thesis.

### **Chapter-4**

This Chapter has discussed all the Characterization details and the working principles of the different Characterization Techniques used in this study.

### **Chapter-5**

Chapter-5 compiles the results of HA powder synthesis from the wet chemical method. Powder processing phase evolution, phase stability, strength and microstructure of the Calcined and Sintered HA has been discussed in this Chapter.

## **Chapter-6**

This Chapter discusses the HA scaffold fabrication by a Fugitive method using Naphthalene (NA) granules as Pore Former. The effect of NA content on the porosity, strength and microstructure has been discussed. The role of microstructure on the in-vitro activity has also been discussed.

## **Chapter-7**

This Chapter elaborates the HA scaffold preparation by gel casting route with Methyl Acrylamide (MAM) and Methylene-Bis-Acrylamide (MBAM). In this scaffold preparation method, NA was additionally used as a pore forming agent. The effect of NA addition during Gel Casting has been discussed with respect to the microstructure, strength, and in-vitro bioactivity.

## **Chapter-8**

Chapter-8 describes the HA scaffold preparation by Protein Coagulation Casting method using Natural Egg White as a pore former. The effect of Egg White: Water (EWH) ratio on the foaming behavior, foam stability has been discussed. The microstructure, strength, and in-vitro bioactivity has also been explained.

## **Chapter-9**

In this Chapter, the entire work is summarized, and the outline for the future work has also been provided.

Further, it is important to note that all the references have been compiled together as a separate Reference list after 9<sup>th</sup> Chapter. Each reference has been tagged with the Chapter number.

# *Chapter 1*

## *Introduction*

# 1. Introduction

Calcium Phosphate based ceramics is an important member of biomaterials family. To be used as a biomaterial, the calcium phosphate compound should show a certain degree of bioactivity and bioresorbability [1.1-1.3]. Among the different calcium phosphates, Hydroxyapatite (HA)  $[(Ca_{10}(PO_4)_6(OH)_2)]$  and Tricalcium Phosphate (TCP)  $[(Ca_3(PO_4)_2)]$  have been widely used as biomaterials. While TCP shows a higher degree of bioresorbability and also bioactivity, HA shows bioactivity but limited dissolution [1.4]. In spite of being less bioresorbable than TCP, HA illicit better bio response when compared with other ceramic oxides, namely, Alumina and Zirconia [1.5]. It is also a proven fact that the bioactivity of HA is a complex issue and can be affected by powder synthesis method [1.2]. The other factors that affect the bioactivity are the degree of crystallinity, stoichiometry (Ca/P ratio), environmental effect ( $CO_2$ ,  $H_2O$  or dry atmosphere), sample porosity, etc.[1.2-1.4]. Porous HA scaffolds show different dissolution behaviour than a dense HA [1.6]. Among the porous material, the bioactivity differs between a macro-porous and a mesoporous scaffold. Since, this thesis is going to study and discuss the processing and properties HA scaffold, it will be justified to present first a brief introduction to HA. Accordingly, the Introduction will be presented in two parts. The first part will discuss the crystal structure, phase stability and instability of HA along with the need of porous HA. The second part will elaborate the different routes available for making a porous scaffold.

## 1.1 Hydroxyapatite

Hydroxyapatite (HA) is the mineral phase of apatite family. The chemical formula of HA is  $(Ca_{10}(PO_4)_6(OH)_2)$  having Ca/P molar ratio 1.67. The actual mineral phase of bone is Ca-deficient HA or bio-apatite with a variable Ca/P ratio from 1.5 to 1.67 [1.7]. It is thought that the slow bio-mineralization kinetics is responsible for Ca-deficiency in bio-apatite. HA exists in two different crystal structure, viz. hexagonal ( $a = b = 9.432\text{\AA}$ ,  $c = 6.881\text{\AA}$ ,  $\gamma = 120^\circ$ ) and monoclinic ( $a = 9.42\text{\AA}$ ,  $b = 2a$ , and  $c = 6.88\text{\AA}$  and  $\gamma = 120^\circ$ ) [1.8]. The two crystal forms of HA differ in the orientation of the  $(OH^-)$  groups. In the hexagonal variety, the two adjacent  $(OH^-)$  groups are oppositely aligned. On the other hand, the  $(OH^-)$  in monoclinic variety have the same direction within one column and different direction among the adjacent columns (Fig. 1.1(a and

b)). The crystal structure of HA permits wide compositional variations due to the possible replacement of  $\text{Ca}^{+2}$  and  $(\text{PO}_4)^{-3}$  by other cations and anions. While  $\text{Ca}^{+2}$  can be replaced by  $\text{Sr}^{+2}$ ,  $\text{Ba}^{+2}$ ,  $\text{Mg}^{+2}$ , the  $(\text{CO}_3)^-$  group can replace the  $(\text{PO}_4)^{-3}$  or  $(\text{OH})^-$ . Thus, two different type carbonated apatite (CA) (Type A and Type B) can result in anion substituted HA [1.6].

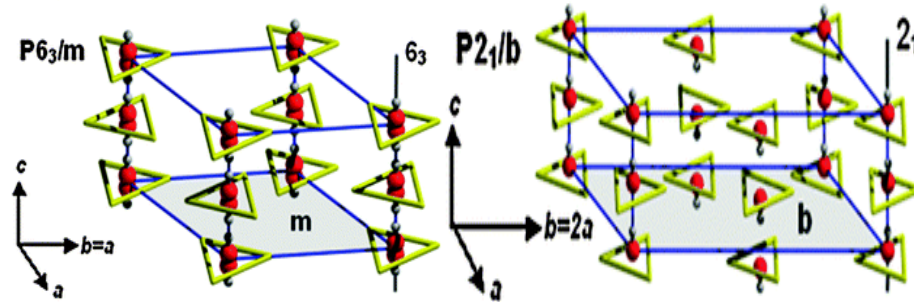


**Fig.1.1 Crystal Structure of HA (a) Hexagonal ( $\text{P6}_3/\text{m}$ ) and (b) Monoclinic ( $\text{P2}_1/\text{b}$ ) [1.8]**

These substitutions in the synthetic HA are often intentional to mimic the natural bone composition. It is claimed that the carbonated apatite crystals in the natural bone have both trivalent and divalent cation substitution [1.9]. These substitutions do not necessarily increase the crystallinity of HA and often causes distortions within the crystal lattice [1.6]. It is possible that these distorted HA show a different resorbability.  $\text{Sr}^{+2}$  and  $\text{Mg}^{+2}$  have been found to increase the solubility of HA. On the other hand,  $\text{Fe}^{+2}$  and  $\text{Mn}^{+2}$  have retarded the growth of HA. Quite often, the dopants have adversely affected the thermal stability of HA [1.10]. Webster et al [1.11] have observed that the divalent and trivalent doping have enhanced the adhesion and cell differentiation. It is also reported that  $\text{Sr}^{+2}$  and  $\text{Mg}^{+2}$  doping have reduced the osteoclastic activity and have enhanced the osteoblast activity [1.12]. Si substitution in HA has increased the bone apposition over pure HA. The anionic substitution like fluorine (Fluorapatite) and chlorine (Chloroapatite) have also increased the stability and crystallinity of HA [1.13-1.14]

The usually accepted crystal shape of Carbonated Apatite (CA) in the bone mineral is nano-rod shape [1.6]. However, there are contrasting viewpoints also; who claim that the original CA crystal is a thin plate-shaped crystal, and a rod-like or a needle-like shape can only happen during heat treatment [1.15].

The phase stability of calcium phosphate is influenced by pH, temperature, the environment, presence or absence of water vapour in the environment, Ca/P ratio, etc.

[1.4 - 1.6]. At the body temperature and in contact with body fluid or simulated fluid,  $\text{CaHPO}_4 \cdot 2\text{H}_2\text{O}$  (brushite) is stable for  $\text{pH} < 4.2$ . Above  $\text{pH} > 4.2$ ,  $(\text{Ca}_{10}(\text{PO}_4)_6(\text{OH})_2)$  (HA) is the stable phase. Some authors have verified and established that Ca/P ratio is one of the determining factors for dissolution of HA [1.10-1.16]. With respect to a dense HA, the dissolution increases in macro or microporous HA. The presence of water vapour also affects the phase stability of HA during sintering. De Groot [1.18] proposed the following CaO – P<sub>2</sub>O<sub>5</sub> phase diagram and stated that in the presence of water vapour, HA is stable up to 1350°C [1.16-1.17.]. The phase diagram is valid in the temperature range as shown in Fig. 1.2 and in the presence of 500 mm Hg water vapour pressure. The shaded area in the Phase diagram is used for HA stabilization

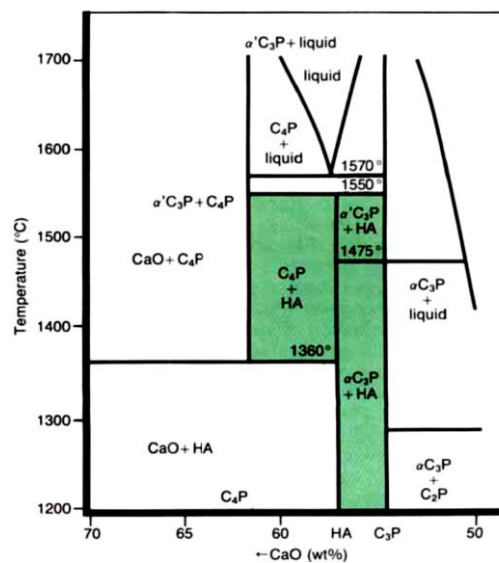


**Fig.1.2 Phase diagram of CaO-P<sub>2</sub>O<sub>5</sub> system in presence of 500 mm Hg Water Vapour pressure [1.18]**

Hench mentioned [1.4] that the bone bonding behaviour of dense HA and porous HA were different. Quoting Jarcho [1.19], Hench commented that an ultra-thin bonding zone is present in dense HA. This results in a steep gradient in the elastic modulus at the interface between HA and bone making the implant unstable. On the other hand, a macro-porous (pore size > 100µm) HA produced rapid tissue growth and good osteointegration [1.19-1.20]. Microporous HA has shown a remarkable improvement in bone formation [1.21]. Thus, porous HA is more suitable as a scaffold material in Tissue Engineering.

Thus, the second part will discuss the different types of porous material and the general method for preparing them. The techniques described in the following section are in general and not specific to the production of porous HA. Since the property

requirement of the porous material varies from one application to another, the methods are also many. Some of those methods have also been used for the preparation of porous HA.

Finally, the third part of the Introduction summarizes in a Tabular form, the widely used porous HA production method that have been compiled from the different literature.

## **1.2 Porous Ceramics**

According to the Griffith's Theory [1.22], ceramics is inherently brittle leading to catastrophic failure of a component made from ceramics. It was noticed that the residual pores were the origin of many such failures. Therefore, traditionally, attempts were made to make dense ceramics to minimize the residual porosity in the sintered samples and to increase the strength. However, dense ceramics exhibited poor thermal shock resistance as well as low fracture toughness. Thus, the second generation of advanced ceramics development focused on increasing the resistance to crack propagation. The research on advanced ceramics led to the development of porous ceramics. It has been well documented that pores, cracks, micro cracks were found to be effective crack arrestors [1.23]. A wide range of porous ceramics with porosity varying between 20-95% is now available for different applications areas. Some of the application areas are filtration [1.24-1.27], sound absorption [1.28], chemical filling [1.29], bio-ceramics [1.30], chemical sensors and catalyst supporters in many fields including metallurgy [1.31], chemical engineering [1.32], environmental protection [1.33] etc.

## **1.3 Classification of Porous Ceramics**

Porous samples have been classified into (i) macro porous structure (pore size larger than 50 nm) (ii) mesoporous structure (pore size between 2-50 nm) and microporous (pore size smaller than 2 nm). This classification is based on IUPAC [1.34]. Fig. 1.3 shows the classification along with the typical application. Fig.1.3 shows that, the pore size chiefly governs the application areas of porous materials. The Figure also shows that though filters are among the major application areas of porous ceramics, the pore size varies from one type of filter to another filter. Thus, while macro porous materials are used as diesel particulate filters, mesoporous materials are used for ultrafiltration with a molecular weight cut off of the matters (MWCO) being  $10^3$  - $10^6$ .



Micro filters are used for nano filtration (MWCO=200-10<sup>3</sup>) as well as reverse osmosis (MWCO=100). Since this thesis is dealing with macro porous scaffold materials, more emphasis will be focused on the processing of different macroporous materials although other porous materials will also be discussed, albeit briefly.

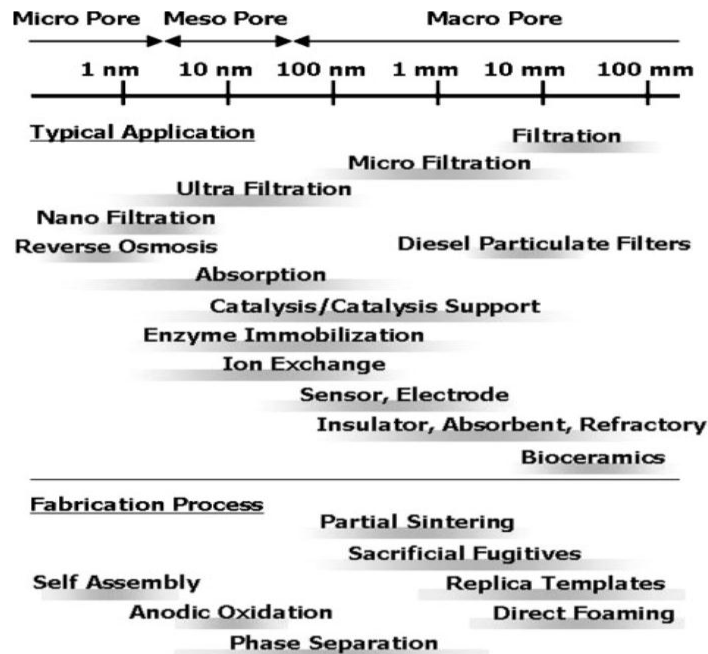


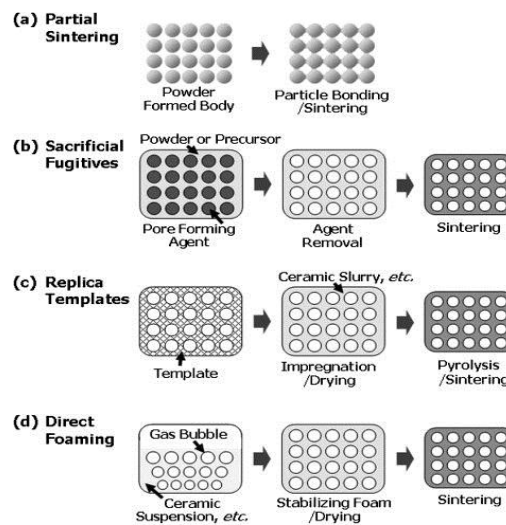
**Fig.1.3 Classification of porous materials by pore size and application areas**  
[1.13]

#### 1.4 Fabrication of Porous Ceramics

A review of the processing of porous materials summarizes four representative processing methods that are being widely used for porous material fabrication [1.29,1.35,1.36]. These four methods are (a) Partial Sintering Method [1.37,1.38] (b) Sacrificial fugitive removal Method [1.39] (c) Replica templates [1.40], (d) Direct foaming [1.41-1.42]. Besides these four, some other innovative scaffold fabrication methods have also been introduced recently. These are Rapid prototyping [1.43], Fusion Deposition Modeling [1.44], Stereolithography [1.45], Selective Laser Sintering [1.46], Additive Manufacturing and Micro-syringe Deposition Technique [1.47] and Paste Extrusion [1.48-1.49] etc. Over and above the porous structures mentioned above, another class of porous ceramics has also been put into use recently. Such porous ceramics is called hierarchal porous ceramics. Such porous ceramics consists of two or three different level of pore sizes - macroporous, mesoporous and macroporous integrated into a single body. Porous ceramics with such a hierarchical porosity level often proves to be advantageous in many specialized

applications due to the synergistic effects of each type of porous layer. The application areas of hierarchical porous ceramics include a catalyst, filters (for liquids or gases), extraction, separation, sorption, and scaffolds for biological applications [1.50]. These ceramics are prepared by different processing methods like templating [1.51], impregnation [1.36], phase separation [1.52], coating [1.53], leaching [1.54] etc.

The principle of macro-porous ceramics fabrication has been elaborated by Luyten [1.55]. In his review paper, Luyten has discussed those synthesis methods that are based on dry and wet powder processing techniques. The targeted applications of such ceramics are catalytic supports, diesel particulate filters, molten metal filters, biomedical scaffolds for tissue engineering and ceramic membranes. The four conventional routes for porous ceramics fabrication [Fig.1.4] have been reviewed by Studart et.al [1.29], Colombo et.al [1.31], Ohji et. al [1.56] and Hammel et.al [1.57]. In the following sections, the principles of these four conventional processing routes will be discussed. At the end, a brief discussion on the recent non-conventional routes that have been recently used will be included.



## 1.4 Representative fabrication processes of macro-porous ceramics [1.56]

### 1.4.1 Partial Sintering Method

The Partial Sintering method is the most conventional and one of the oldest routes for producing porous ceramics. As the name suggests, the sintering of powder compacts is terminated before the final stage of densification begins. The process leads to a stronger ceramics due to enhanced neck growth and bonding between particles resulting from evaporation-condensation or surface diffusion process [1.58]. The neck area (which governs bonding) and the pore size (and hence the porosity) is controlled

by the initial particle size of the compact and extent of particle sintering. A finer particle size will lead to a better sintered body as well as lower pore size. Therefore, as a rule of thumb; the particle size should be about 5 times the desired pore size [1.36]. However, porous ceramics produced through partial sintering method usually have less than 50% porosity, and, therefore, this route is not suitable for producing highly porous (> 50 vol% porosity) ceramics [1.38]. Several process modifications have also been adopted for making a strong but porous ceramics through partial sintering. Some of these methods are Pulse electric current sintering (PECS) [1.59-1.61], combination of Partial sintering and Powder decomposition [1.62], Partial sintering through reaction bonding [1.63-1.64], Oxidation- bonding process [1.65] etc. The PECS process, the more popular of the partially sintering variety was originally proposed by Oh et.al [1.66]. The process involves partial sintering of the prepared body in which an electric discharge between particles takes place during sintering. This phenomenon promotes neck growth and bonding between particles. The method has been successfully employed for Al<sub>2</sub>O<sub>3</sub> based porous ceramics. The combination of Partial sintering and Powder decomposition has also been successful in fabricating strong porous ceramics [1.67] in  $\alpha$ -Al<sub>2</sub>O<sub>3</sub>/Al (OH)<sub>3</sub> and ZrO<sub>2</sub>/Zr(OH)<sub>4</sub> system. Similarly, the processing route of partial sintering through reaction bonding has been employed for CaZrO<sub>3</sub>/MgO, CaAl<sub>4</sub>O<sub>7</sub>/CaZrO<sub>3</sub> and CaZrO<sub>3</sub>/MgAl<sub>2</sub>O<sub>4</sub> based porous ceramics system. The process is based on the principle of Decomposition sintering where the decomposed product/ precipitates formed on the grains initiate neck growth between grains. Porous Silicon nitride with high aspect grains has been partially densified by the addition of Yb<sub>2</sub>O<sub>3</sub> as a sintering aid. Green et. al [1.38] observed that the elastic modulus of the porous ceramics fabrication through partial sintering was 10% of the elastic modulus of the fully dense body.

#### **1.4.2 Replica Technique**

The replica technique for porous ceramics fabrication is probably among the oldest available techniques [1.40]. The basic principle involved consists of following three steps [1.68-1.70]:

- (i) to impregnate a cellular structure (or template) with the precursor solution or ceramic suspensions,
- (ii) to remove the excess solution /slurry from the pores of template after the template has been impregnated, so that only the solid part of the strut is coated with slurry and,

(iii) to remove the template by firing at high temperature so that only the ceramic skeleton remains. This method thus produces a positive replica of the template.

A large number of templates that have been used for replica technique can be broadly classified as (a) Synthetic templates and (b) Natural templates. Tiemann [1.71] has defined a template as a porogen only if a univocal relationship exists between porogen's own structure and the final structure of the porous material. Usually, the stable templates are hard pore forming agents. Ideally, a template should not alter its size during the forming operation. The complete removal of the template during the firing process should be easy, and resultant pores should have the same shape as that of the original template.

#### **1.4.2.1 Synthetic Template**

The majority of the synthetic templates are polyurethane foams (PU). They are also known as polymeric sponges and accordingly this technique is also known as Sponge replica technique [1.40]. This cheap, user-friendly and flexible method has been widely accepted in research laboratories and industries for producing macroporous ceramics [1.72]. The presence of sharp pore corners or edges are reduced the strength. A sharp pore corner was related to the inefficient draining of excess slurry from the impregnated polymeric sponge. Usually, roll processing is employed for squeezing out the liquid. The other method of removing the excess slurry is through centrifuging of impregnated scaffold [1.73-1.74]. It is claimed that this latter process is more efficient than roll processing [1.75-1.76]. Macro porous ceramics having 40-95% porosity could be prepared by this method. The pores have high interconnectivity with the minimum cell size being 200 $\mu$ m. However, the strength of these reticulated ceramics is quite low, particularly at high porosity level due to cracking of struts at higher porosity level [1.42].

#### **1.4.2. 2. Natural Templates**

Many natural cellular structures like wood, coral have unique pore morphology and complex pore microstructures, which cannot be reproduced synthetically. Therefore, wood structures and corals have been used as a template material for preparing macro-porous ceramics. The lost wax process or "replamineform" introduced by White et.al [1.77] is one such method used to replicate the natural coral structure. The method consists of obtaining a negative replica of the coral cellular structure by

replicating with molten wax. After the leaching of the external coral structure by acid treatment, macroporous ceramics are obtained by impregnating the negative wax replica with the slurry. Pyrolysis removes the wax replica during sintering. Hydrothermal treatment of cellular corals has converted corals to HA [1.78]. The biomimetic route can also be used to prepare porous ceramics from a wood template by converting wood to cellular carbon preform. The carbon preform thus obtained is either infiltrated with sol at room temperature or with gases at high temperature that on oxidation gives cellular ceramics [1.79].

#### **1.4. 3 Sacrificial Fugitives**

Sacrificial Fugitive route for porous ceramics fabrication is also known as sacrificial template method. In this method, a composite structure of ceramic and fugitive is made and on the removal of the sacrificial fugitive phase, a porous network is obtained. This porous network forms a negative replica of the sacrificial fugitive that has been used to prepare the two-phase composite structure [1.80]. Depending on the nature of fugitive, its removal can be through a pyrolysis step, a sublimation step or a washing step [1.81-82]. The composite is treated with an appropriate solvent for fugitive dissolution. In each of these fugitive removal steps, the prepared ceramic component should be rigid or strong to resist deformation of the porous structure during the fugitive removal step. One of the critical steps in this processing is the preparation of a homogeneous biphasic composite. The three common routes for biphasic composite preparation are:

- (a) Compaction of a powder mixture containing the fugitive [1.80]
- (b) Slurry processing of the powder and fugitive followed by consolidation through wet colloidal routes like tape casting, slip casting, etc. [1.83].
- (c) Impregnation of pre - compacted porous network of fugitive with ceramic suspension [1.84].

The integrity of the final porous network will depend largely on how efficiently fugitives have been removed. This step is critical and often requires long thermal treatments at the appropriate temperatures [1.85]. Since, in this process, porosity, pore morphology and pore size are solely controlled by fugitives, this method, therefore, provides an opportunity for modifying the pore architecture through an appropriate choice of fugitives.

#### **1.4.4 Foaming Technique**

Both aqueous and non-aqueous foams have found wide application areas involving public life and industrial processes. Some of the primary applications of foams are in the fire extinguisher, packaging industry, food and cosmetics, as well as for manufacturing bulk porous material that can be used as insulators, filters, catalyst etc. [1.42].

##### **1.4.4.1 Direct Foaming**

The ceramic suspension can be foamed by introducing gas or air in the suspensions either through chemical reactions or by adding a foaming agent [1.42] or by mechanical frothing of the suspension [1.86-87]. The foam needs to be stabilized and retained during the processing and drying of the sample. The removal of the foam during sintering creates pores in the sample. This simple and easy process can produce a wide range of porous ceramics with porosity as high as 95% [1.88]. The critical issue in this method is the long term stability of the generated foam [1.89-1.90]. It has been observed that the liquid foams, thus produced have high interfacial gas-liquid area and therefore, do not possess long time stability. With time, the initially generated spherical gas bubbles grew to large polyhedral cells [1.91].

The destabilization of spherical foams results from the thermodynamic change taking place in the wet foam for reducing the overall free energy of the system. The three main destabilization steps are drainage (creaming), coalescence (film rupture) and Ostwald's ripening. When the gas and liquid phase of the foam get physically separated due to gravity effect, the phenomenon is known as "Drainage of liquid foam". As a result of drainage, the lighter gas bubbles move in an upward direction, and the heavier liquid moves down. The lighter and separated foams collect at the top and form a dense layer of bubbles which is known as "cream". With time, the bubbles collected at the top rearrange, cluster and deform to form highly packed large polyhedral cells. This phenomenon is known as "Coalescence" [1.92]. Fig. 1.5 shows the three stages of bubble formation and cluster formation. Coalescence is the process of merger of the two or more contacting bubbles into a single bubble. The addition of long chain surfactants stabilizes the bubbles by reducing gas-liquid interfacial energy [1.93]. Destabilization of bubbles due to the difference in the internal pressure of different sized bubbles is known as Ostwald ripening. The internal pressure difference results in the diffusion of gas from smaller bubbles to bigger bubbles. As a result big

bubbles grow and the smaller bubbles collapse. This factor can also be controlled by modifying the gas-liquid interfacial energy as mentioned in Fig. 1.5.

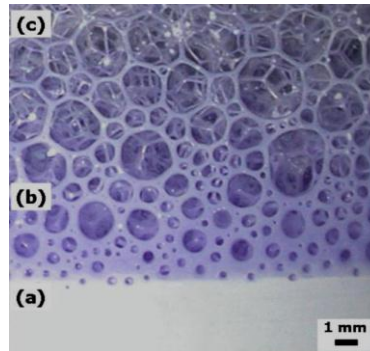


**Fig.1.5 Different stages of foaming in an aqueous suspension, (a) suspension stage (b) Suspension to wet Foam transition (c) Coalescence and Polyhedral structure formation [1.86]**

It has been observed that the addition of colloidal particles (to the foam) result in the attachment of bubbles to the particles. The colloidal particles get attached to the gas-liquid interface and lower the overall system energy [Fig. 1.6]. The energy of attachment is given by [1.94]

$$G = \pi r^2 \gamma_{LG} (1 - \cos\theta)^2 \text{ for } \theta < 90^\circ \text{ (When } \theta < 90^\circ) \dots\dots\dots (1.1)$$

$$G = \pi r^2 \gamma_{LG} (1 + \cos\theta)^2 \text{ for } \theta > 90^\circ \text{ (When } \theta > 90^\circ) \dots\dots\dots (1.2)$$

Where  $\theta$  is the contact angle and  $\gamma_{LG}$  is the liquid – bubble interfacial energy.

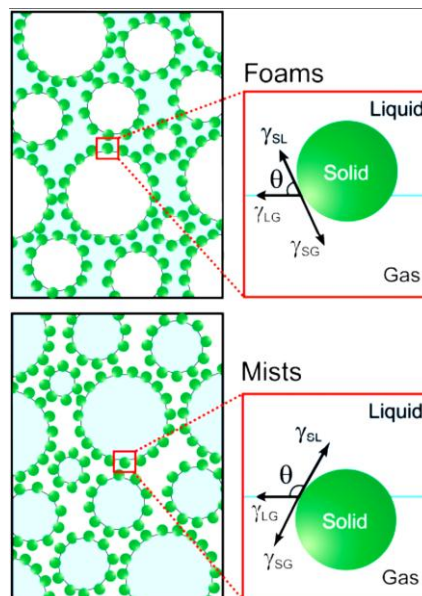


**Fig.1.6 Changes in the interfacial energy of Foam on the absorption of colloidal particles at the gas–liquid interface [1.95].**

However, it has also been noticed that long chain surfactants can only slow down the coalescence and disproportionation of bubbles but cannot prevent it [1.95]. Albumin

and other proteins show relatively better bubble stability but only for a limited period [1.96]. In view of the above, it can be concluded that porous ceramics prepared from direct foaming technique require a setting agents to “freeze” the microstructure well before initiation of the bubble coalescence and disproportionation starts. Accordingly, two types of foaming techniques are possible for the manufacturing of foamed ceramics - (a) Surfactant stabilized foams [1.42], (b) Particle stabilized foams [1.95]. The basic processing steps for these two techniques have been discussed in the following sections.

#### 1.4.4.2 Surfactant Stabilized foams

As discussed in the previous sections, the foam stability in a system can be enhanced by the adsorption of surfactants and biomolecules at the gas-liquid interface that decrease the interfacial energy  $\gamma_{LG}$ . The surfactants can be (i) short chain (low molecular weight) fatty acids and alcohols or (ii) long chains fatty acids and proteins [1.92]. In the former case, alcohols (ethyl, iso-butyl, iso-amyl) as well as acids (acetic, formic, butyric) acts as surfactants. The resultant foams are stable for a short period before coalescence. For the second case, long chain fatty acids (glycerol, polyoxyethylene) and proteins (albumins) [1.96] are the surfactants added for foam stabilization. The surfactants suitable for foam stability can be non-ionic, anionic, cationic and protein. Emulsification of a homogeneously dispersed alkane or air-alkane phase is also a unique method of direct foaming of aqueous ceramic suspension [1.86-1.87].

#### 1.4.4.3 Particle stabilized foams

Gonzenbach [1.95] reported that partially hydrophobic particles can be attached to the gas-liquid interface of foam which can help to stabilize the foam or bubble (Fig. 1.7).

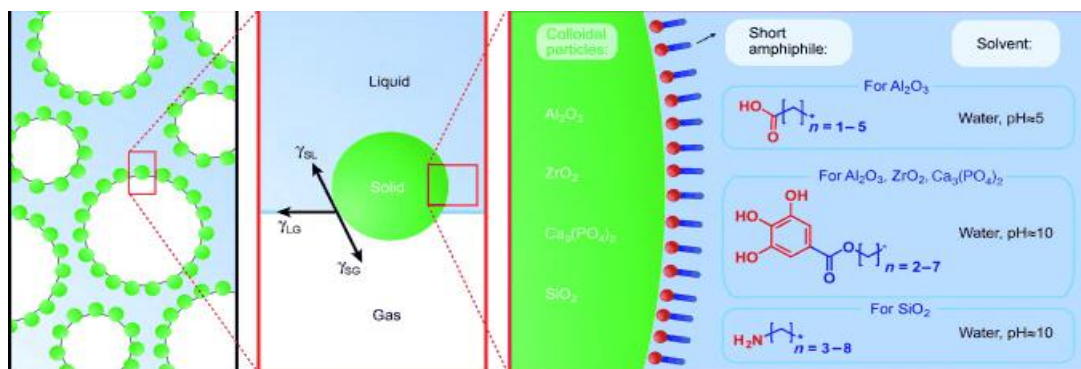


**Fig.1.7(a) and (b) Stabilization of gas bubbles by colloidal particle, (c) adsorption of partially lyophobic particles at the gas-liquid interface [1.95].**



The attachment of a partially hydrophobic particle requires an optimization of  $\gamma_{LS}$ ,  $\gamma_{LG}$  and  $\gamma_{SG}$  or in other words by the wetting of the particle by wet foam. The author also commented that appropriate surface modification of particles in suspension provides stabilization of a large gas-liquid interfacial area and provide long time stability of the foams. The surface lyophobicization of particles could be achieved through the adsorption of short-chain amphiphilic molecules on the particle surface. The amphiphilic molecules should have less than eight carbon atoms and should have high solubility and high critical micelle concentration in the aqueous phase. Fig. 1.7 represents the possible mechanism for particle attachment at the gas- liquid interface by modification of their surface wetting properties.

#### **1.4.4.4 Foam stability through in-situ polymerization and by Protein Coagulation**

One of the techniques for attaching stable foam is to incorporate a gelling substance that gel the porous structure so that the foams are “frozen” before they collapse. Typically, the gelling substances are organic monomers like methyl methacrylate [1.97], acrylamide and another acrylate [1.98]. Recently, many eco-friendly gelling systems have also been used. Some of these are potato starch, agar, agarose, etc. These monomers can be polymerized by adding a peroxide-amine as an initiator and catalyst. The induction period for the start of the reaction should be long enough for completion of casting but short enough for arresting the film drainage. The dried gel is heated to remove the polymers and then sintered to obtain porous macro structure [1.42]. The gel is known to retain the foamed structure, preserving both the micro and the macrostructures [1.100].

Protein Coagulation Casting (PCC) is another type of direct foaming technique that use Egg-White as the protein source [1.96]. However, besides egg-white, other natural or synthetic proteins (e.g bovine serum albumin) can also serve the same purpose [1.100]. The process depends on the foaming ability of the protein that can be enhanced by modifying the surface active properties. The adsorption of amphiphilic protein molecules at the air-water interface alters the hydrophobicity as well as surface tension thus enabling foaming of the suspension through a mechanical agitation. During the foaming process, the agitation breaks down the protein structure causing unfolding of protein chains. On thermal treatment, an irreversible three-dimensional gel network forms and the cast body turns into the rigid body with

porosity [1.96]. The total porosity obtained through PCC process is dependent on the fraction of protein, solid loading and viscosity of the suspension.

In the preceding sections, the four major methods for porous ceramic processing viz. Partial Sintering method, Sacrificial fugitive removal method, Replica templates and Direct foaming have been briefly discussed. There are a few other processing techniques that have also been used for porous ceramics fabrication. These are Freeze casting [1.101] Hydrolysis Assisted Solidification method [1.102], Additive manufacturing [1.103], Direct fused deposition [1.104] etc. The processing principles of these methods are briefly discussed in the following sections.

### 1.4.5 Porous Ceramics through Freeze Casting

In the freeze casting technique, an aqueous or non-aqueous suspension is cooled below the freezing temperature of the solvent so as to solidify the solvent. For example, in the case of an aqueous suspension, water is frozen out as ice. The frozen solvent is removed through sublimation process on heating the suspension at low pressure. This removal of solvent makes a porous structure with unidirectional channels (Fig.1.8 and 1.9) [1.105]. The solidification conditions are decided by the solvent used for making the slurry. While sub-zero temperature is required if the solvent is water, room temperature is sufficient to solidify camphene based suspensions. The directional solidification of solvent and its removal results in porous channels that run from bottom to top of the sample. The morphology of the channels is solvent dependent. Ice crystals give lamellar pores; camphene or camphene /naphthalene result in dendritic pore morphology.

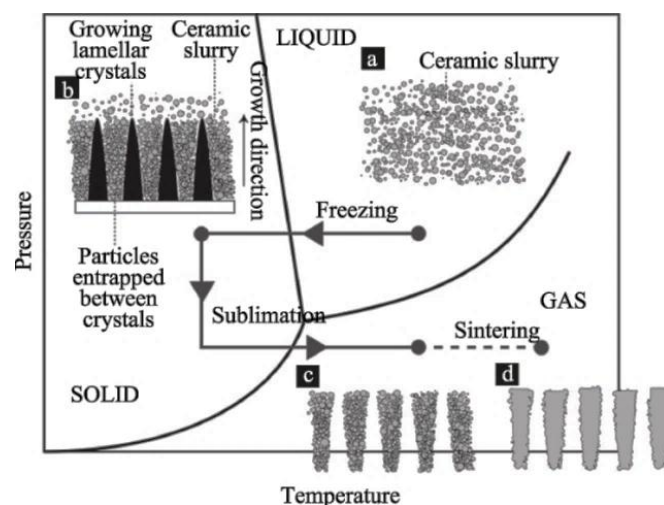


**Fig. 1.8 Different Stages of Freeze Casting [1.106]**

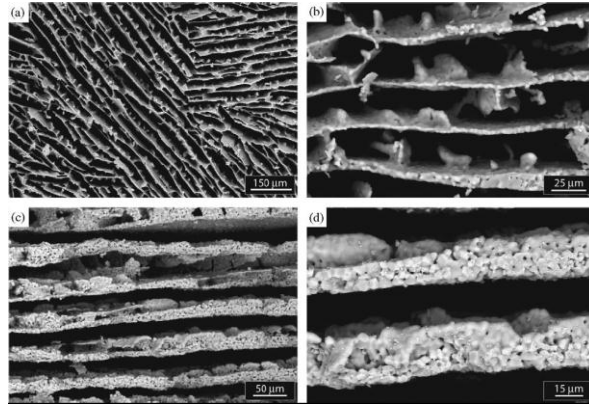


**Fig. 1.9 Microstructure of Porous HA samples prepared by Freeze Casting [1.107].**

A porous structure form is the result of the interaction between the solidification front and the ceramic particles. Two factors need to be satisfied for obtaining porous ceramic samples via Freeze Casting. These are: (a) the ceramic particles in the suspension must be rejected from the advancing solidification front and entrapped between the growing crystals and (b) the solidification front must have a non-planar morphology. The freeze casting methods have been widely used for processing porous biomaterials for tissue engineering. The unidirectional porous structure obtained through this route closely mimic the natural biomaterials. The method is also used for preparing a host of other porous materials with good interconnectivity for use in SOFC, electrodes, Catalytic filtration/ Separation devices.

#### **1.4. 6 Porous Ceramics using Additives Manufacturing Techniques**

Although, the processing routes for macro-porous ceramics that have been discussed till now are widely used for the preparation of porous scaffolds and porous materials; these methods suffer from one inherent defect. The tailoring of pore morphology, pore size, and pore interconnectivity with no closed pore condition is difficult to achieve. In other words, fine-tuning of the macro porous ceramics is not possible. The resultant scaffolds often have low strength and variable properties. Additive Manufacturing Technique (AM) is among the newer technique that is gaining popularity because of certain potential benefits [1.108]. The wide versatility of the Additive manufacturing or Rapid Prototyping software permit custom-made parts or microstructure to be fabricated without using expensive tooling or moulds (Fig. 1.10). It is claimed that the microstructural control of the prepared scaffold is better as compared to other traditional pore forming technique. There are two different modifications of Additive

manufacturing technique-(i) The direct AM fabrication and (ii) The indirect AM fabrication. In the direct AM fabrication, the porous ceramic structure can be fabricated directly using ceramic powders, colloidal solutions, or paste. The scaffolds are prepared by 3D printing [1.109] alone or in combination with a micro-syringe system [1.103]. The calcium polyphosphate ceramic component is developed layer by layer. The sacrificial photopolymer layer is introduced through a micro-syringe. The removal of the sacrificial photo-polymeric removal during subsequent heat treatment results in a porous scaffold.

In the indirect AM technique, a polymer or wax mould is created using AM technique that serves as the negative replica of the desired ceramic structure. The ceramic slurry is cast into the mould and after setting and hardening; the mould is removed by heating. Moulds have also been prepared using stereo lithography, inkjet printing, etc. [1.109]. As already mentioned, Rapid prototyping (RP) has emerged as one of its kinds for part manufacturing technique for low volume production items. In this technique, the parts can be directly fabricated using CAD data description without the need for any specific part or any specific tooling. The tool creation, as well as the part fabrication, can be done by RP technique itself [1.110]. The technique requires a Fused Deposition Modeling (FDM) machine for controlled porosity fabrication. One of the unique features of FDM technique is the accurate control of pore size, shape as well as the internal architecture of the porous body.

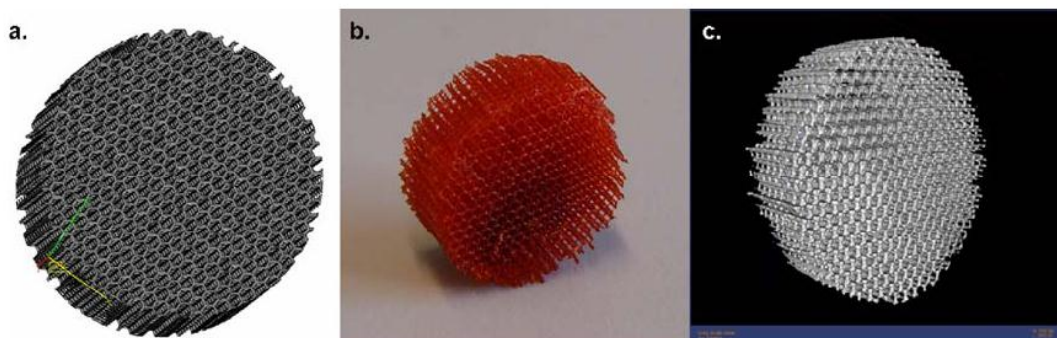


**Fig. 1.10 Porous HA Scaffold fabricated by stereolithography (SLA). (a) Model generation by CAD, (b) Fabricated scaffold, (c) Micro-CT scan of the scaffold.**

**[1.110]**

In the next page, Table 1.1 summarizes the different scaffold fabrication methods that have been used for preparing porous HA scaffolds.

**Table 1.1 Porous Hydroxyapatite Scaffold Fabrication Method**

Fabrication Method	Pore Forming Agents	References
Use of a porous structure using volatile pore former	Napthalene, PVA, PMMA, Polystyren microspheres, lentil, sugars, sago, sucrose	Yasuaki (1995) [1.15], Shi Hong Li et al (2003)[1.16], Tas et.al (2004) [1.117], B. Kundu et. al (2004) [1.118], M. Klenke et. al (2007) [1.119], Tang et.al (2008) [1.120], A. Amera et. al, (2011) [1.121], Ray.et.al (2010) [1.122] D. Tadic et al.(2004) [1.123], Sopyan et.al (2007) [1.124]
Admixture of water soluble porogen	NaCl, NaNO <sub>3</sub> , KCl	
Solvent casting/salt leaching	NaCl	Bartol et al.[1.125]2008, Wosek et.al 2015[1.126], Mehrabnian et.al 2011[1.127]
Replamineform process	Marine corals, Marine vertebrate	White and co-workers (1972) [1.128], Ohgushi et. al (1992) [1.129], Weindling et.al (1992) [1.130],Nandi et.al (2015) [1.131]
Direct foaming Technique	H <sub>2</sub> O <sub>2</sub> ,CaCO <sub>3</sub> , Citric Acid, Carbonic salts	I.H. Arita et. al (1995)[1.132], Dhara et al (2001)[1.134], Itatani et al (2003)[ 1.135], A F Lemos et. Al (2004)[136], Potoczek M et.al[122], (2008), Spoyan[1.137]
Starch consolidation Method	Starch	0. Lyckfeldt et.al (1997)[138], Rodriguez-Lorenzo et. al (2002)[139], Ahmed et.al (2015) [140]
Selective Laser Sintering	PLLA microspheres	Shuai 2013[1.141], Zhou 2008[142],Zhou 2010[1.143], ,
Electrophoretic deposition	No fugitive. The porosity was controlled by deposition thickness	Ma et.al (2003)[1.144], Yousefpour (2007)[145], Farrokhi-Rad(2014)[1.146]
Polymeric sponge method	Sponge	K. Schwartzwalder et.al, 1963 [1.147], Woyansky et.al (1992)[1.148], Sopyan (2009)[1.149], Jo et. al, (2009)[1. 150], Ramay et al. (2005)[1.151]
Microwave vacuum sintering	Tri-sodium citrate	Sundaram et.al (2008) [1.152], Feng et. al 2014 [1.153]
Rapid prototyping or solid freedom fabrication	3-D porous prototype made by layer by layer manufacturing technique	Brady and Halloran and Wilson et al.(1997)[1.154,1.155], Armillotta (2008)[1.156 ], Kim 2011[1.157]

## 1.5 Porous Hydroxyapatite and its Biomedical Applications

In recent years, (HA) has been widely used as a material for orthopedic and dental applications due to its close chemical similarity to the inorganic component of bone.

Its enhanced biocompatibility and bioactivity help to restore the damaged calcified tissues [1.23]. It is widely used for various bone repairs and as coatings for the metallic artificial device to improve their biological properties. The porosity aids in tissue growth and their bonding with the HA. However, the lower mechanical strength of pure HA has hampered its use as a bone implant material because of conflicting requirements of porosity and strength [1.111, 1.112]. HA having controlled pore size distribution as well as the interconnecting porosity exhibits strong bone bonding ability. The interconnected pores provide the pathway through which tissue growth can take place leading to a strong mechanical and biological fixation of the implant with the host tissue [1.113]. The dimension and the morphology of the pores are crucial factors for better osteointegration. It is accepted that a pore sizes in the range of 100-150  $\mu\text{m}$  is required for both bone in-growth and blood supply, but osteoconduction could be possible even with 50  $\mu\text{m}$  pore size. However a higher pore size in the range (200-500  $\mu\text{m}$ ) is desirable for colonization of osteoblast, fibrovascular in-growth and the deposition of new bone. [1.114].

Therefore, although porous HA is gaining importance in Tissue Engineering, the control of pore size and pore microstructure, pore interconnectivity and the mechanical load bearing capacity are critical factors in determining the end utility [1.112]. It is also a well-known fact that ceramic materials are inherently brittle, and the load bearing capacity of any material (including ceramic materials) has an inverse strength –porosity relationship. To overcome the strength-porosity conflict, bio-composite has been prepared involving HA and a bio polymer. Though it has solved the issue, the objective of preparing a suitable (conforming to the acceptable limit of strength and pore size issue) scaffold only with HA remains an active subject of research [1.111-1.114]. The difficulties observed in the preparation of such a scaffold has provided the stimulus for the present work.

# *Chapter 2*

## *Literature Review*

## 2. Literature Review

### 2.1 PART-A: HYDROXYAPATITE POWDER SYNTHESIS

Calcium phosphate based ceramics, because of its good biocompatibility are effective as a bio ceramic material. The two more important members of this group are Hydroxyapatite  $\text{HA}(\text{Ca}_{10}(\text{PO}_4)_6(\text{OH})_2)$  and  $\beta$ -TCP  $(\text{Ca}_3(\text{PO}_4)_2)$ [2.1]. HA is an important constituent of natural bone, and efforts have been made to mimic properties of natural bone in the synthetic HA. Synthetic HA has shown reasonably good bone bonding ability though it is inferior to bio-glass. When integrated with musculo-skeletal system, HA does not show any toxic side effects. The low mechanical strength of HA prevents it from being used in load bearing applications [1.4]. Efforts have been made to improve the strength of HA either by changing the crystal shape or by doping with  $\text{Mg}^{+2}$  and  $\text{Zn}^{+2}$  to simulate the HA crystals found in natural bone [2.2]. Another factor that also affects the applicability of HA is the phase stability and dissolution behaviour of synthetic HA. A single phase, pure, highly crystalline HA is stable till  $1300^\circ\text{C}$ , but the temperature range of phase stability changes with the degree of crystallinity, impurities, as well as Ca/P ratio. A poorly crystalline material as well as a Ca-deficient HA (Ca/P<1.67) will partially change to  $\beta$ -TCP about  $1200^\circ\text{C}$  [2.3]. In-vivo Bio-resorbability is the other factor that affects the performance of HA. A pure HA is less bio-resorbable and on the other hand,  $\beta$ -TCP is highly resorbable. In extreme cases, the high resorbability of TCP destroys the scaffold before appreciable bone bonding has taken place. Therefore, it has been a regular practice to use an optimum mixture of HA and  $\beta$ -TCP for providing the desired level of bone bonding along with structural stability. It has also been noted and reported by many researchers that the stability of HA is also related to the HA powder synthesis method [2.4]. The type of precursors (solid/ liquid) as well as the powder processing route will alter the HA stoichiometry and particle size. The precursor types also affect the phase stability at high temperature [2.4,2.5]. It has generally been observed that finer is the degree of mixing of the starting powder/precursor; the closer is the synthesized HA composition to the stoichiometric composition. The increasing degree of mixing follows the trend:

Liquid-Liquid> Liquid-Solid> Solid-Solid

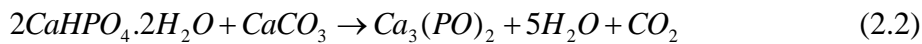
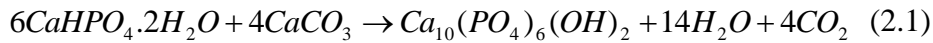


Thus, a reaction between two solid oxides (solid-state) will have the least degree of mixing and that between two liquid precursors (e.g Sol-gel coprecipitation, Spray pyrolysis) will have the highest degree of mixing and hence will produce stoichiometric HA compositions as well as fine HA crystals. The diphasic mixture containing a solid and a liquid precursor will have the intermediate degree of mixing. Therefore, from the phase stability view point, HA synthesized through sol –gel route, precipitation route and spray pyrolysis method will show a highly stable phase. The use of pressure-temperature correlation of aqueous or non-aqueous solvents gives two other exotic methods, viz. Freeze Drying and Hydrothermal Synthesis. In Freeze-Drying, the precipitation of crystals is triggered by reducing the temperature of a solution and in hydrothermal synthesis, the same result is achieved by using the combination of high pressure and high temperature. The other striking feature of these two routes is that the particle morphology can be altered by manipulating the synthesis parameters. It has been said by many authors [2.1.2.4] that the phase stability and bioactivity properties of HA largely depend on the stoichiometry of HA. Since the stoichiometry of HA will change from one processing route to another, it will also alter the particle size and bioactivity. While the solid state route is cheap and user-friendly, it compromises with the phase purity, stoichiometry. The process also needs high temperature processing and often re-calcination steps are required to complete the reaction. Many such issues are taken care of in the solution synthesis routes (precipitation, sol-gel, and spray pyrolysis, freeze drying, and hydrothermal synthesis) [2.4]. But these processes may require costly chemicals and detailed infrastructure. In the present day scenario, nearly all HA synthesis routes are solution based. Therefore, this section will put the focus on the solution chemistry-based routes. The solid state route will retain its usual importance.

### **2.1.1 Solid State Route:**

The Solid State route is the oldest technique involving the reaction between two or more solid reactants to form a compound. The starting materials may be two oxides or a mixture of carbonate and phosphate etc. For the typical HA powder, synthesis CaO (or CaCO<sub>3</sub>) and phosphate salts are being mixed in the molar ratio and reacted at high temperature (> 1000°C) to form hydroxyapatite (HA). The synthesized HA often shows a mixture of other compounds (CaO or TCP) along with HA. Sometimes long calcination time is also required to ensure better yield. Rao et.al. [2.5] carried out the Solid State Reaction between Tricalcium Phosphate (TCP) and Ca (OH)<sub>2</sub> (in the desired molar) at 1250°C. The product phase depended on the molar ratio between TCP and Ca

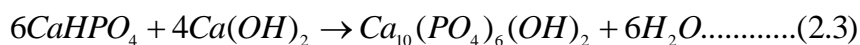
(OH)<sub>2</sub>. For 3:2 and 3:3 molar ratio, pure HA formed at 1000°C after 8 hours. When the CaP molar ratio was 3:1 and 3:1.5 HA and β-TCP mixture resulted and for 3:4 ratio HA and free CaO was obtained. It was also observed that the same phase distribution could be achieved by calcining the mixture for 2 hours between 1150-1250°C. Yang et.al [2.6] prepared biphasic HA and TCP mixture through the solid state reaction between CaHPO<sub>4</sub> .2H<sub>2</sub>O (brushite) and CaCO<sub>3</sub> at 1300°C for 2 hours. The solid state reaction for HA and TCP phase formation is given below



The authors observed that the different biphasic mixture of HA and β-TCP were formed by varying CaHPO<sub>4</sub>.2H<sub>2</sub>O and CaCO<sub>3</sub> ratio between 1.5 and 2.0. Koonawoot et.al [2.7] prepared HA via solid state reaction between CaCO<sub>3</sub> and (NH<sub>4</sub>)<sub>2</sub> HPO<sub>4</sub>. The calcination temperature was varied between 1150°C to 1300°C and the dwell time was varied from 2 to 5 hours. The HA phase formation was found to depend on the ratio of Ca:P, calcination temperature and dwell time. Even at the highest calcination temperature and at Ca/P=1.67, the phases after calcination were a mixture of HA, TCP, and CaO.

### 2.1.2 Mechano-Chemical Synthesis:

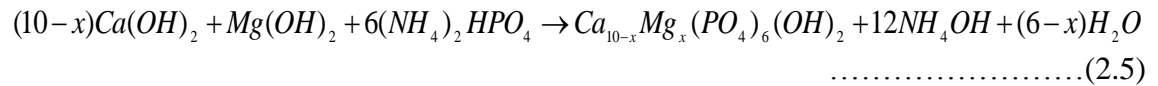
In an original mechano-chemical synthesis route, the compound is formed due to the intensive grinding of its mixtures. Originally developed for the synthesis of some “difficult to synthesize” compounds like silicides and carbides, the process has now been extended to a wide variety of compounds including oxides. Usually, the mechano-chemical synthesis is carried out in a small high energy mill called Spex mill. In the Spex mill the charge and the mill under goes low-frequency high amplitude vibration in all the three dimensions. Although, the exact mechanism for the compound formation by this process is not clear, it may be due to the initiation of a possible self-propagation high-temperature process after prolonged milling. The mechano-chemical synthesis process has now been extended to the synthesis of HA. Naisiri-Tabrizi et.al [2.8] synthesized nanorods and nano granules of HA through mechano-chemical synthesis. The raw materials were either CaHPO<sub>4</sub> + Ca (OH)<sub>2</sub> or CaCO<sub>3</sub> + CaHPO<sub>4</sub>. Depending on the raw materials, HA formed by the following two reactions:





It was observed that when HA formed according to the first reaction, residual CaHPO<sub>4</sub> was detected even after 80 hours milling. But for the second reaction, only HA was present even after 40 hrs of milling.

KCB Yeong [2.9] studied mechano-chemical synthesis of nano-crystalline HA starting from CaO and CaHPO<sub>4</sub>. The materials were mixed in the molar ratio of 3:2. It was observed that HA started to form only after 15 hours of milling. Between 15-20 hours, a mixture of HA and CaHPO<sub>4</sub> was present and single phase HA with average particle size of ~25nm. The resulting density was 98.20% at 1200°C for 2h. Sharifah Adzila et.al [2.10] synthesis Mg-doped HA by the planetary mill. The (Ca+Mg)/P molar ratio was kept 1.6. Intensive milling for 15 hours produced HA as per the following reaction.

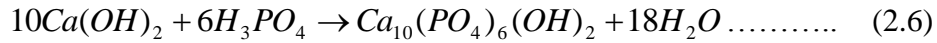


It was observed that with an increase in MgO upto 5mol%, the HA peaks loses its sharpness and the FWHM of the peaks increase. Rhee. et.al [2.11] investigated the effect of liquid medium used during milling (water and acetone) on the formation of HA phase. HA was synthesized by milling a mixture of Calcium Pyrophosphate (CaP<sub>2</sub>O<sub>7</sub>) and Calcium Carbonate (CaCO<sub>3</sub>). It was observed that the powder that was milled in water had single phase HA after 6 hours milling while the powder milled in acetone had TCP+HA phase.

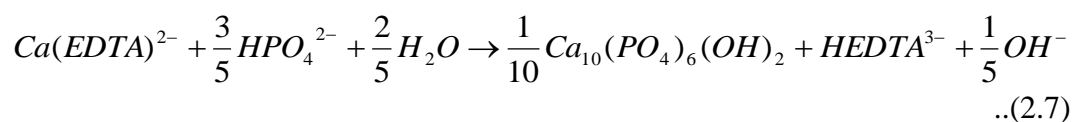
**2.1.3 Wet chemical route:**

The wet chemical route of powder synthesis is quiet popular among the researchers. The method ensures molecular level mixing of the precursors, homogeneity in the overall composition of the product, fine particle size, control of particle shape and size through the modifications of process parameters, etc. Among the difficulties, the requirement of an elaborate setup, cautious experimentation for reproducibility can be mentioned. However, as the advantage outweighs the difficulty, it is among the most widely used powder synthesis method. For HA, a host of chemicals as a source of Ca and P have been used till date. The list includes Ca(OH)<sub>2</sub>, Ca(NO<sub>3</sub>)<sub>2</sub>. 4 H<sub>2</sub>O, Ca(EDTA)<sup>2-</sup>, CaCl<sub>2</sub>, etc. for Ca source. Either NH<sub>4</sub>OH or NaOH has been used as the precipitating agent.

Akao et.al [2.12] prepared Ca-Phosphate using  $\text{Ca(OH)}_2$  and  $\text{H}_3\text{PO}_4$ . Though the authors could not stabilize HA, this process has been followed by later researchers for the synthesis of HA. Bouyer et.al [2.13] systematically studied the synthesis of HA nanocrystals. The authors followed the raw materials and chemical reactions of Tagai et. al. [2.14]



The reaction temperature was varied between 20°C and 850°C. It was observed that needle shape crystals were obtained at a lower synthesis temperature, and a more equiaxed crystal were obtained at high synthesis temperature. Tagai et.al [2.14] also observed that the reaction temperature determines the crystalline nature of HA. For a lower synthesis temperature ( $T < 60^\circ\text{C}$ ), single crystalline nano HA are obtained and for  $T > 60^\circ\text{C}$ , polycrystalline HA was observed. Jarcho et.al [2.15] used a mixture of  $\text{Ca(NO}_3)_2 \cdot 4\text{H}_2\text{O}$  and  $(\text{NH}_4)_2\text{HPO}_4$  to synthesis stoichiometric HA. They observed that to prevent agglomeration and to obtain fine particles ( $< 100\text{nm}$ ), the solution required be stirred for 24 hrs at room temperature. Kivrak et.al [2.16] prepared a wide variety of HA-TCP biphasic mixture using  $\text{Ca(NO}_3)_2 \cdot 4\text{H}_2\text{O}$  and  $(\text{NH}_4)_2\text{HPO}_4$ . They observed that the pH of the precursor solutions determined the final phase assemblage. It was noted that higher fraction of TCP was obtained when the pH of  $(\text{NH}_4)_2\text{HPO}_4$  and  $\text{Ca(NO}_3)_2 \cdot 4\text{H}_2\text{O}$  were 4.0 and 8.0 respectively. For a pH combination of 10.7 and  $> 9$  respectively, HA fraction was higher than 80%. It was also observed that the higher was the temperature of  $\text{Ca(NO}_3)_2 \cdot 4\text{H}_2\text{O} - (\text{NH}_4)_2\text{HPO}_4$  mixed solution, the higher was HA yield. For best result, the mixed solution temperature should be 65°C. Cunniffe et.al [2.17] synthesized nano HA powder through the wet chemical precipitation method. The starting raw materials were  $\text{CaCl}_2 \cdot 2\text{H}_2\text{O}$ ,  $\text{Na}_3\text{PO}_4 \cdot 12\text{H}_2\text{O}$ . NaOH was used as the precipitating agent. The authors observed that a reduction in the concentration of initial reaction reactants ( $\text{CaCl}_2 \cdot 2\text{H}_2\text{O}$  and  $\text{Na}_3\text{PO}_4 \cdot 12\text{H}_2\text{O}$ ) reduced the particle size of synthesized HA, but the yield was also lower. It was further noted that the pH of the reaction vessel was important in controlling the yield and particle size was obtained in the pH range 8-9.5. Janackovic et.al [2.18] prepared HA through a precipitation technique according to the following equation.



The precipitant was urea instead of NaOH, and it was noted that the urea addition in place of NaOH resulted in a homogeneous precipitation. The precipitated HA preferentially grew along (001) on increasing the reaction temperature, precursor concentration or reaction time. Manuel et.al [2.19] also synthesized HA from a mixture of  $\text{Ca}(\text{OH})_2$  and  $\text{C}_3\text{H}_6\text{O}_3$ . To the mixture,  $\text{H}_3\text{PO}_4$  was added to make  $\text{Ca/P}=1.67$ . The precipitation was carried out at  $\text{pH}=10$  upon the addition of  $\text{NH}_4\text{OH}$ .

#### **2.1.4 Sol-gel Synthesis:**

Sol-gel route of powder synthesis is a very reliable and reproducible method for powder synthesis. Since the components are mixed in the liquid state, a very homogeneous and stoichiometric composition could be achieved. The entire sol-gel process can be divided into two groups: (a) particulate sol-gel process, and (b) polymeric sol-gel process. In the particulate sol-gel, the sols contain 100nm particles dispersed in a suitable solvent. In the polymeric sol-gel process, the precursors are the alkoxides or the polymer derived precursors. Either of the sol-gel processes has been utilized for the synthesis of single and multi-components ceramic powder, ceramic fibers, coating, and bulk ceramics.

The extension of sol-gel process for the synthesis of stoichiometric HA is rather new. The sol-gel process provides molecular level mixing of Ca and P precursors which helps to achieve stoichiometric HA composition. By controlling the sol-gel process parameter, a wide range of particle morphology- i.e., spherical particles to elongated particles can be achieved. The finer initial particle size of HA permits low temperature (900-1000°C) sintering of HA, which in turn suppresses the possibility of HA-TCP decomposition. The advantage of the low-temperature processing of sol-gel derived ceramics is best utilized in coatings. In the normal plasma sprayed HA or HVOF HA coating, the extremely high deposition temperature (600-1000°C) provides difficulty of retaining the proper chemistry of deposited HA. The fast cooling rate of the coating also affects the chemistry and stability of HA coating. In contrast to this, the sol-gel coated HA coating provides better structural integrity of film and lower degradation of the underlying metal substrate. However, it is to be noted that even within the sol-gel process, different precursor sets provide different results. Different results may be obtained even when the same process of hydrolysis and polymerization reaction is followed. It was agreed among different researcher group that the chemical nature of the precursors controlled the stoichiometry as well as HA crystallization temperature. The results from some of literature on the sol-gel synthesis of HA have been provided in the

following paragraphs. Masuda et. al. [2.20] first synthesized HA using calcium diethoxide  $[\text{Ca}(\text{OEt})_2]$  and triethyl phosphate  $[\text{PO}(\text{OEt})_3]$  above  $600^\circ\text{C}$ . Gross et.al observed [2.21] that a minimum of 24 hours aging time is required for stabilizing and to obtain CaO free HA. Jillavenkatesha [2.22] used a mixture of Calcium acetate and Triethyl phosphate and prepared pure HA. Brendall et.al [2.23] prepared HA using  $\text{Ca}(\text{NO}_3)_2 \cdot 4\text{H}_2\text{O}$  and  $\text{C}_6\text{H}_5\text{PCl}_2$ , which were impure and poorly crystallized. The gel route of HA synthesis was investigated by Takahashi et.al [2.24]. Heating a mixed gel  $\text{Ca}(\text{NO}_3)_2 \cdot 4\text{H}_2\text{O}$  and Phosphonoacetic acid at  $700^\circ\text{C}$  produced HA. Qiu et. al. [2.25] made use of  $\text{Ca}(\text{NO}_3)_2$  and  $\text{NH}_4\text{H}_2\text{PO}_4$  to synthesize HA in a highly basic solution. HA was obtained on calcination at  $400^\circ\text{C}$ , and further increase in the calcination temperature only helped in the better crystallization of the synthesized HA. The low-temperature synthesis of HA was studied by Lopatin et. al. [2.26]. They utilized a combination of Calcium nitrate Tetra hydrate and N-butyl acid phosphate to prepare HA at  $300^\circ\text{C}$ . At  $300^\circ\text{C}$ , the synthesized HA was poorly crystallized and required highly temperature calcination for improved crystallization. It was also observed by Jillavenkatesha et.al [2.22] that among the different phosphorous alkoxides, triethyl phosphate had poor hydrolysis at room temperature and required a combination of higher temperature and prolonged aging.

The sol-gel route has also been used for making HA coating on different substrates. Chai et.al [2.27] used two different sources of calcium (Calcium Diethoxide and Calcium Propionate) separately with Triethyl Phosphite to prepare HA coating. It was observed that Calcium Propionate – Triethyl phosphite yielded HA at  $500^\circ\text{C}$ . Weng et. al. [2.28] used the alcoholic solution of calcium nitrate and phosphorous pentoxide to prepare crystalline and dense coating. Liu et.al [2.29] prepared HA coating at low temperature ( $300\text{-}400^\circ\text{C}$ ) from a mixture of Triethyl Phosphite and Calcium Nitrate. All sol-gel HA samples (bulk or coating) gave near stoichiometric and uniformity in composition. However, the major difficulty of using sol-gel process is the extremely hygroscopic nature of Phosphorous alkoxides. This required the use of protective and controlled atmosphere environment for synthesis. These factors made the sol-gel process less approachable by common researchers.

### **2.1.5 Hydrothermal Synthesis Route:**

Hydrothermal synthesis is another popular processing technique for the production of nano particles. In essence, hydrothermal synthesis is the process to carry out single or

multiphase reactions at elevated pressure and temperature. According to Yoshimura [2.30], hydrothermal synthesis can be defined as any heterogeneous reaction occurring in an aqueous medium. However, the reactions should take place under high temperature –high pressure ( $>100^{\circ}\text{C}$ ,  $>1\text{atm}$ ) condition in a closed vessel. One of the important aspects of hydrothermal reaction is the control of particle size and shape by varying the synthesis condition. In a natural bone, the apatite crystals are elongated. Probably, this particular crystal shape along with other biological factors provides the unique load-bearing capacity of natural bone. Research in the area of dispersed system or composites also reports that a circular or plate-shaped crystals act to reinforce the composites. Such crystals can also accelerate the bio-mineralization process. Therefore, hydrothermal synthesis has become an important synthesis process for HA. Neira et. al prepared [2.31] HA crystals of different morphologies with  $\text{Co}(\text{NH}_2)_2$  as a precipitating agent from  $\text{Ca}(\text{NO}_3)_2 \cdot 4\text{H}_2\text{O}$  and  $(\text{NH}_4)_2 \text{HPO}_4$  under gentle hydrothermal condition ( $T_{\text{max}}=90^{\circ}\text{C}$ ). A range of crystal shapes (plates, hexagonal prisms, and needle) was obtained by varying the P-T combinations. Suchanek et.al [2.32] synthesized HA via hydrothermal treatment for 24 hours at  $200^{\circ}\text{C}$  and 2 MPa pressure. They observed that L/D of crystals prepared in the propan-2-ol medium was 2-3, and L/D increased to 5-8 when one wt% KCl additive was used. Neira et.al [2.33] prepared hexagonal whiskers of HA crystals using  $\text{Ca}(\text{NO}_3)_2 \cdot 4\text{H}_2\text{O}$ ,  $(\text{NH}_4)_2 \text{HPO}_4$  and  $\text{NH}_4\text{OH}$ . From a series of experiments, it was concluded that the optimum hydrothermal precipitation condition  $90^{\circ}\text{C}$  temperature and 3-3.5 pH. Loo et. al [2.34] have schematically described the crystallization behaviour of HA obtained in a combination of normal condition and hydrothermal condition (Fig.2.1). Fig. 2.2 describes the effect of pH, temperature and hydrothermal duration on the morphology of HA obtained under different hydrothermal condition.

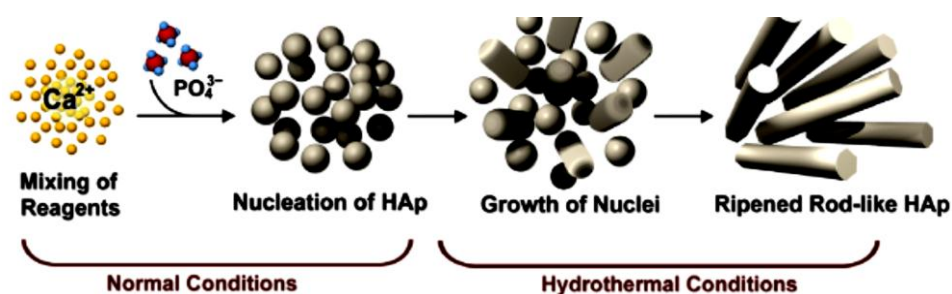


**Fig. 2.1 Synthesis of HA nanoparticles by two-step process of Hydrothermal route [2.34]**

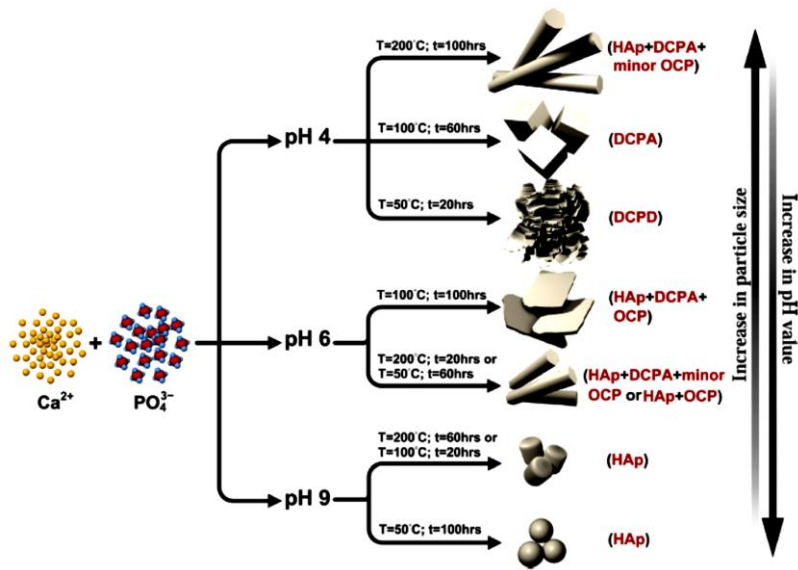
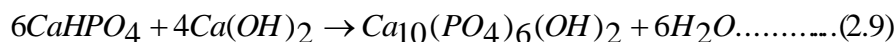


**Fig. 2.2 Effect of temperature, pH and hydrothermal duration on morphology, particle size and phase of CaP powder [2.34]**

### 2.1.6 Hydrolysis Method:

Hydrolysis method involves the reaction of components or chemicals in the presence of water. Usually in the hydrolysis method, different commercially available calcium-phosphate (CaP) compounds [Octa calcium phosphate (OCP), Dicalcium phosphate anhydrous (DCPA), and Dicalcium phosphate dihydrate (DCPD), etc.] have been studied. These compounds react with water present in the system to produce HA. A few of the hydrolysis reactions for producing HA is given below:



These hydrolysis reactions produce HA through dissolution –precipitation reaction. This implies that the crystallization of HA is preceded by the formation of a transient phase akin to some intermediate compound in many wet chemical precipitation routes. Among the different CaP compounds, DCPA and DCPD being acidic are unstable in the basic pH environment and change to the stable HA phase [2.35]. Seo and Lee hydrolyzed commercial HA via refluxing in the presence of EDTA and obtained HA whiskers. However, in the presence of  $H_2O_2$ , HA crystals were formed when the solution pH was 8-9. TCP has also been hydrolyzed to obtain HA crystals of different morphologies.



Some results have been presented by Ten-Huisen and Brown [2.36] which depicted the kinetics of transformation, the morphology of the transformed product, aspect ratio, etc.

### **2.1.7 Emulsion Method:**

Emulsion means a uniform mixture of two or more immiscible liquid under a specific condition. Emulsions in Ceramic Oxide Systems have been widely used for preventing agglomeration or clustering of particles in a suspension. However, the technology has now been extended to synthesize fine agglomerate free powders as well as to control the powder morphology. The efficiency of the emulsion strongly depends on the nature and type of (ionic, nonionic and block co polymer) surfactants. The relative size ratio of the hydrophobic tail and hydrophilic head manipulate the growth of nanoparticles. The emulsion method of particle preparation is carried out on three different emulsion systems. The three systems are a water-in-oil, oil-in-water and water-in-oil-water system. The three systems are schematically described in Fig. 2.3. The synthesis of HA is usually conducted in a water-in-oil emulsion system. The particle or the crystal morphology is controlled by the nature of the surfactants usually polyoxyethylene and CTAB combination is used). Sun et. al. [2.37] synthesized single crystal HA nanorods (8-15 nm diameter and 25-30 nm length). While polyoxyethylene acted as a tridimensional stabilizer, CTAB served the purpose of electrosteric stabilization of the micro emulsion system. Guo et.al [2.38] reported that for a mixed surfactant system (TX-100 and Tween-80), a wide distribution of particle size was obtained. Lai et. al. [2.39] worked on the kinetics of reverse micelle system and opined that during HA synthesis, the first nuclei was an amorphous DCPA rather HA. M Sadat-Shojai et.al. [2.40] prepared nano HA (75-98nm) using an emulsion of CTAB, n-pentanol, and Span60. They commented that the nonionic surfactant Span 60 prevented the elongated growth of HA and CTAB controlled the particle size. The micelles in the emulsion method acted as a template for particle growth and morphology. The presence of different surfactants also helps to disperse and stabilize the particles in the suspension through electrostatic stabilization process thereby controlling the particle size.

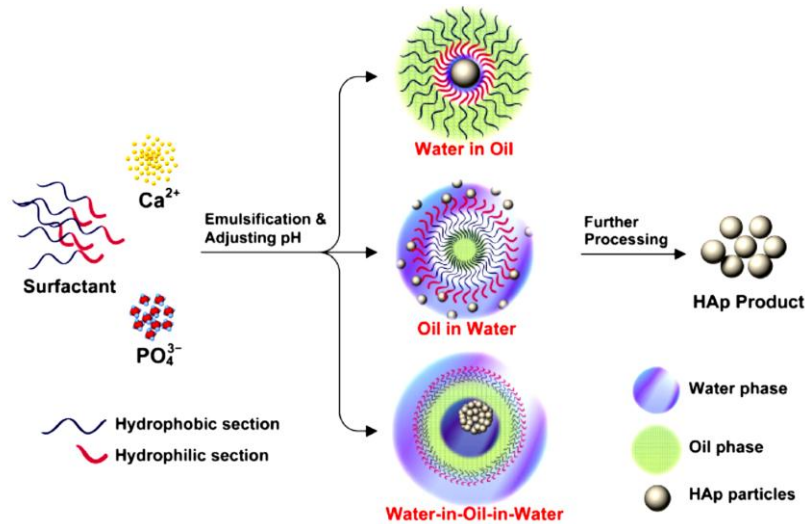


**Fig. 2.3 Schematic representation of the mechanism of three important emulsion synthesis of HA nanoparticles [2.41].**

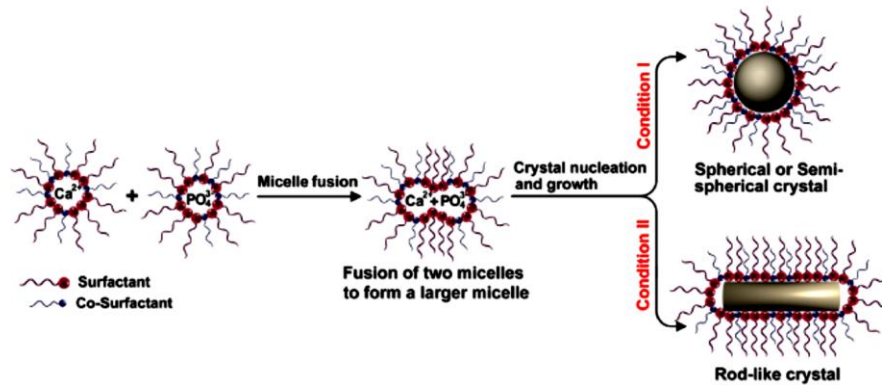


**Fig. 2.4 Spherical and Rod like morphology of HA nanoparticles by reverse micelle system [2.40, 2.41].**

### 2.1.8 Combustion Synthesis:

Solution Combustion Synthesis or Combustion Synthesis has been first reported by Pechini et. al. [2.42]. Since then, Combustion Synthesis has been used to synthesize a wide spectrum of ceramic oxides and compounds -both single component as well as multi-component. In essence, Combustion Synthesis uses a fuel and an oxidant to combust the gelled precursor mixture, often one or both the precursors can act as the oxidant. The usual combinations are citrate-mixture, glycine-nitrate, urea-nitrate, etc. When the process is extended to the synthesis of HA, the most widely used precursors mixes are  $(\text{Ca}(\text{NO}_3)_2 \cdot 4\text{H}_2\text{O})$  and  $(\text{NH}_4)_2\text{HPO}_4$  [2.42-2.45]. The precursor mix is subsequently gelled by adding either a single or combination of fuels to control the flame temperature. The nitrate-fuel gel mix is then heated in a furnace at  $300^\circ\text{C}$  when

the sudden ignition of the gel mixture takes place. The exothermic reaction completes the reaction between Ca and P and during cooling, HA crystallizes. A different combination of fuel-oxidant results in different powder characteristics. Ghosh et. al. [2.43] have reported that a small amount of glucose addition to either urea or glycine reduces the flame temperature. The higher amount of glucose controls the flaming during the combustion reaction. Ghosh et. al. [2.44] further reported that higher fuel/oxidizer ratio reduces the crystallite size. Higher flame temperature and lower crystallite size is obtained from a stoichiometric glycine/Ca (NO<sub>3</sub>)<sub>2</sub> ratio. Another report observed that excess fuel produced a high surface area HA powder [2.45-2.47]. Sasikumar and Vijayraghavan [2.45] used citric acid and succinic acid to prepare HA. When either Citric acid or Succinic acid was used, Carbonated HA resulted. When mixtures of both the acids were used, β-TCP formed. Pratihari et. al [2.48] synthesized HA particles by Citric acid – Nitrate solution combustion method using (Ca(NO<sub>3</sub>)<sub>2</sub>·4H<sub>2</sub>O), ((NH<sub>4</sub>)<sub>2</sub>HPO<sub>4</sub>). The authors observed that the crystallization of HA from amorphous gel takes place at higher calcination temperature (550-950°C). The crystal size of observed HA was 12 nm and 58 nm at 550°C and 950°C respectively. Phase pure HA powder was obtained at 1200°C.

### **2.1.9 Spray Pyrolysis:**

In the spray pyrolysis process, the mixed precursor solution containing Ca and P ions are sprayed into a hot chamber or inserted in the hot zone of a furnace. Rapid decomposition of salts takes place followed by crystallization to the corresponding oxides or compounds. The particle size depends on the droplets produced in the hot gas. Sometimes, the solution is being ultra-sonicated while the same is being sprayed into the hot chamber. The additional use of the ultrasonic energy helps to reduce the droplet size and hence fine particle size of the product obtained. Vallet-Regi et. al. [2.49] used fine droplets (2-4 μm) of a mixed solution of CaCl<sub>2</sub> + (NH<sub>4</sub>)H<sub>2</sub>PO<sub>4</sub> by passing the solution through an ultrasonic generator. Submicron HA particles were produced by passing the aerosol droplet through the hot zone of a tubular furnace kept at 500°C. Aizawa et. al [2.50] observed that when urea was used during spray pyrolysis carbonated HA resulted. It was further noted that the addition of urea reduced the particle size of HA which was attributed to the foaming action of CO<sub>2</sub>. Aizawa also investigated the effect of two-stage pyrolysis on the stoichiometry of spray pyrolyzed HA powder. Using Ca (NO<sub>3</sub>)<sub>2</sub> and (NH<sub>4</sub>)<sub>2</sub>HPO<sub>4</sub> mixed solution in the ratio 1.67, the pyrolysis was carried out in two

stages. In the first stage, the furnace temperature was 400°C and in the second stage the temperature was 850°C. The resultant HA was phase pure and stoichiometric. Cho et. al. [2.51] have used flame pyrolysis to prepare nano-HA of the stoichiometric composition. They also reported that PEG addition increased the particle size of HA. The major disadvantages of spray pyrolysis are resultant agglomerated HA powder. The aggregation occurs due to the agglomeration and the partial sintering effect of nano particles at the high temperature. An et. al. [2.52] resolved the issue of agglomeration through the addition of some specific salts (e.g NaNO<sub>3</sub>) in the precursor solution. On heating Ca(NO<sub>3</sub>)<sub>2</sub>, H<sub>3</sub>PO<sub>4</sub> and NaNO<sub>3</sub>, mixed spray mist at 700°C, the molten NaNO<sub>3</sub> coats the particles and prevents agglomeration. The NaNO<sub>3</sub> is removed by washing the crystalline powder.

#### **2.1.10 Biomimetic Synthesis:**

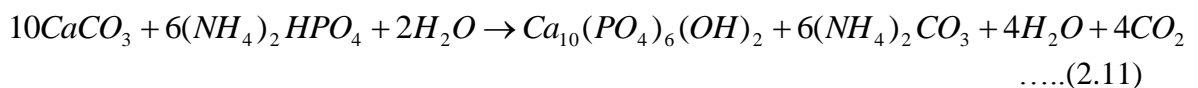
The biomimetic synthesis of HA or apatite like crystals in Simulated Body Fluid (SBF) has been first proposed by Tas et. al. [2.53]. The synthesis process involves precipitation of HA at the constant temperature of 37.4°C. Usually mixed an aqueous solution of Ca(NO<sub>3</sub>)<sub>2</sub> and (NH<sub>4</sub>)<sub>2</sub> HPO<sub>4</sub> is used. The basic idea is to mimic the natural growth of apatite that takes place “in vivo” in the body in the presence of human plasma. SBF is a well-known metastable buffer solution (pH-7.4) like human plasma. The high Ca/P ratio (2.5) of SBF makes it susceptible to apatite precipitation upon suitable changes of Ca<sup>+2</sup> and P<sup>+5</sup> concentration. The addition of the mixed solution of Ca(NO<sub>3</sub>)<sub>2</sub> +(NH<sub>4</sub>)<sub>2</sub> HPO<sub>4</sub> raises the Ca/P ratio of SBF to 40. The higher pH allows easy precipitation of an amorphous calcium phosphate (ACP). Upon calcination, ACP turns to HA and CaO phase mixture.

Wan et. al.[2.54] studied the precipitation of HA on Bacterial Cellulose (BC) in SBF. The BC matrix was prepared either with CaCl<sub>2</sub> or was first phosphorylated followed by CaCl<sub>2</sub> treatment. The treated BC samples were immersed in 1.5 SBF at 37°C for 7 or 14 days. The results show that flowers like apatite has formed on the surface. The results also confirmed that CaCl<sub>2</sub> treatment alone or bone phosphorylation and CaCl<sub>2</sub> treatment is required to induce proper crystallization of HA on BC. Nayak et.al [2.55] studied the biomimetic deposition of HA with BSA addition. It was observed that 0.5% BSA addition to the Ca(NO<sub>3</sub>)<sub>2</sub>. 4H<sub>2</sub>O solution promoted stoichiometric HA precipitation and growth after 48 hours of aging in SBF. Santosh et. al. [2.56] used the biomimetic synthesis process to prepare HA. Carboxylated carbon nanotubes used for the

fabrication of HA carbon nanotubes were formed due to the deposition of HA on CNTs. The results indicated that the HA deposition took longer time (21 days) when the aging was done at room temperature. At the temperature of 37°C, the deposition required only seven days. The results indicate the importance of aging temperature for biomimetic deposition. Frazer et. al. [2.57] studied the preparation of HA coating through accelerated biomimetic synthesis. The prepared SBF was stabilized by the citric acid buffer. NiTi alloys were used as the substrate and 5SBF concentration was used for biomimetic synthesis. It was observed that when the NiTi substrates were pretreated, the rate of SBF growth was faster.

#### **2.1.11 Synthesis of HA from biowastes:**

HA powder can also be synthesized from different biological sources or bio wastes. Some of these are eggshell, fish scale, marine organism, etc. (Fig-2.5). Egg shell primarily consists of 95-97% CaCO<sub>3</sub>. On calcination, egg shells provide CaO. This CaO is subsequently converted to Ca(OH)<sub>2</sub>. A reaction between as prepared Ca(OH)<sub>2</sub> and suitable phosphorous precursors result in Ca-HA [2.58]. Calcined egg shell (CaO) can also be reacted with HCl or HNO<sub>3</sub> to form CaCl<sub>2</sub> and Ca(NO<sub>3</sub>)<sub>2</sub> respectively to be used for HA synthesis. Boonyang et. al. [2.59] prepared HA from the hydrothermal treatment of different crocodile eggshell and phosphate precursors. Calcium carbonate present in the skeleton of various marine species has also been utilized for HA synthesis, mostly under hydrothermal conditions. The possible reaction sequences are



The other advantages of using marine calcium source are the possible porous structure of the structure during the HA synthesis. Nayak et. al. [2.60] used the extracts of different bio-wastes during the synthesis of HA by a biomimetic process. The bio-extracts used were potato peel, calendula, orange peel and papaya leaf extracts. The extracts of these wastes contain medium to large chain biomolecules that acted as a template for HA nucleation and growth. Depending on the composition of the extract, different morphologies of HA were obtained. Further, these biomolecules, due to their affinity towards for Ca<sup>+2</sup> ions also controlled the particle growth. In almost all these cases, around 50 nm primary HA crystals could be observed. Sinha et. al. [2.61] studied the synthetic polymer and biopolymer mediated templates to precipitate hydroxyapatite by a biomimetic process. The authors used calcium nitrate – PVA and Calcium nitrate –

BSA gels as the starting block.  $(\text{NH}_4)_2 \text{HPO}_4$  solutions were added to these gels and aged for 48 hours. Removal of the biopolymers resulted in the separation of HA. It was observed that the precipitation of HA took place in the porous network of the biopolymers mimicking the natural bone. Fig. 2.5 schematically describes the use of different bio-wastes for the HA powder synthesis. It can be seen from the Figure that the bio-waste template control the HA size and shape.

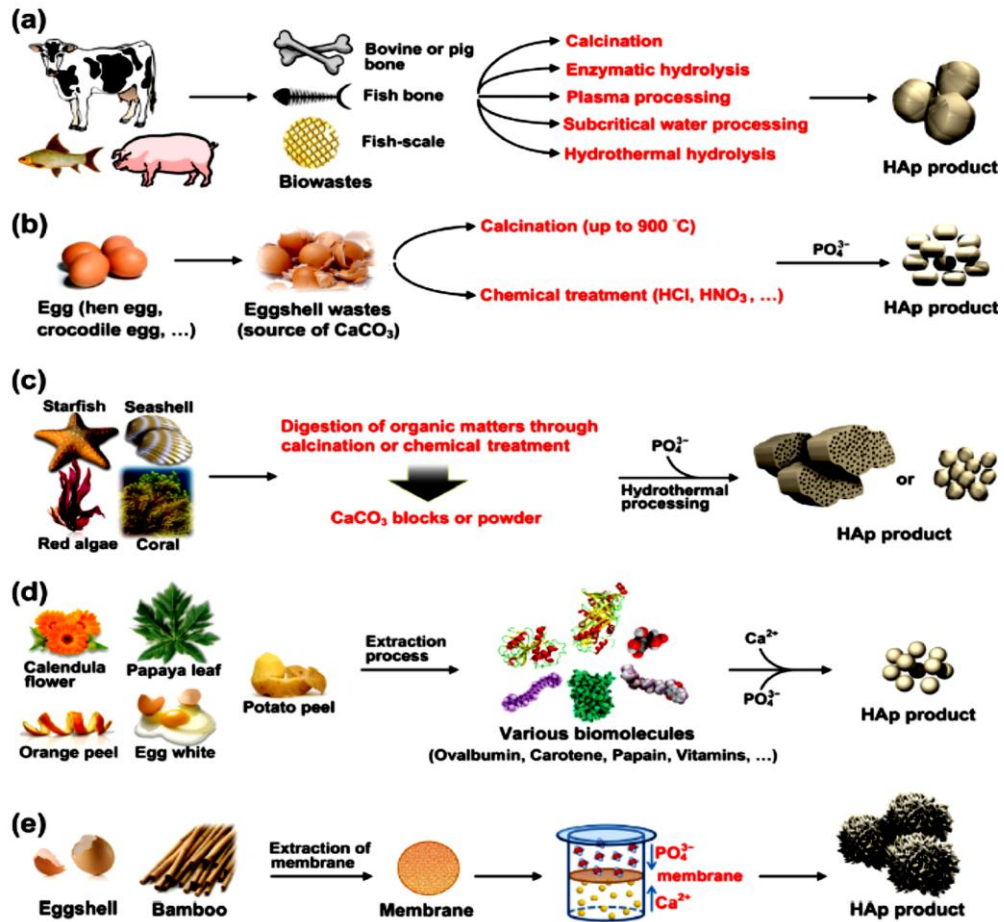


**Fig.2.5 Use of different biowastes for HA Synthesis (a) From bones and fish scales, (b) From egg shells, (c) From marine organism, (d) From naturally derived biomolecules, (e) From bio- membrane templates [2.58, 2.62]**

In this section, the different methods of HA powder preparation have been elaborated. The literature on the different synthesis methods, and their relative merits and demerits have also been discussed above. Table 2.1 provides a consolidated summary of the different methods that has been used for HA powder synthesis. The Table also lists the stoichiometry, and the synthesis parameters for HA powder synthesis.

**Table-2.1 Consolidated Summary of the Different HA powder Synthesis Methods [2.60]**

Powder Processing Methods		Precursors	Phase purity	Ca/P ratio of HA	Crystal Size	Calcination Temp (°C)	References
Solid State Powder	Solid state method	[Ca(NO <sub>3</sub> ) <sub>2</sub> ·4H <sub>2</sub> O, (NH <sub>4</sub> ) <sub>2</sub> HPO <sub>4</sub> , and KOH] and flux (KNO <sub>3</sub> and LiNO <sub>3</sub> )	Usually low (Repeated Reaction.)	Variable	Usually micron	500 -1250	Pramanik etal (2007), Teshima et.al (2009)
	Mechano- chemical method	Ca(OH) <sub>2</sub> , CaHPO <sub>4</sub> , CaCO <sub>3</sub> , (NH <sub>4</sub> ) <sub>2</sub> H <sub>2</sub> PO <sub>4</sub>	Low	Usually non-stoichiometric	nano		Honarmand (2010) Fahami et.al (2011),
Semi – Wet and Wet Precursor Method	Chemical precipitation	Ca(NO <sub>3</sub> ) <sub>2</sub> ·4H <sub>2</sub> O and (NH <sub>4</sub> ) <sub>2</sub> HPO <sub>4</sub>	Variable	Non-stoichiometric	Usually nano	600-750	Sadat-Sajola et al (2013), Ye et al (2010)
	Hydrolysis method	CaHPO <sub>4</sub> and Ca <sub>4</sub> (PO <sub>4</sub> ) <sub>2</sub> O	Usually high	Stoichiometric	Variable		Sturgeon et al (2009), Shih et al (2005)
	Sol-gel method	Ca(NO <sub>3</sub> ) <sub>2</sub> ·4H <sub>2</sub> O and (NH <sub>4</sub> ) <sub>2</sub> HPO <sub>4</sub>	Variable	Stoichiometric	Nano	400-1000	Ruban et al (2010), Ioiatescu et al (2009)
	Hydrothermal method	CaCl <sub>2</sub> and H <sub>3</sub> PO <sub>4</sub> solution	Usually high	Stoichiometric	Nano or micron		Zhang et al (2011), Jokic B et al (2011)
	Emulsion	calcium nitrate and phosphoric acid	Variable	Non-stoichiometric	Nano	450 -650	Saha et al (2009), Sadat-Sajol et al (2008)
	Sono-chemical method	Ca(H <sub>2</sub> PO <sub>4</sub> ) <sub>2</sub> and Ca(OH) <sub>2</sub> solution	Usually high	Variable	Nano		Rouhani etal (2010), Han et al (2009)
	Combustion method	Calcium nitrate–di-ammonium hydrogen orthophosphate with urea and glycine as fuel	Usually high	Variable	Usually nano	300-700	Ghose etal (2011), Sobczak etal (2009)
Temperature assisted Synthesis	Pyrolysis method	Ca(NO <sub>3</sub> ) <sub>2</sub> , (NH <sub>4</sub> ) <sub>2</sub> HPO <sub>4</sub>	Variable	Usually stoichiometric	Nano to micro	800	Aizawa et.al (1999), Wakiya (2010)
	Synthesis from biogenic sources	Fish scale, Egg shell	Usually high	variable	Variable	1000	Mondal et al (2010), Lombardi et al (2011)
	Combination procedures	Calcium nitrate tetra hydrate and sodium phosphate dibasic anhydrous	Usually high	Usually stoichiometric	Usually nano	950	Kalita et. al (2010), Vani etal (2011),

## 2.2 PART B: POROUS SCAFFOLD FABRICATION ROUTES

In Part-A of the literature review, the different methods for the HA powder processing have been discussed. The review revealed that depending on the processing route, the powder morphology will vary. The need for specific powder morphology may require some specific process to be adopted. However, it is better to adopt a processing route that will yield a powder with desired Ca/P ratio and phase stability. The powder property, in the long run, may also affect the scaffold property due to the difference in sintering behaviour, dissolution property, etc. However, irrespective of the powder synthesis route, all scaffold fabrication will start with a powder and depending on the end use; the different scaffold fabrication route may be adopted. The following sections will describe the different scaffold fabrication routes used by different research groups. The fabrication routes discussed below could be broadly grouped into five groups:

(a) Sacrificial Fugitive Removal Method, (b) Replica Method, (c) Gel Casting and Foaming, (d) Protein Coagulation Casting and other Foaming Methods and (e) Advanced Manufacturing Techniques.

### 2.2.1 Sacrificial fugitive method:

Engine et. al. [2.63] studied the processing of porous HA through slurry casting method using methyl cellulose as pore former. During the burn off of the methyl cellulose the samples foamed. The foamed ceramic parts were sintered at 1250°C. Through the control of methyl cellulose concentration and amount, porosities in the range of 60-90% were obtained.

Li et. al. [2.64] studied the porosity development in HA. The samples were prepared by dual phase mixing method using PMMA resin. The porosity of HA was 50%, and though the pores were open, interconnection were few. Since it was impossible to increase PMMA without causing structural degradation, additional foaming agents were used for creating porosity in the range 70%. The additional foaming agents were either a combination of NaHCO<sub>3</sub> and citric acid or CaCO<sub>3</sub> and Citric acid or NH<sub>4</sub>HCO<sub>3</sub> and Citric acid. It was concluded that foams created the open path way for the removal of PMMA and maintained the structural integrity.

Rodriguez-Lorenzo [2.65] prepared porous hydroxyapatite using starch consolidation technique. The swelling behaviour was utilized for creating a porous structure. A wide



variety of starch (5-65vol %) content was used to study the porosity development in HA. The highest porosity achieved was 70%.

Li et. al. [2.66] also studied the development of porous biphasic calcium phosphate (BCP) by dual phase mixing. Like his previous study, 60% porous BCP could be prepared by adding PMMA resin. For higher porosity level, 10% Naphthalene (flake/crystal) were added during the mixing of BCP with PMMA in the slurry. The other variation for increasing the porosity was to bubble N<sub>2</sub> gas in the BCP+PMMA slurry before casting. It was observed that the porosity level increased to 76% with NA granules and with N<sub>2</sub> gas bubbling, the porosity increased to 70%. However, the permeability study revealed that permeability was not only dependent on porosity but also on the macro porous structure and connectivity.

Li et. al. [2.67] also reported the porous hydroxyapatite scaffolds preparation through dual-phase mixing of pore formers. The usual pore former was PMMA resin that resulted in 50% porosity. The addition of NA improved the porosity to 60%.

Peon et.al. [2.68] prepared porous hydroxyapatite and naphthalene in a ratio so as to obtain 50% porosity. They used naphthalene with a particle size smaller than 250µm as a porogenic agent. The obtained porous blocks had 47% porosity with interconnection diameter of 100 µm approximately.

Yang-Lie et.al. [2.69] prepared porous hydroxyapatite using two types of starch. One starch was water soluble (WS) starch, and the other one was an insoluble (IS) starch. For identical starch content, it was observed the WS starch created smaller pore size and lesser interconnections. With IS starch, larger pore size and more interconnection were observed. The difference in the pore sizes was related to the solubility of WS starch vis-à-vis insolubility of IS starch. On reacting with water, WS starch produces a viscous coating that reduces the pore size and also provided the binding action, thereby providing lesser interconnections.

Collin et.al. [2.70] prepared macroporous biphasic calcium phosphate ceramics using a combination of sucrose particles and naphthalene granules. The pore formers were either 35 or 55 vol%, and the ratio of sucrose to naphthalene was either 1:1 or 1:5. It was observed that at higher sucrose content (1:1) and 35 vol% pore former, the melting of sucrose filled up the voids created by naphthalene. The melting of sucrose created channel pores and higher macro porosity. For sucrose: naphthalene 1:5 and total pore

former 55%, the macroporosity remained constant, but the total porosity increased implying an increase in mesoporosity.

Zhang et. al. [2.71] prepared a macro porous composite of Calcium Phosphate Cement (CPC) and chitason. Mannitol was also introduced into CPC for developing self and fast hardening cement. The mannitol served the additional job of creating macropores. The percentage of mannitol was 0 (no mannitol) to 75%. After the removal of mannitol, macro pores of 50 to 200  $\mu\text{m}$  were formed. The macropores, were irregular shaped, elongated as well as spherical depending on how the mannitol was spread in the composite. It was also observed that the dissolution of mannitol resulted in the conversion of TTCP and DCPA to HA. Thus, the set cement had higher HA content.

Klenke et.al. [2.72] studied the effect of pore size on the vascularization in the ceramic bone substitute. The ceramic bone substitute was prepared from a porous biphasic calcium phosphate (BCP) ceramics (Ca/P=1.66). Porosity was created by adding 0.5%  $\text{H}_2\text{O}_2$  and different sizes of naphthalene particles. Following the removal of  $\text{H}_2\text{O}_2$  and naphthalene, the porous BCP ceramic was sintered at  $1150^\circ\text{C}$ . It was observed that the generated pore sizes were nearly 70% of the original naphthalene size. It was also noted that time required for vascularization was less for large size pores. 210-280 $\mu\text{m}$  pores required 106 hours and 40-70 $\mu\text{m}$  pores required 135 hours for vascularization.

Abdurrahim et. al. [2.73] reviewed the scaffold preparation work in the area of HA, Biphasic calcium phosphate and  $\beta$ -TCP. They commented that the dimension and shape of pores were important parameters in deciding the tissue vascularization. While higher pore sizes permitted easy and faster growth of tissues, the mechanical strength was adversely affected by porosity. Low strength ultimately affected the in vivo durability. They also commented that the biodegradability of HA was the lowest followed by biphasic calcium phosphate and  $\beta$ -TCP.

Sundaram et. al. [2.74] prepared a gelation-starch blend that has been reinforced by HA nanocrystals. Three different volume percent of nano HA (20, 30 and 40vol %) were used. The nano-hydroxyapatite was found to reside within the pores of the base gelation-starch blend. However, the pore size was small for effective cell proliferation.

Tanget.et.al. [2.75] used different sized polyester microsphere to create micro porous HA structure. They sintered the green disk at  $1250^\circ\text{C}$  for 5 h to obtain the porous

scaffolds. The developed porous HA had different porosity associated with a different pore diameter. For example, 46.5% porosity was found for  $436 \pm 25$  nm pores, 41.3% for  $892 \pm 20$  nm pores and 34.7% for  $1890 \pm 20$  nm pores.

Swain et. al. [2.76] used naphthalene and a combination of naphthalene and benzene to achieve high strength porous HA. The obtained scaffold had phase purity till  $1250^{\circ}\text{C}$  without decomposition to  $\beta$ -TCP. The porosity was 60% with a compressive strength of  $\sim 11$  MPa. It was observed that the naphthalene dissolved in benzene giving interconnected and uniform pores while only naphthalene content scaffold had non-uniform pores. The pore diameter was in the range of  $\sim 40$ – $100$   $\mu\text{m}$ .

Se-Wonyook et.al. [2.77] studied the processing of porous hydroxyapatite scaffolds by freeze drying of Hydroxyapatite/ Camphene mixture. Low compressive strength and cracking of the porous scaffold was noted at low solid loading. To overcome this factor, 10-30 vol% polystyrene polymer was added to HA /Camphene mixture. The compressive strength was 2.5 times of no polystyrene added scaffold.

Bakhtiari et.al. [2.78] investigated the biphasic calcium phosphate/gelatin nanocomposite scaffolds by the freeze-drying method. This composite was chosen as a replacement of BCP/collagen composite that required costly collagen. In contrast, gelatin is a low cost and biocompatible material. To prepare BCP-gelatin composite, at first porous BCP was prepared by mixing. BCP and naphthalene particle ( $500\mu\text{m}$ ) were mixed in the ratio 3:2. Sintering at  $1400^{\circ}\text{C}$  resulted in a porous scaffold. BCP-gelatin composite was prepared by infiltration of gelatin in porous BCP scaffold for 4 hours at pH 7, followed by freeze drying at  $80^{\circ}\text{C}$  for 7 hours. The scaffold had the pore size of  $100$ - $200\mu\text{m}$ . The pores were interconnected.

Kundu [2.79] et.al. investigated the localized drug delivery system using porous HA-scaffold. Two different naphthalene (50 and 60 vol %) content used with calcined HA. Calcined HA powder and naphthalene were mixed in two different percentages 50 and 60. The sintered porous HA had an average pore size  $\sim 110\mu\text{m}$  with an interconnectivity of ( $10$ - $100\mu\text{m}$ ). These samples had moderately high adsorption efficiency ( $\sim 50\%$ ). On the other hand, the scaffolds with 60% naphthalene had  $140.2\mu\text{m}$  pores. The micropores fraction was less in 60% naphthalene containing scaffolds. It was further observed that at higher naphthalene content, the pore shape changed from spherical to non-uniform

shape with the appearance of ruptured pore walls. The subsurface interconnection was found to be 30-120  $\mu\text{m}$  for 60 vol% and 10-100 $\mu\text{m}$  for 50 vol% samples.

Ray et. al. [2.80] used sucrose as a pore former to prepare porous biphasic calcium phosphate (BCP). The sucrose particle sizes were (567, 407, 257 and 150 $\mu\text{m}$ ). Each of these size fractions were added to the porogen: BCP (v/v) ratio:: 35:65, 45:55 and 55:45. Depending on the sucrose content, the macro porosity (as evaluated by SEM) varied from 35-57%. The results were better than the reference (48%).

Amera et. al. [2.81] prepared porous biphasic calcium phosphate scaffold from different porogens. The porogens used were naphthalene, sugar lentil and sago (known as sabu dana in India). The particle sizes of the porogens were 200-400 $\mu\text{m}$  and BCP: Porogen was 1:3 by weight. The obtained pores were in the range of trabecular bone pore size of 200-400  $\mu\text{m}$  with the oval to round shape of pores. All the samples had nearly 79% porosity. All samples exhibited ALP activity.

Madhavi et. al. [2.82] studied the synthesis of Three-Dimensional Ordered Macroporous (3DOM) structure of HA using ordered templates of polystyrene sphere. The template was impregnated with  $\text{H}_3\text{PO}_4\text{-Ca}(\text{NO}_3)_2 \cdot 4\text{H}_2\text{O}$ . HA was crystallized by calcination at different temperatures between 500-1000 $^\circ\text{C}$ . It was observed that samples fired at 500-700 $^\circ\text{C}$  did retain the macro porous structure. At 1000 $^\circ\text{C}$  a decrease of the 3DOM macro porous structure was observed, although the structure could be retained. TEM observation confirmed that the voids are in the face centered cubic pattern.

In summary, it can be said that the fugitive removal method provides an easy and reproducible way to generate porosity in the HA samples. Depending on the pore former type and amount, the porosity could be either isolated or interconnected. Natural pore formers like naphthalene, sugar, sucrose, sabudana usually produces irregular pores. Pores created through polyester spheres, or ordered templates were near spherical and were arranged in some regular fashion.

### 2.2.2 Gel Casting:

The gel casting method for advanced ceramics processing have started with the invention of Janney and Omatete [2.83]. However, for quite some time, the gel casting method was concerned with the shape forming of complex shapes (turbine blades) and dense ceramics. Later on, the gel casting technology process was extended to prepare porous ceramics also. The idea came from the reports that the gel cast ceramics have high strength when compared with those prepared by other conventional routes. For creating the pores the suspension required to be foamed prior to the setting of the gel. The first reports on the use of the gel casting method for preparing porous HA came from Sepulveda et. al.[2.84]. They used a combination of an acrylate monomer and methylene-bis-acrylamide, APS and TEMED for gel casting. A foaming agent was used to foam the suspension prior to gelation. The gelled body after drying and sintering was porous. The pore size increased with a lowering of the solid content of the slurry samples with 88% porosity had a pore size larger than 200 $\mu$ m.

Hamplin et. al. [2.85] prepared porous HA using unique foaming method. Jones et. al. [2.86] reported the processing of bioactive glass from a gelation process. The sols were foamed prior to process. It was observed that the CaO containing glass composition foamed better and produced higher porosity samples.

Narbat et. al. [2.87] prepared porous HA-gelation composite scaffold. The fabricated slurry was set by freezing at -70°C and had 70% porosity. Bundela et.al [2.88] prepared Pam-Gelation-HA composites through gel casting. The samples show a maximum porosity of 31%.

Monmaturpoj et. al. [2.89] prepared porous hydroxyapatite scaffold using a combination process of gel casting and freeze drying. While gel casting was expected to provide a strong scaffold, the possibility of drying stress defects were eliminated by freeze drying of the gelled component. The authors observed that the ratio of HA to pore former was a critical factor in determining the strength. A higher HA solid loading to pore former ratio helped to retain the bubbles in the slurry. The pore morphology changed from 2D interconnected pores to spherical interconnected pores.

Sadeghilar et. al. [2.90] studied the local tissue reaction and biodegradation HA/TCP porous scaffold. The porous scaffolds were prepared by a combination of gel casting

and polymer sponge method. The authors concluded that resultant scaffold was mechanically stronger. The relative ratio of HA/TCP decided the biodegradability.

Kim et. al. [2.91] studied the pore structure and compressive strength for an HA/TCP glass ceramic. The porous scaffolds were prepared by the combination of gel casting/freeze casting. The authors observed that the sintered scaffolds had two different types of pores. The unidirectional channel pore developed due to the freezing of TBA. The spherical pores were formed due to the foaming action of the gel casting.

Potoczek et. al. [2.92] investigated the fabrication of calcium phosphate scaffold via gel casting route. The ceramic suspension was prepared with 49% solid loading, and agarose solution was used to gel the suspension. The microstructure of the sintered scaffold revealed the spherical pores with spherical windows. The prepared scaffold had a broad pore size distribution (250 to 900 $\mu\text{m}$ ) and a window size of 25 to 250 $\mu\text{m}$ . The study showed that even a small amount of agarose (2.5%) solution was sufficient to wide pore size distribution in the scaffold.

Ramay et. al. [2.93] studied the microstructure and mechanical properties of a porous HA using a combination of gel casting and polymer sponge method. The authors reported that the use of the combination process resulted in a highly porous (71%) with open and uniform pores of 200-400 $\mu\text{m}$ . The compressive elastic modulus was 4-7 MPa, which was closer to the lower limit of cortical bone.

Baradararan et. al. [2.94] prepared a macroporous biphasic calcium phosphate (BCP) scaffold using a combination of gel casting and polymer sponge method. The resultant scaffold had a relatively open and interconnected microstructure of 150-400 $\mu\text{m}$ . The interconnection size was 11-20 $\mu\text{m}$ .

Li et. al. [2.95] studied the development of porous  $\beta$ -TCP scaffold based on gel casting and rapid prototyping technique. The gel casting was achieved using monomers, initiators, accelerators. Additionally paraffin spheres (200-400 $\mu\text{m}$ ) were also added to the ceramic slurry for created additional pores. The resultant could be prepared with wide porosity range (30-70%). The pore size of the scaffold was 200-400 $\mu\text{m}$ . The internal channel, network was created by RP technique, and the channel network size was 600 $\mu\text{m}$ .

Farhangdoust et. al.[2.96] fabricated macro porous HA scaffold by freeze casting method. The solid of HA varied between 7 and 37.5 vol%, and the cooling rate was changed from 2 to 14°C/min. Depending on the solid loading the porosity in the sintered scaffold varied between 45-87% and the compressive strength changed from 0.4 MPA to 60MPa. The pores were also channel pores. Pore size changed with solid loading. The long-axis of the pores changed from 180µm and 7.5% HA loading to 8 µm at 37.5% HA solid. In a similar way and for the same loading, the short axis decreased from 42µm to 5 µm. Thus, at the highest solid loading, the pore nearly turned to the square pore.

### **2.2.3 Freeze Casting:**

The freeze casting technique for scaffold preparation is similar to gel casting with the difference that the rigidity of cast structure is obtained through freezing of the suspension. The pores obtained are highly anisotropic and depends on the growth direction of the ice. On sublimation of the ice crystals, a uniformly spaced lamellar porous structure is obtained. The anisotropic microstructure provides unique mechanical properties of the scaffold. Of late, this technique has also used to fabricate porous Ha scaffold. The following paragraph briefly describes some of the available literature on this technique.

Deville et. al. [2.97] have prepared porous HA scaffold by freeze casting method. The microstructure of sintered scaffold shows that sample had that distinctly different microstructural zone. The bottom part that was in contact the cold finger was dense. The upper zone had cellular pores. In the uppermost zone, lamellar and parallel aligned pores were observed. The useful scaffolds were made from the uppermost zone only.

UGK Wegst [2.98] made a compressive review of freeze casting mechanism and the fabrication principle used for porous biomaterials. The author elaborated the different biomaterial that could be made by freeze casting. The use of camphene and tertiary butyl alcohol (TBA) has also be discussed in the paper.

Zhao et. al. [2.99] have discussed the processing of porous HA by ice-templating. The effect of freezing rate on the pore structure was discussed. The authors observed that a faster cooling decreased the lamellar spacing. An increase in the degree of super cooling and lowering of the initial nucleation temperature changed the porous lamella to a dendritic structure.

Fu et. al.[2.100] studied the freeze casting of HA with solid loading 5-20 vol%. An increase in the solid loading was found to decrease the porosity and pore cross section but increase lamella thickness. It was further observed that glycol addition to the HA suspension (prior to freezing) resulted in finer pores and dendritic structure interconnecting the different HA lamella.

Fu et. al.[2.101] also studied the strength characteristics of the prepared porous HA. The authors noted that the compressive strength of the scaffold was one order of magnitude higher than those reported for the polymer or polymer-ceramic scaffold. However, the observed strength values lower than those reported by Deville et. al. The difference in the strength values was correlated with the slower cooling employed by Fu et. al. A slower cooling rate resulted in larger pore size with a concurrent decrease in strength. However, tissue in growth was found to better as compared to the previous study.

Lee et. al. [2.102] used the camphene based freeze casting method to prepare highly porous HA scaffolds. HA-camphene slurry having different HA solid loading (10,15, and 20 vol%) were used. An increase in the solid loading from 10 to 20 vol% resulted in the reduction of porosity from 75 to 50%. Accordingly, the compressive strength increased from 0.94 MPa (at 10 vol%) to 17 MPa at 20 vol% HA.

In a previous study Fu et. al. [2.101] observed that the addition of certain solvents dioxane and glycerol changed the morphology and pore alignment of porous HA scaffold. In this report, Rehaman and Fu have explained the science behind such a change in the pore morphology. Phase separation of the binary water-dioxane and water-glycol mixtures during freezing was the cause for the observed behaviour. The two organic components could also modify the hydrogen bonding of water resulting difference the morphology of the ice.

Yoon et. al. [2.103] systematically studied the development of large porous channels in the camphene-based freeze cast hydroxyapatite. The author used a very high freezing temperature. The low solidification velocity at the freezing temperature permitted the formation of excessively overgrown camphene crystals. The resultant scaffold had >100µm pore channels and dense HA pore walls. An increase in the solid loading from 10 to 20 vol%, the porosity decreased from 76 to 55% with a consequential increase in compressive strength from 2.5 MPa to 16.7 MPa.



#### 2.2.4 Replica Technique:

The replica method of preparing porous ceramics has started with White [2.104], who used the natural coral as a template to replicate the porous structure. Studies have also been made on the use of wood as a template (wood template) [2.105]. However, the real interest in the replica technique of porous ceramics fabrication started with phenomenal work Schwartzwalder and Somers [2.106]. Schwartzwalder et. al. used polymeric sponges as a template for creating porous ceramics. Since then, different research groups have used the replica technique to prepare different porous ceramics. Since porous HA is an important class of biomaterials, a lot of work has also been carried out on the manufacture of porous HA on the replica method. Some of the results of earlier are presented below:

Tian et. al. [2.107] studied the preparation of the porous HA by impregnating HA slurry in Polyurethane foam. The difficulty encountered with this method is the rapid drainage of the slurry from the foam after impregnation. This resulted in the variable strut thickness and very thin strut. Special sintering schedule was designed to prevent the cracking of the struts. The maximum porosity was 65%, and pore size was 150-40- $\mu\text{m}$ .

Kim et. al. [2.108] prepared HA coated porous  $\text{ZrO}_2$  scaffold using polymeric sponge replica technique. An intermediate fluorapatite (FA) coating was applied on the  $\text{ZrO}_2$  scaffold for preventing the reaction between HA and  $\text{ZrO}_2$ . The FA coated  $\text{ZrO}_2$  scaffolds were subsequently coated with HA to realize HA coated  $\text{ZrO}_2$  scaffold. While the  $\text{ZrO}_2$  scaffold was prepared from a  $\text{ZrO}_2$  slurry using polymeric sponge technique. After sintering of  $\text{ZrO}_2$  scaffold, the scaffold acted as a substrate for subsequent coating by FA and HA. Finally, the coated  $\text{ZrO}_2$  scaffold was sintered at  $1250^\circ\text{C}$ . The porous  $\text{ZrO}_2$  scaffold had a wide range of porosity (74-92%). The macropores were spherical (600 $\mu\text{m}$ ), and the struts were 100-200 $\mu\text{m}$  thick. The thickness of the FA/HA coating was about 35 $\mu\text{m}$ . Thus, there was only a slight change in pore diameter.

Sang-Ho Min et. al. [2.109] prepared porous HA scaffold by polymer sponge replica method. The pore size of the sintered scaffold was 200-400 $\mu\text{m}$ . Mostly, the pores were open and interconnected. Multiple coating ensured thicker struts and lowering of porosity. During the compressive, the samples broke in the elastic brittle manner.

Saiz et. al. [2.110] prepared porous HA scaffold via the polymer foam infiltration method. The sintered showed circular pores of 100-200  $\mu\text{m}$  size. The strut thickness was 10-80 $\mu\text{m}$ .

Appleford et. al. [2.111] prepared porous HA scaffold for in vivo study. The porous scaffold was prepared polymer sponge replica technique. The prepared scaffold had a porosity of 77.4%.

Bakunova et. al. [2.112] prepared porous scaffold of carbonated HA (CHA). Polyurethane matrix was vacuum impregnated with CHA slurry. The sintered scaffold had a porosity of 60-90%. The pores were open and interconnected indicating that they would assist in cell seeding and fixation. PU foams of varying number of pore per inch (PPI) were used to prepare scaffolds with varying porosity. Depending on the foam type the pore size were 50-2000  $\mu\text{m}$ .

Oliveira et. al. [2.113] fabricated macroporous HA scaffold by PU foam impregnation technique. The impregnated foams were centrifuged to ensure uniform distribution of slurry, removal of excess surface slurry and also to prevent the surface skin formation. Micro-CT analysis has studied the pore structure and pore architecture of the HA scaffold. The  $\mu$ -CT scan revealed that the processed scaffold has a uniform pore structure with an average porosity of 68%.

Jo et. al. [2.114] used stretched polymeric membrane to prepare porous scaffold of HA with elongated pores. The basic idea of using elongated pore structure template was to prepare scaffold with an anisotropic structure. Scaffolds with an anisotropic pore structure are expected to provide unusual compressive strength. The authors used stretched polyurethane sponges (stretched to 30, 50 and 60 % elongation) and the scaffold with elongated pores had high compressive strength 3.8 MPa even with 76% porosity.

Sopyan et. al. [2.115] prepared porous HA scaffold. The commercially available cellulose sponge was used which could retain the structure after impregnation. The sintered scaffold contained 100-150  $\mu\text{m}$  macropore. The porosity decreased with the increase in the HA solid loading. It was noted that scaffold prepared from 42wt% solid loading exhibited 34.3% porosity and 10.5 MPa compressive strength.

Swain et. al. synthesized porous HA by polymeric sponge replica method using commercial grade sponge. The sintered scaffold had a porosity of 60% and the majority

of pores were in ~ 50–125  $\mu\text{m}$  and interconnected. It was observed that both strength and porosity of the scaffolds depended on the solid loading and binder content [2.116]

Gervaso et. al. [2.117] studied the processing and characterization of porous HA scaffold prepared through polymer sponge templating technique. The solid loading of HA was 70wt%. The porosities of the scaffold varied between 86-93% depending on the powder characteristics. The macro pore size was 500  $\mu\text{m}$ , and 0.51 MPa was the compressive strength.

Scalera F et. al. [2.118] prepared porous HA by sponge replica method. The synthesized HA powder was calcined at different temperatures (600-900°C) to change the HA crystallinity and crystal size. Low temperature calcined HA showed poor mechanical stability due to high shrinkage, and best scaffold were obtained from 900°C calcined powder. All the scaffold had high porosity (90%) and 500  $\mu\text{m}$  macropores.

Roohani-Esfahani et. al. [2.119] observed the effect of needle-shaped HA nanoparticle shape and size on the properties of a Biphasic Calcium Phosphate (BCP) scaffold. The BCP scaffold was prepared by a replica technique using fully reticulated polyurethane foam. The sintered scaffold was coated with needle-shaped HA particles for preparing the composite structures. The composite was coated with polycaprolactone to provide a biodegradable coating. The developed nanocomposite hybrid scaffold (BCP-HA-Polycaprolactone) had high interconnectivity and porosity (90%) and reasonably high compressive strength.

### **2.2.5 Protein Coagulation Casting:**

Depending on the consistency state of the powder, the shape forming of ceramics can be carried out by following one of the methods given in Table 2.2. The Table shows that the processing steps become more and more critical and complex with the increase in the liquid content. In the forming of porous ceramics involving slurry, two targets are achieved almost simultaneously. The first in the consolidation of ceramics- i.e. the forming of a rigid mass. The second one is the porosity generation in the shaped body. To create a very porous structure (as in scaffold), the foams need to be created and distributed in the slurry. Subsequent removal of the foams will create porosity in the sample. Gel casting is one such method, where the chemical components not only help gelation of the slurry through polymerization reaction but the removal of the polymerized species also helps to create porosity in the cast body.

Protein Consolidation is another novel shape forming method. Tuck et. al. [2.119] have used egg foams to prepare porous ceramics. Lindsten [2.120] have patented the use of albumin for foaming of ceramics. Lyckfeldt [2.122] and later Garrn [2.123] have analyzed the chemistry of protein consolidation as well as the physics of foaming of ceramic suspension using protein.

It has been mentioned by Garrn et.al [2.123] that in the slurry processing of ceramics, proteins play a major role as the slurry changes from deformable state to rigid state. Egg white contain albumin that are globular proteins. A large number of amino acids present in globular protein that chemically reacts with ceramic oxides in the slurry. In a suspension, the R group of the amino acids gets aligned between the aqueous dispersing agent and the ceramic particle surface forming a micelle. Due to their amphiphilic character, these amino groups decreases the surface tension of the slurry and act as a foaming agent.

**Table-2. 2 Different Shape Forming Methods and the Factors affecting the Processing**

Consistency state	Shaping Methods	Drying Shrinkage	Controlling Parameters
Powder, Granules	Pressing, Cold iso-pressing	Less	Powder type, Granulometry, binder, compaction load
Plastic state	Extrusion, Injection Moulding	Medium to less	Degree of pore saturation (DPS) binder- major and minor, type of binder - thermosetting, thermoplastic, injection moulding process
Slurry state	slip casting, gel casting, non-conventional casting, etc.	High to Medium	Slip rheology, Slip stability, deflocculant, Solid loading, Casting time, Drying shrinkage

On heating, these globular proteins are denatured. Denaturation is the breakdown of virgin protein structure. The irreversible denaturation of the protein occurs due to the stabilization of the peptide chain. In case of albumin, the denaturation causes unfolding peptide chains. Subsequent reaction of amino acid side chain causes a tremendous increase of viscosity of albumin and result in coagulation. A change of temperature can also cause the denaturation. Foaming of egg white is due to the presence of lysosome- a relatively stiff, ellipsoidal molecule. Foaming behaviour results from the non-uniform

charge distribution in the lysosome molecule [2.124]. Moreover, albumin can also act as a deflocculant and binder. Three parameters control the physics of foam generation in an egg white-particle mixture. These are: (a) gas inclusion and its distribution by air-mass surface to the interior, (b) foam bubble shape change due to agitation and (c) stability and drainage of foam. Hanselmann et. al. [2.125] observed that under the constant mixing parameters and mixing time, finer and less number of foams will be produced in high viscosity slurry. The lesser number of foam bubbles, as well as finer foam size, is due to the less turbulent action taking place in a high viscosity mass in comparison to a low viscosity mass. During thermal setting of protein, two phenomena also occur. One is the bubble growth and the second is the draining and collapse of bubbles. It has also been reported that the bubble drainage is more in a low viscosity mass. Regarding the relation between the mixing speed of slurry and foam generation, Dhara et. al.[2.126] have reported that tumbling method was efficient in producing uniform size pores. On the other hand, Sopyan et. al. [2.127] used the stirring method as well as egg yolk in creating a porous structure. However, in the work by Dhara, the pores were created due to the foaming action of albumin. But in case of Sopyan, the removal of egg yolk created the porosity.

With this background, the available literature on the processing of HA by Protein Coagulation Casting (PCC) is being discussed in the following paragraphs.

Though the PCC method is being widely used for fabricating porous ceramics, the literature on HA is very few. In most of the reports, alumina has been considered as the host matrix. Secondly, with only a few studies have worked freshly extracted egg white. Many reports are available on BSA protein, Whey protein, dried albumin powder from egg white, etc. Working with extract provides easy control of the foaming parameters because the relative purity of the materials.

Maria-Pan Ginebra et.al [2.128] used a protein based foaming agent to prepare a macro porous HA foams. The authors started with albumin (7-10%) and  $\alpha$ -TCP to prepare calcium deficient HA. The authors also observed that the macroporous ceramics was injectable through a commercial syringe.

Sopyan et. al. studied the processing of Alumina-HA composite [2.129]. The samples were prepared by protein foaming – consolidation method. Two different varieties of HA was used. One was sol-gel derived HA, and the other was commercial HA. A slurry

containing the two powders-i.e alumina and HA along with egg yolk, starch were stabilized into a slurry state, cast, dried and sintered at different temperatures between 1250°C - 1550°C. 16 to 30 wt% HA was added to the alumina. The porosity of the sintered composite specimens (with sol –gel derived HA) decreased with the increase in sintering temperature. The porosity was 52.10% at 1250°C and 46.5% at 1550°C. In case of Alumina-commercial HA composite, the porosity dropped from 48.5% to 44.6%. The pore size was in the range of 20-50µm. It was also observed that the porogenic addition of yolk porosity increased from 46.9% to 70.3%

Sepulveda [2.130] prepared porous HA from foaming of the gel. Usual gel casting compositions were used for gelling. However, prior to gelation, the suspension was agitated by a double blade mixer. Relative porosities of the sintered samples varied between 72 and 90%. Mercury porosimeter result showed that both cylindrical and ink bottle-shaped pores were present. The maximum pore size of the sample measurable by porosimeter was 340µm and beside that pores of 1-2mm were also present. The authors concluded that by controlling the foam volume to slip volume, the pore size could be varied.

Ribeiro et. al. [2.131] prepared macro porous biphasic calcium phosphate (BCP) by albumin consolidation technique. The prepared macro porous scaffolds were studied for osteointegration and biocompatibility in vivo. The microstructures of the sintered samples show large spherical pores (200-500µm) along with open channel pore interconnection. The interconnection was in the size range 50-100µm. In vivo tests on rabbits showed that the implanted scaffold was entirely filled with trabecular bone after four weeks of implantation.

Lemos et. al.[2.132] prepared porous HA using synthetic egg albumin both as a foaming agent and a binder. Depending on the amount of egg albumin (5-20%) in water, the porosity varied from 74 to 78%. The microstructure showed many interconnections at high albumin content. The authors also commented that using albumin only, the porosity development was not satisfactory.

Lemos [2.132] also used treated potato starch both as a consolidator and a foaming agent for preparing porous HA. For this work, Sodium Lauryl Sulphate (SLS) was used as a supplementary foaming agent. The foaming agent varied from 1.7 to 10 wt% and within that different ratio of starch and SLS was used. The microstructural studies

revealed that predominantly open pores were obtained. The use of SLS promoted open pore formation. However, beyond 2.5 wt% total foaming agent, no significant effect on the porosity development could be observed.

### **2.2.6 Foaming Agents other than starch or albumin**

Besides the use of egg white, albumin (globular protein) and potato starch as a foaming agent and binder, researcher has also used other foaming agents like  $H_2O_2$

Some of those literature are reported below:

Wootichaiwat et. al. [2.134] have reported porous HA using both a sacrificial template and a foaming agent. In his study,  $H_2O_2$  was used as the foaming agent and PMMA granules were used as a template. Using only PMMA (as a sacrificial template), the porosity level was 52-75%. On the other hand, when  $H_2O_2$  was used as the foaming agent, the porosity level was between 82-85%. Thus,  $H_2O_2$  acted as an efficient pore former.

Kim et. al. [2.135] prepared porous HA scaffold using commercial polyol and isocyanate as the polymer foaming agent. The HA-polyol slurries contained varying polyol content (20, 30, 40 wt %). The isocyanate content was 27.8% of polyol. The dried cast body was prepared at 1200°C and 1350°C. During sintering, polyol/isocyanate first evolved  $CO_2$  gas giving smaller pores, and the subsequent pyrolysis of polyol/isocyanate created larger pores through pore coalescence.

Hwang et. al. [2.136] prepared porous HA by  $H_2O_2$  foaming method and by combining  $H_2O_2$  foaming with PU sponge replica. When  $H_2O_2$  alone (20% addition) was used as the foaming source, the porosity was 58-72% with a wide pore size (50-1500  $\mu m$ ). The combination of  $H_2O_2$  and PU sponge produced 68-74% porous scaffold and narrow pore size distribution (600-750  $\mu m$ ). Based on the above observation, the authors commented that the pore size control through  $H_2O_2$  foaming alone was difficult

Almirall et. al. [2.137] prepared a porous calcium deficient hydroxyapatite (CDHA) by  $H_2O_2$  foaming. During the foaming of CDHA, two reactions took place. The decomposition of  $H_2O_2$  gave rise to foam, and the released  $H_2O$  reacted with CDHA to produce carbonated apatite. With  $H_2O_2$  foaming, a maximum porosity of 66% was obtained. The authors also commented that by varying the liquid-powder ratio as well as  $H_2O_2$  concentration, the pore size and porosity could be controlled.

The literature reviews recorded in this chapter till now are related to the sample processing steps that have been carried out in the present investigation. However, besides these literature, there are other research papers on the processing of porous HA and related materials through different methods. Some of these advanced methods are Rapid prototyping, Robocasting, Fused Deposition Modeling etc

Rapid prototyping (RP) is the generic name of the Computer Aided Designing and Manufacturing process for producing customized product. The RP technique was a “layer manufacturing technique”. Details of RP process are available in Reference [2.138-2.139]. Woesz et.al [2.140] reported porous calcium phosphate ceramics fabrication by rapid prototyping Stereolithography technique was used to obtain a pore size of 450 $\mu$ m. E Saiz et. al.[2.141] used Robocasting to prepare porous hydroxyapatite scaffold. Using “layer manufacturing technique” the porous scaffold was prepared. Simon et. al. [2.142] prepared 3D periodic HA scaffold by direct-write assembly using HA ink. Kutikov et. al. [2.143] prepared amphiphilic polymer/HA composite scaffold by Rapid Prototyping. Dong-Han et. al. [2.144] prepared customized Craniofacial Tissue Engineering Scaffold through Rapid Prototyping

From the above discussion it can be concluded that over and above the rather conventional techniques like gel casting, foaming, newer component-aided techniques like (RP) Stereo-lithography, Robocasting Fused Deposition Modeling can also be used for preparing porous HA scaffold.



### 2.3 PART C: IN-VITRO BIOACTIVITY – PROCESS AND MECHANISM

The preceding sections have discussed the processing of HA powder through different powder processing routes and the different scaffold fabrication routes. In the present work, the scaffolds have been prepared from HA powder prepared in the laboratory. Among the different characterizations of the scaffolds, in-vitro bioactivity is an important one. The method for carrying the in-vitro test has been discussed in Chapter 3. This section will discuss the apatite formation mechanism as discussed by different research groups.

The invitro bioactivity test is an easy and simple method of approximating the bioactivity of a bioactive scaffold. However, this evaluation provides only a qualitative or a semi-quantitative estimation of the bioactivity. The principle of bioactivity test involves the immersion of bioactive samples in a suitable liquid medium for a specific period. The composition of the suspending liquid should be such that it should permit the dissolution of the sample. The earlier studies on the bioactivity concentrated mostly on the dissolution behaviour [2.145]. The more recent studies also evaluated the growth of apatite on the scaffold. Since, in this work, the in-vitro studies form the major part of scaffold characterization, a brief review of the literature dealing with the mechanism of HA dissolution in SBF and the invitro formation of apatite crystals has been presented in the following paragraph.

Klein et. al [2.145] studied the dissolution behaviour of HA and Tri-calcium Phosphate in lactate buffer at 37<sup>0</sup>C, pH 5.2. They observed that the dissolution behaviour depend on the stoichiometry and crystallography of the material. The observed dissolution rate of  $\beta$ -TCP was three times higher than the HA crystal.

Klein et. al [2.146] further studied the effect of different solvent on the dissolution rate of different calcium phosphate. The authors selected three calcium phosphate compositions viz. Tetra calcium phosphate (TTCP), Tri-calcium Phosphate (TCP) and HA. All the three calcium phosphate compositions were subjected to the dissolution tests in four different buffer solutions - lactate, citrate, Gomoris and Michaelis buffer. It was observed that in lactate and citrate solution, the dissolution of TTCP and TCP was nearly same followed by HA. In the other two buffer solutions, the dissolution decreased in the order TTCP>TCP>HA. It was concluded that the dissolution decreased at higher pH.

LeGeros [2.147] reviewed that biodegradation and bioresorbability of calcium phosphate ceramics. The author noted that since the in-vivo biodegradation occurs in an acidic pH, the invitro dissolution condition become important to monitor. The author also commented that the biodegradability and bioresorption depend on the composition, stoichiometry, and the solution conditions. It was observed that the dissolution rate was enhanced at lower pH, i.e., acidic condition.

Hench [2.148] suggested that Tris-Buffer, Simulated Body Fluid can be used to study the bioactivity of calcium phosphate ceramics. The in-vitro study leads the formation of an apatite layer on the surface of calcium phosphate. The presence of apatite layer helps in bone bonding.

Lin et. al. [2.149] studied the invitro-bioactivity of different calcium phosphate ceramics in distilled water. The study revealed that both  $\alpha$  and  $\beta$  TCP as well as a mixture of ( $\alpha+\beta$ ) TCP composition. The results showed HA acted as the seed for nucleating the apatite crystals.

Kwon et. al.[2.150] studied the dissolution behavior of  $\beta$ -TCP and HA/ $\beta$ -TCP composite powder. The authors studied the effect of initial Ca/P ratio, pH of the Ringers solution on the in-vitro dissolution behaviour. It was observed that TCP powder exhibited the highest dissolution rate followed by HA/ $\beta$ -TCP composite powder.

Kim et.al [2.151] studied the in-vitro biomineralization process on HA. The authors used TEM study to observe the surface structure of the SBF aged HA. The apatite formation took place in the three stages. In the first stage, Ca-rich calcium phosphate (Ca/P=1.83) formed. In the second stage, amorphous Ca-lean phosphate (Ca/P=1.47) formed. Finally, in the third stage, Ca/P ratio increased to 1.65 with the formation of needle-like crystals of nano apatite.

Kukubo et.al [ 2.152] used serum added SBF to study the apatite formation on sintered HA. The authors observed that apatite formed in a manner similar to that of pure SBF. The formed calcium phosphate had low Ca/P ratio. The rates of structural changes of apatite in the serum containing SBF was lower than that of pure SBF.

Salcedo et.al [2.153] studied the structural changes occurring in porous HA- $\beta$ -TCP composites during in-vitro aging. The starting porous scaffold had a random orientation of macro and micropores with interconnectivity. The authors observed a change in

overall porosity and pore size after 60 days of immersion. The changes in the pore architecture were correlated to the progressive dissolution of  $\beta$ -TCP in the SBF. The apatite crystallization was preceded by an incubation period.

Liu [2.154] carried out the theoretical analysis of calcium phosphate precipitation in SBF. The authors calculated the nucleation rate based on the heterogeneous nucleation model. Based on the thermodynamics study, the authors concluded that HA precipitation exhibits a higher driving force in comparison to octa calcium phosphate (OCP) and dicalcium phosphate (DCP). The precipitation of DCP is thermodynamically possible only when the Ca/P of SBF increases to a high value with respect to the original SBF value.

So, to conclude, it can be said that many different solutions have been used for the estimation of apatite formation in vitro. Out of them, SBF appears to be most reliable and widely acceptable. The nucleation of apatite is preceded by a dissolution process of HA in SBF. The nucleation requires a seeding of HA. It has been reported that though the dissolution of TCP is higher than HA, the nucleation of apatite in TCP is minimal. However, some controversies exist regarding the viability of this test and its subsequent applicability for in vivo estimation. In spite of these different opinions, SBF treatment appears to be very useful first-hand information on bioactivity.

## *Chapter 3*

# *Motivation and Plan for the Present work*

### **3. Motivation and Plan for the Present work**

This Chapter is a summary of the literature of Porous Ceramics, HA powder preparation, and scaffold fabrication. The discussion on the summary has also identified the area for further research. In the end, an outline of the work plan with a flow diagram has been elaborated.

#### **3.1 Summary of the Literature and Motivation for Work**

The literature review consisted of three parts. In Part-A of the literature review, the different methods for the HA powder processing have been discussed. It was observed that HA powder prepared from the combination of two solid oxides (solid-state) will have the least degree of mixing. On the other hand, HA prepared from the reaction between two liquid components (sol-gel, co-precipitation, spray pyrolysis) will have the highest degree of mixing, stoichiometric HA compositions as well as fine HA crystals. The diphasic mixture containing a solid and a liquid precursor will have the intermediate degree of mixing. Therefore, from the phase stability viewpoint, HA synthesis through sol-gel, precipitation and spray pyrolysis method will show a highly stable phase. Freeze drying and hydrothermal synthesis are the two other popular methods that utilize the pressure-temperature correlation of aqueous or non-aqueous solvents. The other advantage of these two routes is the ease of particle size and morphology manipulation by controlling the synthesis parameters. While solid state route is cheap and user-friendly, it compromises with the phase purity, stoichiometry, the need for high-temperature processing and often the requirement of re-calcination steps. Many of these issues have been taken care of in the solution synthesis routes (precipitation, sol-gel, spray pyrolysis, freeze drying, and hydrothermal synthesis). But these processes may require costly chemicals and detailed infrastructure. In the present scenario, nearly all HA synthesis routes are solution based. The review revealed that depending on the processing route, the powder morphology will vary. The need for specific powder morphology may require some specific process to be adopted. However, it is better to adopt a processing route that will yield a powder with desired Ca/P ratio and phase stability. The powder property, in the long run, may also affect the scaffold property due to the difference in sintering behaviour, dissolution property, etc. Part B have summarized the available literature on porous HA processing. The literature have categorized into four different Sections - (a) sacrificial fugitive removal method, (b) gel casting, (c) replica technique and (d) protein coagulation casting and foaming.

The available literature showed that fugitive method is the easiest to carry out, but may lead to a non-uniform porous microstructure. The pore size distribution may be wide with irregularly shaped pores due to localized clustering or agglomeration of fugitives. The higher amount of fugitives provides a more desirable microstructure but only at the cost of fracture strength. The gel casting route, on the other hand, results in the uniform microstructure, spherical pores, and mechanically strong body. However, it was noted by some authors that gel casting alone had a smaller pore size distribution and may require additional means to improve porosity and pore size. Thus, often gel casting was used in combination with a solid fugitive addition or the use of the synthetic template. Freeze casting can be termed as another variation of gel casting in which the gelation is achieved at cryogenic temperature. The beauty of the technique is the achievement of fully lamellar pores to a combination of the lamellar and spheroidal pore by modification of the process variables. The replica technique turned out to be one of the most reproducible and efficient methods for porous HA preparation. By modifying the PPI (Pores per inch) of the foam, the pore size and interconnectivity could be easily modified. The formation of weak struts was sorted out by multiple coating or by using a slurry of higher loading. The use of stretched template modified the pore size to anisotropic pores that exhibited unique mechanical properties.

Protein coagulation casting/ Foaming is an eco-friendly system using different protein for shape forming and foaming. The presence of amino acids and lysosome permits easy foaming of the slurry when agitated. By varying the protein/water ratio, different degree of foaming could be achieved. There are some reports on the use of freshly extracted chicken egg white as coagulator-cum-consolidator as well as a foaming agent. However, unlike synthetic protein (BSA, Serum albumin, etc.), egg white contains a large volume of water that may affect the actual estimation of the protein difficult. Secondly, in freshly extracted egg white, there is always a possibility for contamination by egg yolk. Egg yolk is detrimental to foaming and the mixing of egg white and yolk in freshly extracted egg white can neither be ruled out nor controlled. Therefore, the foaming behaviour of freshly extracted egg white protein may be difficult to reproduce. In the literature that has been studied in this Chapter, synthetic egg white protein or albumin powder has been used for foaming. A brief mention has also been made on the advanced technique like Rapid Prototyping, Stereo-lithography, and Robocasting for customized porous scaffold preparation. At the same time it can also be mentioned that this advanced technique require specialized and costly infrastructure.

Part C of the Literature Review chapter has discussed the bioactivity characterization of the fabricated porous HA by in-vitro aging in Simulated Body Fluid (SBF). The last section of the literature review has elaborated the mechanisms of in-vitro bioactivity and the different factors affecting the bioactivity evaluation. The invitro bioactivity test is an easy and simple method of obtaining a qualitative or a semi-quantitative estimation of the bioactivity. The earlier studies on the bioactivity concentrated mostly on the dissolution behaviour. The more recent studies also evaluated the growth of apatite on the scaffold. Many different solutions have been used for the estimation of apatite formation in vitro. Out of them, SBF appears to be most reliable and widely acceptable. The nucleation of apatite is preceded by a dissolution process of HA in SBF. However, some controversies exist regarding the viability of this test and its subsequent applicability for in vivo estimation. In spite of these different opinions, SBF treatment appears to be very useful first-hand information on bioactivity.

To conclude this chapter, the following points can be reiterated:

- (a) The fugitive method is easy to perform, but the porosity and microstructure may not be reproducible. A Large fraction of a fugitive is required for creating open and interconnected structure.
- (b) Gel Casting provides spherical pores and stronger scaffold. But gel casting alone may not be sufficient for the desired level of interconnectivity. Often it may require the combination of a foaming agent, a template or a fugitive to homogenize the microstructure.
- (c) The replica technique is easy to perform, and a wide variety of microstructure can be obtained. The wide variation in the scaffold microstructure can be achieved either by pretreatment of template (stretched template) or in conjunction with gel casting
- (d) Protein Consolidation Casting has a wide possibility, when synthetic proteins (albumin, BSA, Serum albumin) are used, the process control is easy. The control with freshly extracted egg white is difficult but possible. The use of binder and the control of foam drainage rate are the key parameters for microstructural control. In view of these discussions, the next Section proposes the plan of work for this study.

### **3.2 Plan of Work:**

The summary of the literature has pointed out that gel casting and protein consolidation are the two methods that are being widely used to prepare HA scaffold. The fugitive method is also popular for industrial production. Among these, the Fugitive method involving solid fugitive is the easiest method though the microstructure may not be

reproducible. So, there is always a possibility to improve the porosity and pore connectivity by controlling the microstructure. Gel casting produces porous but strong ceramics. Some literature have commented that in gel casting, spherical and sometimes smaller pores are obtained. To improve the pore size distribution of the scaffold, gel casting method will be studied with the additional use of naphthalene to the more porous structure.

Protein Coagulation Casting (PCC) is another method useful for porous HA fabrication. Many pieces of literature are available on the PCC method. However, except a few reports, the use of freshly extracted natural egg white has been avoided. The majority of the work has been carried out using Freeze Dried Purified Egg White Flakes, BSA Protein or Whey Protein. Therefore, the use of a natural egg white extract as a foaming and binding is worthy of study. At the same time, literature has also pointed the importance of phase pure and stoichiometric HA on the scaffold properties. Many authors have mentioned that the porosity development, properties, and invitro activity is strongly influenced by starting powder purity.

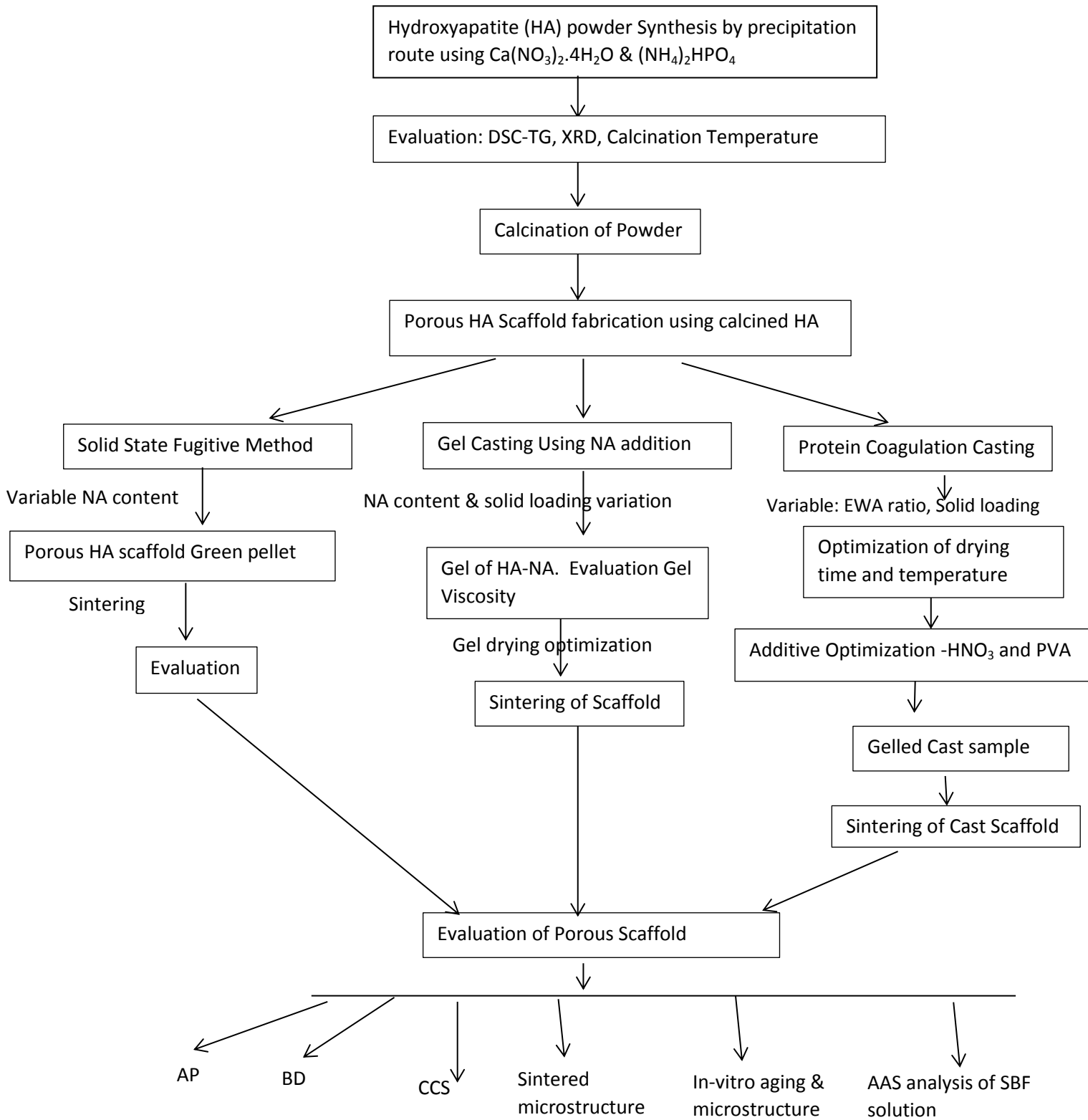
Therefore, summarizing the above points, the proposed plans of work for this thesis are as follows:

- (a) Synthesis of phase pure and stoichiometric HA powder from the wet chemical route. In this study stoichiometric HA (having lower bioresorbability) has been consciously chosen in order to study the effect of pore size and porosity on the fabricated scaffold properties.
- (b) Fabrication of porous HA scaffold by three distinctly different routes and to study the porosity, strength as well as bioactivity. The effect of processing on the morphology of apatite precipitation will also be studied.
- (c) The effect of porosity on the density and strength of the prepared scaffold will be studied.
- (d) In all the fabricated scaffolds, the bioactivity tests will be limited to SBF aging only. This choice is because the main aim of the thesis is to study the effect of different processing on the development of different porous microstructure. SBF aging was carried out to observe the effect of porosity and pore size on the dissolution behaviour of porous scaffold. Since the dissolution will be associated with the growth of apatite layer, the effect of microstructure on apatite growth will be observed. Finally, a few



selected composition of the porous scaffold will be tested for cell viability and cytotoxicity behavior.

**FLOW CHART / METHODOLOGY OF PLANNED WORK**



# *Chapter 4*

## *Characterization Techniques*

## **4. A review of the Characterization Techniques used in this Study**

### **4.1 Background**

This chapter discusses the experimental techniques that have been used throughout the thesis for characterization of HA powder and the porous HA scaffold. The scaffolds have been prepared by three different methods, viz., solid state route, gel casting and protein coagulation casting using egg white. The rationale behind this chapter is to describe at one place the principles involved in different characterizations, the instrumental parameters used for the measurement and the need for such characterizations regarding the present study.

As already mentioned in the Introduction Chapter, HA used in this study have been synthesized in the laboratory by a wet chemical route using  $\text{Ca}(\text{NO}_3)_2 \cdot 4\text{H}_2\text{O}$  and  $(\text{NH}_4)_2\text{HPO}_4$ . The addition of  $\text{NH}_4\text{OH}$  achieved the precipitation of amorphous powder. The as precipitated amorphous powder was subjected to thermal decomposition analysis for evaluating the crystallization behavior and calcined to study the phase evolution of HA. Post calcination, the polycrystalline HA powder was characterized for BET surface, particle size by Zetasizer particle size analyzer, SEM, XRD for phase identification and densification behavior by dilatometer. The porous HA scaffold was also characterized for porosity, pore size distribution, compressive strength, microstructural analysis and in vitro aging in SBF. The HA slurry used for Gel Casting and the egg white used in Protein Coagulation were also studied for slurry rheology.

### **4.2 Thermal decomposition behaviour of precipitated powder**

Differential Scanning Calorimetry (DSC-TG) is a thermoanalytical technique in which the enthalpy change in the sample due to physical and/or chemical reactions is measured with references to a standard sample. Thermogravimetry (TG) is another thermal characterization in which the weight loss of the sample due to the above physical/chemical changes is recorded. Therefore, in a simultaneous DSC-TG both the enthalpy change and the corresponding weight loss of the sample on heating are recorded as a function of time /temperature. The experiment is conducted at a constant heating rate in either air ambient or under a specific gas environment. The types of reactions that can

be studied in DSC-TG are decomposition, crystallization, glass transition temperature, melting, etc. Some of these changes are associated with weight change (decomposition, oxidation) while others (melting, crystallisation) will not involve a weight change. All these reactions are manifested either as endothermic ( $-\Delta T$ ) or as exothermic ( $+\Delta T$ ) peak. The shape and nature of the peaks also give information on the type of reaction, e.g, a broad exothermic peak with an associated weight loss indicates simultaneous oxidation and crystallisation. An inflection point in DSC indicates a change of Glass Transition temperature ( $T_g$ ). Similarly, an exothermic peak with a weight gain indicates simultaneous oxidation and crystallisation. The onset and peak temperature of decomposition and oxidation reactions are affected by heating rate and packing behaviour of powder in the reaction crucible. The area under the curve can also be used for determining the reaction kinetics. Details of the DSC-TG mechanisms and the factors affecting the reactions can be obtained from the classical literature on this subject [4.1].

In the present investigation, simultaneous DSC-TG was carried out to study the decomposition of amorphous Ca-P compound and its progressive crystallisation into HA. The investigation was carried out on a simultaneous DSC-TG (Netzsch STA 449C, Germany) at a heating rate of 10 °C/minute.  $\alpha$ - $Al_2O_3$  was used as the reference material, and the experiment was conducted in Ar atmosphere. The DSC-TG was also utilized to study (i) the decomposition behavior of naphthalene (Chapter 6), the decomposition behavior of HA-MAM-MBAM gels (Chapter 7) and to study the decomposition behavior of Egg White (Chapter 8).

### **4.3 Particle size analysis of HA by Dynamic Light Scattering Technique (DLS)**

Particle size affects many important properties of ceramics. In dry powder processing, particle size controls the packing and densification behavior. In the slurry state, it controls the stability of slurry and packing behavior of cast. A finer particle size usually implies higher reactivity and densification. In the sintered sample, it is reflected through a finer grain size, higher strength. For HA, finer particle size also implies higher dissolution in SBF and a faster apatite formation. Therefore, the determination of particle size is an important characterization required in ceramic fabrication. In this work, particle size and size distribution of calcined HA was measured by DLS technique using Malvern Nano Zetasizer (Malvern ZS). The instrument works on the principle of measuring the diffusion

of particles moving under Brownian motion and converts this data to particle size and distribution using Stokes-Einstein equation [4.1].

$$D = \frac{k_B T}{6\pi\eta r} \dots\dots\dots(4.1)$$

Where D is the diffusion constant,  $k_B$  is Boltzmann's constant T is the absolute temperature,  $\eta$  is the dynamic viscosity and r is the radius of the spherical particle.

The instrument is attached with a Non-Evasive Back Scatter (NIBS) Technology for recording higher sensitivity even at higher suspension concentration. Refractive index for both of the HA and water was considered as 1.5 and 1.33, respectively, and absorption of HA powder was 0.01 [4.2]. HA particles were dispersed in an aqueous medium in distilled water. The dispersion was ultrasonicated for 10 minutes. The suspension thus prepared was used for particle size analysis. The wavelength of laser source was nm.

**4.4 Specific surface area of HA powder:**

The specific surface area of powder is an important parameter related to the fineness of the powder. Specific surface area is the surface area per unit mass of powder. A finer powder (smaller particle size) will have a higher surface area. Therefore, the measurement of specific surface is another approach to predict the powder behaviour, flow properties, sinterability of the powder.

The specific surface area, of the powder is measured from the adsorption of Nitrogen gas when the powder is kept at liquid nitrogen temperature (77.4 K). The specific surface area per unit mass  $S_M$  is given by the equation

$$S_M = \frac{N_A V_m A_m}{V_{mol} M_s} \dots\dots\dots(4.2)$$

where  $N_A$  is Avogadro's number,  $A_m$  is the area occupied by one adsorbate molecule ( $16.2 \times 10^{-20} \text{ m}^2$  for  $N_2$  and  $19.5 \times 10^{-20} \text{ m}^2$  for Kr),  $V_{mol}$  is the volume of 1 mole of gas at the standard temperature and pressure.  $V_m$  is the volume of gas adsorbed for monolayer adsorption, and  $M_s$  is the mass of the sample.

Assuming that all the particles in the powder are spherical, the average particle diameter ( $d_{BET}$ ) can be calculated from BET surface area as per the following equation [4.3]

$$d_{BET} = \frac{6000}{BET_{sa} \times \rho} \dots\dots\dots(4.3)$$

The degassed powder sample was inserted into a low-temperature bath, and N<sub>2</sub> gas was passed over the sample. The volume of adsorbed nitrogen gas was measured from a change in volume in the gas. The surface area of calcined HA powder was determined by BET apparatus (Quantachrome/AUTOSORB-1). About 40mg of the sample was taken in the sample cell and degassed at 150°C in vacuum up to a maximum of 3 mbar [4.2].

**4.5 Phase evolution and phase stability of HA by XRD**

X-Ray Diffraction (XRD) is a widely used non-destructive characterization for determination of crystalline structure and phase. XRD analysis involves the irradiation of the sample (powder or bulk) with a beam of monochromatic x-ray radiation and recording the position and intensity of the diffracted beams as a function of goniometer position (2θ). The instrument works on the principle of Bragg’s diffraction

$$\lambda = 2d \sin\theta \dots\dots\dots(4.4)$$

Where λ is the wavelength of X-rays, d= interplanar spacing (or d-spacing) and θ is the diffraction angle. The phase analysis of HA on heating the as precipitated HA powder was carried out by X-ray diffraction (XRD). The XRD patterns of the calcined HA powder was recorded as a function of calcination temperature. This characterization not only provided information on the crystallization sequence of HA with calcination temperature. It also indicated if the powder was single phase or multiphase or if there was a phase change with calcination temperature [4.4]. In the present study, the HA phase and its stability with calcination temperature has been studied through Philips PANalytical powder X-ray diffractometer. The diffraction patterns were recorded with CuK<sub>α</sub> radiation (λ=1.542Å) and was fitted with Ni filter to separate the K<sub>β</sub> radiation. X-rays were generated at 35KV/30mA. The samples were scanned in a continuous mode at a scanning rate of 0.02/sec. The HA, β-TCP and CaO peaks were identified by comparing the d-spacing of the observed peaks with the respective JCPDS reference XRD files. For this study, File No 84-1998 was considered for HA, 70-2065 for β-TCP and 82-1691 was the

reference file for CaO. All pattern identification of HA,  $\beta$ -TCP and CaO was made by comparing the sample peaks with the standard file.

#### **4.6 Study of the Functional groups by Fourier Transform Infrared Spectroscopy**

FTIR study involves the interaction of IR frequency with the functional group molecules present in the compound. The interaction will lead to the absorption of IR energy whenever there is a resonance between the natural frequency of vibration of molecules and that of IR radiation. Thus, it can provide useful information about the different functional groups present in the compound that will help in compound identification. More than compound identification, this technique can also be used for ascertaining the presence or absence of impurities in the material. Therefore, IR or FTIR is routinely being used for determining the phase purity of the synthesized material. In this thesis, the phase purity of the synthesized HA powder was studied by FTIR spectroscopy (Perkin Elmer, RXI, USA) in the wave number range  $4000\text{-}400\text{ cm}^{-1}$  in KBr pellet mode. KBr powder was mixed with HA powder in the weight ratio 1:20 and the mixed powder was pressed in a hydraulic press at 3 Ton load. The presence of KBr reduces the scattering effect and increase the signal to noise ratio [4.5].

#### **4.7 Densification study of HA particle by Dilatometer**

A Dilatometer is generally used to study the shrinkage/expansion measurement of a material as a function of temperature. It is also used for evaluating the sintering processes of ceramics, martensitic transformations in the quenching of steel, de-vitrification of glasses, dimensional changes during chemical reactions and phase changes of solid materials [4.6]. The shrinkage of green HA compact during its sintering has been studied by Dilatometer (Netzsch, Germany, DIL 402C). In a dilatometer, the dimensional change of the sample on heating or cooling is recorded as a function of temperature or time. The dimensional change of the sample on the heating is recorded by a Linear Variable Differential Transducer (LVDT). The LVDT signal is electronically processed to record the change in the dimension of the sample. In the present study, rectangular bars ( $25 \times 5 \times 2\text{ mm}^3$ ) of green HA compacts were heated at  $3^\circ\text{C}/\text{min}$  in Ar atmosphere till  $1300^\circ\text{C}$ . The change in the dimension ( $dL/L_0$ ) of the sample as a function of temperature was recorded.

#### 4.8 Bulk Density and Apparent Porosity Measurement

The Bulk Density (BD) of a porous system is the mass per unit bulk volume of the material

Apparent Porosity (AP) refers to the amount of void (or pores) within a volume of porous solid. The value of porosity is measured as a fraction or percentage. The True Porosity includes the volume of the sealed pores also [4.7].

The BD and AP of the all porous samples were measured by Archimedes principle. The dry and weighed samples were suspended in water kept inside a beaker and were either evacuated in a vacuum evacuator or boiled for the removal of bubbles to come out from the sample. During the evacuation process, the water goes inside the open pores. The samples were kept in vacuum for further 30 minutes to allow penetration of water in the pores. After the scheduled period, the beaker was removed from the vacuum desiccator, and the suspended and soaked weight of the samples was measured.

The B.D and A.P of sintered sample were measured as per the following formula (4.5) and (4.6).

$$\text{B.D (gm/cc)} = \frac{D}{W-S} \dots\dots\dots(4.5)$$

$$\text{A.P (\%)} = \frac{W-D}{W-S} \times 100 \dots\dots\dots(4.6)$$

Where D- Dry weight of the sample, S- Suspended weight of the sample, W- Soaked weight of the sample [3.7].

#### 4.9 Cold Compressive strength (CCS)

Cold Compressive strength (CCS) of the material is the value of uniaxial compressive load that causes the fracture or the failure of the material. Experimentally, this is determined by breaking a specimen under compression at an increasing load. The compressive strength of the porous scaffold (14mmφ x 8 mm height) was measured by Universal Testing Machine (H10 KS Tinius Olsen) using a load cell of 10 KN at a cross head speed of 0.5 mm/minute. The compressive strength was determined from the following equation below

$$\text{CCS} = \frac{P}{A} \dots\dots\dots(4.7)$$

Where, P = Load in KN and A = Cross sectional area of the cylindrical sample



The CCS of the scaffolds show different load-displacement curve in comparison to the solid sample. Here the failures occur by an elastic-brittle fashion. This type of behaviour is observed due to the presence of pores and struts in the sample [4.8].

#### **4.10 Microstructure by Scanning Electron Microscope (SEM)**

Scanning electron microscope uses the electron beam to generate the images. Due to the very small wavelength of electron and high energy, a large depth of field is achievable in SEM. As a result of the large depth of field, a 3-D image of the grains and pores can be observed. The high energy electrons interact with the sample and generate either a secondary electron image (SE) or a back scattered image (BSE). FESEM is an upgraded version of SEM where the electrons are generated through Field Emission Guns (FEG) instead of the normal thermionic emission. The microstructure of HA particles were observed in a Field Emission Scanning Electron Microscopy (FESEM) (Nova Nano 450, FEI USA). The samples were sputter coated with gold for 3 minutes in Argon atmosphere (Quorum Technology, Q150R ES). Some of the scaffolds were also observed in an SEM (JEOL JSM-6084LV). For SEM observation, the samples were sputtered coated with Gold. The samples were observed at lower magnification in SE mode.

#### **4.11 Slurry Rheology**

The study of Slurry Rheology essentially implies the study of shear stress and viscosity of the slurry with increasing shear rate. The study provides the information on the stability of the slurry under a shear stress. While most of the ceramic slurries exhibits shear thinning behaviour, some slurry may exhibit a shear thickening behaviour also. On disturbing such slurry, it will thicken up or lose fluidity. Such slurry is not suitable for casting. In a casting process, shear thinning slurry with a gelling capacity in a short time is desirable.

The particle size, size distribution, deflocculant, binder content and additives affect the slurry rheology. In this study, slurries were prepared for fabricating scaffolds by gel casting and protein coagulation casting method.

Therefore, the study of slurry rheology becomes an important parameter to optimize the solid loading, deflocculant concentration, binder content, etc. for the workable slurry. The rheological behavior of HA slurry was measured using Rheometer (Rheolab QC, Anton Paar, USA). Rheological tests were performed at 25 °C in the shear rate in the range 0.1-

250 s<sup>-1</sup> with a concentric-cylinder with 1.33 mm gap between the inner and outer cylinder walls.

#### 4.12 Mercury Intrusion Porosimeter

Mercury intrusion porosimeter measures the pore size and porosity. Mercury is intruded in the pores of the sample by increasing the pressure on the mercury. All mercury porosimeter operates on the Young-Laplace or Washburn equation [4.9]

$$\Delta P = \gamma \left( \frac{1}{r_1} + \frac{1}{r_2} \right) = \frac{2\gamma \cos\theta}{r} \dots\dots\dots(4.8)$$

Where r = radius of the Capillary pore,  $\gamma$  = liquid-vapor interfacial tension,  $\theta$  = contact angle between the liquid and capillary wall.

One of the basic assumptions in the above equation is the presence of only cylindrical pores. The methodology consists of evacuating the samples followed by the intrusion of mercury at an increasing pressure. According to Washburn equation, the larger pores will be filled first at a lower pressure and the smaller pores will require a higher pressure. The volume of mercury intruded in the sample depends on pore size, shape and interconnectivity. Nature of pore and pore size distribution was evaluated through porosimetry (Poremaster-33, Quantachrome, USA). The sintered HA scaffolds were placed in the sample holder. The sample holder was evacuated to remove the entrapped gases and occluded materials. The evacuated sample is infiltrated with mercury at increasing pressure. For this model of porosimeter, the minimum pressure was 0.951 psi that translated to a pore size of 224  $\mu\text{m}$ . Thus pores larger than 224  $\mu\text{m}$  could not be detected by this instrument. Therefore, porosimeter data represents only a partial picture of pore sizes present in the samples.

#### 4.13 In-vitro Bioactivity

Hydroxyapatite (HA) is a bioactive material. When implanted in vivo, it exhibits a positive response towards the tissues without any negative side reaction. It has been documented by many authors that the bioactivity of HA is associated with the dissolution of HA and the subsequent precipitation of calcium phosphate as apatite through a series of intermediate reactions. The bone bonding phenomenon with the implant realizes through the intermediate apatite layer. All these experiments require an animal testing.

The sequence of these “in vivo” reactions has been simulated in a laboratory without the need of an animal testing. This simulated test is known as invitro bioactivity in Simulated Body Fluid (SBF). Kukubo et.al [4.10] and Tas et.al [4.11] have given the prescription for SBF having the concentration of different ionic species in the same proportion as in human body plasma. The invitro bioactivity is carried out by immersing HA in the SBF for different specific tissue periods. The sequence of apatite formation is observed by determining the chemical composition of the layer formed due to ageing. In the present investigation, the bioactivity test is performed by immersing HA scaffold in SBF. The SBF was prepared in the laboratory following the procedure described by Tas [4.11]. According to the literature, in the process of apatite formation, the ionic concentration of SBF changes due to the dissolution of HA in SBF. The dissolution results in the change in  $\text{Ca}^{+2}$  and  $\text{P}^{+5}$  concentration of SBF. Subsequently, when apatite crystals grow from SBF, the concentration of  $\text{Ca}^{+2}$  and  $\text{P}^{+5}$  of SBF will further change. In this study, such a change of  $\text{Ca}^{+2}$  and  $\text{P}^{+5}$  is monitored by measuring  $\text{Ca}^{+2}$  and  $\text{P}^{+5}$  of SBF after different aging time. The concentration of  $\text{Ca}^{+2}$  and  $\text{P}^{+5}$  has been determined in an Atomic Absorption Spectrophotometer (AAS) (Perkin Elmer AS 800). The used SBF solution has been aspirated through a graphite electrode. For  $\text{Ca}^{+2}$  determination Ca hollow cathode lamp (423 nm) and for  $\text{P}^{+5}$ , Phosphorus hollow cathode lamp (223.6 nm) has been used. The change in the light intensity due to the electron transition of Ca and P atom is monitored and compared with a standard  $\text{Ca}^{+2}$  and  $\text{P}^{+5}$  solution. The formation and growth of apatite layer were studied by observing the SBF aged samples in FESEM. The SBF aged samples were properly washed with DI water and dried. The dried samples were coated with Gold-Platinum coating and observed in the SE mode.

#### **4.14 Preparation of Simulated Body Fluid (SBF)**

Simulated Body Fluid (SBF) has been prepared at room temperature using the chemicals and methods prescribed by Kukubo [4.11]. The list of chemicals used for SBF preparation is given below:

**Table 4.1 Batch Composition for SBF Preparation**

Sl. No	Chemicals	Amount required (gram/Liter)
1	NaCl	6.547
2	NaHCO <sub>3</sub>	2.268
3	KCl	0.373
4	Na <sub>2</sub> HPO <sub>4</sub> .2H <sub>2</sub> O	0.178
5	MgCl <sub>2</sub> .6H <sub>2</sub> O	0.305
6	CaCl <sub>2</sub> . 2 H <sub>2</sub> O	0.368
7	Na <sub>2</sub> SO <sub>4</sub>	0.071
8	(CH <sub>2</sub> OH) <sub>3</sub> CNH <sub>2</sub>	6.057
9	HCl [1M]	40mL (Total)

The chemicals in the Sl. No 1 to 5 was sequentially added to 700 mL DI water taken in a clean and dry 2000 mL plastic beaker. The sequential addition of chemicals was carried out with the restriction that the next chemical in the sequence was added only after the complete dissolution of the preceding chemical. After the addition of fifth chemical [MgCl<sub>2</sub>.6H<sub>2</sub>O], 15 mL of 1M HCl was slowly added to the solution to lower the pH and to avoid turbidity of the solution. After the addition of 15mL HCl, chemicals in the serial No. 6 to 8 were also added sequentially and only after the complete dissolution of the preceding chemical. Following the addition of eight chemical, the solution temperature was raised to 37°C and remaining 25mL 1M HCl was slowly added from a burette to bring the pH to 7.4. During HCl addition, an additional volume of DI water was also added to make the volume to 1 Liter. The prepared SBF was cooled to room temperature and was stored in a sealed container in a refrigerator.

#### **4.1.15 Cytotoxicity evaluation through MTT [3-(4, 5-Dimethylthiazol-2-yl)-2, 5-Diphenyltetrazolium Bromide] Assay**

The cytotoxicity of a scaffold is evaluated by estimating the living cell after the cell has been cultured for growth in the scaffold material. In the present context, the cytotoxicity of the prepared scaffold was evaluated by quantifying the viable cells through a staining method [4.12]. The colourimetric assessment of viable cells is used on tetrazolium salt of

MTT. The chemical formula of tetrazolium salt is (4, 5-dimethyl thiazol-2-yl)-2-5 diphenyl tetrazolium bromide. This compound measures the mitochondrial dehydrogenase enzyme and measures only for the living cells. The process consisted of dissolving the MTT [3-(4,5-dimethylthiazol(-2-yl)-2-5-diphenyltetrazolium bromide] in PBS and added in the culture plate of L929 mouse osteoblast. After the required 24hrs of incubation with 5% CO<sub>2</sub> at 37 °C, the dark formazon crystals were dissolved in dimethyl sulphoxide. The absorbance was measured in a spectrophotometer at 540nm wavelength. The difference in the absorption with respect to a control sample (without living cell) provided the Cytotoxicity evaluation.

## *Chapter 5*

# *Synthesis of Hydroxyapatite powder*

## 5. Synthesis of Hydroxyapatite powder

### 5.1 Background

Chapter-1 has provided an overall view of the porous material, the different processing routes for fabricating porous scaffold and their relative merits and demerits. It has also been mentioned that most the scaffold processing routes are also applicable for the processing of porous HA scaffolds. A consolidated list of the different HA scaffold fabrication route has also been provided. Chapter-2 has discussed on the different research that has been carried out in the area of HA scaffolds and the properties of porous HA scaffolds. In the course of the discussion, it was also pointed out that particle size, shape, and crystallinity has considerable influence on the in-vitro bioactivity. Thus, it was important to decide the method to be used for HA synthesis. Out of many methods available for HA synthesis [5.1-5.12], co-precipitation is one of the most user-friendly method, cheap with good compositional uniformity and reproducibility. However, within the realms of co-precipitation, there are various combinations of raw materials that have been used by different groups for precipitation of HA. Some of these are  $\text{Ca(OH)}_2/\text{H}_3\text{PO}_4$  [5.13]  $\text{Ca(NO}_3)_2 \cdot 4\text{H}_2\text{O}/(\text{NH}_4)_2\text{H(PO}_4)$  [5.14],  $\text{Ca-EDTA}^{2-}/\text{HPO}_4^{2-}$  [5.14.],  $\text{Ca(OEt)}_2/\text{PO(OEt)}_3$  [5.15],  $\text{Ca(OH)}_2/\text{C}_3\text{H}_6\text{O}_3$  [5.16]  $\text{Ca(NO}_3)_2 \cdot 4\text{H}_2\text{O}/\text{C}_6\text{H}_5\text{PCl}_2$  [5.17.] etc. In the present work,  $\text{Ca(NO}_3)_2 \cdot 4\text{H}_2\text{O} / (\text{NH}_4)_2\text{H(PO}_4)$  combination has been chosen as the raw materials. The choice of precursors has been decided on the basis of the previous work done in our laboratory with this set of precursors. In the previous study, the experimental parameters had been properly optimized to produce a stoichiometric crystalline HA ( $\text{Ca/P}=1.67$ ) [5.18]. The HA powder synthesized by the above co-precipitation route has been used for processing of porous scaffolds of HA by three different routes. These are (a) solid state route using HA powder and powder pore former, (b) Gel casting route in which HA powder mixed with an initiator and an accelerator, and, (c) Foaming method wherein HA powder is mixed with egg white protein with the later acting as foaming agent. A question may arise on the rationale of choosing a stoichiometric HA for scaffold fabrication. It is well known that the efficiency of both in-vitro and in vivo bioactivity depend on the phase composition [5.14-5.17]. The combination of HA and a biphasic HA (HA+TCP) has shown better bioresorbability and bonding in comparison to

stoichiometric HA [5.17-.18]. Knowing this fact very well, in the present study, stoichiometric HA was consciously chosen as a scaffold material in order to investigate the effect of porosity on the dissolution behavior of a stoichiometric HA.

## 5.2 Raw Materials and Experimental Procedure

The starting raw materials for HA powder synthesis were 1M di-ammonium hydrogen phosphate ( $(\text{NH}_4)_2\text{HPO}_4$ ) (Merck, India, GR grade) and 1M calcium nitrate ( $\text{Ca}(\text{NO}_3)_2 \cdot 4\text{H}_2\text{O}$ ) (Merck, India, GR grade). The mixing of the precursors and the precipitation of the hydroxides was carried out at room temperature that varied from  $25^\circ\text{C}$  to  $30^\circ\text{C}$  depending on the season. Firstly, separate one molar concentration stock solution for each of ( $\text{Ca}(\text{NO}_3)_2 \cdot 4\text{H}_2\text{O}$ ) and ( $(\text{NH}_4)_2\text{HPO}_4$ ) were prepared by dissolving the respective chemicals in deionized water. The individual stock solutions were sequentially mixed (in the appropriate volume ratio so has to yield  $\text{Ca}/\text{P}=1.67$ ) in a 1000 ml beaker. The mixed precursors were homogenized by stirring for 2 hours on a magnetic stirrer. The mixed solution was turbid. A few drops of concentrated  $\text{HNO}_3$  were added to the mixed solution to remove the turbidity and to obtain a clear solution. The precipitation was carried out at 10.5 pH by dropwise addition of  $\text{NH}_4(\text{OH})$  to the vigorously stirred solution. The end point of the reaction was marked by the presence of a voluminous milky white precipitate. The as formed precipitates were aged for 24 hours at room temperature to allow the growth and stability of precipitate. The aged precipitate was washed with hot deionized water to remove excess ammonia and  $\text{NH}_4\text{NO}_3$  followed by washing with propanol. The process was repeated 5-6 times to bring down the pH near 7-8. The propanol washed precipitate was oven dried ( $80^\circ\text{C}$ ) for 24 hours. The HA is expected to form following the chemical reaction:

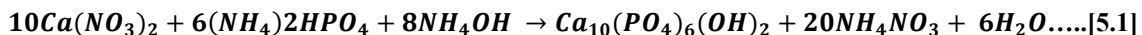
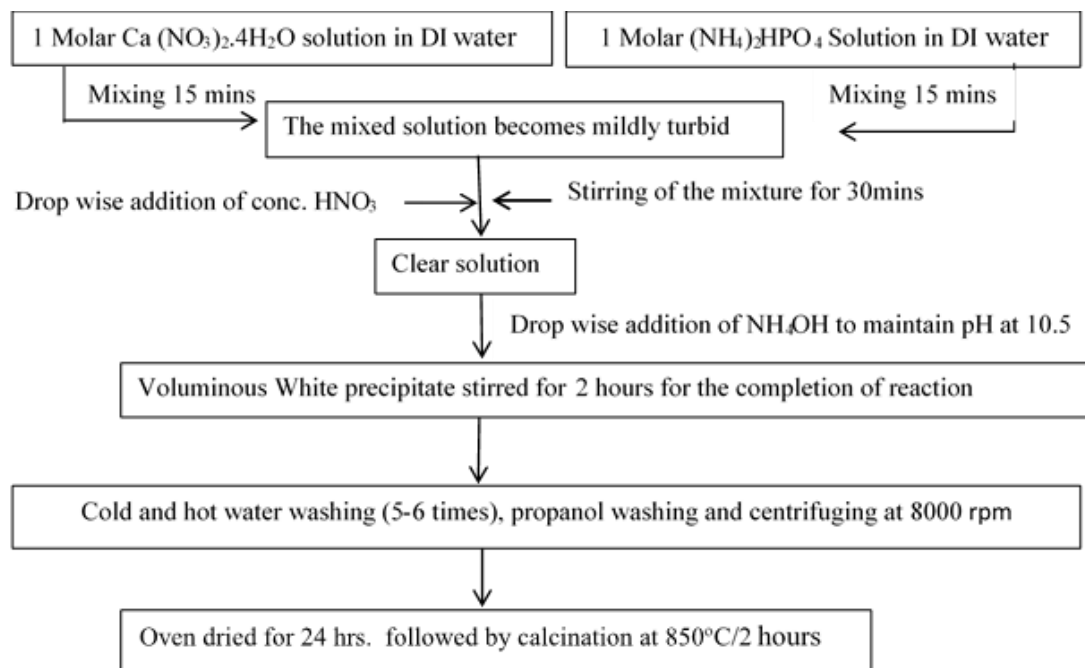


Figure 5.1 outlines the detailed procedure and experimental conditions for HA powder preparation.





**Fig. 5. 1 Process Flowchart for the synthesis of HA using  $\text{Ca}(\text{NO}_3)_2 \cdot 4\text{H}_2\text{O}$  and  $(\text{NH}_4)_2\text{HPO}_4$**

### 5.3 Characterization of as precipitated and calcined powder

#### 5.3.1 Thermal analysis of HA precipitates

The thermal decomposition and crystallization behavior of dried precipitates of amorphous calcium phosphate was studied by simultaneous DSC-TG ((Netzsch, Germany, STA449C). The samples were heated at  $10^\circ \text{C}/\text{min}$  in an argon atmosphere (Fig 5.2).

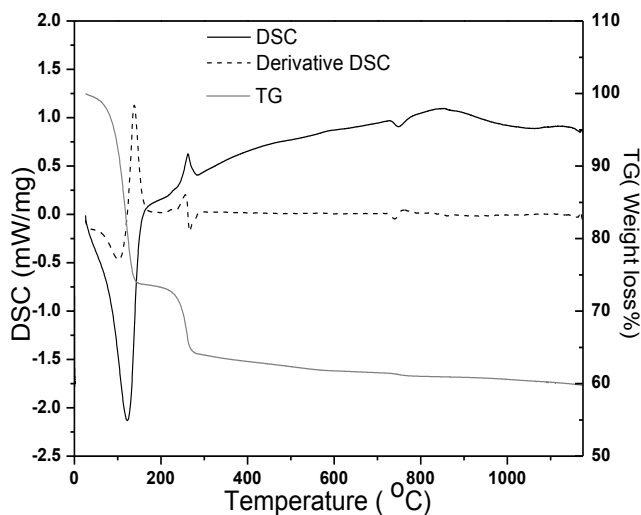


**Fig. 5.2. DSC-TG of Amorphous Calcium Phosphate precipitate**

The DSC plot has endothermic peaks at  $< 100\text{ }^{\circ}\text{C}$ ,  $120\text{ }^{\circ}\text{C}$ , and  $720^{\circ}\text{C}$ . The exothermic peaks are observed at  $220\text{ }^{\circ}\text{C}$ ,  $275\text{ }^{\circ}\text{C}$  and at  $860\text{ }^{\circ}\text{C}$  (broad exothermic peak). All the above-mentioned peaks are associated with some weight loss. The first endothermic peak at  $<100\text{ }^{\circ}\text{C}$  and associated with a weight loss of  $\sim 3\%$  can be assigned to the loss of surface water or moisture present on the sample surface. The second peak at  $\sim 120\text{ }^{\circ}\text{C}$  is very sharp strong peak associated with  $\sim 22\%$  weight loss is due to the loss of physically absorbed water. A very small exothermic peak follows at  $\sim 220\text{ }^{\circ}\text{C}$  with a weight loss of about  $2\%$  that is mostly likely due to the oxidation of some ammonia remaining in the sample. The small but sharp exothermic peak at  $275\text{ }^{\circ}\text{C}$  is assigned to the oxidation of left over  $\text{NH}_4\text{NO}_3$  in the washed precipitate.

A gradual and a positive slope change in DSC curve is observed between  $280^{\circ}\text{C}$  and  $750^{\circ}\text{C}$ . A small endothermic peak is observed at  $750^{\circ}\text{C}$ , probably due to the amorphous to crystallization transition. This slope change usually indicates a series of exothermic reactions. The derivative of DSC curve does not show any derivative peak or weight loss indicating the absence of any reaction involving weight loss. XRD patterns of the powder calcined between  $275\text{ }^{\circ}\text{C}$ , and  $750\text{ }^{\circ}\text{C}$  show that the peaks corresponding to HA gradually emerge out from an initially amorphous material. Upto  $750^{\circ}\text{C}$ , the d-spacing differs from the ideal HA d-spacing. These have been discussed in detail in Section 4.2.3.1 (Phase Analysis). At  $750^{\circ}\text{C}$ , an endothermic peak is observed which is immediately followed by a broad exothermic peak around  $850^{\circ}\text{C}$ . The peak at  $750^{\circ}\text{C}$  is most likely due to amorphous to crystallization transformation. The XRD pattern of powder calcined at  $850^{\circ}\text{C}$  shows that the d-spacing of powder closely matches with stoichiometric HA. Thus, the DSC-TG pattern confirms that powder need to be calcined at  $850\text{ }^{\circ}\text{C}$  or higher temperature to obtain well crystallized stoichiometric HA powder.

### **5.3.2 Study of phase evolution in calcined HA**

#### **5.3.2.1 Phase analysis by X-ray diffraction**

The sequential phase evolution of HA on the calcination of precipitated amorphous calcium phosphate has been studied through XRD. The samples were calcined at seven different temperatures with  $275^{\circ}\text{C}$  being the lowest and  $900^{\circ}\text{C}$  being the highest calcination temperature. These different calcination temperatures were finalized on the

basis of DSC-TG plot and intended to cover the entire temperature range over which decomposition, oxidation and crystallization temperature reactions were expected to take place. The XRD pattern of the as dried and precipitated powder has been included (as reference sample) which show that the as precipitated powder is amorphous. The XRD pattern of all the calcined powders is expected to show the gradual phase evolution and crystallization leading to the formation of stoichiometric HA. The discussion on the phase evolution and identification is based on the three most prominent peaks of HA in the  $2\theta$  range  $30^\circ$ - $40^\circ$ . These peaks are  $2.812\text{\AA}$  (121),  $2.776\text{\AA}$  (112),  $2.718\text{\AA}$  (300). Fig. 5.3(a) shows the XRD pattern of all the calcined samples in the  $2\theta$  range  $20^\circ$  -  $60^\circ$ . Fig 5.3 (b) and 5.3 (c) show the XRD patterns of the calcined HA with respect to prominent peaks of HA in the  $2\theta$  range  $30$ - $40^\circ$ .

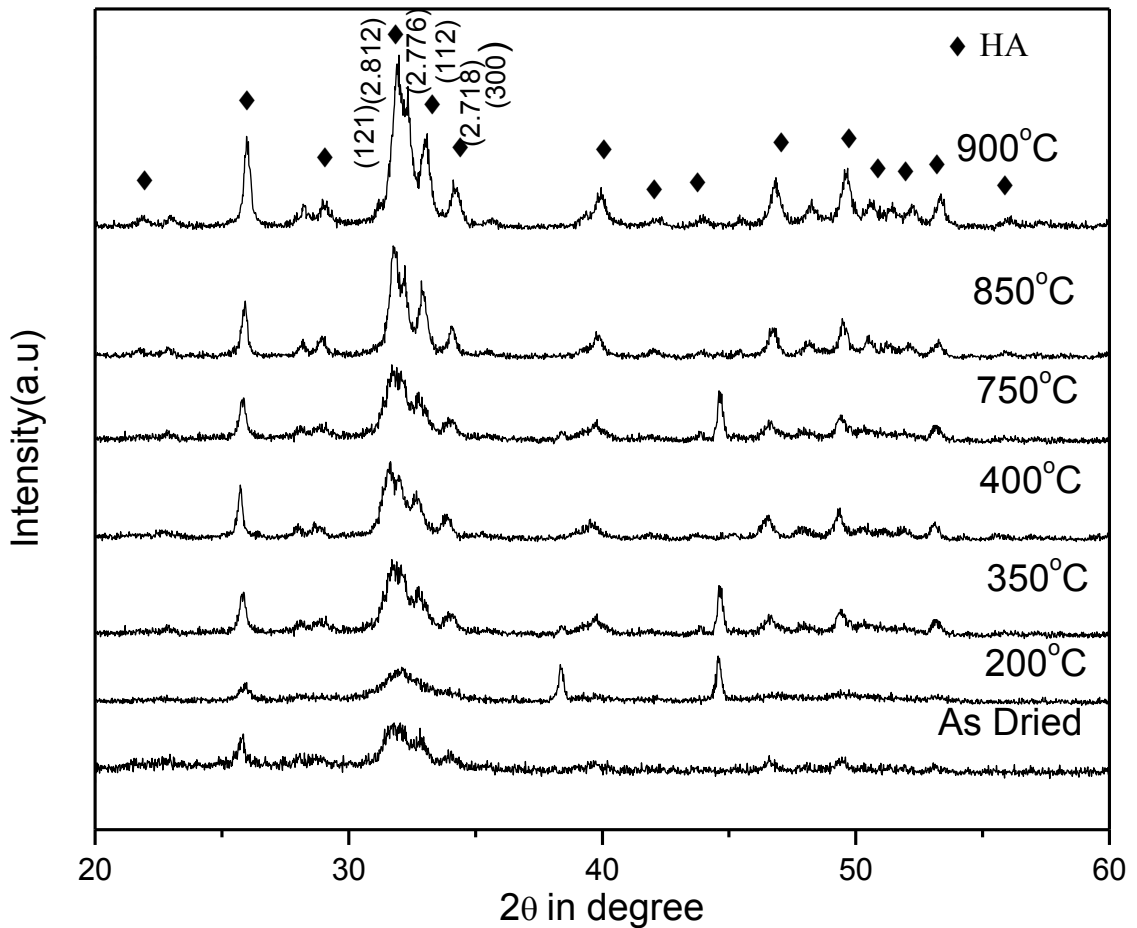


**Fig.5.3 (a) XRD plots for powder calcined between 200 and 900°C.**

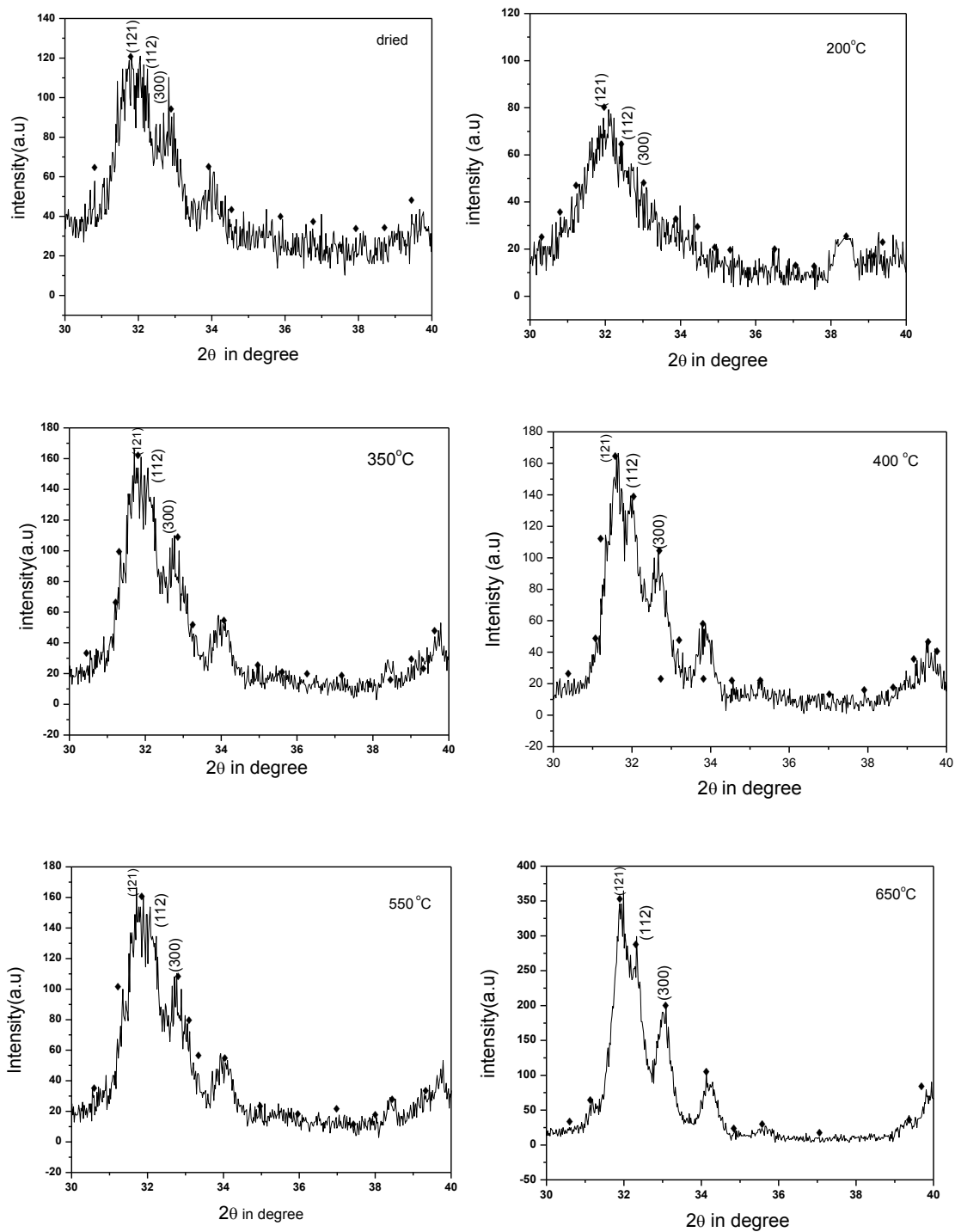


**Fig. 5.3 (b) XRD pattern of HA calcined at different temperatures (200-650 °C) showing the triplet peak of HA in the  $2\theta$  range 30-40°.**

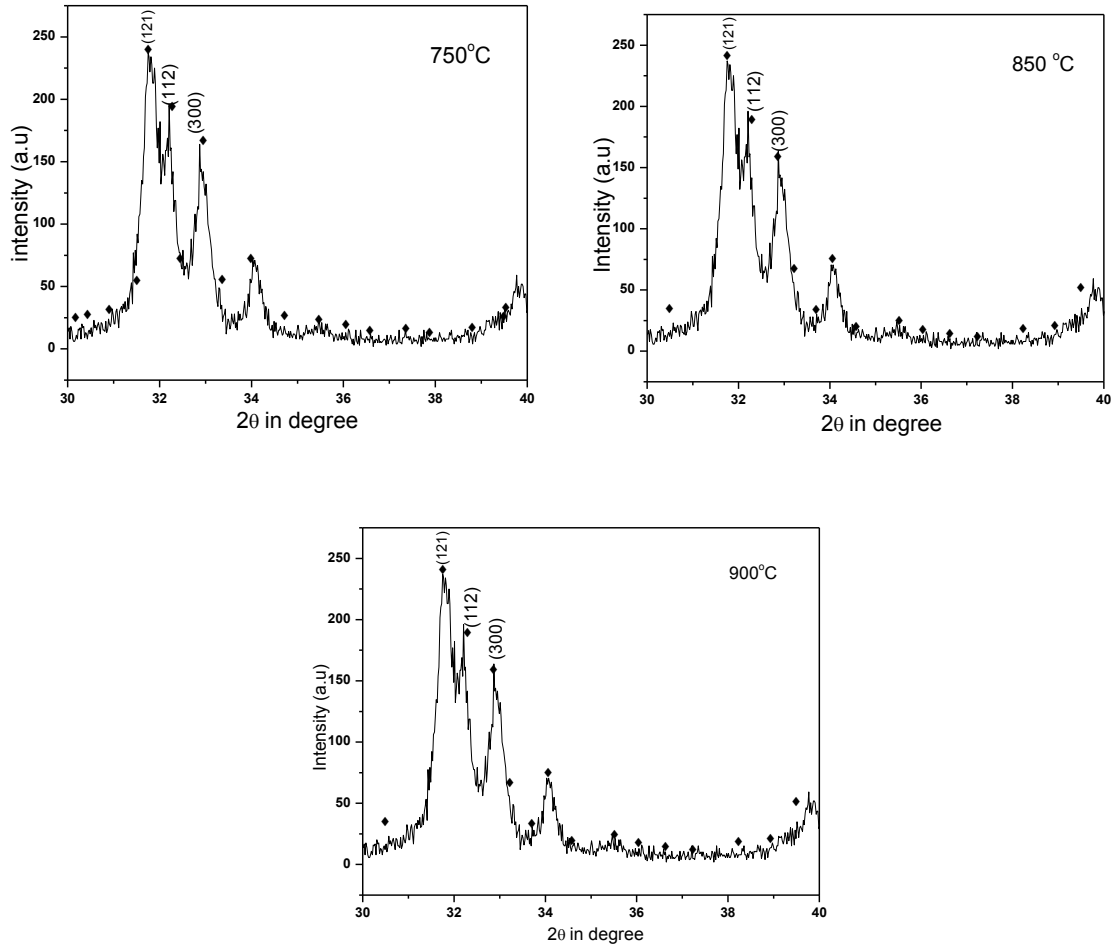


**Fig. 5.3 (c) XRD pattern of HA calcined at 750°C, 850°C, 900°C showing the triplet peak of HA, in the 2θ range 30°-40°**

As can be seen from the patterns, at lower calcination temperatures (up to 750°C), the peaks are mostly asymmetric, broad and with shoulder peaks or doublets appearing around the main peak positions. With the increase in the calcination temperature, this asymmetry gradually smoothens out and symmetric peak start appearing. The changes in the peak shape and peak position with increasing calcination temperature is distinctly visible from 750°C onwards. The following Table also lists the d-spacing of the three prominent peaks of HA as mentioned below.

**Table 5.1 d-spacing of three prominent HA peaks (Å) at various temperatures range**

Calcination Temperature (°C)	d-spacing of three prominent HA peaks (Å)		
	Peak 1 (121)	Peak 2 (112)	Peak 3 (300)
200	2.821	2.785	2.730
350	2.820	2.790	2.734
400	2.830	2.799	2.740
550	2.820	2.785	2.734
650	2.804	2.770	2.712
750	2.815	2.777	2.720
850	2.812	2.777	2.719
900	2.812	2.777	2.719
JCPDS Std 84-1998	2.812	2.776	2.718

Thus, from the above discussion, it can be summarized that the as precipitated amorphous calcium phosphate transforms to stoichiometric HA through a series of non-ideal HA phases which exist at lower temperatures (up to 750°C). The XRD pattern of HA powder calcined at 850°C and 900°C matches closely with JCPDS 84-1998. Thus, although 900°C calcined powder would represent the ideal HA d-spacing and hence the crystal structure, the calcination temperature is fixed at 850°C, as this would have a smaller crystallite size and a smaller agglomerate size. A smaller agglomerate size is expected to help in better compaction and sintering of HA powder.

### 5.3.2.2 Phase purity study by FTIR spectroscopy

The phase purity of the calcined HA powder was studied by observing the different functional groups present in the HA calcined at 850°C by FTIR spectroscopy (Perkin Elmer RXI, Spectrum, USA). The spectrum shows a sharp peak at 3572cm<sup>-1</sup> due to (OH)<sup>-</sup> stretching, a shoulder peak at 1041cm<sup>-1</sup> arising from asymmetric ( $\nu_3$ ) stretching and bending vibrations of (PO<sub>4</sub>)<sup>3-</sup> and a triplet between 635 and 570 cm<sup>-1</sup> corresponding to (PO<sub>4</sub>)<sup>3-</sup> ( $\nu_4$ ) bending vibration [5.19]. Thus, the pattern carries the characteristic signature

of HA alone and thus it can be inferred that the calcined powder is essentially single phase HA [Fig.5.4].

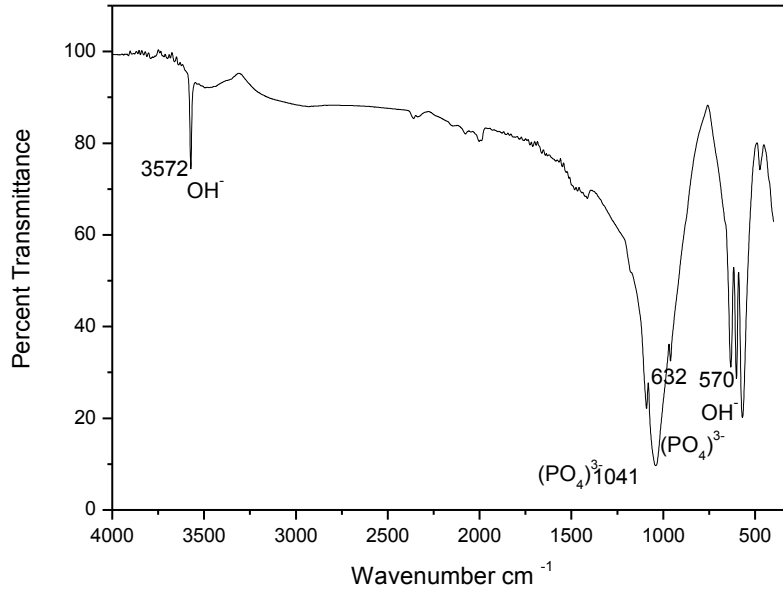


**Fig. 5.4. FTIR spectrum of HA powder calcined at 850 °C.**

### 5.3.3 Particle size distribution and specific surface area of calcined powder

The particle size and size distribution of HA were estimated through dynamic light scattering technique (Zetasizer nanoZS, Malvern) using a 663 nm laser source. The particle distribution was primarily mono-modal with the average particle size being 0.5-1µm as shown in Fig. 5.5. The BET surface area of the powder was 14.9 m<sup>2</sup>/gm.

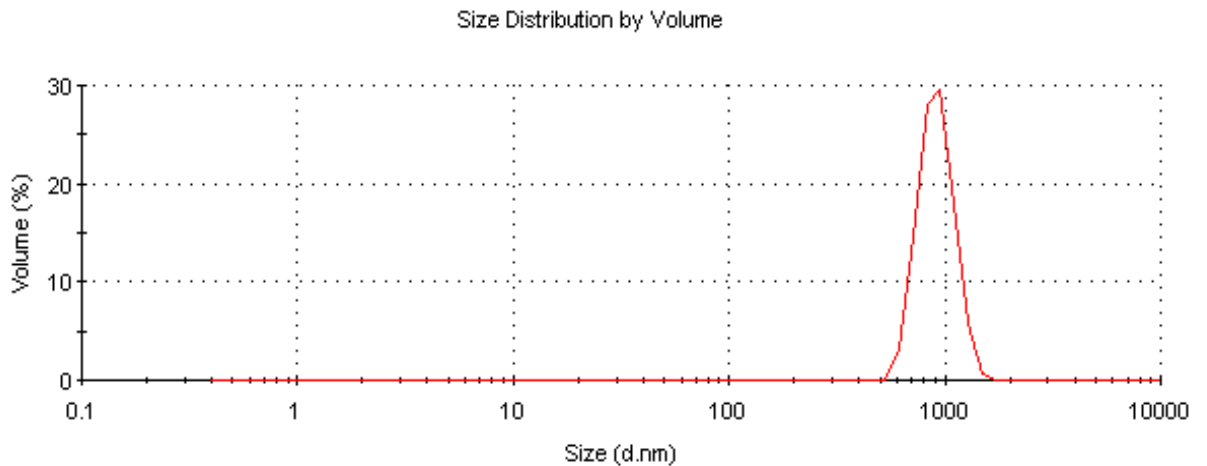


**Fig. 5.5 particle size distribution of calcined HA**

### 5.3.4 Study of HA particle size by SEM

The microstructure of calcined HA powder was observed using Field Emission Scanning Microscopy (FESEM) (Nova Nano 450, FEI USA). For SEM observation, a pinch of powder was dispersed on the carbon tape. Fig. 5.6 (a) (b) and (c) show FESEM image of HA particles calcined at 850, 900 and 1000 °C respectively. The particles are agglomerated with primary particles size in the range 0.5-1 µm. A closer observation on the particles reveals that the particles are mostly elongated with a few near-spherical shapes. These kind of elongated particles have also been observed in a previous study[5.18]. Nayak et.al have also observed that if the precipitation is carried out at pH>10, the particles are elongated. Similar observations have also reported by Ferraz et.al [5.13]. It has been observed by many authors [5.19-5.21] that the transformation of an amorphous calcium phosphate to hydroxyapatite takes place through an intermediate octacalcium phosphate phase. It involves two dimensional nucleation and growth [5.22-5.23]. Viswanath et al [5.24] have shown that during a precipitate reaction, the absence of capping agent can promote 2D growth of HA particles. Clain [5.25] in this classical theory has commented that a low driving force for the growing interface can cause the interface to grow only laterally giving a 2D or elongated shape. Viswanath et. al has also observed plate/ elongated shaped HA crystals when the precipitation pH was above 9. They commented that the elongated morphological growth of HA can be related to the low chemical driving force for 2D particle growth as well as layer by layer growth zone. Nayak et al has also observed elongated HA particles when the pH range was >9.



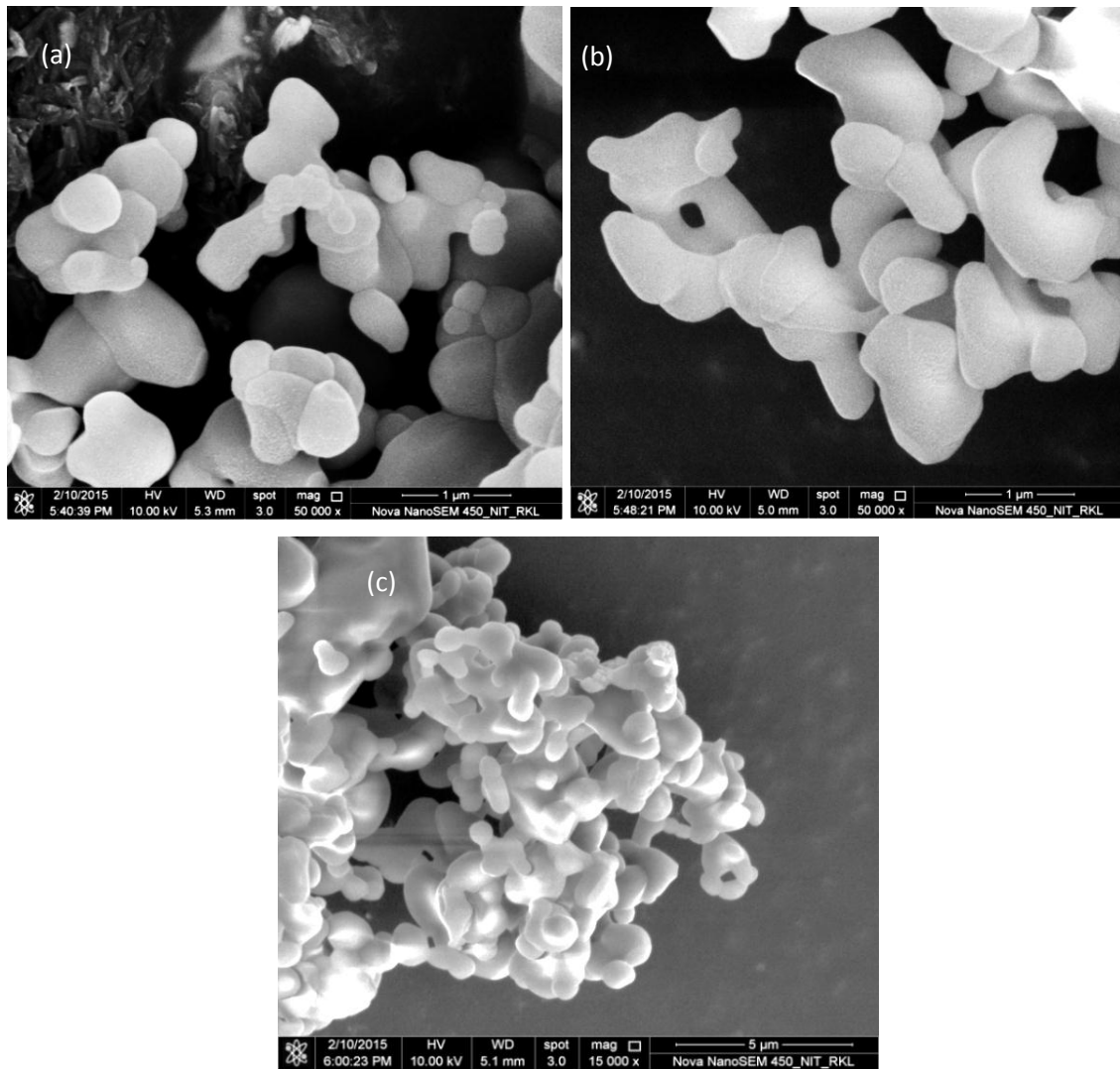


**Fig.5.6. (a) (b) and (c) FESEM image of HA particles calcined at 850, 900 (Scale bar, 1μm and 1000°C (Scale bar, 5μm)**

#### **5.4 Study of densification behavior and sintering behaviour of HA**

The densification behavior of HA was studied by in a Dilatometer (Netzsch, Germany, DIL 402C) at a heating rate of 10°C/min (Fig. 5.7). The curve shows a slight expansion till 820 oC followed by shrinkage that starts around 840oC. The onset of shrinkage marks the start of densification of HA. The derivative shrinkage curve shows that the maximum shrinkage rate (0.10%/min) takes place between 900°C - 910°C. Thus, major densification of HA is expected to be over by 1200°C.

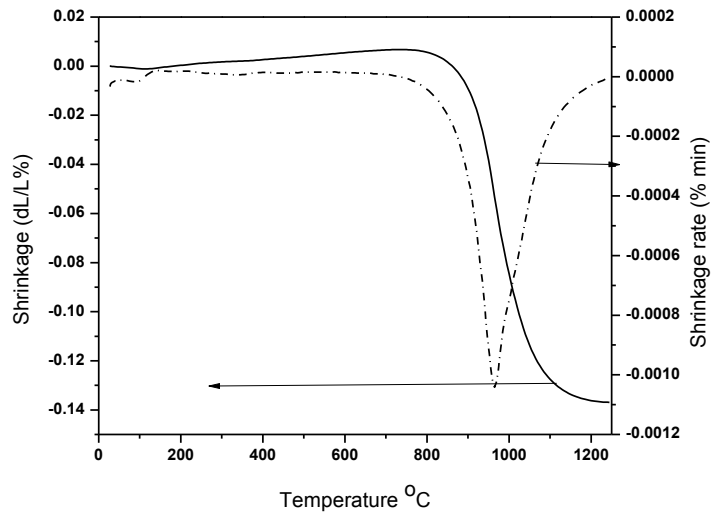


**Fig. 5.7 Densification behavior of HA**

It is also to be noted that the densification behavior was studied at 10°C/min heating rate while during sintering the heating rate was between 3-5°C/min. Therefore, to simulate the sintering schedule, separate HA samples was also studied in dilatometer at 3°C/min heating rate (a separate graph has not been provided). However, no significant change in either the onset of densification temperature or the densification rate was observed. The densification onset temperature was 820°C, and maximum shrinkage rate was around 900°C. The densification curve flattens at 1250°C. Thus, based on the above study, the sintering temperature of HA was carried out at 1250°C.

### **5.5 Study of HA phase stability in the sintered HA**

Figure 5.8 shows the effect of sintering temperature (1000-1300°C) on the phase stability of HA. The XRD pattern of the HA samples sintered till 1250 °C indicate that the peaks correspond to stoichiometric HA, and no additional peak could be identified. The phase purity of HA was further verified by comparing the d-spacing value of the three prominent peaks of sintered HA with JCPDS 84-1998 [(d=2.812 Å, 2.776 Å, 2.718 Å)]. Table-5.2 lists the d-spacing value of HA as a function of sintering temperature vis-a-vis the d-spacing reported in JCPDS 84-1998.

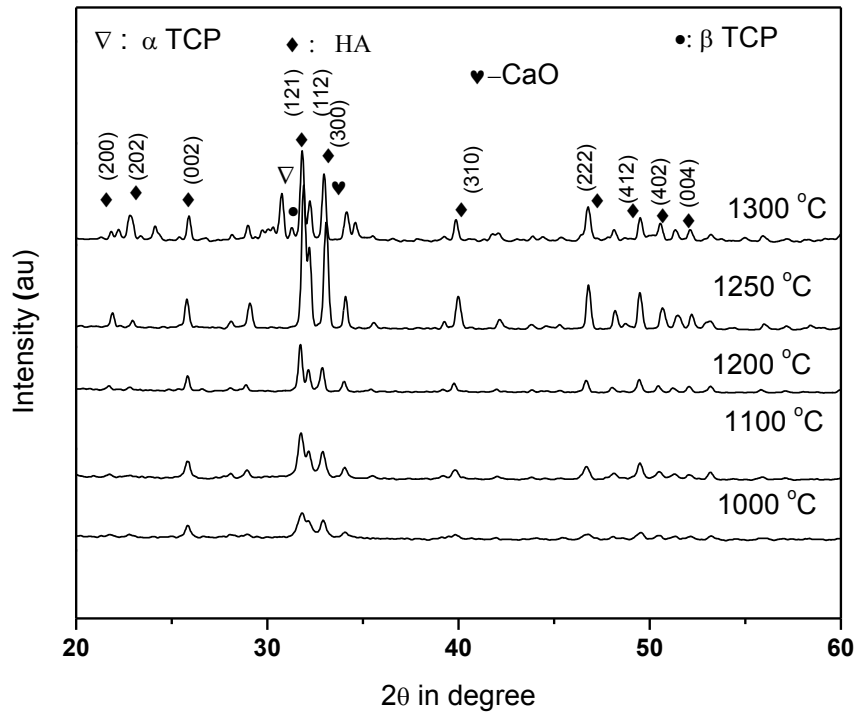


**Fig.5.8. XRD pattern of sintered HA at various temperature (1000-1300 °C)**

**Table-5.2 d-spacing value of HA as a function of sintering temperature**

Sintering Temperature(°C)	d-spacing of three prominent HA peaks (Å)		
	Peak 1(121)	Peak 2(112)	Peak 3(300)
1000	2.812	2.780	2.717
1100	2.812	2.780	2.717
1200	2.814	2.777	2.720
1250	2.816	2.780	2.721
1300	2.806	2.768	2.710
JCPDS 84-1998 (HA)	2.812	2.776	2.718
JCPDS 82-1691 (CaO)	2.398 (200)	1.695 (220)	2.769 (111)
JCPDS 70-2065 (β-TCP)	2.880 (0210)	2.608 (220)	3.209 (214)

Table 5.2 shows that the d-spacing of HA essentially remains unchanged till 1250°C and the pattern match very well with the standard XRD pattern of HA. Therefore, HA phase was stable till 1250°C. However, in the XRD pattern of sample sintered at 1300°C (Fig. 5.8), both  $\beta$ -TCP and CaO phase could be identified along with HA. Moreover, the d-spacing of the three prominent HA peaks changed to 2.806Å, 2.768Å and 2.710Å respectively indicating that HA has partially decomposed to  $\beta$ -TCP and CaO according to following reaction:

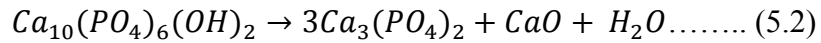
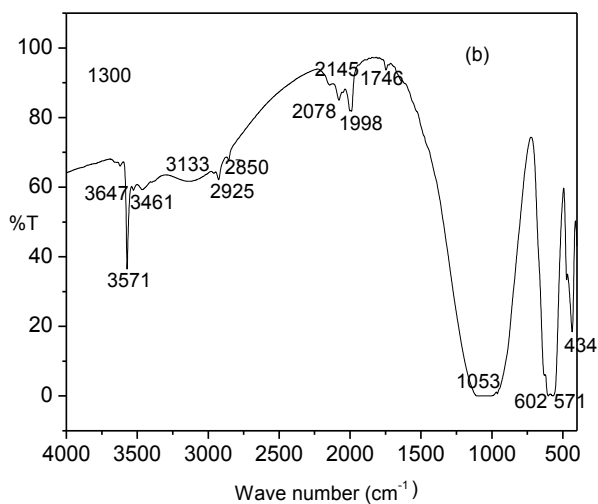
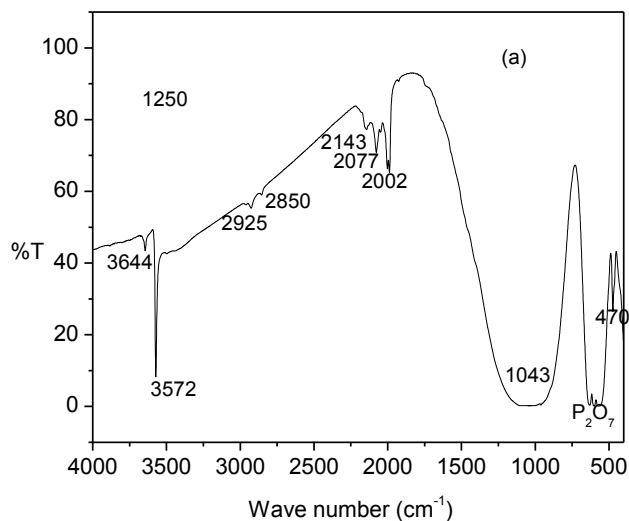


Fig.5.9 (a, b) shows the FTIR spectrum of HA samples sintered at 1250 and 1300°C respectively. Both the patterns exhibit similar features to that of calcined HA. (Fig 5.4) also shows sharp absorption at 3571  $cm^{-1}$  due to the vibration of OH<sup>-</sup> in HA and a broad peak at 1041  $cm^{-1}$  indicating (PO<sub>4</sub>)<sup>3-</sup> ( $\nu_3$ ) asymmetric stretching. Moreover, both the patterns also contain absorption peaks at 2000 to 2500  $cm^{-1}$ . which have been reported to be due to adsorbed (CO<sub>3</sub>)<sup>-2</sup>. The presence of (CO<sub>3</sub>)<sup>-2</sup> peaks in the sintered sample is unusual and appears to be due to (CO<sub>3</sub>)<sup>-2</sup> absorption from the atmosphere during the storage of the sintered samples. The other notable peaks in the 1250 °C sintered HA is the characteristic triplet in the wavenumber 630-570  $cm^{-1}$  due to ( $\nu_4$ ) bending of (PO<sub>4</sub>)<sup>3-</sup> [5.26]. Further, the peak 470  $cm^{-1}$  that are characteristic of HA is absent in the 1300°C sintered HA. However, in 1300°C sintered samples the triplet is not observed. The presence of  $\beta$ -TCP phase in the 1300°C sintered sample was also confirmed by FTIR study of the sintered sample.



**Fig. 5.9. FTIR spectra of HA (a) sintered at 1250 °C and (b) sintered at 1300 °C**

## **5.6. Effect of sintering schedule on bulk density, porosity and compressive strength of sintered HA**

### **5.6.1 Bulk Density and Apparent porosity of sintered HA**

Figure-5.10 shows the changes in the bulk density and apparent porosity of HA sintered at different temperatures between 1150 °C and 1350 °C. The plot shows that while bulk density steadily increase from 1150°C (2.75 gm/cc) to 1250°C (2.93 gm/cc) (i.e. 6.5% increase), the porosity sharply drops from 8.25% (at 1150 °C) to 6.4% (at 1200 °C) (i.e. a

reduction by 22.4%) with increase in sintering temperature. No perceptible change in porosity could be observed between 1200°C and 1250 °C. However, on increasing the

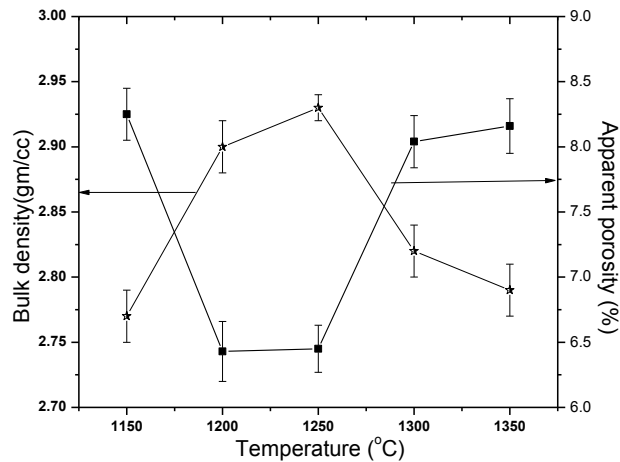


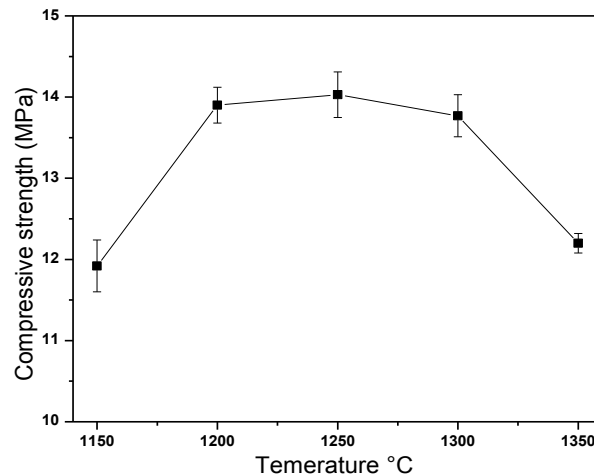
**Fig. 5.10. Effect of sintering temperature on bulk density and porosity**

sintering temperature from 1250 °C to 1300 °C, the porosity increased from 6.4% to 8.12% (+26.3%) while density drops to 2.82 gm/cc (-4%). The drop in porosity between 1150°C to 1200°C can be attributed to increased densification of HA thus leading to a reduction in porosity value. the subsequent increase in porosity between 1250 °C to 1300 °C is attributed the decomposition of HA leading to the formation of  $\beta$ -TCP and free CaO. It has been reported in the literature [5.27] that such a phase transformation is associated with dihydroxylation of HA lattice leading to the porous structure. The bulk density continues to decrease beyond 1300°C, albeit more gradually, due to the increased amount of TCP formation.

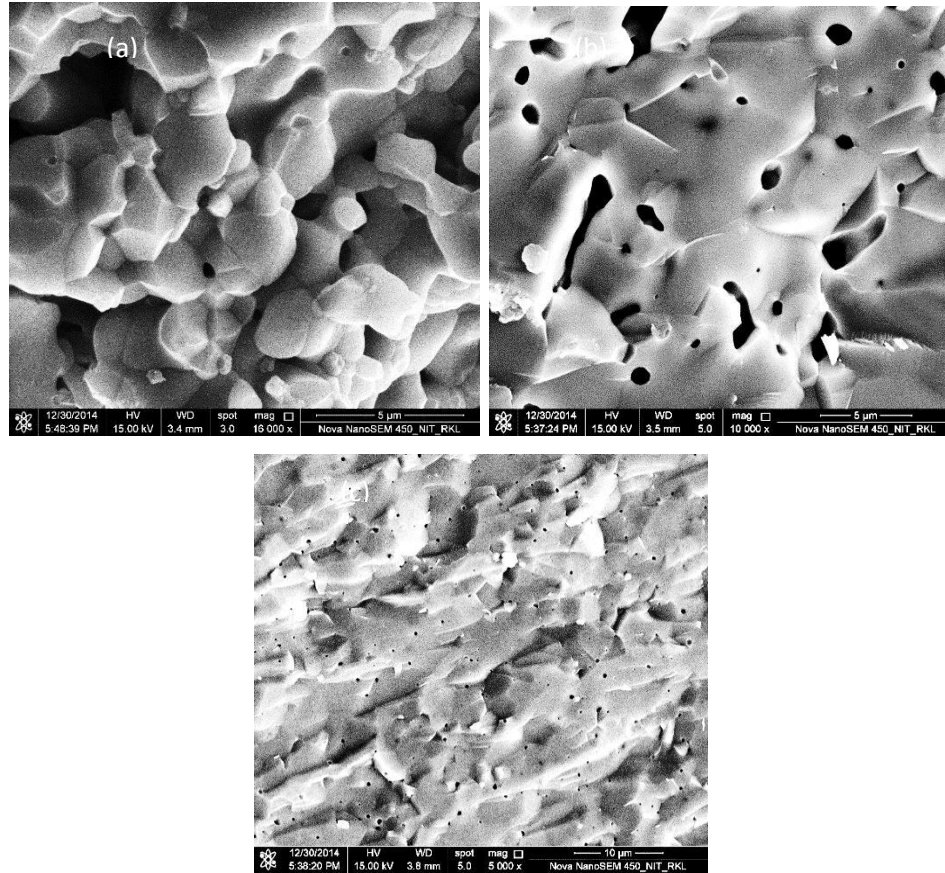
### 5.6.2 Effect of Sintering Temperature on Cold Compressive Strength (CCS)

Fig. 5.11 shows the variation of compressive strength with temperature. The strength increases from 11.9 MPa at 1150 °C to 14 MPa at 1200 °C. Between 1200 and 1250 °C, the strength marginally increases, and the average CCS value at 1250 °C is 14.30 MPa. Following this, the strength drops to 13.6 MPa at 1300 °C and after that, decreases to 12.1 MPa at 1350 °C. A comparison with Fig.5.11 indicates that the increase in strength between 1100 °C to 1250 °C is due to enhanced densification of HA till 1250°C. The decrease in strength from 1250°C to 1300 and 1350°C is due to the porosity sintered from  $\beta$ -TCP.

From the XRD plot, (Fig. 5.8), it is estimated that about 30% HA converts to TCP at 1300°C. This conversion creates porosity (both inter and intra granular porosity) as revealed from SEM image. Fig. 5.12 (a) and (b) shows the FESEM image of the fractured surface of HA sintered at 1250°C and 1300°C respectively. The samples sintered at 1250°C (Fig. 5.12(a)) show a dense structure and lower porosity. The grain size of HA is in the range of 0.5-1  $\mu\text{m}$ . The microstructure shows mostly intergranular porosity. Fig. 5.14 (b and c) shows the microstructure at 1300°C. The microstructure shows large grains and porous structure. Both inter and intra granular porosities are present. The grains have increased 2 to 5  $\mu\text{m}$ . Fig. 5.12 (c) shows the lower magnification of HA samples sintered at 1300°C. Even at lower magnification porosities are visible. The microstructure also shows a few bright spots or small particles. All these effects lead to a decrease in strength at 1300°C and 1350°C. It has been documented in the literature [5.20] that the HA to  $\beta$ -TCP transformation takes place with the exsolution of CaO. Thus, the bright spot in the microstructure correspond to CaO.



**Fig.5.11. Effect of sintering temperature on compressive strength**



**Fig.5.12** Microstructure of fractured surface of sintered HA at (a) 1250 (a) and (b, c) 1300 °C (Scale bar, 5 $\mu$ m (a&b), 10  $\mu$ m (c)).

### **5.6.3 Effect of soaking Time on bulk density, apparent porosity and cold compressive strength of the sintered HA**

In the previous section, the effect of sintering temperature on apparent porosity and bulk density of sintered HA was discussed. It was observed that HA was stable till 1250 °C. The sintered sample had a high density (93%) and low apparent porosity (6.5%). This section presents the effect of soaking time at 1250 °C on bulk density and apparent porosity of sintered HA. The bulk density was the highest after 2 hours soaking (Fig. 5.13), and no further improvement in the bulk density was noted at longer soaking periods. But since, there was a possibility of grain growth at longer soaking period, the soaking time was fixed at 2 hours. Similarly, the highest CCS was also obtained after 2 hours soaking at 1250°C (Fig 5.14)



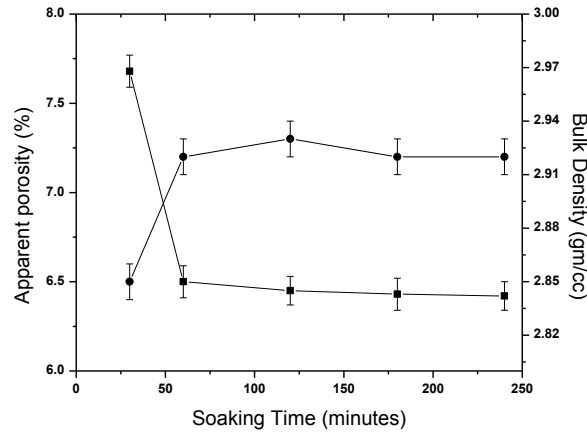


**Fig. 5.13 Effect of soaking time on the porosity and bulk density of sintered HA**

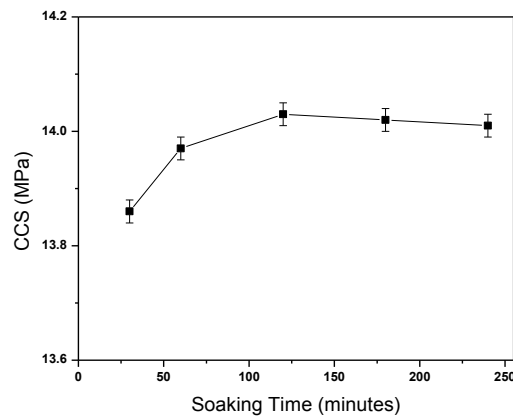


**Fig. 5.14. Effect of soaking time on the compressive strength of sintered HA**

## 5.7 Conclusions

Phase pure HA was prepared from  $\text{Ca}(\text{NO}_3)_2 \cdot 4\text{H}_2\text{O}$  and  $(\text{NH}_4)_2\text{HPO}_4$  by wet precipitation route. The calcined powder ( $850^\circ\text{C}$ ) had a fine particle size of  $0.5\text{-}1\mu\text{m}$ . During calcination, crystallization of HA took place and well crystallized HA formed at  $850^\circ\text{C}$ . Calcined powders were agglomerated. The purity of HA phase was retained up to  $1250^\circ\text{C}$ . Above  $1250^\circ\text{C}$ , HA partially decomposed to  $\beta\text{-TCP}$  and  $\text{CaO}$ . The highest strength was  $\sim 14.3\text{ MPa}$  at  $1250^\circ\text{C}/2\text{hrs}$  that corresponded to 93% density. The microstructure showed faceted grains with a grain size ranging between  $2\text{-}5\mu\text{m}$  for samples sintered at  $1250^\circ\text{C}$  and grains with size  $5\text{-}10\mu\text{m}$  for samples sintered at  $1300^\circ\text{C}$ . The result showed that the sintering temperature and sintering time is a crucial factor that influences shrinkage, densification and microstructural properties of HA ceramics.

## *Chapter-6*

# *Porous HA scaffolds through solid state route*

## **6. Porous HA scaffolds through solid state route**

### **6.1 Background**

The previous chapter discussed the processing of HA powder by wet precipitation method using inorganic precursor solutions. It was found that the prepared HA powder was phase pure and retained its phase stability till 1250°C. Therefore, it was concluded that this HA powder could be used for fabricating porous scaffold through different forming routes. This chapter discusses the porous HA fabrication through solid state mixing of HA powder and pore former. In this study, naphthalene (NA) granule has been used as pore former. The scaffold making process involves mixing of HA powder and NA granules in different volume fraction followed by shape forming, sintering of scaffold and the characterization of sintered porous HA. The effect of varying the volume fraction of NA granules on the porosity and pore size distribution of porous HA has been studied. The effect of porosity on pore size distribution, compressive strength, microstructure, and in vitro aging behavior has also been studied.

### **6.2 Raw materials and processing of pellets.**

#### **6.2.1 Raw materials**

Calcined HA powder and NA granules were the starting raw materials for this study. The HA powder has been prepared using  $\text{Ca}(\text{NO}_3)_2 \cdot 4\text{H}_2\text{O}$  and diammonium hydrogen phosphate ( $(\text{NH}_4)_2\text{HPO}_4$ ) as detailed in Chapter-5. The NA granules were purchased from Loba Chemie, India. The as received NA granules were sieved through 300  $\mu\text{m}$  screen and the fraction retained on 200  $\mu\text{m}$  sieve (average size 250 $\mu\text{m}$ ) was used as the starting granule size of NA. In the present study, five different NA vol% (30, 40, 50, 60 and 70) was used in HA powder for fabricating the porous HA scaffold by solid-state mixing route.

#### **6.2.2. Mixing and Compaction of HA-NA mixed powder**

HA powder and NA granules were first dry mixed in an agate mortar and pestle for 30 minutes. During the mixing process, intensive mixing or grinding with excessive force was consciously avoided for minimizing the grinding of NA granules during the mixing operation. To the mixed HA-NA powder, PVA solution was added in a drop wise manner to make it a moist mixture. From the volume of PVA solution added, it was found out

that nearly 4% PVA was added in the powder. The powders were hydraulically compacted in a cylindrical die (15mm  $\phi$  x 5mm height) at a compaction load of 5 Ton (Carver Inc, UK). The compacted pellets were dried in an oven and sintered at 1250°C (Bysakh and Co, Kolkata, India). Slow heating rate (@2 °C/min) was maintained till 700 °C to permit removal of moisture and burnout of PVA. Most of the NA evaporated during the drying step. Additionally, a holding time of 2 hours was also provided at 700 °C to ensure complete removal of decomposable material and organics before the onset of sintering. Beyond 700 °C, the temperature was increased at 3°C/min till 1250°C and a dwell time of 2 hours was provided at 1250°C to ensure temperature homogenization and completion of sintering. The sintered samples were cooled by normal cooling in the furnace itself.

### 6.3. Results and Discussion

#### 6.3.1 Removal of the pore former and Binder

Fig. 6.1 provide the DSC-TG of green HA-50NA pellet. The plot shows endothermic peaks at 100°C and 200°C respectively. The TG plot shows a total weight loss ~ 40 % between 80°C and 180°C.

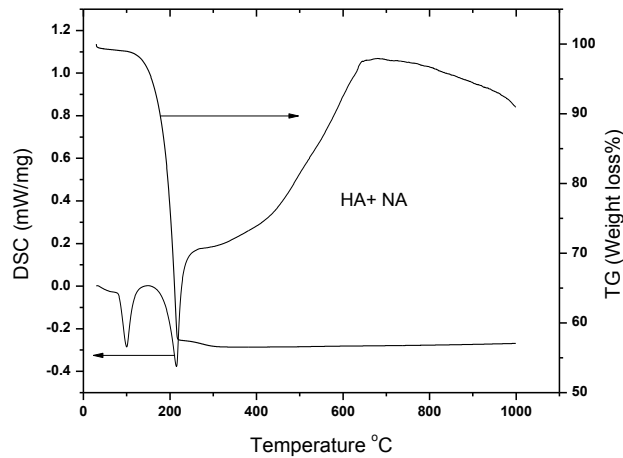


**Fig. 6.1 DSC-TG of as pressed HA- 50NA pellet**

The first of the two endothermic peaks correspond to the melting of naphthalene and the second corresponds to evaporation of naphthalene [6.1]. The broad peak between 600-800°C accounts for the decomposition and oxidation of PVA. It is to be noted that though the weight loss is completed by 300 °C, the oxidation of decomposed PVA is not

complete till about 600 °C. Thus, the scaffold required careful heating till 600 °C and preferably at a slow rate for preventing cracking and disruption of samples.

### 6.3.2 Bulk density (BD) and apparent porosity (AP) of the sintered HA-NA Scaffold.

The changes in the bulk density (BD) and apparent porosity (AP) of sintered scaffolds with NA content is shown in Fig 6.2. AP increases with increase in NA vol%, and the increase in AP with NA shows a near linear variation. Similarly, the bulk density of the samples decrease with increase in NA content, and the highest BD (1.9gm/cc) was obtained for HA- 30NA samples. It can be further noted that the AP of the samples matches well with vol% NA added, i.e., 30% naphthalene addition generates nearly 30% porosity. However, at 70 vol% NA addition, the samples were extremely porous so though porosity values have been recorded, these samples could not be tested for porosimetry analysis.

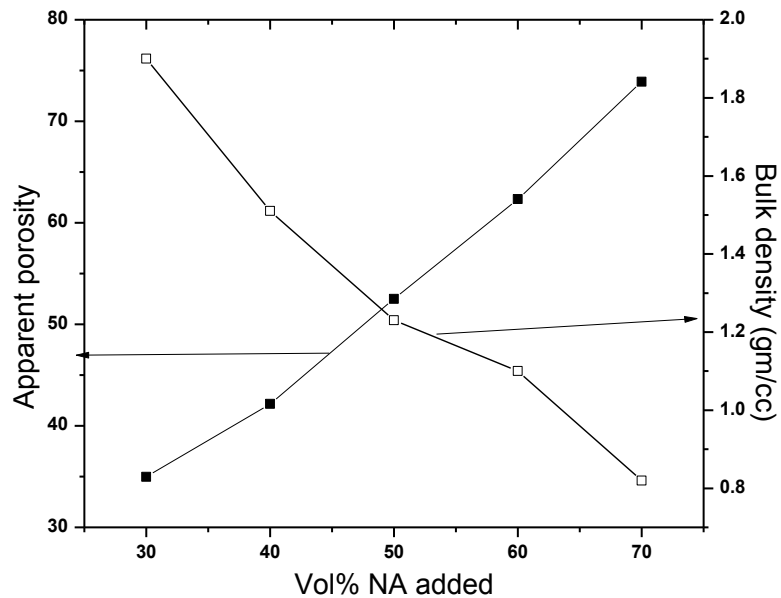


**Fig. 6 .2 Variation of Bulk Density (BD) and Apparent Porosity (AP) of sintered scaffolds with NA content**

### 6.3.3 Pore size distribution of HA-NA scaffold

Fig. 6.3 (a-d) show the pore size distribution of HA-NA scaffold with different NA content (30, 40, 50 and 60 vol %). Fig. 6.3 (a) shows the pore size distribution of HA-30NA scaffold. The pore size distribution shows that majority of pores lie in the range of 2-20 μm. Some pores are also observed on the lower pore size (< 0.1 μm) which may be

due to intra and inter granular porosity. A small peak is observed at 50  $\mu\text{m}$ . However, as already mentioned (Section 4.3.5), this distribution is only approximate as the instrument can detect only up to 224  $\mu\text{m}$  pore size. Therefore, a true representation of pore size can only be obtained by correlating pore size data with microstructure.

The pore size distribution of HA-40NA sample is shown in Fig. 6.3 (b). The plot shows that maximum population of pores lie in the range 0.1-1  $\mu\text{m}$  and the pore population in the size range 1-10  $\mu\text{m}$  is rather less. However, pores in the size range 10-50  $\mu\text{m}$  are also present in significant numbers.

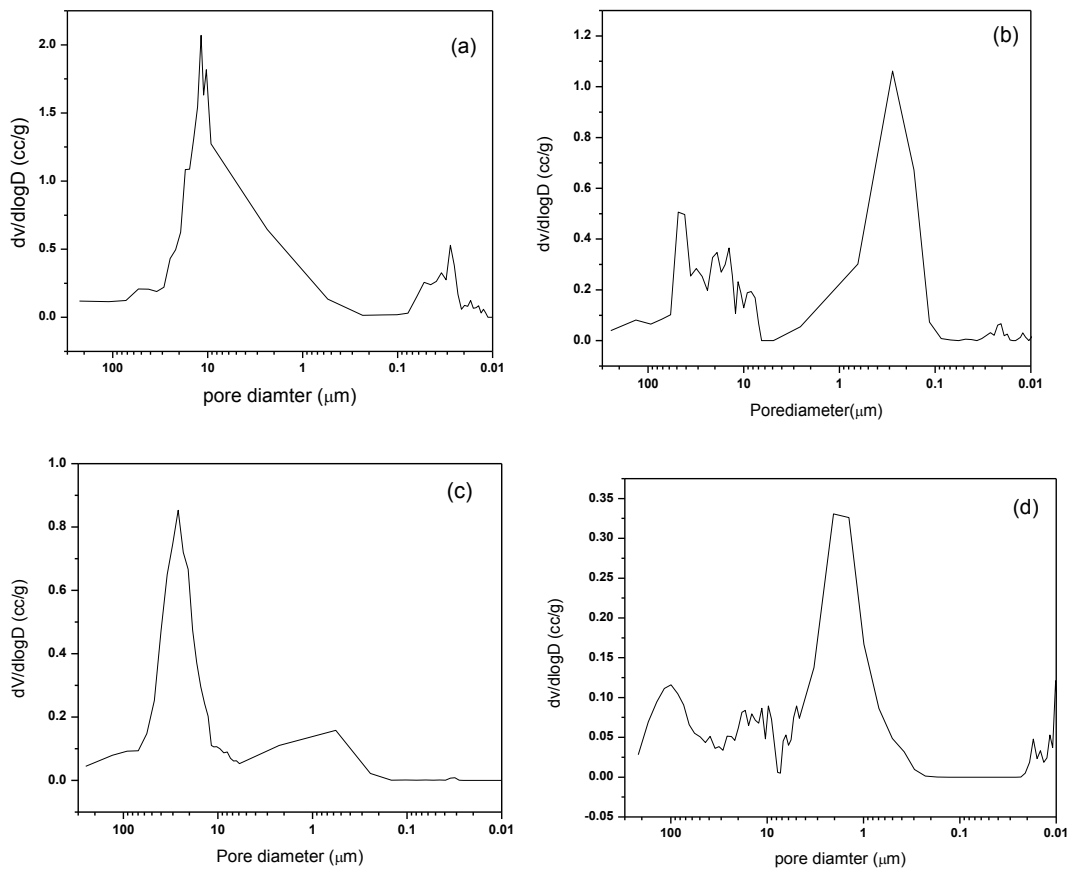


**Fig.6.3. (a-d) pore size distribution of HA-NA scaffold with different NA content (a) HA-30NA, (b) HA-40 NA, (c) HA-50NA and (d) HA-60NA**

Fig.6.3 (c) represents the pore size distribution of HA- 50 NA samples. The pore size distribution essentially shifts to bimodal distribution with maximum The pore size distribution of HA-60NA sample is shown in Fig. 6.3 (d). The distribution in this sample has shifted to lower pore size range (0.2-7  $\mu\text{m}$ ) though pores in the higher pore size range (100-200  $\mu\text{m}$ ) is also present. The higher populations of lower pore size pore size are

probably due to the small pores on the pore walls. Thus, this sample is expected to have higher pore connectivity and possibly large pores. Hence, the exact pore features can only be understood by studying the SEM microstructure that is discussed below. However, it is to be understood that the pore size distribution provided by mercury porosimeter is only a partial representation of actual pore size distribution. The absence of pores in the size range  $>200\ \mu\text{m}$  does not mean pores of such size are not present. These large pores could not be identified and detected by the porosimeter.

#### **6.3.4 Microstructure of sintered HA-NA scaffold**

Fig. 6.4 (a) to Fig. 6.4 (e) describes the microstructures of porous HA (with NA content varying from 30-70 vol %) prepared from the solid-state mixing of HA and NA. The microstructures were taken on the sintered surface of the samples. Fig. 6.4 (a) shows the microstructure of HA-30NA samples. Large pores ( $200\ \mu\text{m}$ - $300\ \mu\text{m}$ ) along with smaller pores ( $50$ - $100\ \mu\text{m}$ ) are present. Pores with still smaller sizes can be seen on the walls of the pores (encircled area in Fig 6.4.a). The microstructures appear to be relatively dense. With the increase in NA content to 40 vol% (HA- 40 NA), the microstructure appears to have opened up. Fig. 6.4 (b) shows that the microstructure of HA-40 NA consists of large pores ( $\sim 300\ \mu\text{m}$ - $200\ \mu\text{m}$ ) (marked A), medium pores ( $\sim 100\ \mu\text{m}$ ) (marked B), and smaller pores ( $\sim 50\ \mu\text{m}$ ) (marked C). While some pores are isolated pores, other pores have pore on the pore walls (Part A and B), hinting at interconnectivity. These interconnected pores are in the size range  $10$ - $50\ \mu\text{m}$  with large sized interconnections mostly found within or on the walls of large pores ( $100$ - $200\ \mu\text{m}$ ). A few isolated pores are also found on the sample surface. Thus, the microstructure indicates that on increasing NA content more open porosity, as well as interconnected porosity, is created. The microstructure of HA-50vol% NA (HA-50NA) (Fig. 6.4 (c) shows a very porous and open microstructure. A wide range of pore sizes varying from  $> 300\ \mu\text{m}$  to  $50\ \mu\text{m}$  can be observed. In contrast to HA-40 NA sample, this particular sample shows that most of the pores are interconnected. The interconnection sizes can be as large as  $75$  to  $100\ \mu\text{m}$ . In spite of high porosity, this sample exhibit reasonably high strength ( $\sim 1.6\ \text{MPa}$ ) and, therefore, can be a good scaffold material. In the HA-60NA (60 vol% NA) sample, the microstructure is highly porous, and large pores ( $> 200\ \mu\text{m}$ ) are abundant. In general, most of the pores are of larger size ( $50\ \mu\text{m}$  and higher). The result proves that with

increasing NA content, pore sizes increase and at the same time, some NA agglomerate giving larger pores, while some other granules are crushed during pressing giving a lower pore sizes. There are some pores that are  $> 300 \mu\text{m}$ .

Pores having size  $>300 \mu\text{m}$  are due to possible agglomeration of NA granules during solid state mixing. Fig. 6.5 (e) shows the microstructure of HA-70NA (70 vol% NA) samples. This microstructure projects a more flaky type microstructure indicating highly porous sample. The pores are larger than  $300 \mu\text{m}$  and show a very porous structure. The structure appears to have a layer like features due to high NA content. This type of structure is expected to have low fracture strength, and this is observed (Fig. 6.5. (a). A sudden drop in strength is observed as NA content increases from 60 to 70 vol% along with a comparable increase in porosity level.

Thus, it could be summarized that the results suggest that the fabricated porous HA scaffold prepared by the solid-state mixing of HA and NA granules could produce a wide range of porosity with varying microstructures and strength. At lower NA addition (30 and 40 vol% NA), the samples appear to be relatively dense and with lesser interconnections. However, the structure opens up at 50, and 60 vol% NA addition and a highly porous microstructure result having interconnected pores. Finally, at 70 vol% NA addition (HA-70NA) the microstructure appear to be more of a flaky nature, highly porous and large pore size. The strength data correlate well with the microstructure.



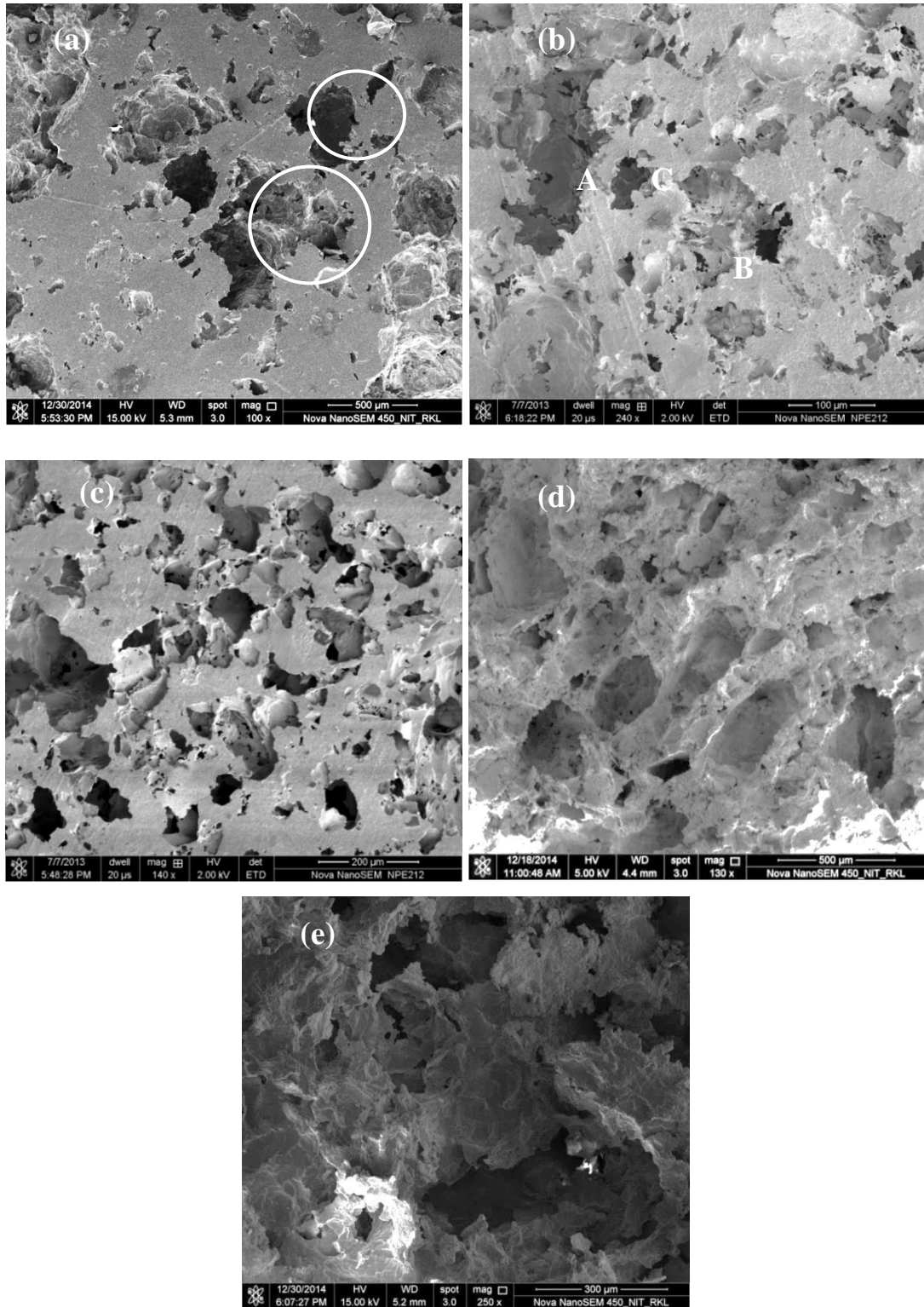


**Fig. 6.4 (a-e) Microstructure of HA-NA scaffold with different NA content (a) HA-30NA, (b) HA-40 NA, (c) HA – 50NA, (d) HA- 60 NA and (e) HA -70 NA**

#### 6.4 Porosity and Strength of Sintered HA-NA Scaffold

In the preceding section, it was mentioned that naphthalene content and porosity were directly related. It was also observed that an increase in naphthalene by 10 volume fraction resulted in the increase of nearly an equivalent volume fraction porosity. It is also well known the load bearing capacity of the scaffold has a direct correlation with the solid area available for withstanding the load. Therefore, it is natural that an increase in porosity will lead to a reduction in the load bearing capacity or strength. Fig. 6.5. (a) presents the strength vs. porosity plot. It was found that with the increase of pore former, the porosity increases, and simultaneously the compressive strength (CCS) decreases. HA-30vol%NA samples have the highest possible strength (7.99 MPa), and HA-70NA had the lowest strength (0.89MPa) (Table-6.1). But at still higher composition (>HA-70NA), the strength could not be prepared properly because of the resultant mechanically weak and fragile samples. Therefore, this factor restricted the further addition of NA. Thus, 70vol% NA was the maximum permissible vol% of pore former that could be used for HA scaffold preparation by pellet pressing methods.

The linear relationship between porosity (P) and the logarithm of compressive strength ( $\sigma$ ) was plotted and is given in Fig. 6.5 (b). It shows that  $\ln\sigma$  vs. porosity of HA porous samples satisfy the following equation (6.1).

$$\sigma = \sigma_o \exp(-bP) \quad \text{..... (6.1)}$$

Where, b is constant, and  $\sigma_o$  is the compressive strength for zero porosity sample, i.e., HA at 1250°C -14.3 MPa s. A plot of  $\ln(\sigma)$  vs volume fraction porosity (P) [Fig. 6.5 (b)] yields a straight line with a negative slope. The slope gives the value of 'b' and for this study it was found to be 0.042. The negative slope indicates that as the porosity increases, the load carrying capacity of the scaffold decreases. The decrease in the strength is the result of the increased porosity or void space in the sample due to lesser connectivity among the solid materials. Thus, the strut are becoming thinner and the load bearing capacity of the scaffold decreases. In this kind of porous scaffold, there are essentially two phases, viz. solid phase and the void phase. At the lower NA content, the HA phase is the continuous phase and the pore phase is the discontinuous phase. This implies that the pores are discreetly separated in the solid HA phase. With the increase in the NA

content, the solid phase decreases and the pore phase increases. Thus, at the highest NA content, the pore phase become the major phase.

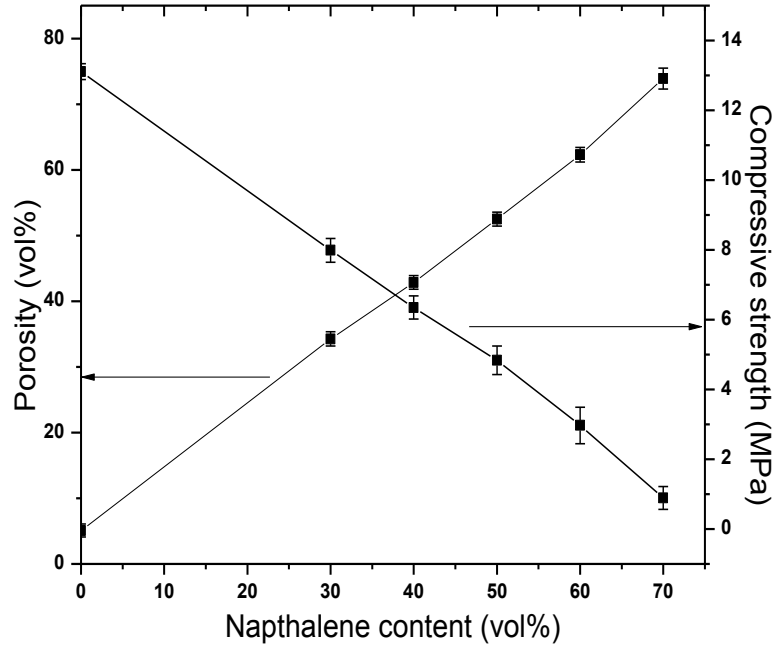


**Fig. 6.5 (a) strength and porosity plot of porous HA-NA with changes in the naphthalene content**

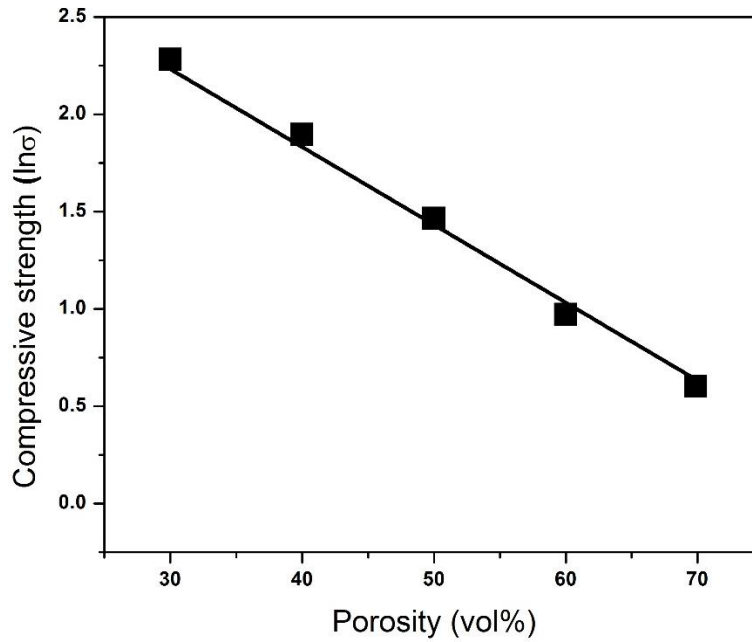


**Fig. 6.5 (b) A Plot of  $\ln\sigma$  vs. vol percent porosity**

**Table-6.1 Bulk Density, Apparent Porosity, Closed Porosity and Strength of porous HA scaffolds prepared by solid state route using NA granules**

NA (vol%)	Bulk Density (gm/cc)	Apparent Porosity (%)	Closed Porosity (%)	(CCS) (MPa)
30	1.9	34.98	4.89	7.99
<b>40</b>	<b>1.51</b>	<b>42.16</b>	<b>10.05</b>	<b>6.35</b>
50	1.23	52.50	8.57	4.84
60	1.1	62.32	2.86	2.97
70	0.82	73.89	0.16	0.89

### 6.5 In-vitro aging behaviour of porous HA scaffolds

The in vitro aging behavior of porous HA scaffold prepared by solid-state route was studied by aging the scaffolds for different time periods in SBF till seven weeks. The dissolution of HA during aging was monitored through weight loss measurement on aging. The microstructure of SBF aged samples provided information on the growth of apatite layer as well as on the surface covered rate for scaffolds with different porosity. Changes in the  $Ca^{+2}$  and  $P^{+5}$  concentrations in the spent SBF with aging time provided the information on the dissolution of HA in SBF. The results of these studies have been discussed in the following sections.

#### 6.5.1 Microstructure of SBF aged porous HA Scaffold

The microstructure of 21 days SBF aged porous HA scaffolds (HA-30NA, HA-40 NA, HA-50 NA and HA-60NA) are shown in Fig. 6.6 (a) to Fig. 6.6 (d). The microstructures show that apatite growth takes place on HA surface. The surface coverage has increased from HA-30NA samples to 60NA sample. The apatite particles have spherical morphology. A closer observation of 30, 40, 50 and 60NA containing HA samples reveal that the apatite growth starts from the surface of predominantly large grains that are

situated near a pore. In fact, the growth is also observed on the pore edges (encircled area). The progressive increase in porosity on increasing NA vol% 30 to 60 is reflected in the greater surface coverage of HA-60NA. A cluster of large apatite particles is also seen in Fig. 6.6 (d). Thus, it can be concluded from the above microstructures that a porous sample will promote a faster and greater deposition of apatite. The deposition will predominantly start from the grains that are porous or which are situated near the pores. To study the apatite deposition path and the changes in deposit morphology with aging time, HA-30NA was chosen because this sample had the lowest deposition rate. Therefore, this sample could be aged for longer periods (35 days) without appreciable coverage by apatite layer.

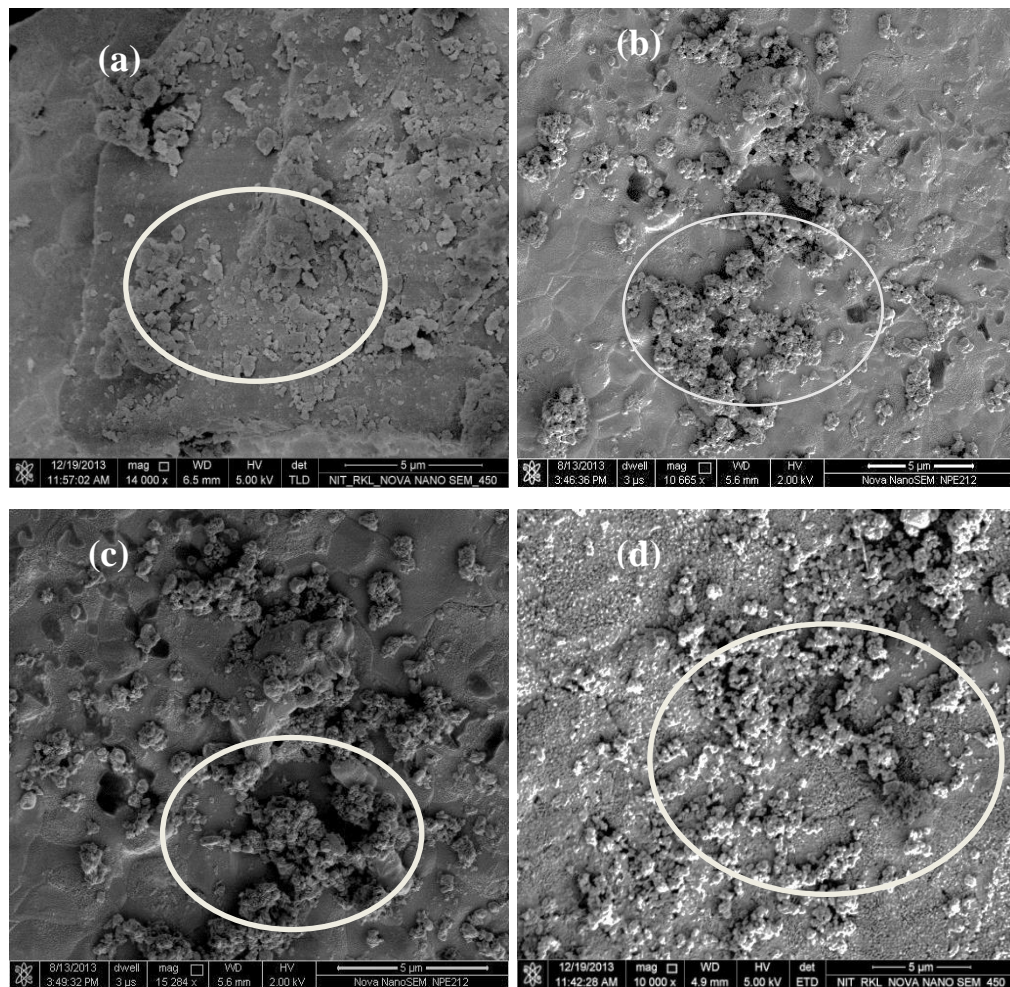


**Fig. 6.6 (a-d) (Scale bar, 5 μm) Microstructure of HA-NA scaffold with different NA content-30, 40, 40 and 60 vol % respectively**

Fig. 6.7 (a) to (d) show the microstructure of HA-30NA samples which have been aged for 3, 5 and 35 days. Fig. 6.7 (a) show the microstructure after three days aging, and Fig.6.7(b) is the microstructure of the sample at higher magnification. The microstructure reveals that the apatite deposits grow from the surface of the grains. In a few spots, apatite deposits have also formed on the grain boundaries. Fig. 6.7 (c) show that after five days elongated deposits start forming on the surface of the grains on which fine deposits have already been formed. These elongated deposits are absent on the grains on which no finer deposits have formed earlier

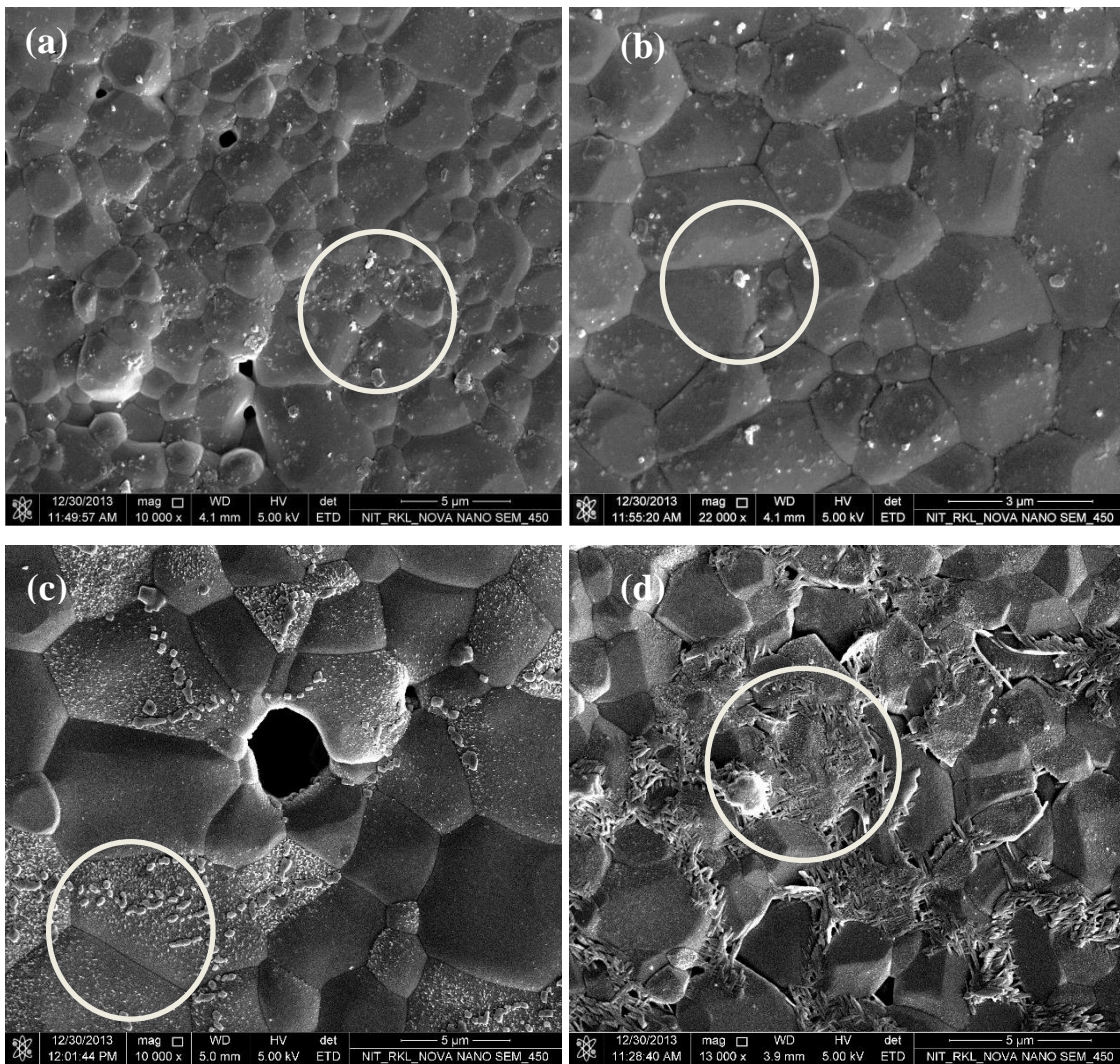


**Fig. 6.7** Microstructure of HA-30NA scaffold with different aging time. (a) microstructure after three days aging, (b) microstructure after three days aging at higher magnification (c) microstructure after five days aging, (d) microstructure after 35 days aging.

Fig. 6.7 (d) shows the microstructure after a prolonged aging period (35 days). This microstructure shows that the growth of elongated deposits has taken place on the grains on which fine grain deposits have formed. In a few place, deposits are also present on the grain boundaries. Some of these deposit clusters appear as woven fabrics due to their crisscross structure. It is also noted that at this stage of deposition also, the grain surfaces are the preferable place for apatite deposition. Gibson et. al. [6.2] and Porter et. al. [6.3] have also observed similar effects. Daculsi et. al. [6.4-6.5] also commented that dissolution process is necessary for apatite formation, and the presence of dislocations on the grain surface accelerates the dissolution process and grains are the preferable sites for apatite deposition.

Thus from this study, it can be concluded that NA granules can be mixed with HA powder to prepare porous HA-NA scaffold. The porosity, strength and pore interconnectivity depend on the fraction of NA added. 50 (HA-50NA) and 60 vol% (HA 60 NA) added HA-NA scaffold have a higher porosity as well as interconnected pores. But the higher porosity reduced the strength drastically. At 70 vol% NA addition (HA-70NA), very fragile scaffolds produced. The pore size distribution shows higher porosity in 50 and 60 vol% NA added samples. SBF aging show that 50 and 60 vol% NA have good surface coverage of apatite layer by 21 days. The microstructure analysis of HA-30NA aged samples reveals that grain boundaries are the preferable sites for first apatite deposition as well as for subsequent growth.

### **6.5.2 Weight loss behaviour of the scaffolds during aging in SBF**

Fig. 6.8 (a) shows the mechanism of apatite formation as proposed by LeGeros [6.7] Fig. 6.8 (b) shows the weight loss behaviour of HA scaffolds as a function of aging period. The weight loss increases with aging days, and the maximum weight loss is recorded between 21-28 days. For pure HA, HA-30NA as well as HA-40 NA samples, the maximum weight loss was recorded after 21 days of aging. However in HA-50NA and HA-60NA samples, the peak weight loss was recorded after 28 days. The weight loss decreased with further aging. Le Geros proposed that under the favorable condition of solution pH and temperature, the HA crystals will undergo partial dissolution at the site (Fig 6.8 .a). The dissolution will result in the increase of  $\text{Ca}^{+2}$  and  $\text{P}^{+5}$  in the solution. If

the solution has pre-existing  $\text{Ca}^{+2}$  and  $\text{P}^{+5}$  ions (as in SBF), the dissolution will result in saturation of SBF. The next step in the precipitation of amorphous apatite containing different ions like  $\text{Ca}^{+2}$ ,  $\text{Mg}^{+2}$ ,  $\text{CO}_3^{2-}$ ,  $\text{HPO}_4^{4-}$ ,  $\text{PO}_4^{3-}$ . Under acidic condition these amorphous precipitates will convert to more stable compounds like DCPD and OCP. With increase in aging period, carbonated apatites will form from DCPD and OCP.

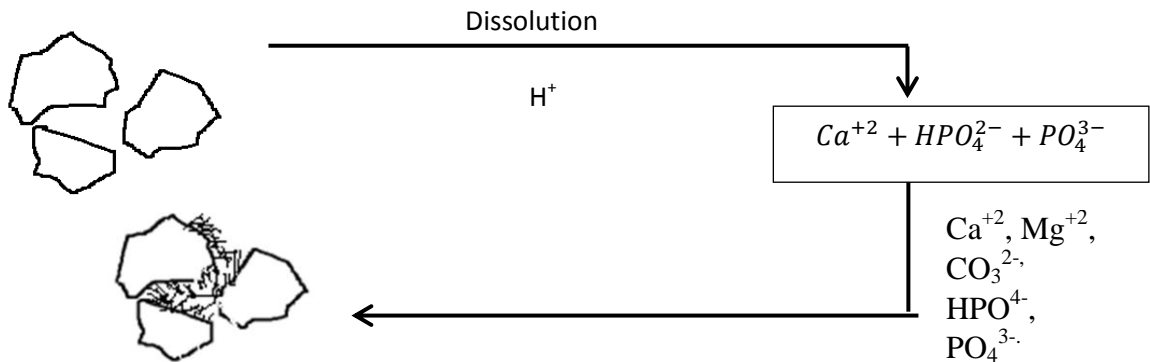


**Fig: 6.8 (a) Mechanism of apatite formation [6.7]**

Van Kamenade and De Bruyn [5.6] have proposed that the precipitating sequence for SBF depends on the pH of the SBF solution. At a temperature  $37.4^\circ\text{C}$  with pH between 6.7-7, the precipitation sequence is  $\text{DCPD} \longrightarrow \text{OCP} \longrightarrow \text{HAP}$ .

H.M Kim et.al [6.8] proposed that the biomineralization process includes three characteristics stages. In the initial period, pH increases and amorphous Ca-rich (Ca/P=1.83) Ca-P compound forms. In the second stage, pH decreases and forms Ca-poor amorphous Ca-phosphate (Ca/P=1.47). In the third stage, Ca/P ratio increases to 1.65 and apatite forms.

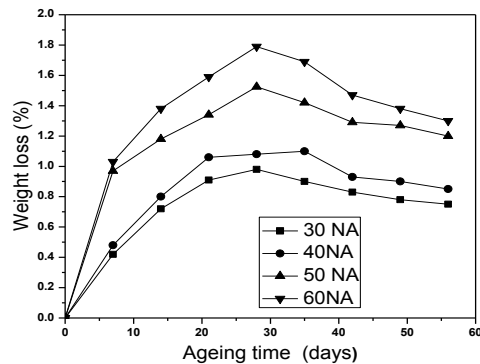


**Fig. 6.8 (b) Weight loss behaviour of HA scaffolds as function of aging period**



Thus, in Fig.6.8, the increase in weight loss is a consequence of higher dissolution. Further, in HA-50NA and HA-60NA samples, higher porosity allows dissolution to be continued for a longer duration and thus prolongs the weight loss period. The lower porosity in HA-30 NA and HA-40 NA samples causes the dissolution to reach its maximum value earlier (14 days). The dissolution of HA in SBF raises the concentration of  $\text{Ca}^{+2}$  in SBF. According to Kim et. al. [6.8] the interaction of HA with SBF ultimately results in the formation of apatite crystals. It is proposed that there are three stages of HA–SBF interaction, leading to the formation of apatite crystals. In the first stage, dissolution of HA increases the  $\text{Ca}^{+2}$  concentration of SBF. This results in the formation of Ca-rich amorphous Ca-phosphate. In the second stage, the  $(\text{PO}_4)^{-3}$  of SBF reacts with Ca-rich Ca-phosphate to form Ca-lean Ca-phosphate. Thus, the concentration of  $\text{P}^{+5}$  in the SBF decreases. In the third stage, the Ca-lean Ca-phosphate react with both  $\text{Ca}^{+2}$  and  $(\text{PO}_4)^{-3}$  of SBF to crystallize apatite crystals. Depending on the dissolution behavior of HA, the crystallization of apatite crystals will be different. The deposition of apatite crystals on HA results in weight gain at longer aging periods. The pH of SBF (Fig. 6.9) increases from 7.4 to 7.6 till 21days that can be correlated with the dissolution of HA in SBF.

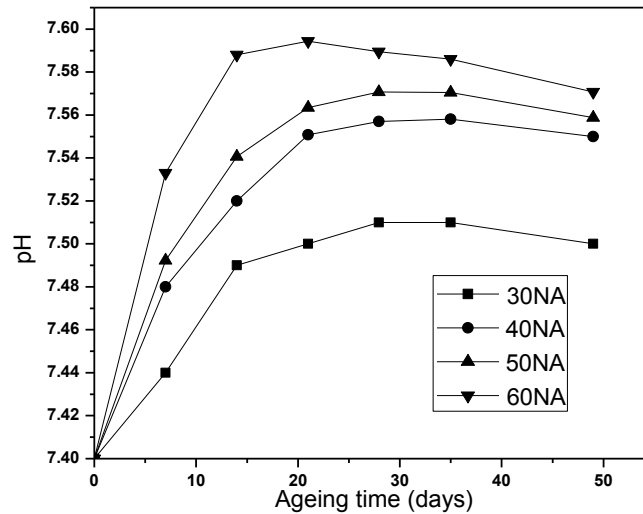


**Fig. 6.9 Change in pH with ageing time of HA-NA**

### 6.5.3 Change in the $\text{Ca}^{+2}$ and $\text{P}^{+5}$ concentrations

Fig.6.10 shows the changes in  $\text{Ca}^{+2}$  concentration of SBF as a function of aging days. It is observed that the  $\text{Ca}^{+2}$  concentrations in SBF increase from its initial value (277 ppm) to 285 ppm in 21 days. The extent of increase in  $\text{Ca}^{+2}$  concentrations is more for higher NA containing samples. After 21 days, the  $\text{Ca}^{+2}$  concentrations start decreasing and reach a value between 280 and 281 ppm irrespective of the composition. On the other hand,  $\text{P}^{+5}$  concentration decreases with aging time. (Fig. 6.11). The increase in  $\text{Ca}^{+2}$  in SBF appears to be the due dissolution of HA. This point can be verified by weight loss behaviour of HA (Fig 5.8). It appears that the dissolution of  $\text{Ca}^{+2}$  in SBF increases the saturation level of  $\text{Ca}^{+2}$  in SBF. This probably results the precipitation of amorphous Ca-Phosphate [6.8]. With increasing in aging time, the amorphous precipitate converts to crystalline apatite.

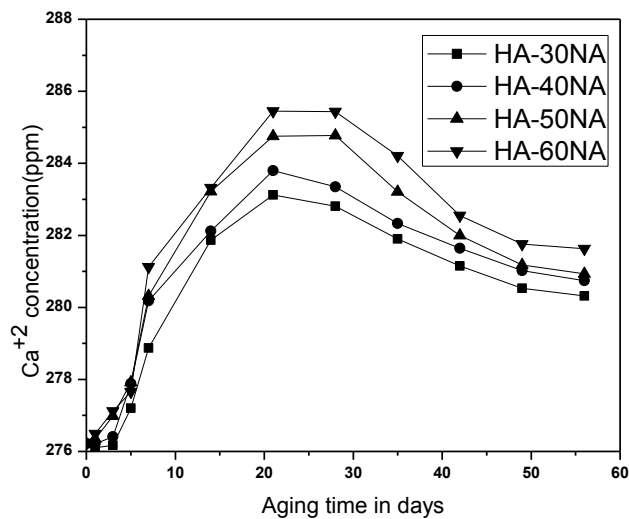
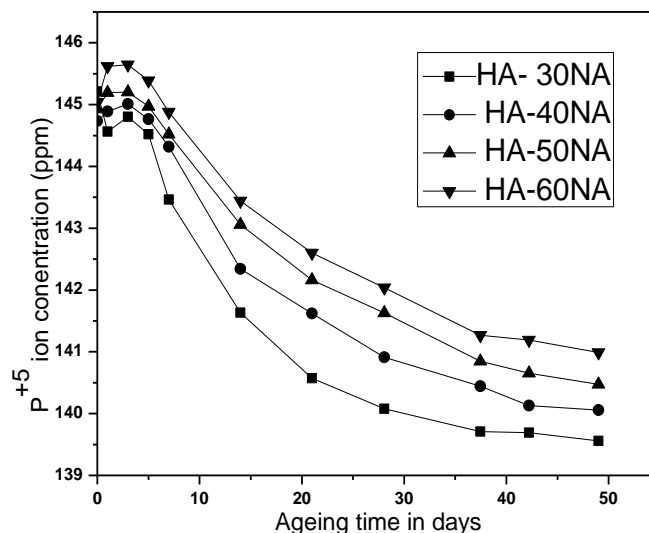


Fig. 6.10 Change in  $\text{Ca}^{+2}$  concentration of SBF with aging time



**Fig. 6.11. Change in P<sup>+5</sup> concentration of SBF with aging time.**

## 6.6 Conclusions

This Chapter discussed the fabrication of porous HA scaffold using NA granules as the pore former. At lower NA (HA-30NA and HA-40NA) compositions, the samples appear to be relatively dense and with lesser interconnections. The structure opens up at 50 and 60 vol% NA addition producing a porous and interconnected microstructure. At 70 vol% NA addition (HA-70NA) the microstructure appears to be more of a flaky nature, highly porous with large pore size. The compressive strength decreases with the increase in the porosity. HA-30NA samples have the highest compressive strength (7.99 MPa), and HA-70NA had the lowest strength (0.89MPa). The microstructure of the SBF aged samples show that the apatite particles initially have a spherical morphology. The apatite growth starts from the surface of predominantly large grains or from the grains that are situated near a pore. It is possible that such grains have higher dissolution rates. Thus, the study shows that by controlling the pore former (NA) content, a wide variety of having physical and mechanical can be produced.

# *Chapter-7*

## *Porous HA by Gel casting*

### *Route*

## 7. Porous HA by Gel casting Route

### 7.1 Background of the present work:

Chapter 6 discussed the processing of porous HA structure by Solid State Fugitive removal method using naphthalene (NA) granules as the pore forming agent. The processing was cheap and easy to handle, but the results showed that it suffered from a serious drawback. The distribution of NA granules in HA matrix was not homogeneous, often agglomerating to form large sized pores, particularly at a higher volume fraction of NA addition. Thus, the pore sizes in the sintered scaffold often exceeded the initial granule size of NA. It was also noted that some naphthalene granules were crushed during dry pressing of pellets thereby producing very small meso or micro pores. Therefore, though solid state route was simple, it did not always produce the desired microstructure, particularly at a higher volume fraction of naphthalene. In view of the above fact, another processing route viz. Gel Casting was adopted for making a porous HA. The Gel Casting route adopted in this thesis is slightly modified from the conventional gel casting route. In this method, NA granules are also added to the slurry before the slurry is gelled. Therefore, it is expected that the combination process will create a porous structure in two ways. Firstly due to the removal of polymer network and secondly due to NA granule removal. Hence, it will be possible to modify the pore structure (over and above that obtained from gel casting) by varying the NA volume fraction.

The scientific background of gel casting technique and its adaptability to produce a wide spectrum of microstructure have been elaborated in Chapter 1 and 2. In essence, gel casting is a near net shape forming technique involving gelation of the slurry due to in-situ polymerization of organic additives. The basic mechanism in gel casting is the formation of a macromolecular gel network in which the ceramic particles are virtually “frozen”. To achieve these gel structures, gel casting compositions consist of a monomer, a cross linker, free radical initiator and a catalyst. The gels essentially contain a hydrogel made up of three-dimensional polymeric network and water. This 3D polymeric network provides stability as well as the insolubility of the gel, giving it a rigid structure. In the presence of water, these hydrogels swell due to the balance between the

dispersing forces acting on the hydrolyzed polymeric chain network and the cohesive forces that prevents water from penetrating the hydrogel network [7.1]. The hydrogels in gel casting system are usually formed by co-polymerizing a monomer with a crosslinking agent. The monomer is monofunctional, and the crosslinking agent is multifunctional. In the present study, Methyl Acrylamide (MAM) was the monomer, Methylene-bis-acrylamide (MBAM) acted as the crosslinker. Ammonium Persulphate (APS) and N N Tetra Methylethylenediamide (TEMED) performed the roles of free radical initiator and catalyst respectively [7.1-7.5]. However, in all the gel casting method, the porosity and pore shape and size is dependent on the type and amount of monomer. Therefore, in this study, an attempt has been made to modify the microstructure and the pore architecture by a combination of fugitive and gel casting. The additional use of NA as a fugitive has provided another parameter for controlling the porosity and pore connectivity [7.3]. Therefore, the present work slightly differs from the conventional gel casting or freeze casting method studied earlier on two counts. Firstly, in this study, combined use of monomer and fugitive has resulted in a high degree of porosity along with variation in pore size which more than that achieved by gel casting alone. This kind of work has been reported by Chen et.al [7.3]. Secondly, most of the reports on gel casting have been made in the solid loading range of 40-70%. However, in the present study, the effect of low solid loading (30-55 volume %) has been investigated. This second part has not been studied in detail earlier. The cast samples were sintered at 1250 °C and characterized for pore shape and size, strength, microstructure, in-vitro aging and cytotoxicity test.

## **7.2 Raw Materials and Processing**

The aqueous Gel Casting slurries were prepared using the following components (Table - 7.1.). The function of each component has also been included in the Table-7.1. The different components were mixed in the sequence prescribed in Fig 7.1.1. A stable HA slurry was prepared by adding Darvan C (1mL /100gm HA powder) as a dispersant. Naphthalene (NA) particles (average particle size 250µm) were also added to stable HA slurry prior to the gelation of the slurry. The addition of NA particles was expected to produce a higher degree of porosity in HA over and above that created by Gel Casting itself. Table-7.2 shows the slurry composition and NA content required for preparing slurry compositions containing different NA.

**Table-7.1 Components of Gel casting slurries**

Materials	Source	Function
Calcined HA	Synthesized in the laboratory for this work	Ceramic component
Methyl Acrylamide (MAM) (C <sub>2</sub> H <sub>3</sub> CONH <sub>2</sub> )	Merck, India (GR grade)	Monomer
Methylene-Bis-Acrylamide (MBAM) [(C <sub>2</sub> H <sub>3</sub> CONH) <sub>2</sub> CH <sub>2</sub> ],	Merck, India (GR grade)	Crosslinking agent
Ammonium Persulphate (APS), (NH <sub>4</sub> ) <sub>2</sub> S <sub>2</sub> O <sub>8</sub>	Merck, India (GR grade)	Free radical initiator
N, N, Tetra Methylethylenediamine (TEMED)	Merck, India (GR grade)	catalyst

Due to the low density of NA, uniform mixing of NA granules in HA slurry was difficult and often it required longer and intense stirring. Accordingly, the mixed slurries of HA + NA were stirred at 900 rpm for 30-45 minutes to ensure homogeneous mixing of NA particles in the slurry. Longer stirring time was employed for the higher volume fraction of NA to ensure better mixing and dispersion of NA in the slurry. The HA + NA mixed slurry was transferred to a petroleum jelly-coated Teflon moulds (46mm  $\phi$  i.d. x 5mm height). Post mould filling, the mould was gently tapped to remove the entrapped air as well as for even distribution of slurry in the mould. The casts were dried in a water bath (40<sup>0</sup>C) for 2 days following which the casts were demoulded, and oven dried at 80<sup>0</sup>C for 24 hrs. The samples were carefully heated till 650<sup>0</sup>C (heating rate 2<sup>0</sup>C/min). A hold time of 2 hours was provided at that temperature for facilitating easy removal of monomers, initiators, accelerators, other organics as well as NA. Finally, the samples were heated to 1250<sup>0</sup>C for final densification of samples. From 650<sup>0</sup>C to 1250<sup>0</sup>C, heating rate was 3<sup>0</sup>C/min with a holding time of 2 hours at the peak temperature. Figure 7.2 shows physical appearance of the sintered samples.

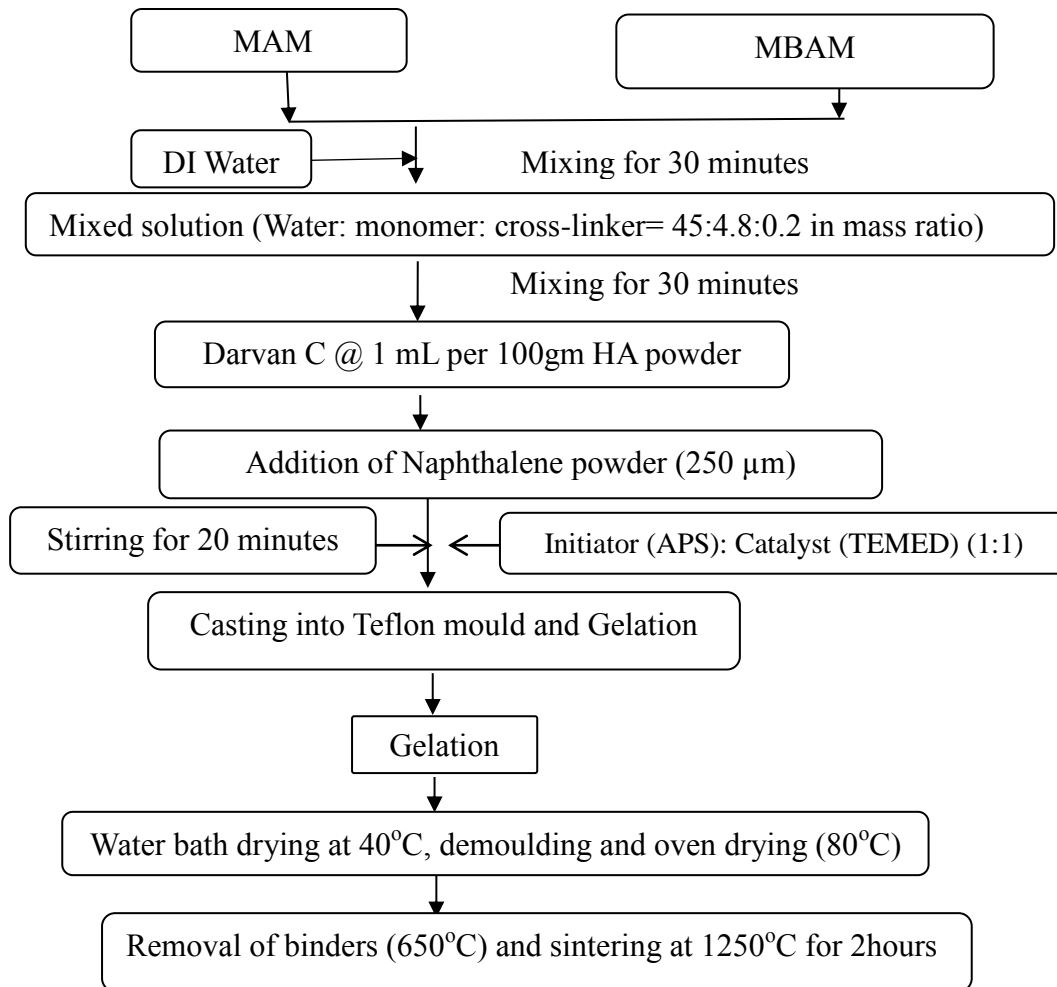


**Fig. 7.1** Flowchart for the processing of Gel cast porous HA scaffolds using Naphthalene.

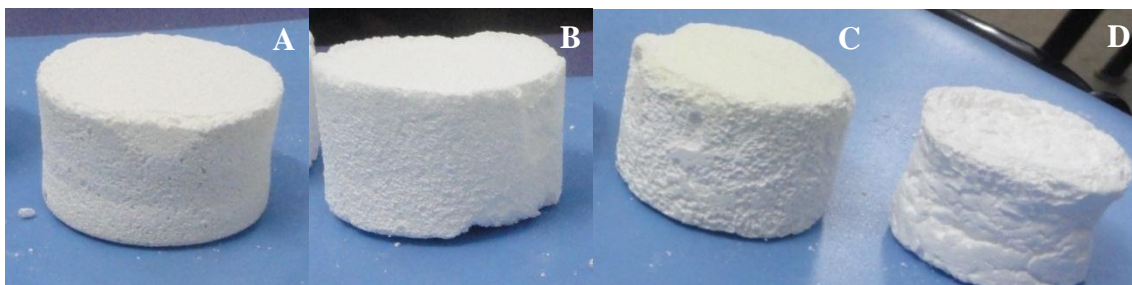


**Fig. 7.2** Physical appearance of sintered HA scaffolds prepared by gel casting (Sample A-15NA, B-25NA, C-35NA, and D-45NA)



**Table-7.2 Slurry composition for scaffold preparation**

Sample Code	Vol % HA	Naphthalene (Vol. %)
0NA	30.0	-
15NA	35.0	15
25NA	40.0	25
35NA	42.0	35
45NA	45.0	45
55NA	47.0	55

### 7.3 Thermal behavior of the dried Gel

Fig.7.3 shows DSC-TG diagram of the as dried gel. The DSC curve has a number of peaks. At 100°C, it has an endothermic peak associated with weight loss of about 5%. This weight loss is due to the removal of adsorbed water from the gel. The exothermic peak at 230°C is due to the oxidative decomposition of polyacrylamides which starts around 220°C. At this temperature, imidization reaction of acrylamide releases ammonia.



The hydrolysis of methyl acryl amide produces Ethanoic acid and ammonia. This reaction is associated with weight loss and is completed by 277°C. The second reaction starts around 310°C involving the breakdown of the polymeric backbone of amide and decomposition of imides formed the first reaction [7.5]. The reaction is over by 390°C. Following this, two exothermic peaks are observed at 410°C and 660°C. These exothermic peaks are due to the oxidation of volatiles and carbon residues from the decomposition of MAM and MBAM.

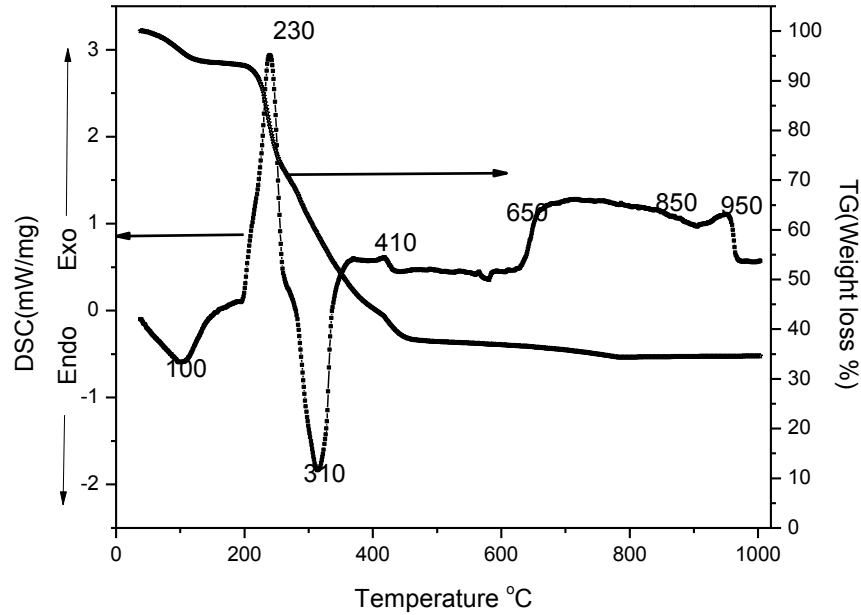


**Fig.7. 3. DSC-TG of dry gel cast HA**

#### 7.4 Slurry Rheology

The rheology of the slurries was measured as a function of solid loading. The maximum solid loading (55 vol %) corresponding to the acceptable limit of pourability was taken as the maximum permissible solid loading for successful gel casting. Fig. 7.4 (a) and 7.4 (b) show the effect of solid loading on the shear stress-shear rate as well as viscosity-shear rate behavior respectively of HA slurries. The shear stress-shear rate plots have been obtained in both upturn (increasing shear rate) and downturn (decreasing shear rate) mode. It was observed that slurries with solid loading less than 42 vol% were very fluid and showed negative shear stress value. Only slurries of 42 vol% and higher solid loading showed the characteristics shear thinning behavior. For such slurries, the shear stress increased with the shear rate rapidly during at low shear rate, and more gradually at the higher shear rate. A typical hysteresis was observed between the shear stress and shear rate. Because the slurries would show a power law behavior, the shear thinning constant ( $n$ ) was calculated from the slope of  $\ln(\eta)$  vs.  $\ln(\dot{\gamma})$  plot. It was observed that all the slurries showed shear thinning behavior with  $n$  value of 0.25 to 0.40. Fig. 7.4 (c) shows the representative shear stress-shear rate graph for 55 vol% solid loading. The difference in shear stress in the upturn and downturn mode at zero shear rate is  $\tau_{gel}$  or an index of

structural buildup. Fig. 7.4 (d) shows the variation of  $\tau_{gel}$  for all the composition between 42 and 55vol% which shows that the index of structural buildup increases with solid loading. This implies that at higher solid loading, the samples will have a lower casting time and the cast may have low porosity and it may be difficult to cast slurry with very high  $\tau_{gel}$ . Fig 7.4. (e) shows the variation of steady state viscosity (measured at  $200\text{ s}^{-1}$ ) with solid loading for all the compositions. It is seen that the steady state viscosity is 7 Pa.s for 30 vol% solid loading and it is 12 Pa.s for 35 vol%. The low viscosity of these two slurries resulted in poor cast properties and these samples cracked after drying. However, the viscosity is 22 Pa.s for 40 vol% and it produced crack free samples. The viscosity increased further with increase in solid loading and at 47 vol% solid loading the viscosity (71 Pa.s) corresponding to “pourable” and castable slurry was observed. The maximum viscosity was 256 Pa.s for 55 vol% solid loading and slurries became more viscous were difficult to pour. Therefore, the maximum solid loading in this investigation was restricted to 47 vol%.

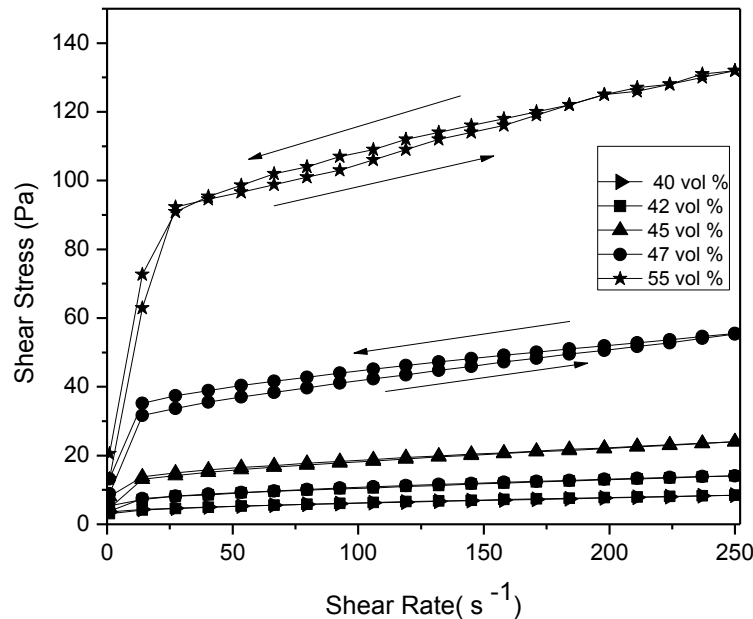


**Fig. 7.4(a) Shear Stress versus Shear Rate plot of HA slurry as a function of HA solid loading.**

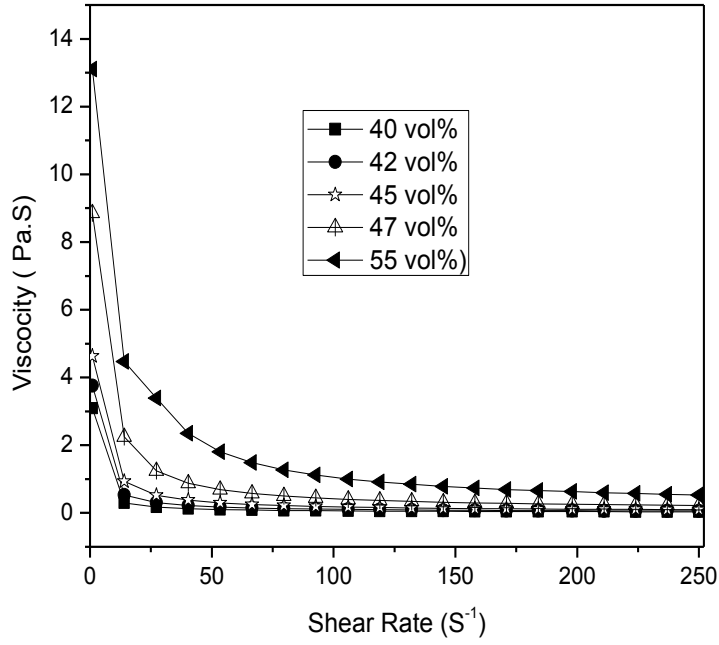


**Fig. 7.4(b) Viscosity-Shear rate plot of HA slurry as a function of HA solid loading.**

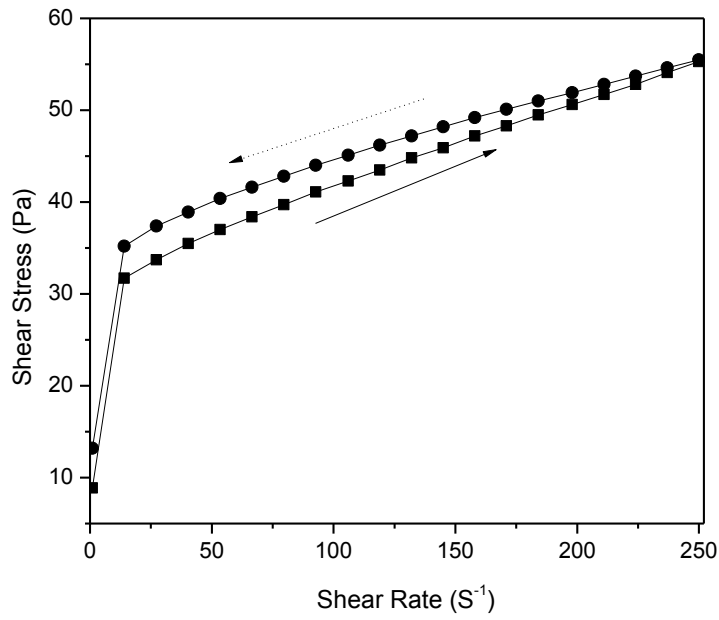


**Fig.7.4(c) Shear Stress – Shear Rate plot for 55 vol% solid loading of HA slurry**

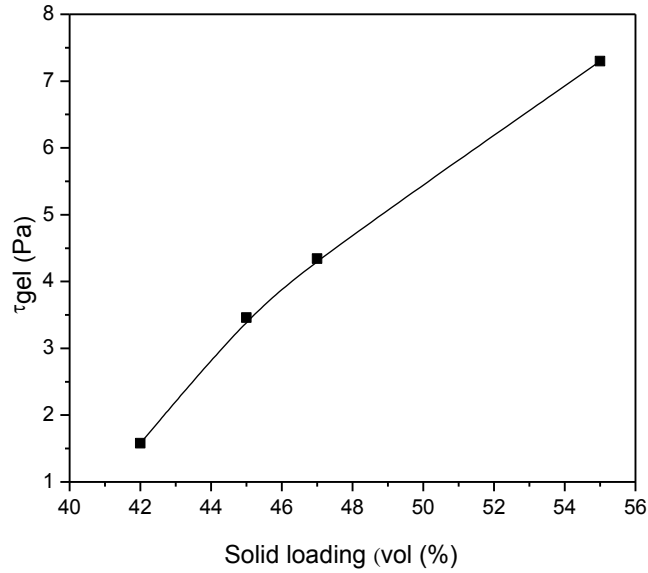


**Fig.7. 4(d) Variation of  $\tau_{gel}$  with solid loading**

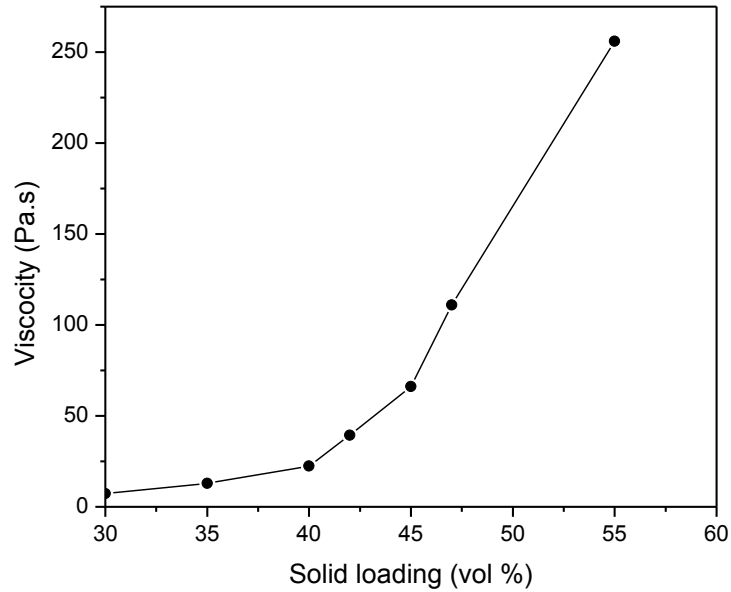


**Fig.7. 4(e) Variation of steady state viscosity of HA as a function of HA solid loading.**

### 7.5 Effect of Naphthalene content on strength and porosity of porous HA

Fig. 7.5 (a) and 7.5 (b) and Table-7.3 show the effect of the addition of NA on porosity and strength of the gel cast scaffolds, respectively. It was found that with the increase of NA, the porosity increased and simultaneously the bulk density and compressive strength decreased. Without NA addition, the porosity was  $22 \pm 3$  %, and corresponding strength

was  $7.51 \pm 0.1$  MPa. As already explained, NA was added to create higher porosity sample. At 45% NA addition, the porosity was nearly 75%, and strength reduced to about 1 MPa, which is close to the literature value [7.6-7.9] for this level of porosity. At still higher NA content (55 vol %), the sample had high porosity. The compressive strength for these samples could not be measured because high porosity resulted in mechanically weak and fragile samples. Therefore, the strength limiting factor restricted the maximum percentage of NA to 45vol%. Compressive strength values for samples were matching the literature value [7.7-7.9] as well as close to the reported compressive strength of human cancellous bone that ranges between 2-12 MPa [7.7].

A plot (Fig. 7.5.c) of compressive strength ( $\sigma$ ) against porosity (P) shows that strength ( $\sigma$ ) exponentially decreases with increase in volume fraction porosity and follows the relation.

$$\sigma = \sigma_0 \exp(-bP) \dots \dots \dots (7.1)$$

Where, b is constant, and  $\sigma_0$  is the compressive strength for zero porosity samples. A plot of  $\ln(\sigma)$  vs volume fraction porosity (P) [Fig. 7.5(c)] yields a straight line with a negative slope. The slope gives the value of 'b' and for this study it was found to be 0.04. The negative slope indicates that as the porosity increases, the load carrying capacity of the scaffold decreases.

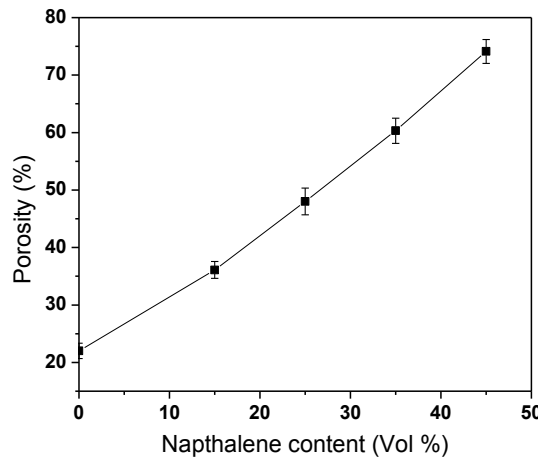


**Fig.7.5 (a) Variation of porosity as a function of naphthalene content**

The decrease in the strength is the result of the increased porosity or void space in the sample due to lesser connectivity among the solid materials. Thus, the strut are becoming thinner and the load bearing capacity of the scaffold decreases. In this kind of porous

scaffold, there are essentially two phases, viz. solid phase and the void phase. At the lower NA content, the HA phase is the continuous phase and the pore phase is the discontinuous phase. This implies that the pores are discretely separated in the solid HA phase. With the increase in the NA content, the solid phase decreases and the pore phase increases. Thus, at the highest NA content, the pore phase become the major phase

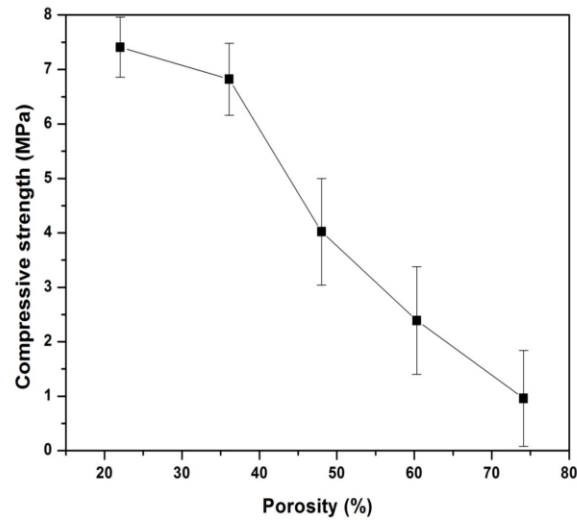


**Fig. 7.5(b) Variation of compressive strength as a function of porosity.**

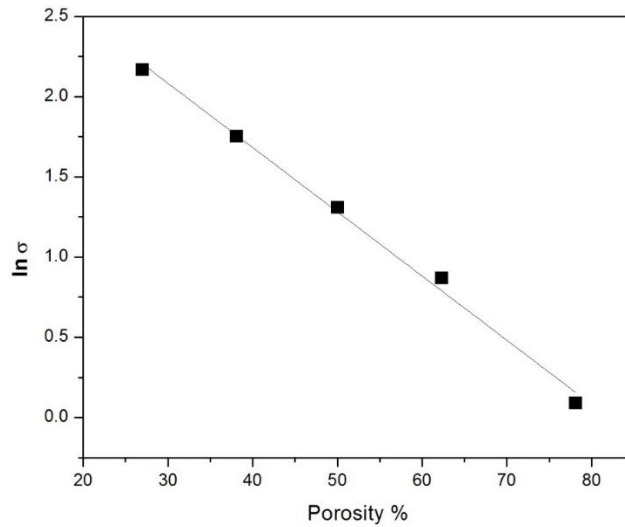


**Fig. 7.5 (c) Semi-logarithmic plot of Compressive Strength and Porosity.**

**Table-7.3 Density, Porosity and strength of porous HA scaffolds**

(NA) (vol%)	Bulk Density (BD)	Apparent Porosity (%AP)	Closed Porosity (%CP)	Compressive Strength (CCS) (MPa)
0	2.18	22.02	8.09	7.41
15	1.85	36.10	5.37	6.82
25	1.48	48.02	5.15	4.02
35	1.09	60.32	5.19	2.39
45	0.74	74.11	2.47	0.96

### 7.6 Porosity and pore size distribution of Gel Cast Porous HA scaffold

The pore size distribution data [dv/dlogD] vs. pore size] of a gel cast porous HA-NA samples are shown in Fig. 7.6 (a) to Fig. 7.6 (e). The plots show that the pore size distribution is altered by NA addition. In the 0NA gel cast samples (Fig. 7.6 (a)), a shallow peak between 0.3-5 $\mu$ m indicate that some pores are present in that range. A double peak between 2-8  $\mu$ m confirms that there are some pores in the range 2-5  $\mu$ m and 5-8  $\mu$ m. A small peak in the range 30-50  $\mu$ m indicate that pores are also present in the 30 -50  $\mu$ m range but the majority of the pores lie between 8-20  $\mu$ m. A broad and low hump is observed around 200  $\mu$ m that implies there are a few isolated pores in the 200  $\mu$ m range. The dv/d (logD) vs. pore diameter plot at 15 vol% NA (Fig.7.6.b) addition shows almost a similar pattern lower and higher pore diameters. On the lower pore diameter side, a shallow hump is observed between 0.2-5  $\mu$ m indicating that some pores are present in that range. Large mercury intrusion value is observed between 10-30  $\mu$ m confirming that majority of the peaks at in the range 10-30  $\mu$ m. The pores of 30  $\mu$ m, 50  $\mu$ m, and 200  $\mu$ m are also present although the number density is less. It can be noted that the porosimeter data can provide pore size information up to 212  $\mu$ m. Pores larger than this range cannot be detected as these will be filled with mercury virtually at zero intrusion pressure. With 25 vol% NA addition (Fig.7.6 (c)) again a shallow and broad hump in the pore size range 0.2-5  $\mu$ m indicate the presence such pores in 25 vol% NA Gel cast samples. After that, a sharp rise in intrusion volume is observed between 10-50  $\mu$ m



confirming the presence of pores in that size range. In the higher size range, a prominent peak at 100-200  $\mu\text{m}$  is observed.

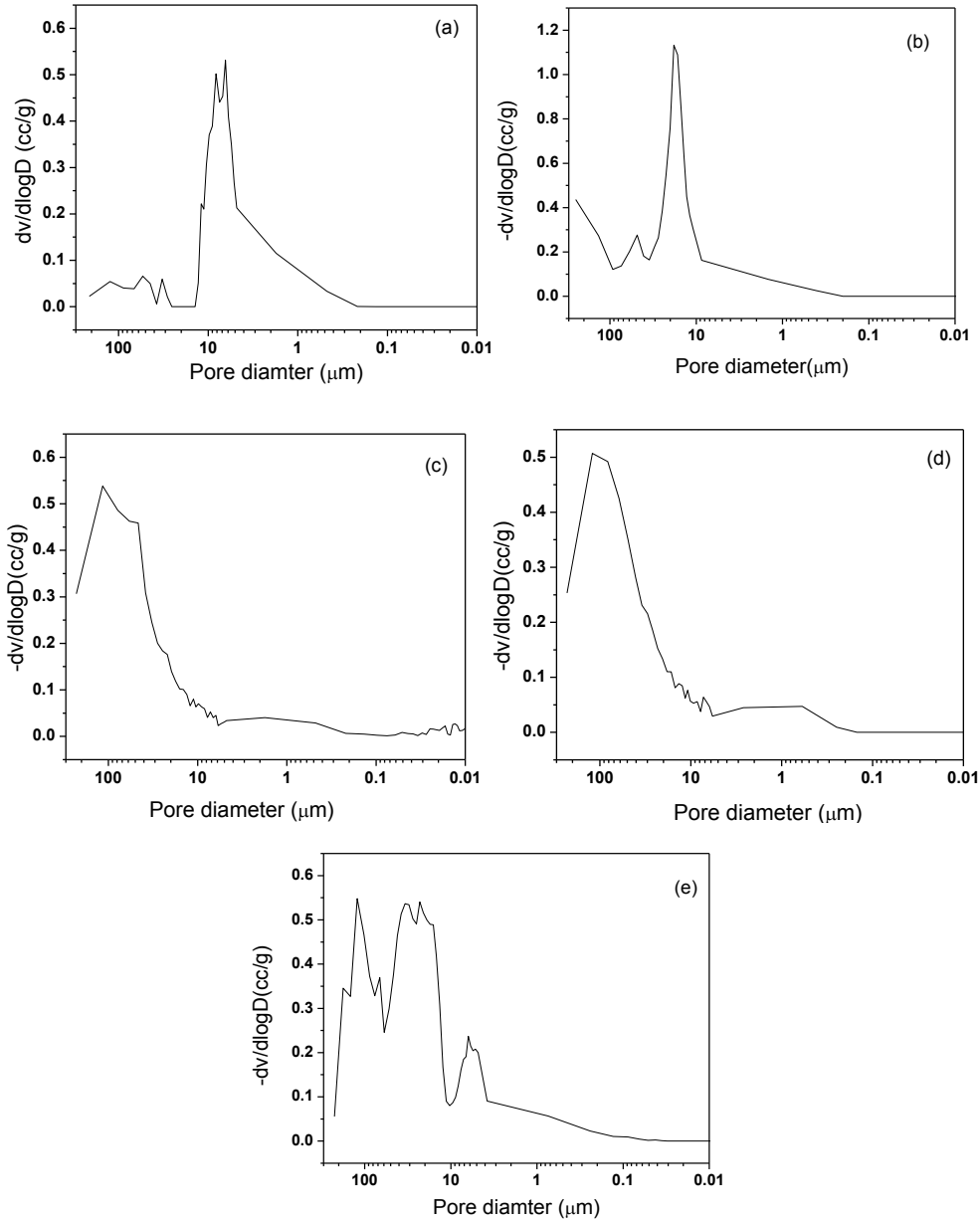


**Fig 7.6 (a-e) Pore size distribution of sintered HA scaffolds prepared by gel casting (a) HA-0 NA, (b) HA-15NA, (c) HA-25NA, (d) HA-35NA, (e) HA-45NA.**

A comparison of the intrusion volumes of 25 vol% NA with 15 vol% NA Gel cast (Fig. 7.6.b) shows that the number fraction of 100-200  $\mu\text{m}$  pores is significant in 25 vol % NA. Fig. 7.6 (d) describes the pore size distribution of gel cast HA samples with 35 vol% NA addition. Similar to the other two previously described samples, a shallow and broad

intrusion peak is observed between 30-200  $\mu\text{m}$  indicating the presence of such sized pores in the sample. It is pertinent to note that with an increase in NA vol%, larger pores (50-200  $\mu\text{m}$ ) start appearing but while bimodal peaks are observed in the previous two compositions, at 35 vol % NA addition, the peak profile is predominantly monomodal. Finally, at 45 vol% NA addition, a drastic change in the pore distribution could be observed. The pore size distribution plot (Fig. 7.5 (e) (for 45 vol% NA added sample) could be divided into 5 different zones. A small peak between 0.05-2.5  $\mu\text{m}$ , a broad but sharp peak at 0.3-10  $\mu\text{m}$ , a broad triplet peak between 10-60  $\mu\text{m}$ , a sharp peak at 80  $\mu\text{m}$  and a triplet between 90-200  $\mu\text{m}$ . Thus at 45 vol% NA addition, the porous sample consists of wide pore size. By comparing with microstructure (Fig 7.7. (a- e)), it can be summarized that in pure gel cast samples, most of the pores lie in 0.3 to 200  $\mu\text{m}$  range. With the increase in NA content, firstly the pore size increases to a higher value. Secondly, the rupturing of pore walls takes place leading to the higher degree of interconnectivity (particularly in 35 and 45 NA samples) increases. Finally, fine pores (meso pores) are created on the pore walls giving rise to a highly porous structure.

### **7.7 Microstructural Analysis of HA scaffold prepared by gel casting**

Fig. 7.7 (a) to 7.7 (e) present the FESEM microstructure of sintered Gel casted porous network. As discussed before, the sintering was carried out at 1250°C for 2 hours. Fig. 7.7 (a) shows the microstructure of gel cast samples without any naphthalene addition (0NA). This microstructure sample was observed in order to understand the porosity and pore size distribution of pure gel cast samples (i.e., without any naphthalene addition). The sample shows that it has two types of pores – a few large pores (100-200  $\mu\text{m}$ ) and mostly small pores (50  $\mu\text{m}$  or smaller). It is also observed that interconnections are present in both large and small pores (encircle area). With the addition of 15vol% NA, a change in the microstructure can be observed (Fig. 7.7 (b). The Figure shows that besides smaller pores (50-100  $\mu\text{m}$ ) (single arrow) larger pore ( $\geq 200$   $\mu\text{m}$ ) (double arrow) are also present in the sample. In Fig. 7.7(c), the number of the large pores (200  $\mu\text{m}$ ) is more. It is to be noted from the selected area that the pore walls are also ruptured leading to interconnected microstructures. In HA-35NA samples, the large pores are around 250  $\mu\text{m}$  and are interconnected. The medium pores are 100  $\mu\text{m}$  in size, and smaller pores are about 50  $\mu\text{m}$ . The larger pores are highly interconnected.

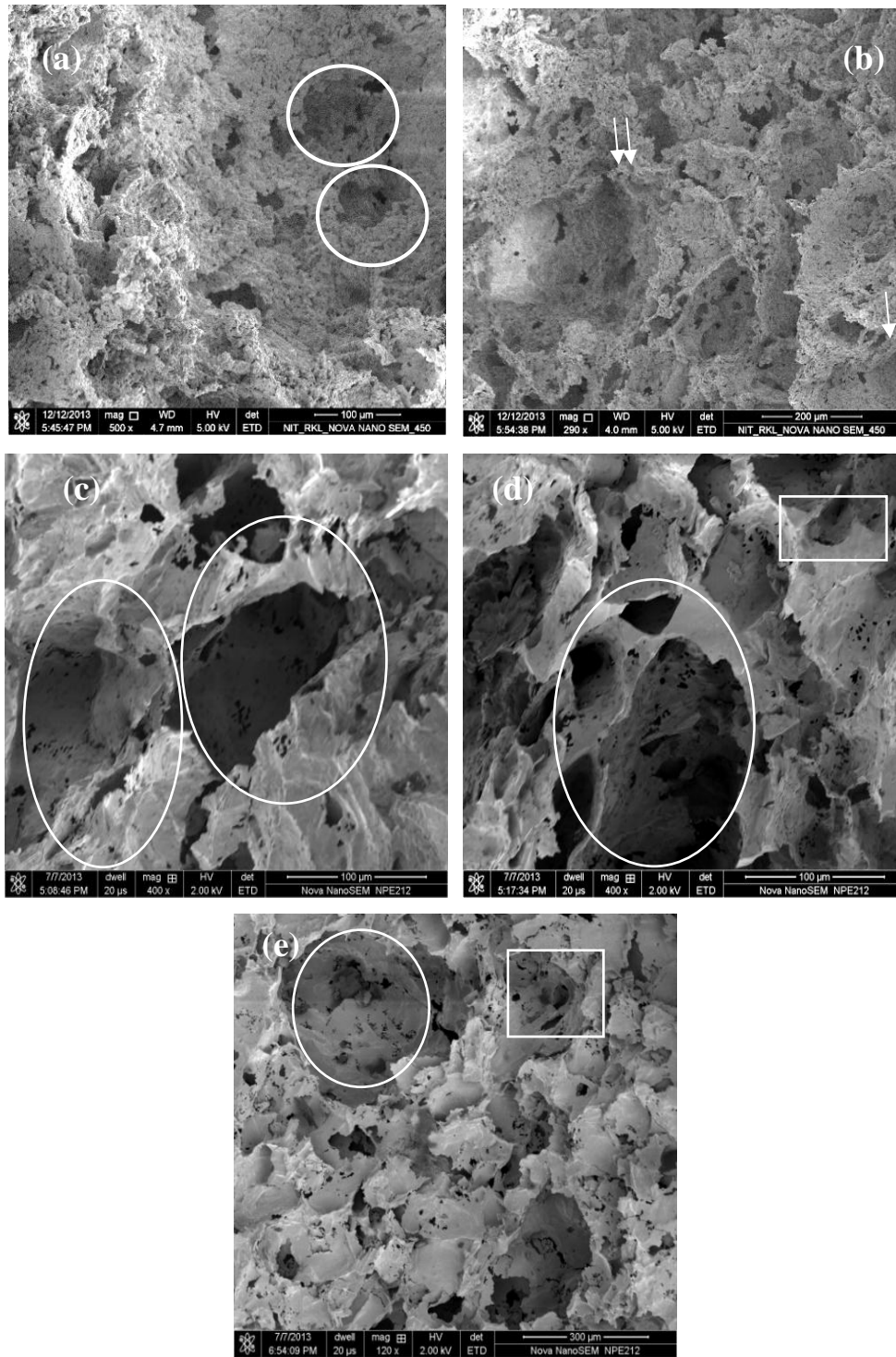


**Fig. 7.7. FESEM microstructure of Gel cast porous HA scaffolds prepared by combination of gel casting and NA addition (a) HA-0NA, (b) HA-15NA, (c) HA-25NA, (d) HA-35NA and (e) HA-45NA.**

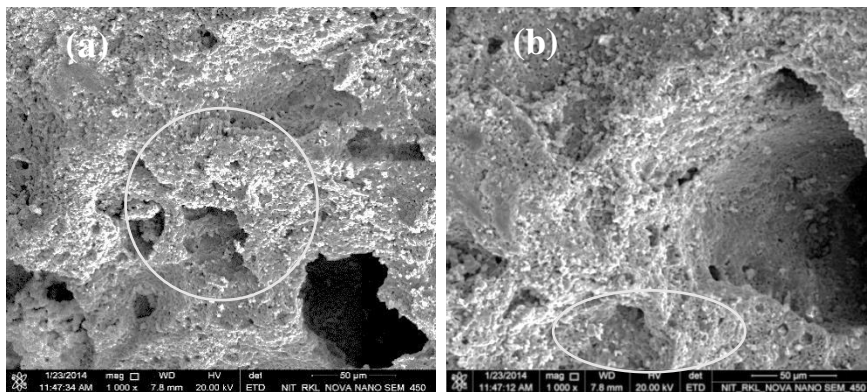
Finally in HA-45NA samples, the large pores are in the range 200-400  $\mu\text{m}$ . Some of the interconnections are of 50  $\mu\text{m}$  size though small pores (< 10  $\mu\text{m}$ ) are also seen (box area).

Thus, the addition of NA to gel cast samples shifts the pore size distribution to large pore sizes. At higher NA (35 and 45 vol% NA), agglomeration of NA result in the creation of very large pores (~400  $\mu\text{m}$ ). The interconnectivity increases with NA content. At higher NA content, fine pores (double arrow) could also be observed on the pore walls. Thus, in the conclusion, it can be said that the combination of Gel casting and NA addition results, in a wide variation in microstructural features which is useful in the preparation of porous scaffolds.

## 7.8 In vitro bioactivity and the formation of apatite layer:

### 7.8.1 Effect of aging days on the apatite layer formation:

Figure 7.8 (a-g) shows the effect of aging time on the apatite layer of HA-35 NA after immersion in SBF for 3, 5, 7, 14, 17, 21 and 28 days respectively. The images show that after 3 days of aging, a few white granular spots are seen which correspond to the apatite particle formation (Fig 7.8.a and 7.8.b). The granular shape were observed till 7 days of aging as shown in the encircled areas in the images (Fig. 7.8 a, b and c). With the increase in aging period (7 days and 14 days) the area covered by the apatite deposit increases (Fig. 7.8.c and 7.7.d). Further, the shape of the deposited apatite layer changes with aging time (Fig.7.8 e-g). At a shorter aging time, it has particle-like morphology, at the intermediate time it has flower morphology and at the highest aging time it has a petal-like appearance. It is also observed from the above Figures that, the surface coverage also increases with increase in aging time. Thus, not only the apatite morphology changes with aging time but also the area covered by the apatite layer changes with aging time.



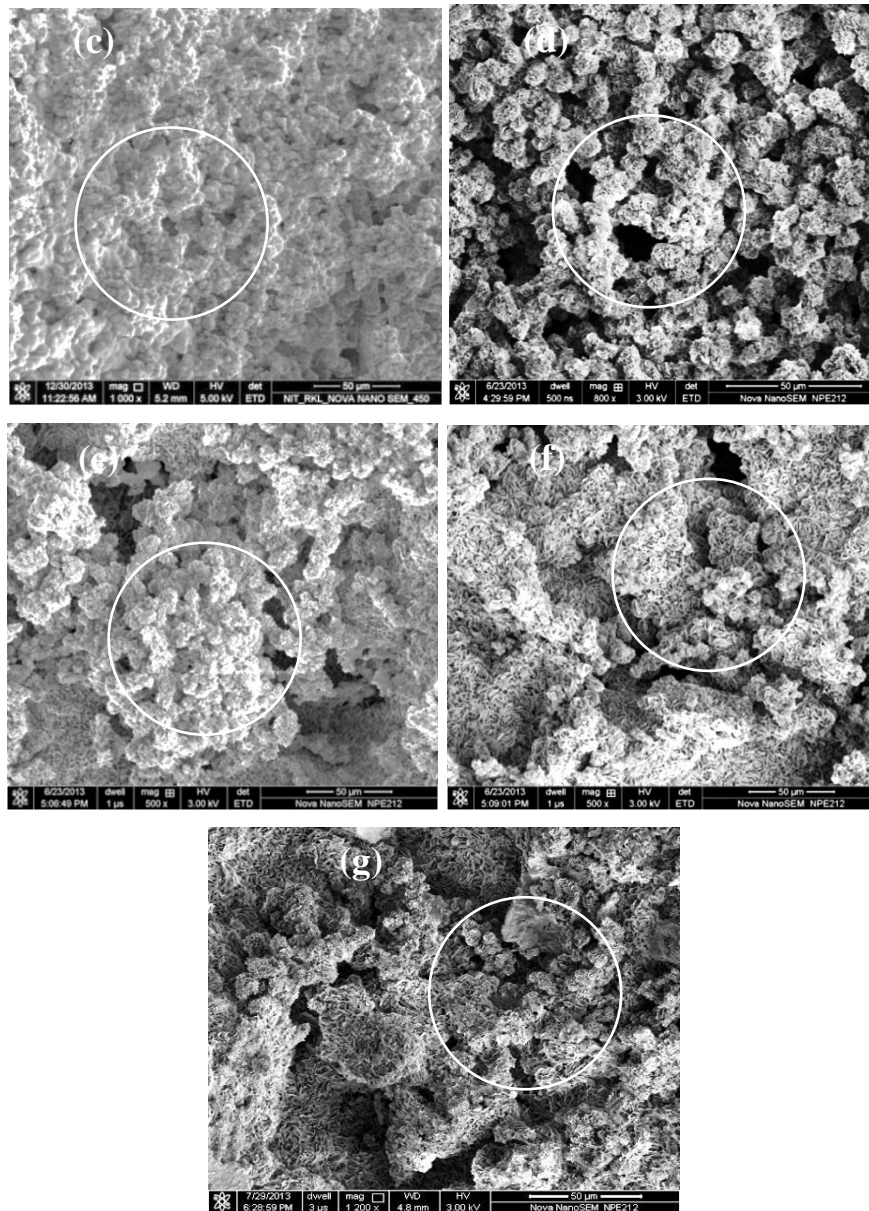
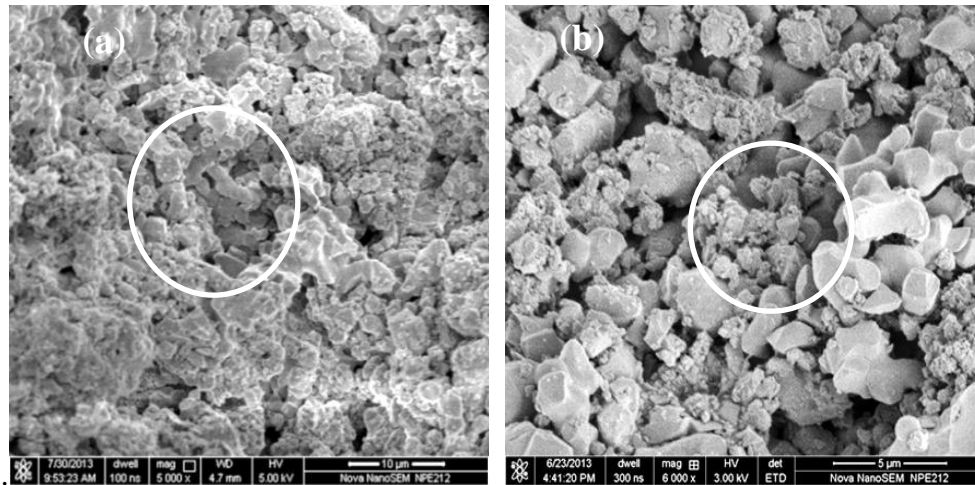


**Fig. 7.8 (a-g). (Scale bar, 50μm)Effect of aging time on the apatite layer of 35 NA after immerse in SBF of 3, 5, 7, 14, 17, 21 and 28 days respectively.**

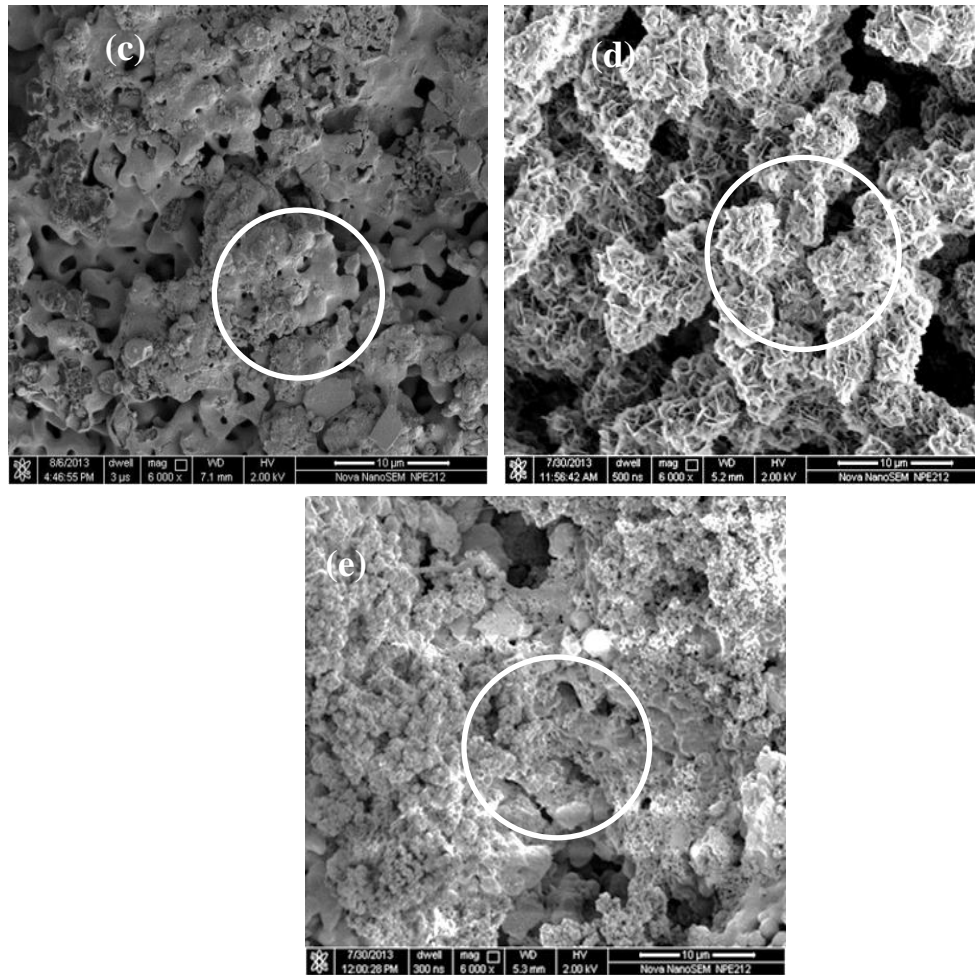
### **7.8.2 Effect of porosity on the apatite layer formation:**

Fig. 7.9 shows the FESEM image of HA scaffolds after soaking in SBF for 21days. The microstructure shows apatite formation on the HA surface. The apatite could be recognized as white precipitates (encircled area) on the sample surface. Fig.7.9 (a) represents the microstructure of only gel casted scaffold without any naphthalene. It is seen that there are a few spots that correspond to apatite deposition. Fig.7.9 (b-e) represents the microstructure with the progressively higher amount of naphthalene and

consequently higher porosity. The micrograph showed that more apatite layer was observed in the higher porosity sample (HA-45NA) as shown in Fig.7.9 (d and e, encircled area). In the lower porosity (HA-15NA) samples [Fig.7.9 (a)], the apatite layer was comparatively less. The higher deposition rate of apatite in higher porosity samples can be related to the faster dissolution of  $\text{Ca}^{+2}$  and its migration through an interconnected porous network of higher surface area [7.10-7.12]. Beyond 21 days, no significant change in surface area coverage could be observed, and all samples were almost fully covered with apatite deposits.



**Fig. 7.9.1 (Scale bar, 10 $\mu\text{m}$ ) FESEM images of SBF aged Gel Cast HA scaffold after 21 days aging (a) HA-0NA, (b) HA-15NA,**



**Fig.7.9. (Scale bar, 10μm) FESEM images of SBF aged Gel Cast HA scaffold after 21 days aging (c) HA-25NA, (d) HA-35NA and (e) HA-45NA.**

### **7.9 Dissolution Behaviour of Gel Cast HA scaffolds on aging in SBF**

The dissolution behaviour of Gel cast HA scaffold was determined by estimating the change in  $\text{Ca}^{+2}$  concentration of the SBF with the progress in aging. SBF solution. The variation of the  $\text{Ca}^{+2}$  concentration in SBF solution with aging time containing the porous HA is shown in Fig.7.10. It is seen that the  $\text{Ca}^{+2}$  concentration of SBF increases slowly in the first week of dissolution and after 1 week the concentration increases rapidly till three weeks (in some case up to four weeks) time. The increase of the  $\text{Ca}^{+2}$  in the SBF solution confirms the dissolution of HA.  $\text{P}^{+5}$  concentration slightly increases from 145 to 146 ppm during the within three days following which it decreases in the increase in aging time (Fig. 7.11). The degree of dissolution of HA in SBF depends on

the impregnation by SBF and in the higher porosity samples, a higher volume of impregnation is achieved. Similar observations were also noted by Ereiba et. al. [7.11]. Kim et also noted [7.12] similar observations as discussed in the previous section.

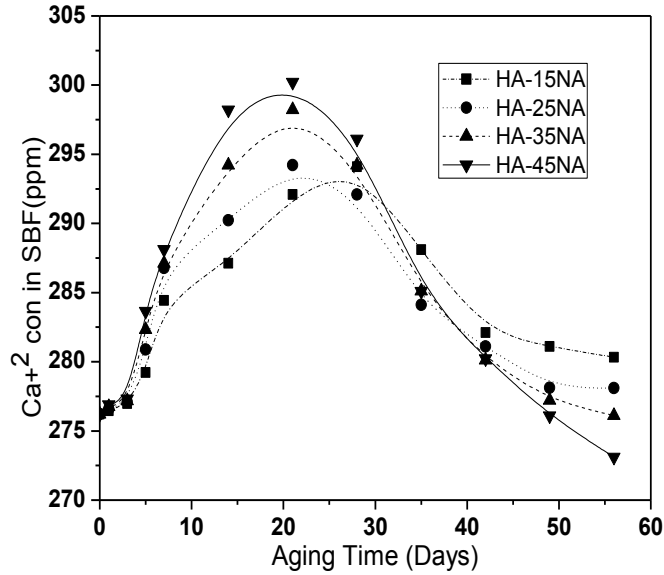


**Fig.7.10. Change in the Ca<sup>+2</sup> concentration of SBF with increase in the Aging Time of HA**

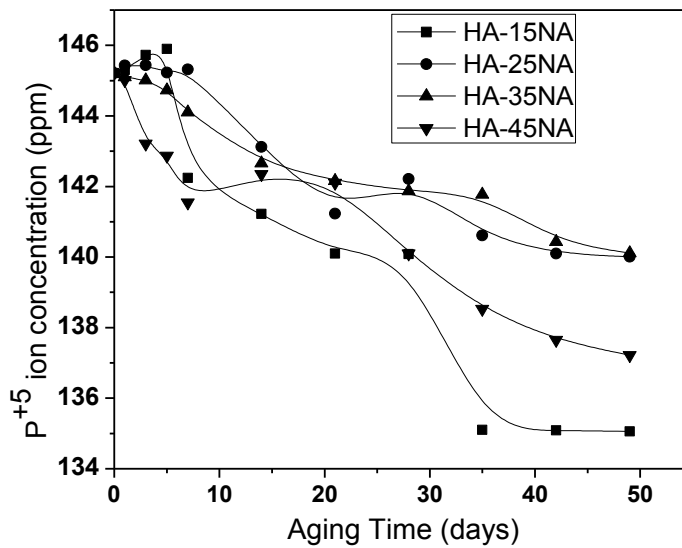


**Fig.7.11. Change in the P<sup>+5</sup> concentration of SBF with the increase in Aging Time**



Thus, it could be concluded that the increase in the  $\text{Ca}^{+2}$  concentration in SBF till 21 days of aging correspond to its dissolution in SBF. The subsequent decrease in the  $\text{Ca}^{+2}$  concentration after 21 days correspond to precipitation of apatite from the SBF solution. On the other hand, the weight loss increased till 21-28 days and then gradually decreased due to the deposition of CaP compound from SBF on the scaffold surface (Fig.7.12). Therefore, the dissolution is dominant till 28 days, and the apatite growth process is dominant after 28 days.

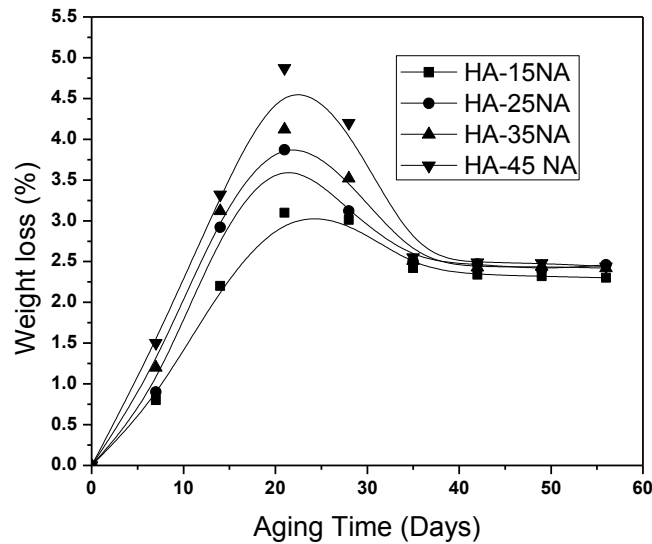


**Fig.7.12. Dissolution of porous HA as a function of Aging Time**

Fig.7.13 shows the effect of aging time on the pH change of SBF solution. The pH of SBF increases till 21 days that can be correlated with the dissolution of HA in SBF. The dissolution leads to an increase in the  $\text{Ca}^{+2}$  concentration. Due to the dissolution of  $\text{Ca}^{+2}$ , the pH increases. After that, the pH decreases as the released  $\text{Ca}^{+2}$  react with  $(\text{PO}_4)^-$  to produce CaP layer as discussed in the Section-6.5.2.

It is anticipated that the dissolution HA in the SBF solution increases the  $\text{Ca}^{+2}$  concentration of SBF. The increased saturation causes the nucleation of apatite first in the form of amorphous CaP ( $\text{Ca/P} < 1.5$ ) compound. With the increase in aging time, the Ca/P ratio of amorphous precipitate increases to 1.65, causing crystallization of apatite [7.12]. During the growth of the apatite coating or precipitates, the pH of the solution decreases due to the consumption of  $\text{OH}^-$  in the solution.

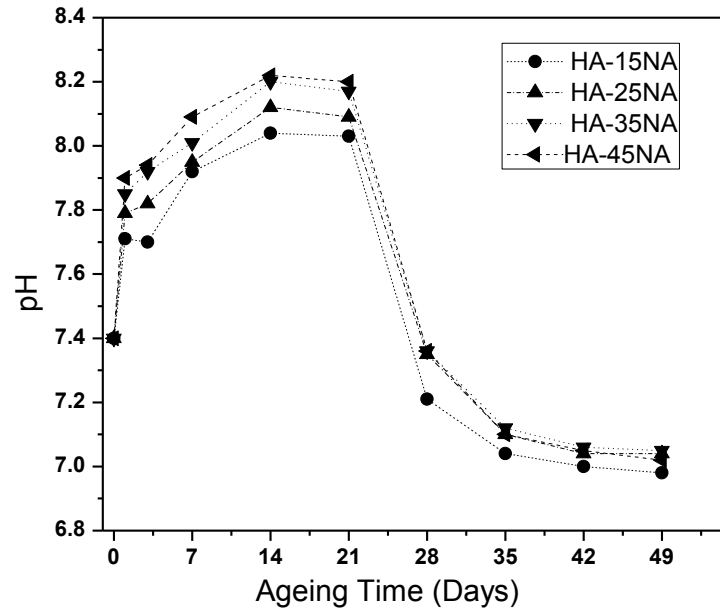


**Fig. 7.13. Effect of Aging time on the pH of porous HA scaffolds**

### 7.10 Cytotoxicity Behaviour

The results of MTT assay show that the cells were able to grow and proliferate favourably. The results also indicate that the porosity provides (HA- 45NA) favourable sites for cell proliferation. However, in the present study, a higher porosity sample (HA-45NA) exhibited only marginally higher cell viability than the less porous sample (HA-25NA) (Fig.7.14 and 7.15). Thus, from the above observation, it can be concluded that both the low and high porosity scaffold prepared in this study permit proper cell proliferation and are expected to show acceptable cytocompatibility along with cell viability properties.

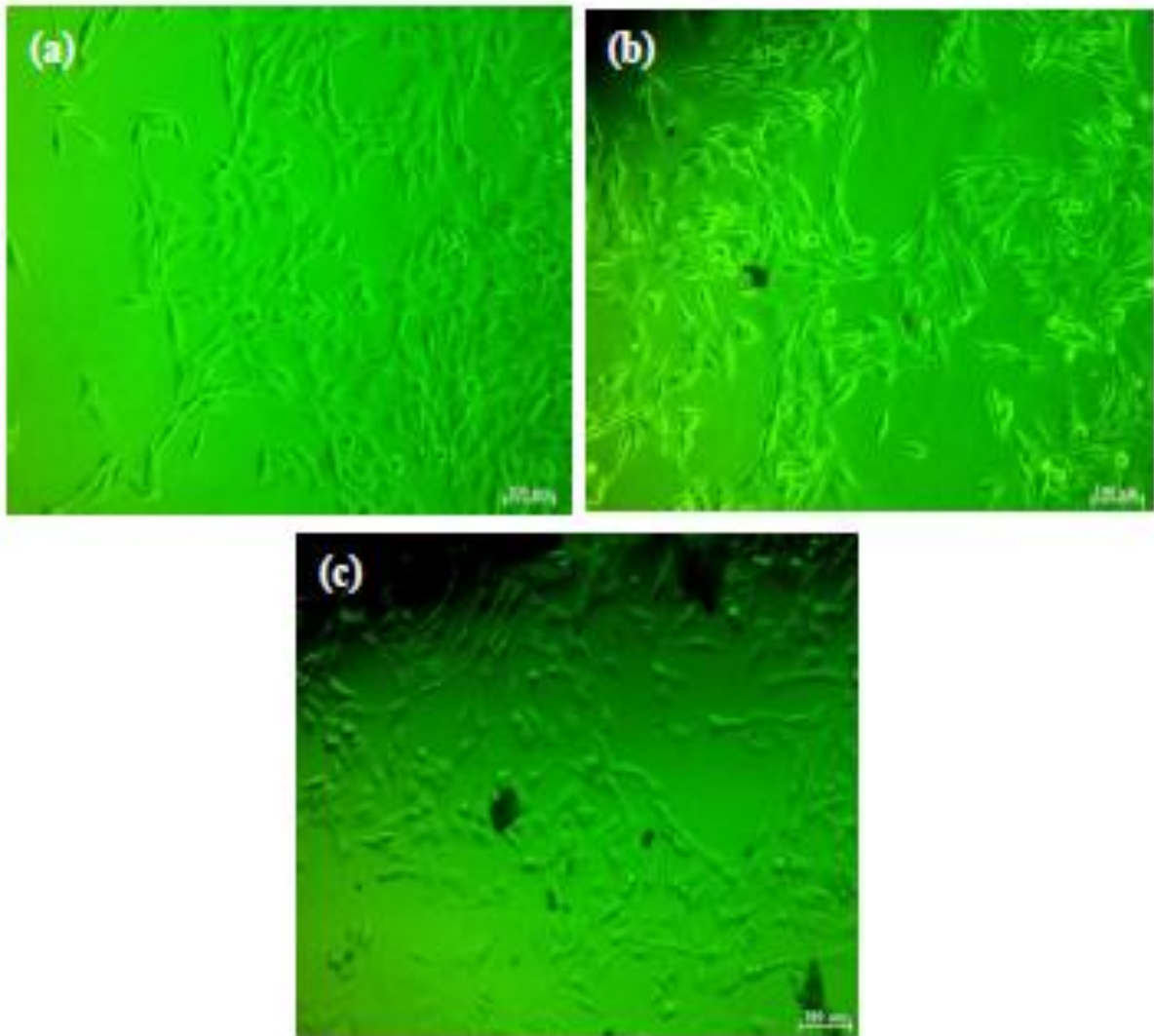


**Fig.7.14. Fluorescence microscopy images of L929 mouse osteoblasts cultured in HA scaffolds after 24h incubation in cell culture medium. (a) Control, (b) HA-25NA , (c) HA-45NA.**

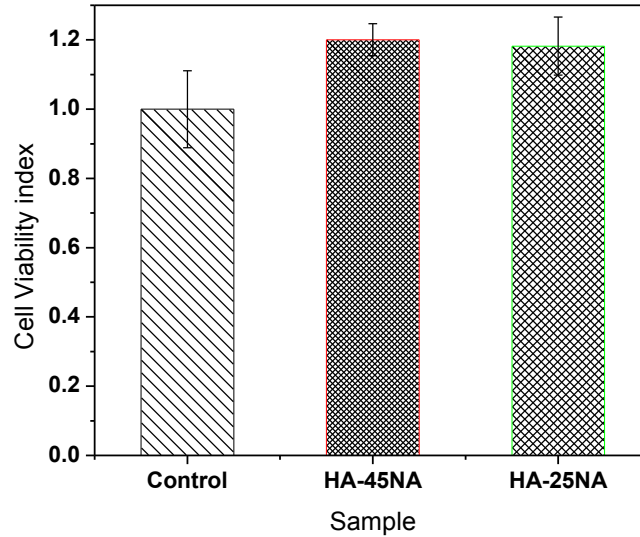


**Fig.7.15. Cell viability index of HA scaffolds. Proliferation is shown relative to the Control sample.**

### 7.11 Conclusions

The present work dealt with the processing and characterization of porous HA scaffold prepared by Gel Casting route. The porous HA scaffold was prepared by incorporation of a volatile material (NA) as the pore forming agent in gel casted samples. By modifying the solid loading, NA content, the porosity and compressive strength could be altered over a wide range. Porous HA scaffold with 60% porosity had open and interconnected pores. Compressive strength of 4.02 MPa was recorded HA-25 NA samples and the compressive strength 0.96 MPa for HA-45NA sample. The processed scaffolds had a wide pore size ranging from 10–150 $\mu$ m. These pores were also found to be interconnected in the macro porous structure. In-vitro aging indicated that apatite has formed HA surface and the deposition rate varied with sample porosity. MTT results indicate that the processed HA scaffold had appreciable biocompatibility.

## *Chapter-8*

# *Porous Hydroxyapatite by Protein Coagulation Casting*

## 8. Porous Hydroxyapatite by Protein Coagulation Casting

### 8.1 Background

Chapter - 7 discussed the processing of porous HA scaffold through gel casting route. It was observed that in pure gel cast samples, the pore sizes were in the range 50-200  $\mu\text{m}$  and the addition of NA granules helped to increase the porosity and pore size of HA. The porosity was dependent on NA content, and the highest porosity (75%) was obtained at HA-45NA addition. However, it was also observed that it was difficult to achieve a homogeneous distribution of NA particles in HA slurry, particularly, at a higher NA addition. The microstructure of the scaffold at 35 and 45 vol% NA additions show that  $\sim 400 \mu\text{m}$  pores are present in the scaffold. Since, the average size of NA granule was  $250\mu\text{m}$ , the presence of pores larger than  $250 \mu\text{m}$  indicate that probably NA particles were agglomerated during the slurry preparation and casting.

It was assumed that the gel cast samples would give the pore size within a narrow range. However, a variation in the pore size was observed. When NA was additionally added, the wide variation in the NA particle size resulted in the further widening of the pore size distribution. Therefore, to avoid the use NA particles as a pore former, scaffold were prepared by Protein Coagulation Casting Method using Egg White (EW). In this chapter, the use of Egg White Protein (without the use of additional NA), will be used for processing of porous HA scaffold. EW is a natural protein that has been used in various foods for creating foamed structure, for stabilizing beverages, etc. [8.1 -8.2]. Natural EW or its derivative (albumin) have a good binding property and can also act as a binder for aqueous slurries [8.3-8.4]. The use of albumin or different globular protein for Protein Coagulation Casting (PCC) has been reported for the first time by Tuck et. al. [8.5]. Lindsten [8.6] have patented the use of albumin for foaming of ceramics. Lyckfeldt et. al. [8.4] have reported a wide variety of macro porous ceramics that could be produced by using different Egg White (EW) and Water (H) ratio. It was also noted that by varying the Egg White: Water (EWH) ratio, the extent of foaming as well as the foam size could be manipulated. This in turn helped to modify as well as control the pore size, porosity and pore shape of the foamed product. The other factor that (for this case) was controlling the stability of the porous structure was the absence or presence of a binder. Although,

EW has its own binding property, sometimes it was necessary to use an additional binder (e.g., sucrose, PVA, agar, etc.) [8.7] for reinforcing the porous structure. The third factor that affected the structure of the porous scaffold was the stability of foams. As already mentioned in the Introduction Chapter, foam stability can be enhanced by adding long-chain surfactants [8.8] and particles [8.9]. There are reports describing the reduction in foam drainage rate on the addition of a surfactant and particles [8.10]. Finally, solid loading is the other important parameter that could control the foaming and drainage behavior. At low solid loading, the strength of the porous scaffold was very poor. Binders,  $\text{HNO}_3$  were used as a coagulating agent for faster setting to avoid these problems [8.3].

From the above discussion, it can be summarized that the EW can be used as a foaming agent for preparing porous scaffolds. The structural integrity, pore size, and shape are controlled by EWH, the addition of binder helps to achieve a stronger porous structure. Given the above, it was felt that the fabrication of a porous structure using natural EW will be advantageous on the following grounds:

- (a) A wide variety of microstructure can be produced by varying EW ratio.
- (b) Different pore structures can be produced by changing the solid loading.
- (c) The use of additional binder can help to retain highly porous structure.

In this work, NA has not been used as an additional pore former. This is due to the fact that EW serves both as a binder (for gelation) as well as a foaming agent. Since the foaming ability, and the foam size can be altered by the factors mentioned above, NA was not additionally added.

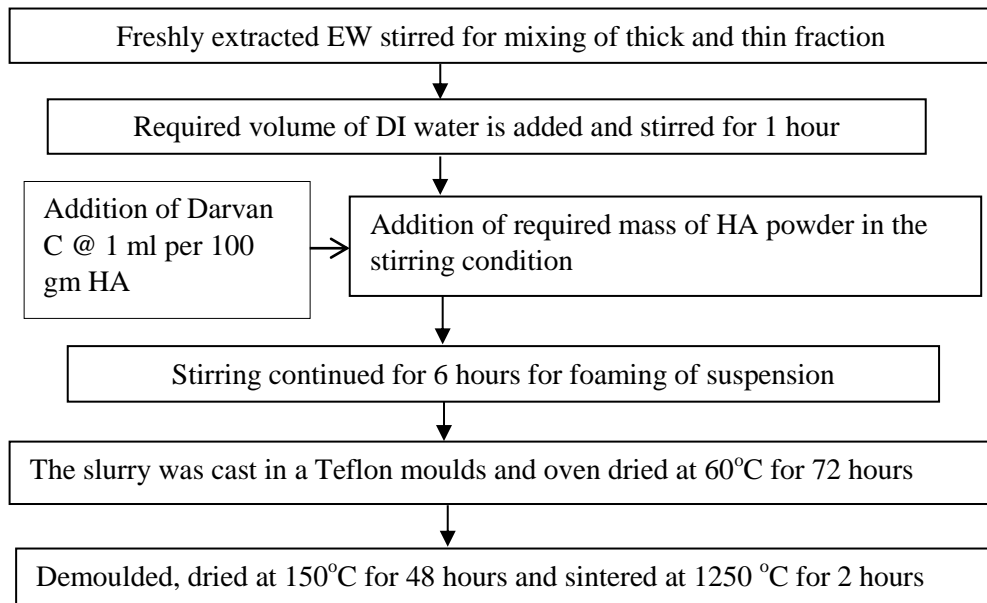
## **8.2 Raw Materials and their Processing**

Table -8.1 lists the raw material and additives required for HA slurry preparation for PCC. Fig-8.1 describes the sample preparation steps. At first, freshly extracted EW was taken in a beaker and stirred on a magnetic stirrer for 30 minutes. The stirring speed was controlled to avoid any foaming of EW. The EW extract is a mixture of a less viscous (thin) and more viscous (thick) components. The stirring was done at a speed that ensured proper mixing of these two components without any noticeable foaming.

**Table-8.1 Raw materials and their Functions**

Raw materials addition	Formulae	Source	Functions
Hydroxyapatite (HA)	$\text{Ca}_{10}(\text{PO}_4)_3(\text{OH})_2$	Prepared in the laboratory	Ceramic component
Darvan C	Ammonium polymethacrylate	RT Vanderbilt Minerals	Dispersant
Egg White (EW)	Protein	Freshly extracted egg white	Foaming agent & Binder

To the mixed EW liquid, required volume of water was added so as to make the different EWH ratio. In the present study, four different EWH ratio (viz. 1:1, 1:2, 1:3 and 1:4) were used. Corresponding to each EWH ratio, four different HA solid loading was used viz. 15, 25, 30 and 35 vol%. Darvan C (as a dispersant) was used in the ratio one mL Darvan C per 100 gm powder. Required mass of HA powder was added, and the slurry was stirred for 6 hours for foaming of suspension.



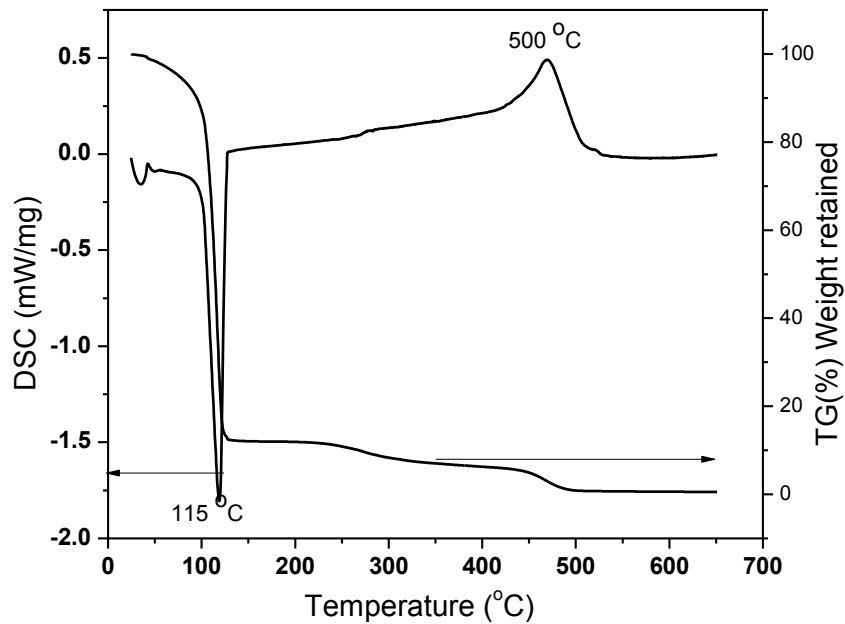
**Fig. 8.1. Processing of porous HA using Protein Coagulation Casting (PCC) method.**



## 8.3 Results and Discussion

### 8.3.1 Thermal Decomposition Behavior of EW:

EW is used in the slurry both as a foaming agent as well as a binder. The structural integrity of the sintered body depended on the smooth and complete removal of EW during firing, and, therefore it was necessary to study the decomposition behavior of EW on heating. Fig. 8.2 shows the DSC-TG plot of pure EW when heated at 1°C/min. The Figure shows that nearly 90% of the weight loss takes place at 115°C implying water is the major constituent of EW. The remaining 10 % weight loss takes place in two stages. The first stage occurs between 250- 350 °C and the second stage happens between 400- 550 °C. The second stage of weight loss is also associated with an exothermic peak at 500 °C. This exothermic peak is related to the decomposition of proteins, vitamins and glucose. Finally, all the combustibles are removed by 550°C.



### 8.2 DSC-TG plot of pure EW

### 8.3.2 Foaming Behavior and the Foam stability

The foaming behavior of pure EW as well as different EWH compositions was studied (Table- 8.2). The foaming behavior was studied without any HA powder addition. Normally, powder addition to the slurry increases the foam stability [8.3]. So, the results of this experiment are expected to improve when the actual powder is added to make a

slurry. The EW, as well as EWH mixtures, were stirred for 3 hours on a magnetic stirrer, and the measurement of the foam height provided the information on the foaming behavior. No significant change in the foam height could be observed after 3 hours stirring. The foam stability was assessed by measuring the liquid drainage rate after the foaming operation was stopped. It was observed that foam height of pure EW was only 1.2 times of the liquid height. The liquid drainage rate was 243  $\mu\text{L}/\text{min}$ , 340  $\mu\text{L}/\text{min}$  and 453  $\mu\text{L}/\text{min}$  for 1:1, 1:2, 1:3 EWH ratio respectively. Table-8.2 also shows that at any EWH ratio, the minimum solid loading that could be cast without crack or defects nearly ten times the foam height.

**Table- 8.2 Foaming behaviour of pure EW as well as different EWH compositions.**

EWH Ratio	Foam Height	Liquid draining rate ( $\mu\text{L}/\text{min}$ )	Minimum solid loading of the cast that could be made crack free
1:1	3.5	243	35
1:2	2.8	340	29
1:3	2.5	453	25
1:4	Negligible		All Solid Loading

### 8.3.3 Properties of dried and sintered Cast bodies

Table 8.3 shows the appearance of the dried bodies made from different EWH ratio and the different solid loading. It is seen from the Table-8.3 that only 35 vol% solid loading samples could be prepared at all EWH ratio. Samples with a lower solid loading cracked either while drying (15 vol% and 25 vol%) or during sintering (30 vol%). Table-8.3 also reveals that with the decrease in EWH ratio, samples with progressively lower solid loading could be made without a crack or defect. Thus, 1:4 EWH ratio was suitable for 15, 25 and 30 and 35 vol% solid loading. 1:3 ratio was acceptable for 25 and 30 and 35 vol% solid loading. 1:2 EWH ratio was fine for for 30 and 35 vol% solid loading and 1:1 EWH ratio was suitable for 35 vol% .The cracking of the samples during drying is related to foam stability and foam drainage during the long drying time. In the following

paragraphs, the effect of these factors has been discussed systematically with reference to the samples prepared in this study.

It has been discussed in the Introduction Chapter that the unstable foams rise upwards leaving the liquid behind. In a cast body, this causes a liquid gradient along the sample thickness. The non-uniform liquid content results in the differential drying shrinkage and hence cracking [8.3]. It has also been discussed that presence of an additive and particle in the slurry can alter the free energy of solid-liquid interface to make stable foam [8.6]. In view of the above, the effect of EWH ratio and solid loading on the foaming behavior and differential drying behavior will be studied.

According to Table-8.3, the extent of foaming decreases with the decrease in EWH ratio from 1:1 to 1:4. Thus, in 1:1 EWH ratio, a higher solid loading (35vol %) was required to stabilize and retain the high volume foam in the cast body. Since, a higher solid loading prevented liquid drainage, 35 vol% samples did not crack. Thus, the results show that for a specific EWH ratio, the solid loading and may be the binder amount need to be optimized. The addition of a binder can significantly reduce the drainage rate and thus the cracking tendency is expected to reduce. This point has been discussed in a later section.

The other factor that can affect the cracking of samples is the drying temperature. Since the lower solid loading samples had higher liquid content, so a lower drying temperature (40-45°C) was chosen to reduce the thermal gradient stress during drying. Some of the samples were also dried under water bath. It was observed that both the combinations resulted in cracked samples. The cracking was because of slower drying rate that caused liquid drainage and differential drying. The setting and hardening of cast samples is due to gelation of EW protein that takes place around 70 - 80°C [8.4]. A separate study has also been carried out to investigate the temperature at which the EW gels. The viscosity of the pure EW was studied as a function of temperature from 40°C to 70°C. It can be seen from Fig 8.3 that the viscosity of the EW does not change till about 60°C. Beyond 60°C, the viscosity rapidly increases and the color of the EW also slowly changes to white. The maximum viscosity is recorded at 68°C. This result matches well with Garnn [8.11] who reported the EW denaturation temperature around 66°C.

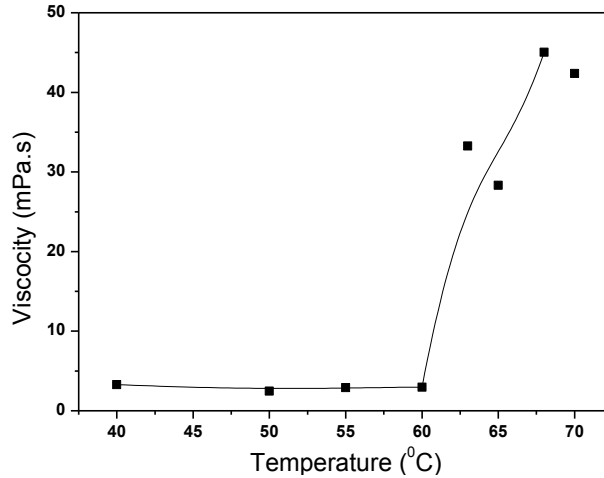


**Fig. 8.3 Viscosity of the pure egg white with temperature**

Thus, ideally the EW containing should be dried close to 70°C to fast setting of the cast and to prevent draining of the foam.

Therefore, either the drying temperature should be at least 70 °C or liquid need to be removed at a lower temperature before raising the temperature of gelation of EW protein. In the present study, when the drying temperature was increased to 75°C, the cracking tendency reduced, although it was not eliminated. However, a higher drying temperature resulted in EW migration to the surface. Following Dhara and Bhargava [8.3], these problems of EW migration was solved by adding concentrated HNO<sub>3</sub> to the slurry just before casting. The addition of concentrated HNO<sub>3</sub> increased the slurry viscosity due to the coagulation of the EW protein and decreased the drying time, drying shrinkage as well as the migration of EW. Without HNO<sub>3</sub> addition, the top surface had a shiny brown layer, and it reduced with HNO<sub>3</sub> addition. However, some of these HNO<sub>3</sub> added sintered samples had cracks on the bottom surface. This cracking was also due to the constrained shrinkage of the samples during drying. The bottom part that was resting on the petridish was restrained from shrinkage during drying and firing due to frictional forces. This resulted in non-uniform drying between the top and bottom surface and caused cracks at the bottom. A similar phenomenon of constrained shrinkage happened during sintering also.

**Table-8.3 Defects in the as dried bodies made from different EWH ratio and different solid loading**

<b>EWH Ratio</b>	<b>Solid Loading</b>	<b>Observations</b>
1:1	15	cracked during drying
	25	cracked during drying
	30	cracked after sintering
	35	formed
1:2	15	cracked during drying
	25	Formed with cracks after sintering
	30	formed
	35	formed
1:3	15	cracked after sintering
	25	formed
	30	formed
	35	formed
1:4	15	formed
	25	formed
	30	formed
	35	formed

**8.3.4 Bulk Density, Apparent Porosity and Compressive strength of the Scaffolds**

Table 8.4 shows the bulk density, apparent porosity and compressive strength of porous HA scaffold prepared by PCC method. The density and porosity of samples at a lower

solid loading (15 and 25vol %) could not be measured for 1:1 and 1:2 EWH ratio due to its extreme fragile nature.

Table-8.4 also shows that for a fixed EWH ratio 1:4, the porosity of the samples decreases with the increase in solid loading. Accordingly, the compressive strength increases from 0.62 MPa to 3.6 MPa. For highly porous samples, (Porosity > 80.15) strength measurements could not be performed due to its extreme fragile nature.

**Table-8.4 Apparent Porosity, Bulk Density (BD), Closed Porosity and CCS of porous scaffolds**

<b>EWH Ratio</b>	<b>Solid Loading (Vol %)</b>	<b>BD (gm/cc)</b>	<b>Open porosity (%)</b>	<b>Closed porosity (%)</b>	<b>Strength (MPa)</b>
1:1	15	cracked during drying			
	25	cracked during drying			
	30	cracked after sintering			
	35	1.02	65.12	2.68	1.80
1:2	15	cracked during drying			
	25	Formed with cracks after sintering			
	30	0.85	70.12	3.08	0.94
	35	1.05	60.40	6.6	1.94
1:3	15	cracked after sintering			
	25	0.65	79.39	0.20	0.85
	30	1.04	64.28	2.72	1.87
	35	1.06	52.48	13.97	2.98
1:4	15	0.63	80.15	0.10	0.63
	25	0.90	68.92	2.58	1.62
	30	1.07	55.62	10.38	2.74
	35	1.10	42.07	22.93	3.59

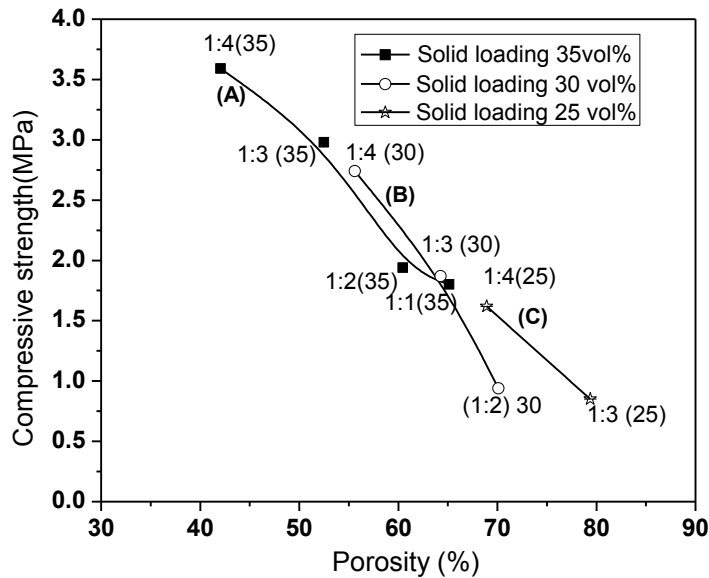


**Fig. 8.4 Effect of porosity on compressive strength for different solid loading**

Fig. 8.4 shows the variation of compressive strength against sample porosity. It may be noted that a simple plot of compressive strength vs. sample porosity is difficult for this case. The sample porosity is affected by EWH ratio, solid loading as well as due to the combined effect of solid loading and EWH ratio. For example, samples prepared from 1:1 EWH and 35 vol% solid loading will have near identical porosity with the samples prepared from 1:3 EWH ratio and 30 vol% solid loading. Thus, to study the effect of porosity on the compressive strength, the solid loading have fixed the porosity has been varied by varying EWH ratio. Fig.8.4 shows the compressive strength variation for such a combination. In Fig. 8.4, curve A represents the compressive strength variation for different EWH ratio at 35 vol% solid loading. Similarly, curve B represents the compressive strength for 30 vol% solid loading and curve C represents the strength for 20 vol% solid loading samples. For 15 vol% solid loading, only one sample (EWH ratio 1:4) could be tested, and the strength value was 0.62 MPa.

Figure 8.4 shows that for any fixed solid loading, the compressive strength decreases with higher EWH ratio. For example, 30% solid loading samples prepared from 1:2 EWH ratio have lower strength with respect to the samples prepared from 1:4 EWH ratio. Apparently, a lower EWH ratio implies lower foaming capacity of EWH. Thus, samples with lower EWH ratio are expected less porous or with isolated pores or smaller pore size. All these factors are expected to increase the strength. However, microstructural

analysis of some selected compositions (among those plotted in Fig 8.4) has been carried out to understand this effect better. Fig. 8.5 (a), (b) and (c) show respectively the microstructure of 35 vol% solid loading samples prepared from 1:4 and 1:3 and 1:1 EWH ratio. The images indicate that a higher porosity, large pore size samples are prepared from 1:1 EWH ratio (Fig. 8.5 (c)). The large pore size and higher porosity sample obtained from 1:1 EWH have caused a lowering of strength. The microstructures of 30 vol% solid loaded samples with two different EWH (1:4 and 1:3) are shown in Fig 8.6 (a) and (b) respectively. Here also, it is seen that 1:3 EWH ratio samples are more porous than the samples prepared from 1:4 EWH ratio. Thus, 30 vol% solid loading samples prepared from 1:3 EWH ratio has lower strength. Similar observation can also be drawn from 25% solid loading sample prepared from 1:4 and 1:3 EWH ratio. (Fig 8.7 (a) and (b)). Samples prepared from 25% solid loading and 1:4 EWH ratio shows a dense structure with small pore size (maximum pore size around 10  $\mu\text{m}$ ). On the other hand, the samples prepared from 1:3 EWH ratio show larger pores ( $> 50 \mu\text{m}$ ) and very porous structure. Thus, even when prepared with the same solid (25%) loading, 1:3 EWH scaffolds have lower strength as compared to the scaffold prepared for 1:4 EWH.

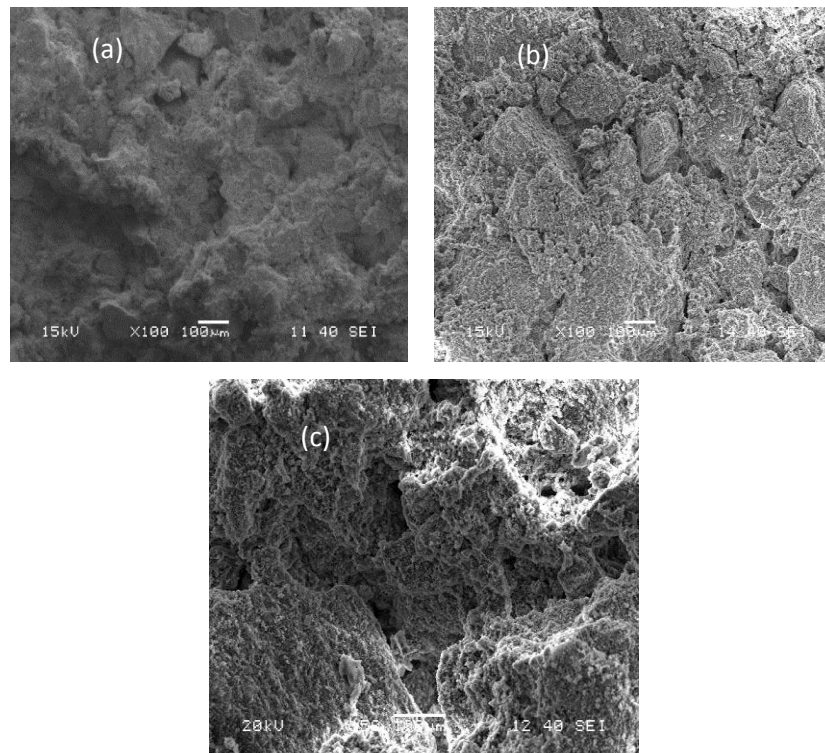


**Fig 8.5 Microstructure of 35% solid loading samples prepared from different EWH ratio, (a) EWH 1:4, (b) EWH 1:3, (c) EWH 1:1**



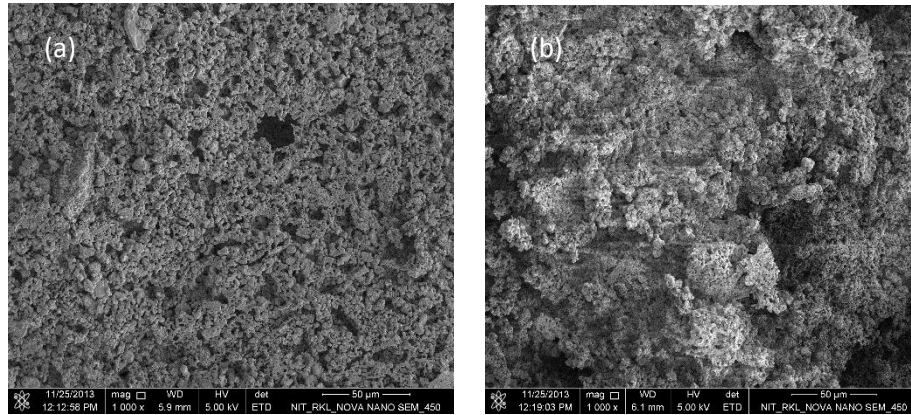


**Fig 8.6 Microstructure of 30% solid loading samples prepared from different EWH ratio, (a) EWH 1:4, (b) EWH 1:3**

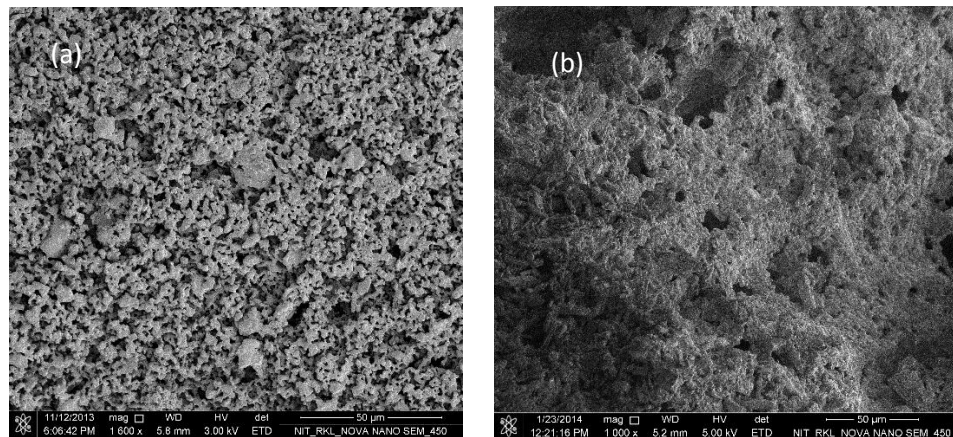


**Fig. 8.7 Microstructure of 25% solid loading samples prepared from different EWH ratio, (a) EWH 1:4, (b) EWH 1:3**

### 8.3.5 Pore size distribution

Fig 8.8 shows the mercury porosimeter results for HA scaffolds prepared from varying EWH ratio and different solid loading. As has been mentioned in the preceding chapters, the porosimeter data provides information on those pores that require a pressure of 0.951 psi or higher for penetration. Thus, the maximum pore size that can be detected by this method is limited to 224  $\mu\text{m}$ . However, even with this instrumental limitation, the pore

size distribution data show that pore size is dependent on EWH ratio as well as solid loading.

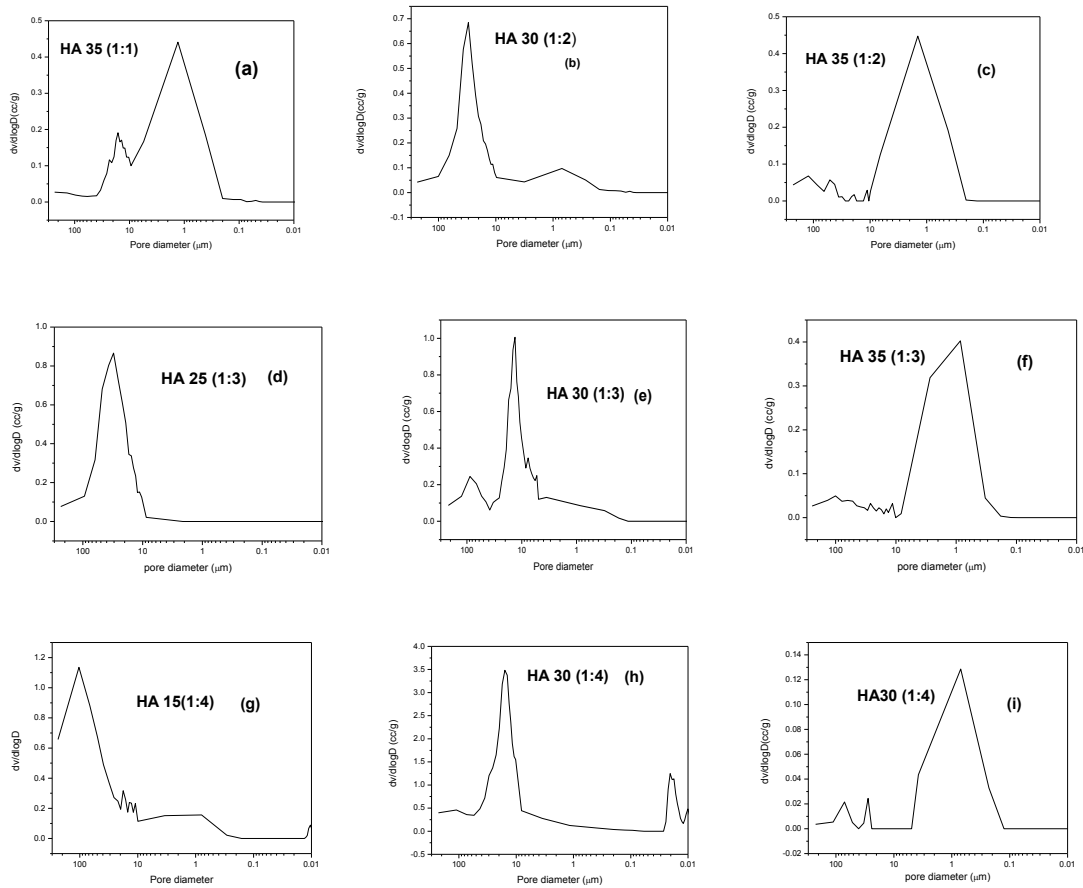


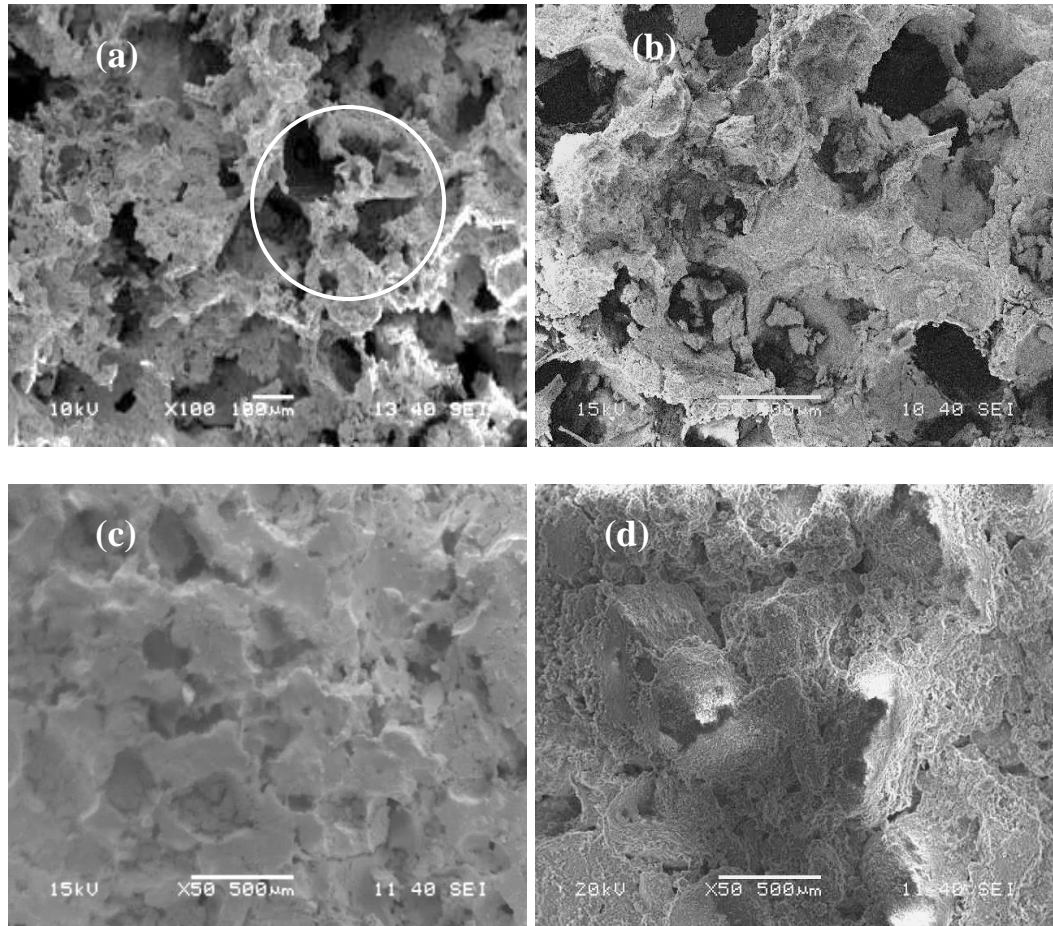
**Fig. 8.8 Pore size distribution for HA scaffolds prepared from varying EWH ratio and different solid loading.**

The porosimeter data has been organized to show the both the effect of varying EWH ratio as well as different solid loading. It has already been mentioned that with 1:1 EWH ratio only 35% solid loading samples could be prepared. Accordingly, Fig. 8.8 (a) shows the porosimetry data of 35% solid loading samples prepared from 1:1 EWH ratio. It is seen that the majority of the pores lie in the 1-10 $\mu$ m. The smaller pore sizes are due to higher solid loading and highly viscous slurry which slow down foaming and bubble formation [Ref]. Fig. 8.8(b) and (c) show the porosimetry data for scaffolds prepared from 1:2 EWH ratio. The data reveals that an increase in solid loading shifts the maximum pore size from 50 $\mu$ m to 1 $\mu$ m. The decrease in the pore size is related to the lower foam ability at higher solid loading. Similarly Fig.8.8 (d-f) show the pore size

distribution of scaffolds prepared from 1:3 EWH and different solid loading (25, 30 and 35%). The Figures show that the trend in the pore size are inversely related to solid loading as mentioned above. Thus, while 25% solid loading scaffolds shows maximum pore population between 50-75 $\mu\text{m}$ , 35% solid loaded scaffolds have a lower pore size of 1-5 $\mu\text{m}$ . Finally, Fig.8.8 (g-i) show the pore size variation of scaffolds prepared from three different solid loading at a constant (1:4) EWH ratio. The graphs show that with the increase in solid loading (15-30vol%) the pore size decreases from >100 $\mu\text{m}$  to 1 $\mu\text{m}$ . A closer observation of the porosimetry plots also indicate that at a constant solid loading (say 30%), changing the EWH ratio from 1:2 to 1:4, also shifts the pores to lower sizes. This can be correlated with the reduced foam ability of EWH at lower EWH ratio. Thus, for achieving a crack free scaffolds with the desired pore size and porosity level, proper combination of solid loading and EWH ratio need to be worked out.

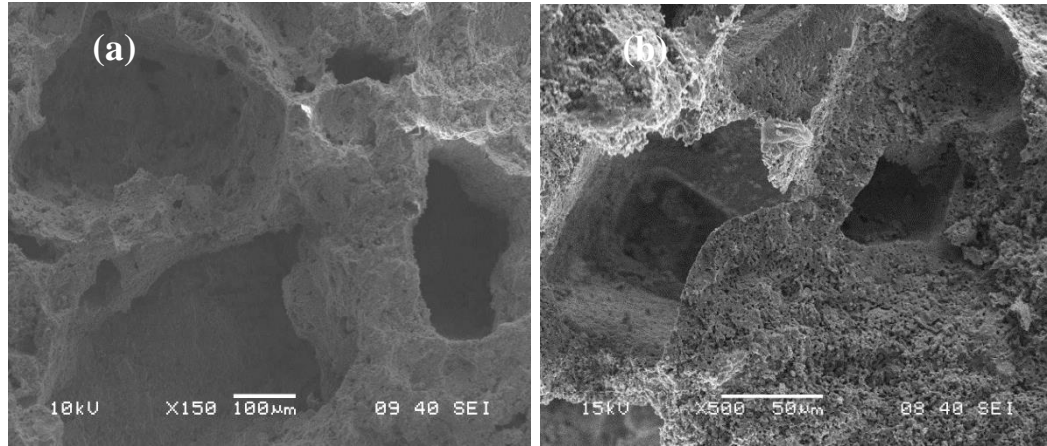
### **8.3.6 Microstructural characterization of HA scaffold in PCC method**

Fig. 8.9 (a-d) show the microstructure of sintered HA scaffold show the microstructure of sintered scaffold prepared with 15 vol% solid loading with 1:1 EWH ratio. The microstructure shows that the sample has high porosity and interconnected pores. The sample was very fragile, and some part was damaged during handling. The encircled area in the Fig. 8.9 (a) shows the microstructure with a damaged strut that was probably damaged during handled. Large pores (250-500  $\mu\text{m}$ ) could be observed. Fig. 8.9 (b) showed the microstructure of HA scaffolds with 25 vol% solid loading and prepared from 1:1 EWH ratio. The pore size is essentially of similar size to that of 8.10 (a) but the interconnectivity is less as compared to 15 vol% samples. At still higher solid loading (30 & 35 vol %), the pore size becomes smaller, more isolated as well as less inter connected. The pores were gradually turning into isolated open pores [Fig 8.9 (c) and 8.9 (d)].



**Fig. 8.9 Microstructure of porous HA prepared with EWH ratio 1: 1 and varying solid loading (a) 15 vol% (b) 25 vol% (c) 30 vol % and (d) 35 vol%**

25vol% samples prepared with 1:2 EWH ratio had 100-250  $\mu\text{m}$  pore size, but the struts are thicker and less porous (Fig. 8.10(a)). At 30 vol% and EWH ratio 1:2, most of the pores were isolated, and pore sizes were between 150-200  $\mu\text{m}$  [Fig. 8.10 (b)]. The reason for lower pore size and lesser interconnectivity is due to the lower EWH ratio. As the water fraction increases, the foaming ability of EWH decreases. So, the foam volume decreases. However, due to relatively higher solid loading, the foams are stabilized but it could produce mostly isolated pores.



**Fig.8.10. a and b Microstructure of Porous Hydroxyapatite prepared with EWH ratio 1:2 (a) 25 vol% Solid loading (b) 30 vol% Solid loading**

Samples prepared from EWH ratio 1:3 were less porous, and pore sizes were also smaller  
Fig. 8.11

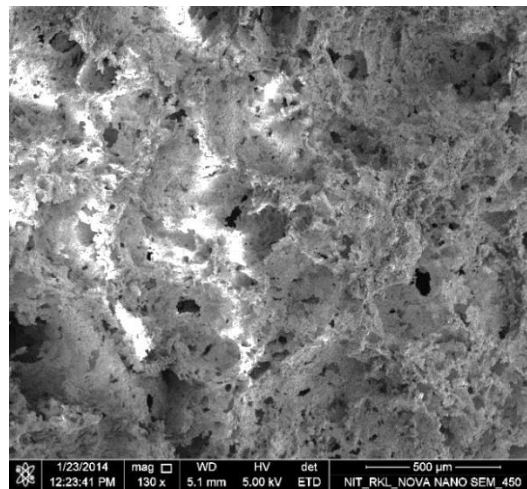


**Fig. 8.11 Microstructure of Porous HA at 25 vol% Solid loading at EWH ratio 1:3**

### 8.3.7 In-vitro bioactivity

#### 8.3.7.1 Effect of aging days on apatite layer formation

Fig. 8.12 (a)- (e) shows the effect of aging period on the SEM microstructure of the SBF aged porous scaffold (30 vol% solid loading, prepared from EWH (1:3). Figure.8.12 (a) to 8.12 (e) represents the microstructure after 3, 14, 17,21 and 28 days respectively.

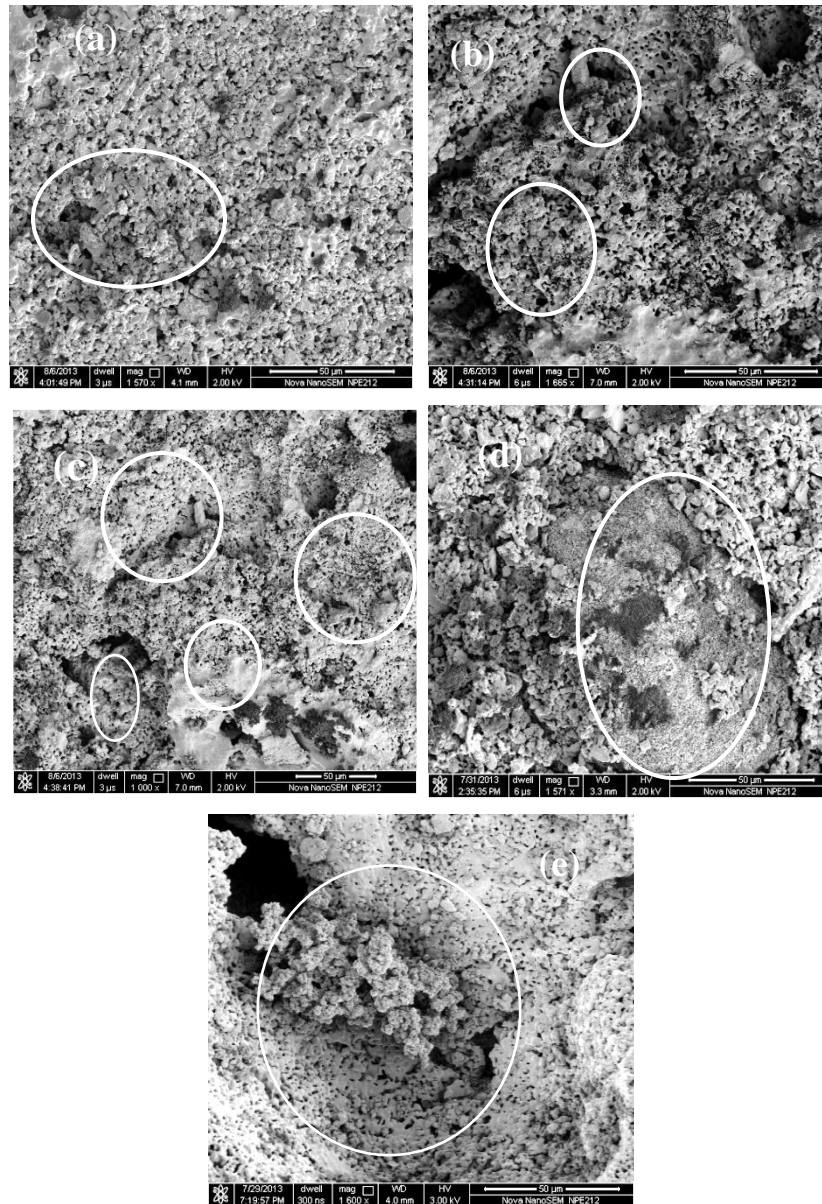


**Fig.8.12. Effect of aging time on the apatite layer formation of porous HA Scaffold prepared from 1:3 EWH and 30 vol% Solid loading. Fig (a-e) represents 3, 14, 17, 21 and 28 aging days respectively.**

After three days, a few granular precipitates are observed (Fig-a, encircled area). The precipitate size increase as also the area covered by the precipitate becomes more after 14 days of aging. The encircled area is more in number after 14 days. After 17 days, a large fraction of the surface is formed to be covered by apatite [Fig 8.12 (c)].

Finally, after 21 and 28 days a wide cluster of apatite has been observed (Fig (d) and (e)). Thus, it is observed that for any composition, the apatite growth increases with the increase in the aging period. It is further observed that the particle or granular like the precipitate change to flower like appearance after 21 days and after 28 days some elongated particles are also seen.

### 8.3.7.2 In-vitro bioactivity and the formation of apatite layer

Fig. 8.13 shows the microstructure of SBF aged HA samples with different solid loading made from EWH ratio 1:3 and aged for 21 days.

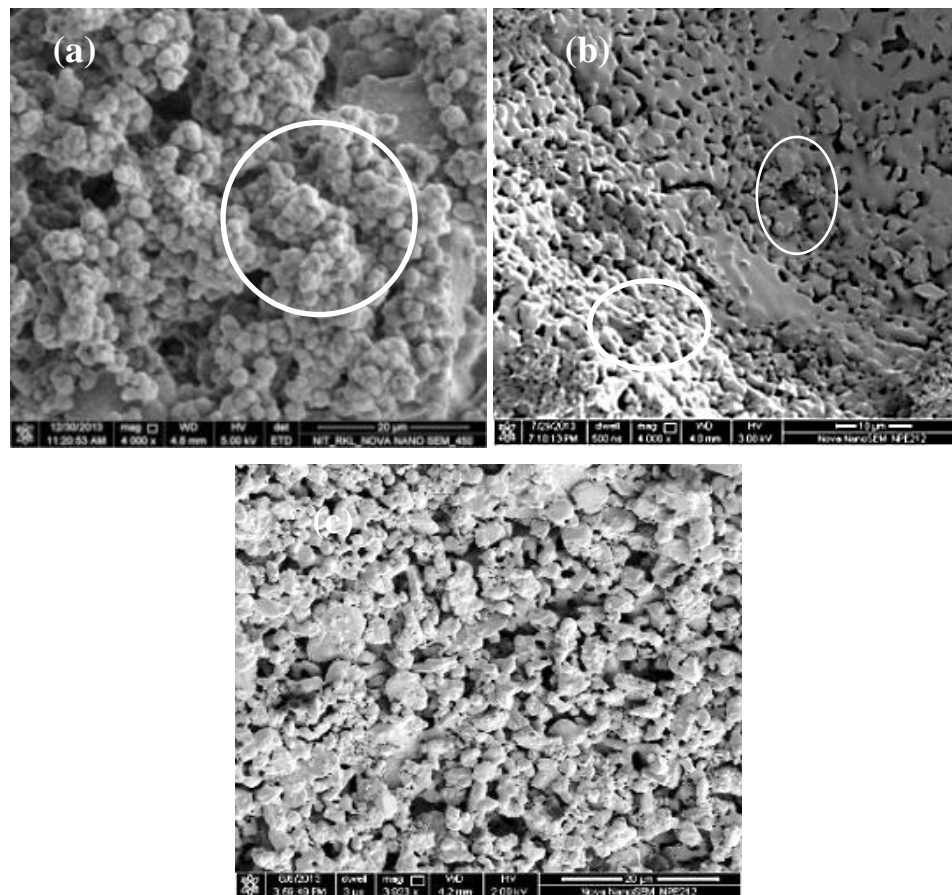


**Fig.8.13. FESEM images of EWH scaffolds after 21 days aging in SBF (a) 25 vol%, (b) 30 vol%, (c) 35 vol%**

The microstructure reveals the effect of solid loading on apatite growth. The apatite growth was highest for scaffolds prepared from 25 vol% solid loading (Fig 8.13.a) and lowest for 35 vol% solid loading samples [Fig8.13 (c)].With an increase in the solid

loading, both the porosity and pore size decreases (Table -8.4), and this results in a slower rate of apatite growth on higher solid loading samples.

### 8.3.7.3. Dissolution Behaviour of Porous HA in SBF

Fig. 8.14 shows the weight loss of the scaffolds as a function of immersion time. It is observed that the weight loss of all the scaffolds increased with the aging time. The weight loss was higher for lower solid loading samples. The maximum weight loss was observed for 15% solid loading sample. The weight loss increased rapidly till 21-28 days and then gradually decreased. The mechanism is discussed in Section 6.5.2

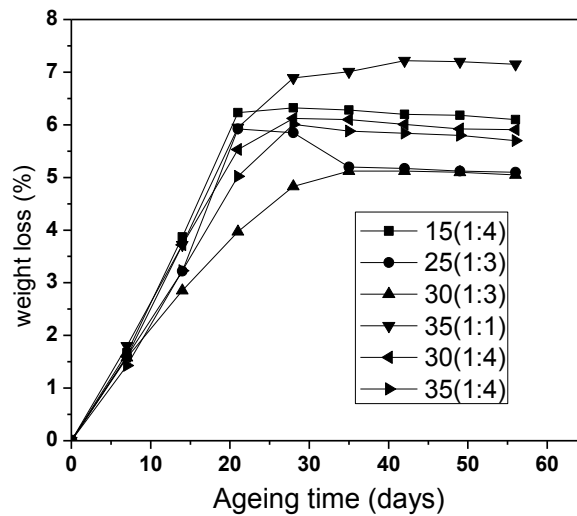
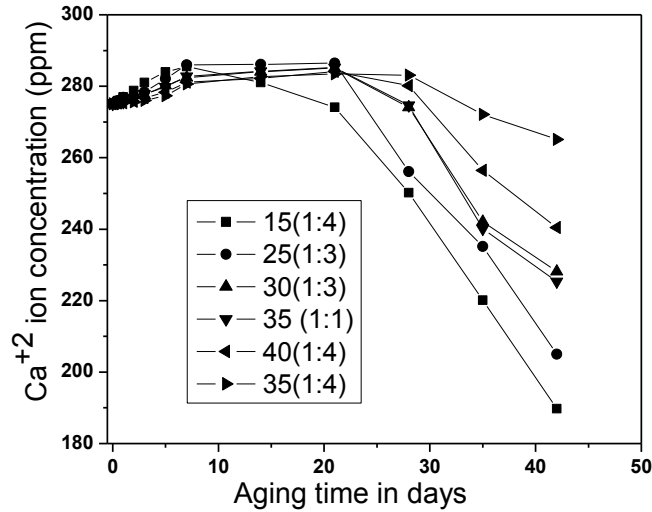


Fig. 8.14. Weight loss behavior of porous HA on SBF aging for different time

### 8.3.7.4. Changes in $\text{Ca}^{+2}$ and $\text{P}^{+5}$ ion concentration

The dissolution behaviour of HA was measured by estimating the  $\text{Ca}^{+2}$  concentration in SBF solution. The variation of  $\text{Ca}^{+2}$  concentration of SBF solution against dissolution time with different solid loading has been plotted in Fig.8.15. It is seen that the  $\text{Ca}^{+2}$  concentration in SBF increases slowly (276 ppm to 285 ppm) during the initial aging period. The time period for constant  $\text{Ca}^{+2}$  concentration was dependent on the solid loading as well as EWH ratio. A higher solid loading as well as a lower EWH ratio prolonged the constancy period. Subsequently, the concentration of  $\text{Ca}^{+2}$  decrease. The increase of  $\text{Ca}^{+2}$  concentration in the SBF solution was due to the dissolution of HA at pH 7.4 and the decrease in concentration coincided with the apatite layer formation. The apatite formation mechanism follows the theory discussed in Chapter 6 (6.5.7).





**Fig. 8.15 Change of Ca<sup>+2</sup> concentration of SBF after ageing of HA for different times**

On the other hand P<sup>+5</sup> concentration changes 145 ppm to 187 ppm within the first three days and after that the concentration of P<sup>+5</sup> decreases with increases in aging time (Fig. 7.16). The change in the Ca<sup>+2</sup> and P<sup>+5</sup> concentrations correspond to the formation of firstly an amorphous Ca-P compound and on further aging the amorphous compound changes to crystalline apatite.

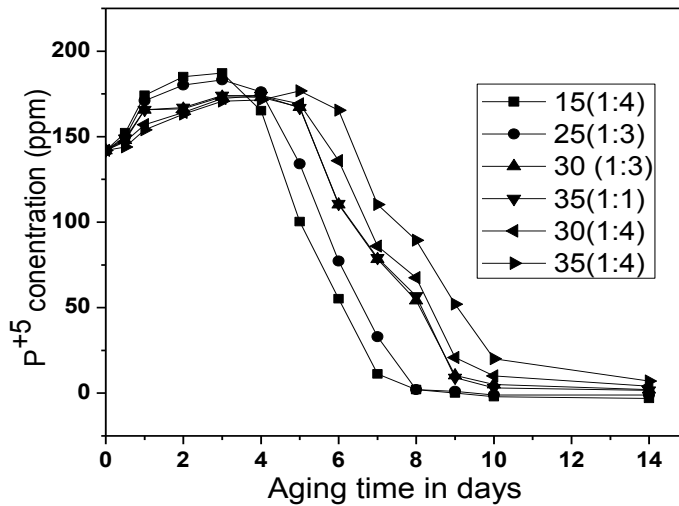


**Fig. 8.16 Change of P<sup>+5</sup> concentration of SBF after aging of HA for different times**

### 8.3.7. 5 Effect of SBF aging of HA Scaffold on the pH of SBF

Fig.8.17 shows the effect of SBF aging time on the pH of SBF. The pH of SBF increased rapidly during the initial period (till seven days). The increase in pH can be correlated with the dissolution of HA in SBF and after that it remained constant till 8-12 day, subsequently the pH started to decrease at longer aging time. The dissolution of HA resulted in an increase of  $\text{Ca}^{+2}$  concentration of SBF thereby increasing the solution pH. After that, the pH decreases due to the nucleation of apatite. The nucleation of apatite depletes the SBF of  $\text{Ca}^{+2}$ , thereby reducing the pH. It has been reported that the formation of apatite layer is the consequence of dissolution –precipitation reaction [8.12]. However, an incubation period often separates the dissolution and precipitation. The constant pH appears to be due to the incubation period. The time duration of the incubation period is shorter for higher porosity scaffolds.

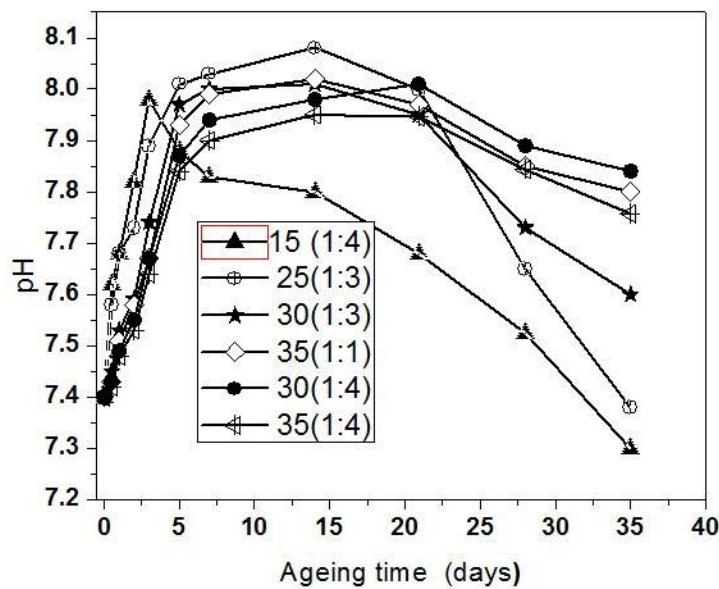


**Fig. 8.17 Effect of SBF aging of HA on pH of SBF solution**

### 8.3.7. 6. Cytotoxicity Behaviour / MTT Test

The cytotoxicity/cell viability of the hydroxyapatite scaffolds was assessed by the cytotoxicity test (Fig. 8.18 & 8.19). The cell viability and cell proliferation activity was studied through MTT [3(4, 5-dimethylthiazol-2yl)-2-5diphenyltetrazolium bromide] (SIGMA, USA) assay. L929 mouse osteoblast was used and after 24 hours incubation period (at 37 °C in 5% CO<sub>2</sub>) the cell viability was observed. For cell viability

measurement, the sterile scaffold along with the control was placed in a UV sterilized 96 well plates (Nunc, Germany). 200  $\mu$ l DMEM (Dulbecco's Modified Eagle medium) with cell concentration of  $10^4$  MG – 63 cells per well was added. The result reveals that the cells were able to grow and proliferate quite quickly. Such observations show that the prepared scaffold has acceptable level of cell viability. Only two samples (HA-25vol% and (HA-30vol%) were tested and any further detail investigation was not done. However, the preliminary study indicate that the cell viability of the scaffold depend on porosity of scaffold. Higher porosity sample (79%) showed higher cell viability than less porous sample. The flurorescence microscopy of the above samples also show that in comparision to the control sample, the cell proliferation ratio in the two porous scaffold is higher. This means that the cell have found the scaffold friendly for proliferation and attachment. However, detail and systematic study on the cell viability was not carried out. This will be a subject of future study.

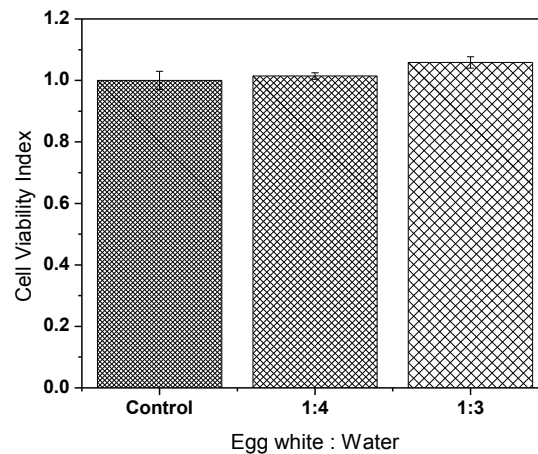


**Fig.8.18 Cell viability index of two HA scaffold samples prepared from different EWH ratio at two different solid loading (25 and 30 vol %). The cell proliferation is shown relative to the control sample.**

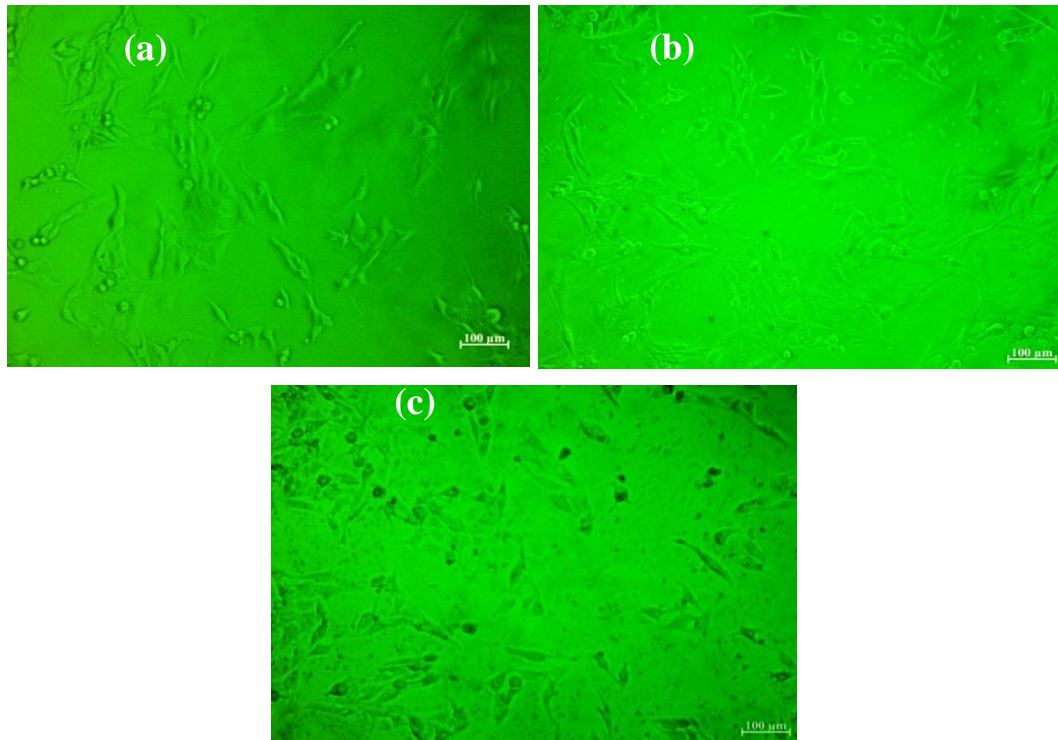


**Fig. 8.19 (Scale bar, 100  $\mu\text{m}$ ) Fluorescence microscopy images of mouse osteoblasts cultured in HA scaffolds after 24 h incubation in cell culture medium. (a) Control, (b) 25 vol% (1:3) [b], (c) 30 vol% (1:4)**

The Fluorescence microscopy image (Fig 8.19) also shows that the cell proliferation is relatively more in 25 vol% samples as compared to 30 vol% samples.

#### **8.4 Conclusions**

The PCC method could produce porous HA with a wide porosity range (40-80%) and reasonable compressive strength (Maximum strength  $\sim 3.59$  MPa). The samples with both micro porosity ( $<10$   $\mu\text{m}$ ) and macro porosity (10-200  $\mu\text{m}$ ) and sometimes with pore size as large as  $\sim 500$   $\mu\text{m}$  (for low solid loading) could be fabricated by this method. Non-uniform shrinkage resulted in cracking and breaking of samples during drying and sintering particularly those prepared from a low solid loading. The results of the present study show that the reported porosity and interconnectivity (qualitative estimation) is lower as compared to the reported value. Samples with lower solid loading could not be prepared from low EWH ratio. The difference in the result can be attributed to the difference in the slurry making method adopted by Dhara et.al. [8.3] vis-à-vis the method obtained for this study. In contrast to Dhara et. al. who used tumbling method for

foaming of the slurry, in the present study, the slurry was prepared by stirring on a magnetic stirrer. In the tumbling method, due to the lesser agitation, the foams could remain attached to the particles. Therefore, high porosity samples could be prepared even with higher solid loading. However, in the present study, the intensive stirring was although producing foams but the same stirring action was preventing foam attachment to the particles. Thus, the non-attached foams could segregate, migrate leading to the collapse of the foam. The higher drainage rate resulted in less interconnected and smaller pores in the sintered samples. Bhattacharyya et.al also made a similar observation [8.13], while working on a different foaming system. Sarangi et. al. [8.14] while working on a different porous ceramic system, observed that tumbling method resulted in uniformly pore size samples with a high degree of interconnectivity. On the other hand, the stirring method produced larger pores, pore segregation, and defects.

*Chapter-9*

*Conclusions and Scope of*

*Future Work*

## 9. Conclusions

The present study focused on the fabrication of porous HA scaffold by three different methods and the study of porosity, strength, microstructure and in vitro aging behaviour. Following are the major findings of this study:

Phase pure HA were prepared from  $\text{Ca}(\text{NO}_3)_2 \cdot 4\text{H}_2\text{O}$  and  $(\text{NH}_4)_2\text{HPO}_4$  by wet precipitation route. The calcined powder (850 °C) had a fine particle size of 0.5-1 $\mu\text{m}$ . During calcination, crystallization of HA took place and well crystallized HA formed at 850 °C. The calcined powders were agglomerated. The primary particles were a mixture of spherical and elongated particles. Since, the precipitation was carried out at 10.5 pH, some of the initially formed spherical particles grew to elongated size. The purity of HA phase was retained up to 1250°C. The highest strength of sintered HA was ~ 14.3 MPa. Above 1250 °C, HA partially decomposed to  $\beta$ -TCP and CaO. The microstructure of HA sintered at 1300°C showed large grains with intragranular porosity indicating decomposition of HA. The intragranular porosity resulted due to decomposition of HA to TCP, CaO and water vapour. The grain size of HA was 2-5  $\mu\text{m}$  at 1250 °C and 5-10  $\mu\text{m}$  at 1300 °C. The result showed that the sintering schedule is a crucial factor that influences shrinkage, densification and microstructure of the HA ceramics.

Porous HA scaffold were fabricated by solid state route using NA granules as the pore former. The results showed that at lower NA addition (30 and 40 vol% NA), the samples appear to be relatively dense and with lesser interconnections. The structure opens up with 50 and 60 vol% NA addition producing a porous and interconnected microstructure. At 70 vol% NA addition (HA-70NA), the microstructure appears to be more of a flaky nature, highly porous with large pore size. The compressive strength decreases with the increase in the porosity. HA-30 vol%NA (HA-30NA) samples have the highest possible strength (7.99 MPa), and HA-70NA had the lowest strength (0.89MPa). The microstructure of the SBF aged samples shows that the crystallized apatite particles initially have a spherical morphology. The apatite growth starts from the surface of predominantly large grains or from the grains that are situated near a pore. It is expected that large grains or grain boundaries will have higher dissolution rate. It is observed that, the dissolution process is necessary for apatite formation, and the presence of dislocations

on the grain surface accelerates the dissolution process and is the preferable sites for apatite deposition. Thus, the study shows that by controlling the pore former (NA) content, a wide variety of microstructure can be produced.

In the gel casting route of scaffold preparation, the porous HA scaffold was prepared by incorporation of a volatile material (NA) as the pore forming agent in gel cast samples. Scaffolds prepared from only gel casting route had a lower pore size ( $< 20\mu\text{m}$ ) and less porosity ( $\sim 22\%$ ). By modifying the solid loading, NA content, the porosity and compressive strength could be altered over a wide range. Porous HA scaffold with 60% porosity had open and interconnected pores. Compressive strength of 4.02 MPa was recorded HA-25 NA samples, and the compressive strength was 0.96 MPa for HA-45NA sample. The processed scaffolds had a wide pore size ranging from 10–150  $\mu\text{m}$ . The rate of apatite growth on the aged samples was porosity dependent. For a fixed solid loading, the morphology of the apatite granules changed from a globular to flowery and finally to a petal shape with an increase in the aging time. MTT results indicate that the processed HA scaffold had biocompatibility.

The Protein Coagulation Casting method could produce porous HA with a wide porosity range (40-80%) and reasonable compressive strength 0.62 to 3.59 MPa. The samples with both micro porosity ( $< 10\ \mu\text{m}$ ) and macro porosity (10-200  $\mu\text{m}$ ) and sometimes pores as large as  $\sim 500\ \mu\text{m}$  (for low solid loading) could be fabricated by this method. In the samples prepared from a lower solid loading, shrinkage resulted in cracking and breaking of samples during drying and sintering. The results of the present study show that the observed porosity and interconnectivity (qualitative estimation) is lower as compared to the reported value. Samples with lower solid loading could not be prepared from low EWH ratio. The addition of 3% PVA to EWH mix reduced the drainage rate. In 1:1 EWH, PVA addition reduced the drainage rate to 158  $\mu\text{L}/\text{min}$ . Thus lower solid loading samples could also be produced (15 and 25 vol %). But these samples were extremely fragile and were damaged during handling or measurement. However, in the present study, the intensive stirring was also producing foams, but the same stirring action was preventing foam attachment to the particles. Thus the intense stirring resulted in



unstabilized foams that could drain out before the setting of the cast. The variation of Egg White viscosity with temperature showed that the gelation of Egg White happens between 65 and 68°C. Therefore, the samples should be dried at 70°C to minimize drainage and cracking of the cast body.

In all the three scaffold processing routes, the prepared scaffolds exhibited an inverse strength-porosity relation. The decrease in strength was more related to the open pores, and closed pores had a minimal effect of strength decrease.

Scaffolds prepared by all the three methods show a similar trend in the dissolution behaviour in SBF. Thus in all the cases,  $\text{Ca}^{+2}$  and  $\text{P}^{+5}$  concentration of SBF increased during the initial aging time during which weight loss also happened due to the dissolution of HA in SBF

The  $\text{Ca}^{+2}$  and  $\text{P}^{+5}$  of SBF usually decreased after 14-21 days during which weight loss also became constant. The results indicate that the formation and deposition of apatite require migration of  $\text{Ca}^{+2}$  and  $\text{P}^{+5}$  from SBF.

In case of Gel cast and PCC method samples, the pH of the SBF solution increased from 7.4 to 8.2 during the initial aging period. The increase in pH was due to the progressive dissolution of  $\text{Ca}^{+2}$  in SBF. The pH decreased after 21 days.

The increase in weight loss during the aging of the scaffold in SBF is due to the dissolution of HA in SBF. According to the literature, the precipitating sequence for SBF depends on the pH of the SBF solution. At a temperature of 37.4°C with pH between 6.7-7, the precipitation sequence is DCPD----OCP-----HAP. The apatite formulation is preceded by the intermediate compound formation.

**Table-9.1 Summary of the major characteristics of the scaffold prepared by three routes. Only the results from comparable porosity samples have been listed**

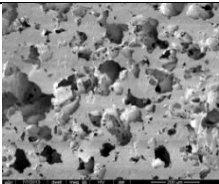
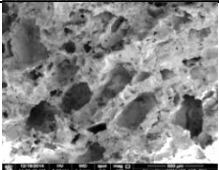
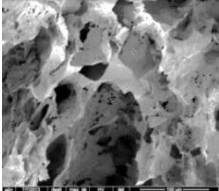
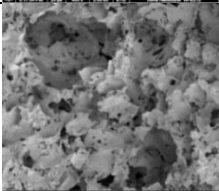
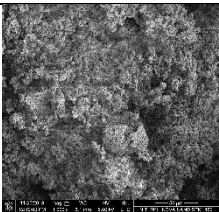
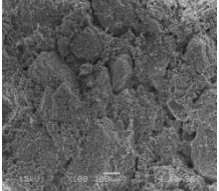
Methods	Composition	Apparent Porosity (%)	Compressive strength (MPa)	Sintered Microstructure	Interconnectivity/ pore size
<b>Solid State Route</b>					
	HA-50NA	52.50	4.84		Yes but few
	HA-60NA	62.32	2.97		Yes, significant Macro, Meso and micro pores are present
<b>Gel Casting with NA</b>					
	<i>HA-25NA</i>	48.02	4.02		Yes, significant Macro, Meso and micro pores are present
	<i>HA-35NA</i>	60.32	2.39		Yes, significant Macro, Meso and micro pores are present
<b>PCC Method</b>					
	30 (1EW:3H)	64.28	1.87		Yes but small interconnection size. The interconnections are less compared to Gelcast.
	35 (1EW:3H)	52.48	2.98		Very few

Table-9.1 shows a comparison of the characteristics of the samples obtained in this study that have been prepared by the three scaffold fabrication route adopted in this study. For this comparison, only those samples (prepared by different routes) have been included which have comparable porosity level. The Table shows that of the three fabrication routes studied, Gel Cast route with NA addition gave the best result. Solid state route had appreciable porosity with interconnectivity, but apatite growth was less. The PCC method produced highly porous Scaffold at high EWH ratio and low solid loading, but these samples were very weak. The interconnectivity was good in those samples, but the samples disintegrate during handling. However, this comparison does not imply that PCC route is unsuitable for Scaffold preparation. The desirable microstructural features could not be achieved due to the different slurry processing adopted for this study. It will be worthwhile to study the scaffold preparation by PCC method from slurries prepared by another method.

#### **Scope of Further Work:**

The results of the present study have opened the following possibility that can be taken up as the future work:

- (a) The porous HA scaffold prepared has been prepared from Wet Chemical Route having mixed particle morphology. It may be worth studying the scaffold properties from a nano HA powder prepared may be through freeze casting.
- (b) The HA scaffold prepared by solid state route had large grain sizes. By preparing the nano HA, the bioactivity behavior can be studied. Moreover, the scaffold prepared from nano HA may have higher strength.
- (c) It may be possible to improve the porosity of Gel Cast scaffold by adding some foaming agent to create additional foams. The porous scaffold prepared by this method may have different porosity and bioactivity.
- (d) The scaffold prepared from Protein Coagulation technique can be further investigated for fabricating a lower solid loaded scaffold, microwave dried scaffold, and tumbling method.
- (e) The kinetics of invitro aging can be studied in greater detail starting from very short time (1 hour) to long time (72 hours or more )

# *References*

## Chapter-1

- 1.1 Lui H. and Webster, T. J. (2007). Nanotechnology for the Regeneration of Hard and Soft Tissues, ed. T.J. Webster (Hackensack, NJ: World Scientific Publishing Co., (1–52).
- 1.2 Chen Q. Z., Wong C. T., Lu W. W., Cheung K. M. C., Leong J. C. Y. and Luk K. D. K. (2004). Strengthening Mechanisms of Bone Bonding to Crystalline Hydroxyapatite in Vivo. *Biomaterials*, 25(18), 4243-4254.
- 1.3 Kotani S., Fujita Y., Kitsugi T., Nakamura T., Yamamuro T., Ohtsuki C. and Kokubo T. (1991). Bone Bonding Mechanism of  $\beta$ -Tricalcium Phosphate. *J. Biomed. Mater. Res.*, 25(10), 1303-1315.
- 1.4 Hench L. L. (1991). Bioceramics: From Concept to Clinic. *J. Am. Ceram. Soc.*, 74(7), 1487-1510
- 1.5 Hench L. L. and Wilson J. (1993). An Introduction to Bio ceramics (Vol. 1). World Scientific.
- 1.6 Shepherd J. H. and Best S. M. (2011). Calcium Phosphate Scaffolds for Bone Repair. *Biomater. Reg. Med.*, 63(4), 83-92.
- 1.7 Bhat S. S., Waghmare U. V. and Ramamurty, U. (2014). First-Principles Study of Structure, Vibrational, and Elastic Properties of Stoichiometric and Calcium-Deficient Hydroxyapatite. *Crystal Growth. and Des.*, 14(6), 3131-3141.
- 1.8 Corno M., Rimola A., Bolis V. and Ugliengo P. (2010). Hydroxyapatite as a Key Biomaterial: Quantum-Mechanical Simulation of its Surfaces in Interaction with Biomolecules. *Phy. Chem. Chem. Phys*, 12(24), 6309-6329.
- 1.9 LeGeros R. Z., Singer L., Ophaug R. H., Quirolgico G., Thein A. and LeGeros J. P. (1982). The Effect of Fluoride on The Stability Of Synthetic And Biological (Bone Mineral) Apatites. *Osteoporosis* (pp. 327-341). Wiley New York.
- 1.10 Lacout J. L., Nounah A. and Ferhat M. (1998). Strontium-Cadmium Substitution In Hydroxy-and Fluor-Apatites. *Annales de Chimie Science des Matériaux*, 23(1), 57-60.
- 1.11 Webster T. J., Massa-Schlueter E. A., Smith J. L. and Slamovich, E. B. (2004). Osteoblast Response to Hydroxyapatite Doped with Divalent and Trivalent Cations. *Biomaterials*, 25(11), 2111-2121.
- 1.12 Rey C. (1998). Calcium Phosphates for Medical Applications. *Calcium Phosphates in Biological and Industrial Systems*. Springer US, 217-251.
- 1.13 Jha L. J., Best S. M., Knowles J. C., Rehman I., Santos D. J. and Bonfield W. (1997). Preparation and Characterization of Fluoride-Substituted Apatites. *J. Mat. Sci: Mater. in Med*, 8(4), 185-191.
- 1.14 Veiderma M., Tõnsuaada K., Knubovets R. and Peld M. (2005). Impact of Anionic Substitutions on Apatite Structure and Properties. , *J. Organomet Chem* , 690, 2638.
- 1.15 Viswanath B. and Ravishankar N. (2008). Controlled Synthesis of Plate-Shaped Hydroxyapatite and Implications for the Morphology of the Apatite Phase in Bone. *Biomaterials*, 29(36), 4855-4863.

- 1.16 Rapacz-Kmita A., Paluszkiwicz C., Slosarczyk A. and Paszkiewicz Z. (2005). FTIR and XRD Investigations on the Thermal Stability of Hydroxyapatite during Hot Pressing and Pressure less Sintering Processes *J. Mol Struct* 744-747, 653.
- 1.17 Newesely H. and Osborn J. F., *Mechanical Properties of Biomaterials*, ed. G.W. Hastings and D.F. Williams, New York, Wiley (1980) 457.
- 1.18 De Groot K., Klein C. P. A. T., Wolke J. D. and de Blieck-Hogervorst J. M. A. (1990). *Chemistry of Calcium Phosphate Bio Ceramics. Handbook of Bioactive Ceramics*, 2, 3-16.
- 1.19 Jarcho M. (1981). Calcium Phosphate Ceramics as Hard Tissue Prosthetics. *Clin. Orthop. Relat. Res.* 157, 259-278.
- 1.20 Hulbert S. F., Hench L. L., Forbers D. and Bowman L. S. (1982). History of Bioceramics. *Ceram. Int.*, 8(4), 131-140.
- 1.21 Polak S. J., Levensgood S. K. L., Wheeler M. B., Maki A. J., Clark S. G. and Johnson A. J. W. (2011). Analysis of the Roles of Microporosity and BMP-2 on Multiple Measures of Bone Regeneration and Healing in Calcium Phosphate Scaffolds. *Acta Biomater*, 7(4), 1760-1771.
- 1.22 Dieter G. E. and Bacon D. (1986). *Mechanical Metallurgy*, McGraw-Hill, New York.
- 1.23 Hench L. L. (1998). Bioceramics. *J. Am. Ceram. Soc.*, 81, 1705–1728.
- 1.24 Twigg M. V. and Richardson J. T. (2002). Theory and Applications of Ceramic Foam Catalysts. *Chem. Eng Res. and Des.* 80(2), 183-189.
- 1.25 Adler J. J. (2005). Ceramic Diesel Particulate Filters. *Int. J. Appl. Ceram Technol*, 2(6), 429-439.
- 1.26 Kelly A. (2006). Why Engineer Porous Materials? *Philos. Trans. R. Soc. A*, 364A, 5–14.
- 1.27 Schüth F. (2005). Engineered Porous Catalytic Materials. *Annu. Rev. Mater. Res.*, 35, 209-238.
- 1.28 Colombo P., (2008). Engineering Porosity in Polymer-Derived Ceramics. *J. Eur. Ceram Soc.*, 28(7), 1389-1395.
- 1.29 Studart A. R., Gonzenbach U. T., Tervoort E. and Gauckler, L. J. (2006). Processing Routes to Macroporous Ceramics: A Review. *J. Am. Ceram. Soc.*, 89(6), 1771-1789.
- 1.30 Takahashi M. (2009). Opportunities of Porous Ceramics Fabricated By Gel Casting in Mitigating Environmental Issues. *J. Eur. Ceram Soc.*, 29(5) 823-828.
- 1.31 Colombo P., Vakifahmetoglu C. and Costacurta S. (2010). Fabrication of Ceramic Components with Hierarchical Porosity. *J. Mater. Sci.*, 45(20), 5425-5455.
- 1.32 Scheffler M. and Colombo P. (2005). *Cellular Ceramics: Structure, Manufacturing, Properties and Applications*. Wiley-VCH Verlag GmbH, Weinheim, Germany 645.
- 1.33 Kaneko K. (1994). Determination of Pore Size and Pore Size Distribution 1. Adsorbents and Catalysts. *Review. J. Membr Sci.*, 96, 59–89.
- 1.34 Liebau F. (2003). Microporous Materials of the Nth-Order: New Classes of Poroates. *Micropor Mesopo Mat.*, 58, 15.

- 1.35 Manoj Kumar B. V. and Kim Y. W. (2010). Processing of Polysiloxane-Derived Porous Ceramics: A Review. *Sci. Technol. Adv. Mater.* 11(4) 044303.
- 1.36 Fukushima M., Zhou Y., Iwamoto Y., Yamazaki S., Nagano T., Miyazaki, H., Yoshizawa Y., Hirao K., Iwamoto Y., Yamazaki S. and Nagano T. (2006). Microstructural Characterization of Porous Silicon Carbide Membrane Support with and Without Alumina Additive. *J. Am. Ceram. Soc.*, 89, 1523–1529.
- 1.37 Nanjangud S. C., Brezny R. and Green, D. J. (1995). Strength and Young's Modulus Behavior of a Partially Sintered Porous Alumina. *J. Am. Ceram. Soc.* 78(1), 266-268.
- 1.38 Hardy D. and Green D. J. (1995). Mechanical Properties of a Partially Sintered Alumina. *J. Eur. Ceram Soc.* 15(8), 769-775.
- 1.39 Weinheim (2002). *Handbook of Porous Solids*, Wiley-VCH, 2923-2970.
- 1.40 Schwartzwalder K. and Somers A. V. (1963). Method of Making Porous Ceramic Articles, US Pat. No. 3090094.
- 1.41 Saggio-Woyansky J., Scott C. E. and Minnear, W. P. (1992). Processing of Porous Ceramics. *Am. Ceram. Soc. Bull.*, 71 (11), 1674–82.
- 1.42 Sepulveda P. (1997). Gel Casting Foams for Porous Ceramics. *Am. Ceram. Soc. Bull.*, 76(10), 61–65.
- 1.43 Yang S., Yang H., Chi X., Evans J. R. G., Thompson I., Cook R. J., and Robinson P. (2008). Rapid Prototyping of Ceramic Lattices for Hard Tissue Scaffolds. *Mater Des.* 29, 1802-1809.
- 1.44 Zein I., Huttmacher D. W., Tan K. C. and Teoh S. H. (2002). Fused Deposition Modeling of Novel Scaffold Architectures for Tissue Engineering Applications. *Biomaterials*, 23(4), 1169-1185.
- 1.45 Bian W., Li D., Lian Q., Zhang W., Zhu L., Li X. and Lin Z. (2011). Design and Fabrication of A Novel Porous Implant with Pre-Set Channels Based On Ceramic Stereolithography for Vascular Implantation. *Biofabrication*, 3(3), 034103.
- 1.46 Shuai C., Gao N., Hu C. Y., Zhou H., Peng Y. S. (2011). Structure and Properties of Nano-Hydroxyapatite Scaffolds for Bone Tissue Engineering with a Selective Laser Sintering System. *Nanotechnology*, 22(28), 285703.
- 1.47 Vlasea M., Shanjani Y., Bothe A., Kandel R., Toyserkani E. (2013). A Combined Additive Manufacturing and Micro-Syringe Deposition Technique for Realization of Bio-Ceramics Structures with Micro-Scale Channels. *Int. J. Adv. Manuf-Technol.*, 68, 2261-2269.
- 1.48 Aneziris C. G., Schärfl W. and Ullrich B. (2007). Microstructure Evaluation of Al<sub>2</sub>O<sub>3</sub> Ceramics with Mg- PSZ- And TiO<sub>2</sub>-Additions. *J. Eur. Ceram. Soc.*, 27, 3191-319
- 1.49 Ma B., Lin L., Huang X., Hu Q., Fang M. (2006). Bone Tissue Engineering Using  $\beta$ -Tricalcium Phosphate Scaffolds Fabricated via Selective Laser Sintering, In *International Federation for Information Processing (IFIP), Knowledge Enterprise: Intelligent Strategies In Product Design, Manufacturing, and Management*, eds: Wang, K., Kovacs, G., Wozny, M., Fang, M.. Boston: Springer, Volume 207.

- 1.50 Schuth F. and Sing K. S. W. (2002). Eds: Weitkamp, J. Handbook of Porous Solids. Wiley-VCH Weinheim.
- 1.51 Guangliang L. (2011). Fabrication of Wood-Like Porous Silicon Carbide Ceramics without Templates. *J. Eur. Ceram. Soc.*, 31(5), 847-854.
- 1.52 Gao F, Lian C., Zhou L., Liu H. and Hu, J. (2014). Phase Separation of Mixed Micelles and Synthesis of Hierarchical Porous Materials. *Langmuir*, 30(38), 11284-11291.
- 1.53 Yuan W., Yuan P., Liu D., Yu W., Deng L. and Chen F. (2015). Novel Hierarchically Porous Nanocomposites of Diatomite-Based Ceramic Monoliths Coated with Silicalite-1 Nanoparticles for Benzene Adsorption. *Micropor Mesopo Mat.*, 206, 184-193.
- 1.54 Prenzel T., Döge K., Motta R. P. O., Wilhelm M. and Rezwani K. (2014). Controlled Hierarchical Porosity of Hybrid Ceramics by Leaching Water Soluble Templates and Pyrolysis. *J. Eur. Ceram Soc.*, 34(6), 1501-1509.
- 1.55 Luyten J., Mullens S. and Thijs I. (2010), Designing with Pores-Synthesis and Applications, *Mat. Technol, VITO1 KONA Powder and Particle Journal*, (28), 131-142.
- 1.56 Ohji T. and Fukushima M., (2012). Macro-Porous Ceramics: Processing and Properties. *Int. Mat. Rev.*, 57(2), 115-131.
- 1.57 Hammel E. C., Ighodaro OL-R. and Okoli, O. I., (2014). Processing and Properties of Advanced Porous Ceramics: An Application Based Review. *Ceram. Int.*, 40(10), 15351-15370.
- 1.58 Kingery W. D., Bowen H. K. and Uhlmann, D. R. Introduction to Ceramics, 1976. John Wiley and Sons, New York.
- 1.59 Oh S. T., Tajima K. I., Ando M. and Ohji T. (2000). Strengthening of Porous Alumina by Pulse Electric Current Sintering and Nanocomposite Processing. *J. Am. Ceram. Soc.*, 83(5), 1314-1316.
- 1.60 Jayaseelan D. D., Kondo N., Brito M. E. and Ohji T. (2002). High-Strength Porous Alumina Ceramics by the Pulse Electric Current Sintering Technique. *J. Am. Ceram. Soc.*, 85, 1267-269.
- 1.61 Akhtar F., Vasiliev P. O. and Bergström L. (2009). Hierarchically Porous Ceramics from Diatomite Powders by Pulsed Current Processing. *J. Am. Ceram. Soc.*, 92(2), 338-343.
- 1.62 Zhang G. J. and Ohji V T. (2001). High-Surface-Area Alumina Ceramics Fabricated by the Decomposition of Al (OH)<sub>3</sub>. *J. Am. Ceram. Soc.*, 84(3), 485-491.
- 1.63 Claussen N., Wu S. and Holz D. (1994). Reaction Bonding Of Aluminum Oxide (RBAO) Composites: Processing, Reaction Mechanisms and Properties. *J. Eur. Ceram. Soc.*, 14(2) 97-109.
- 1.64 She J. H. and Ohji, T. (2003). Fabrication and Characterization of Highly Porous Mullite Ceramics. *Mat. Chem. Phys*, 80(3), 610-614.
- 1.65 She, J. H., Yang, J. F., Kondo, N., Ohji, T., Kanzaki, S., and Deng, Z. Y. (2002). High-Strength Porous Silicon Carbide Ceramics by an Oxidation-Bonding Technique. *J. Am. Ceram. Soc.*, 85(11), 2852–2854.



- 1.66 Oh, S. T., Tajima, K. I., Ando, M., and Ohji, T. (2000). Strengthening Of Porous Alumina by Pulse Electric Current Sintering and Nanocomposite Processing. *J. Am. Ceram. Soc.*, 83(5), 1314–1316.
- 1.67 Deng Z. Y., She J., Inagaki Y., Yang J. F. Ohji, T. and Tanaka Y. (2004). Reinforcement by Crack-Tip Blunting in Porous Ceramics. *J. Eur. Ceram. Soc.*, 24(7), 2055-2059.
- 1.68 Brown D. D. and Green. D. J. (1994). Investigation of Strut Crack Formation in Open Cell Alumina Ceramics. *J. Am. Ceram. Soc.*, 77(6), 1467-1472.
- 1.69 Zhu, X. et. al. (2001). Improvement in the Strut Thickness of Reticulated Porous Ceramics. *J. Am. Ceram. Soc.*, 84(7), 1654-1656.
- 1.70 Vogt U. F., Gorbar M., Dimopoulos-Eggenschwiler, P. Broenstrup, A. Wagner, G. and Colombo, P. (2010). Improving the Properties of Ceramic Foams by a Vacuum Infiltration Process. *J. Eur. Ceram Soc.*, 30(15), 3005-3011.
- 1.71 Tiemann M. (2007). Repeated Templating. *Chem Mater* 20(3), 961-971.
- 1.72 Gauckler L. J., Waeber M. M., Conti C. and Jacobduliere M. (1985). Ceramic Foam for Molten-Metal Filtration. *J. Metals*, 37(9), 47–50.
- 1.73 Pu X. P., Liu X. J., Qiu, F. G. and Huang, L. P. (2004). Novel Method to Optimize the Structure of Reticulated Porous Ceramics. *J. Am. Ceram. Soc.*, 87(7) 1392–1394.
- 1.74 Zhu X. W., Jiang D. L., Tan S. H. and Zhang Z. Q. (2001). Improvement in the Strut Thickness of Reticulated Porous Ceramics. *J. Am. Ceram. Soc.*, 84(7), 1654–56.
- 1.75 Montanaro L., Jorand Y., Fantozzi G. and Negro, A. (1998). Ceramic Foams by Powder Processing. *J. Eur. Ceram. Soc.*, 18(9), 1339–50.
- 1.76 Lange F. and Miller K. T. (1987). Open-Cell, Low-Density Ceramics Fabricated from Reticulated Polymer Substrates. *Adv. Ceram. Mater.* 2(4), 827–31.
- 1.77 White R. A., White E. W. and Weber, J. N. (1972). Replamine form—New Process for Preparing Porous Ceramic, Metal, and Polymer Prosthetic Materials. *Science*, 176(4037), 922.
- 1.78 Heness, G., Ben-Nissan, B. (2004). Innovative Bioceramics. *Mater. Forum*, 27, 104-114.
- 1.79 Ota T., Takahashi M., Hibi T., Ozawa M., Suzuki S., Hikichi Y. and Suzuki H. (1995). Biomimetic Process for Producing SiC Wood. *J. Am. Ceram. Soc.*, 78(12) 3409–11.
- 1.80 Colombo P., Bernardo E. and Biasetto, L. (2004). Novel Microcellular Ceramics from a Silicone Resin, *J. Am. Ceram. Soc.*, 87(1), 152–154.
- 1.81 Hotta Y., Alberius P. C. A. and Bergstrom L. (2003). Coated Polystyrene Particles as Templates for Ordered Macroporous Silica Structures with Controlled Wall Thickness. *J. Mater. Chem.*, 13(3), 496–501.
- 1.82 Bouler J. M., Trecant M., Delecricin J., Royer, J. Passuti, N. and Daculsi G. (1996). Macroporous Biphasic Calcium Phosphate Ceramics: Influence of Five Synthesis Parameters on Compressive Strength. *J. Biomed. Mater. Res.*, 32(4) 603.
- 1.83 Lyckfeldt O. and Ferreira, J. M. F. (1998). Processing of Porous Ceramics by Starch Consolidation. *J. Eur. Ceram. Soc.*, 18(2), 131–40.

- 1.84 Fitzgerald T. J., Michaud V. J. and Mortensen, A. (1995). Processing of Microcellular SiC Foams. *J. Mat. Sci.*, 30(4), 1037-1045.
- 1.85 Lopes R. A. and Segadaes A. M. (1996). Microstructure, Permeability and Mechanical Behaviour of Ceramic Foams. *Mater. Sci. Eng. A—Struct. Mater. Prop. Microstruct. Process.* 209(1–2), 149–55.
- 1.86 Barg S., Soltmann, C. Andrade, M. Koch, D. and Grathwohl G. (2008). Cellular Ceramics by Direct Foaming of Emulsified Ceramic Powder Suspensions. *J. Am. Ceram. Soc.*, 91(9), 2823-2829.
- 1.87 Barg S., Dietmar K. and Grathwohl G. (2009). Processing and Properties of Graded Ceramic Filters. *J. Am. Ceram. Soc.*, 92(12), 2854-2860.
- 1.88 Song H-Y, Islam S. and Lee, B-T. (2008). A Novel Method To Fabricate Unidirectional Porous Hydroxyapatite Body Using Ethanol Bubbles In Viscous Slurry. *J. Am. Ceram. Soc.*, 91(9), 3125-3127.
- 1.89 Tomita T., Kawasaki S. and Okada K. (2005). Effect of Viscosity on Preparation of Foamed Silica Ceramics by a Rapid Gelation Foaming Method. *J. Porous Mat.*, 12(2), 123-129.
- 1.90 Kim H., Lee S., Han Y. and Park, J (2009). Control of Pore Size in Ceramic Foams: Influence of Surfactant Concentration. *Mater. Chem. Phys.*, 113(1), 441-444.
- 1.91 Hunter R. J. (2013). *Zeta Potential in Colloid Science: Principles and Applications (Vol. 2)*. Academic Press.
- 1.92 Pugh R. J. (2001). Foams and Foaming. p. 23–43 in *Handbook of Applied Surface and Colloid Chemistry, Vol. 2*. Edited by K. Holmberg. John Wiley and Sons Ltd, West Sussex.
- 1.93 Hiemenz P. C. and Rayagopalan, R. (1997). *Principles of Colloid and Surface Chemistry*, p. 650. 3rd edition, Marcel Dekker Inc, New York.
- 1.94 Binks B. P. (2002). Particles as Surfactants—Similarities and Differences *Curr. Opin. Colloid Interf. Sci.*, 7(1–2), 21–41.
- 1.95 Gonzenbach U. T., Studart A. R., Tervoort E. and Gauckler L. J. (2006). Ultrastable Particle-Stabilized Foams. *Angew. Chem. Int. Ed.*, 45(21), 3526-3530.
- 1.96 Dhara. S. and Bhargava P. (2003). A Simple Direct Casting Route to Ceramic Foams, *J. Am. Ceram. Soc.*, 86(10) 1645–50.
- 1.97 Cai K., Huang Y., Yang J. L. (2002). Alumina Gel Casting With a New Low-Toxicity System. *Key Eng Mater*, 224(2), 643.
- 1.98 Sepulveda P. and Binner J. G. P. (1999). Processing of Cellular Ceramics by Foaming and In Situ Polymerisation of Organic Monomers. *J. Eur. Ceram. Soc.*, 19(12), 2059–66.
- 1.99 Omatete O. O., Janney M. A., Strelow. R. A. (1991). Gel casting—A New Ceramic Forming Process. *Am. Ceram. Soc. Bull.*, 70(10), 1641–9.
- 1.100 Garrn I., Reetz C., Brandes N., Kroh L. W. and Schubert H. (2004). Clot- Forming: The Use of Proteins as Binders for Producing Ceramic Foams, *J. Eur. Ceram. Soc.*, 24(3), 579–87.

- 1.101 Ortega F. S., Valenzuela F. A. O., Scuracchio C. H. and Pandolfelli V. C. (2003). Alternative Gelling Agents for the Gelcasting of Ceramic Foams. *J. Eur. Ceram. Soc.*, 23(1), 75–80.
- 1.102 Daculsi G., Laboux O., Malard O. and Weiss P. (2003). Current State Of The Art of Biphasic Calcium Phosphate Bioceramics. *J. Mater. Sci.: Mater Med.*, 14, 195-200.
- 1.103 ISO/ASTM, 17296 Standards on Additive Manufacturing (AM) Technologies.
- 1.104 Kalita S. J, Bose S., Hosick H. L. and Bandyopadhyay, A. (2003). Development of Controlled Porosity Polymer-Ceramic Composite Scaffolds via Fused Deposition Modeling. *Mater. Sci. Eng. C*, 23, 611-620.
- 1.105 Fukasawa T., Deng Z. Y., Ando M., Ohji T. and Kanzaki S. (2002). Synthesis of Porous Silicon Nitride with Unidirectionally Aligned Channels Using Freeze-Drying Process. *J. Am. Ceram. Soc.*, 85(9), 2151–2155.
- 1.106 Deville S. (2008). Freeze-Casting of Porous Ceramics: A Review of Current Achievements and Issues. *Adv. Eng. Mat.*, 10(3), 155-169.
- 1.107 Deville S., Saiz E., Tomsia A. P. (2006). Freeze Casting Of Hydroxyapatite Scaffolds for Bone Tissue Engineering. *Biomaterials*, 27, 5480–5489.
- 1.108 Brenne F., Niendorf T., Maier H.J. (2013). Additively Manufactured Cellular Structures: Impact of Microstructure and Local Strains on The Monotonic and Cyclic Behavior Under Uniaxial And Bending Load. *J. Mater. Process. Technol.*, 213, 1558–156.
- 1.109 Tarafder S., Balla V. K., Davies N. M., Bandyopadhyay A., Bose S. (2013). Microwave-Sintered 3D Printed Tricalcium Phosphate Scaffolds for Bone Tissue Engineering. *J. Tissue. Eng. Regen. Med.*, 7, 631-41.
- 1.110 Agarwala M., Bourell D., Beaman J., Marcus H. and Barlow J. (1995). Direct Selective Laser Sintering of Metals. *Rapid Prototyping J*, 1(1), 26-36.
- 1.111 Rezwani K., Chen Q. Z., Blaker J. J. and Boccaccini A. R. (2006). Biodegradable and Bioactive Porouspolymer/Inorganic Composite Scaffolds for Bone Tissue Engineering. *Biomaterials*, 27, 3413-3431.
- 1.112 Karageorgiou V. and Kaplan D. (2005). Porosity of 3D Biomaterial Scaffold and Osteogenesis. *Biomaterials*, 26, 5474–5491.
- 1.113 Sopyan I., Kaur (2009). Preparation and Characterization of Porous Hydroxyapatite through Polymeric Sponge Method. *Ceram Int*, 35, 3161–3168.
- 1.114 Roddriguez-Lorenzo L.M. and Ferreira J.M.F. (2004). Development of Porous Ceramic Bodies for Applications in Tissue Engineering and Drug Delivery Systems. *Mat. Res. Bull.*, 3983-91.
- 1.115 Yasuaki S. (1995). Preparation of Adsorption Catalyst Material. *Jpn. Pat. No. 09108567*.
- 1.116 Li S. H., Wijn J. R., Layrolle P. and Groot K. (2003). Novel Method to Manufacture Porous Hydroxyapatite by Dual-Phase Mixing. *J. Am. Ceram. Soc.*, 86(1), 65-72.
- 1.117 Tas A.C. (2004). Preparation of porous bio ceramics a simple PVA-processing route. *Key Eng. Mater.*, 264-268, 2079-2082.

- 1.118 Kundu B., Sinha M. K., Mitra M. K. and Basu D. (2004). Fabrication And Characterization Of Porous Hydroxyapatite Ocular Implant Followed by an in Vivo Study in Dogs. *Bull. Mater. Sci.*, 27(2), 133–140.
- 1.119 Klenke F. M., Liu Y., Yuan H., Hunziker E. B., Siebenrock K. A. and Hofstetter W. (2008). Impact of Pore Size on the Vascularization and Osseointegration of Ceramic Bone Substitutes in Vivo. *J. Biomed. Mater. Res. Part A*, 85(3), 777-786.
- 1.120 Tang Y., Tang Y., Lv C. and Zhou Z. Preparation of Uniform Porous Hydroxyapatite Biomaterials by a New Method. *Appl. Surf. Sci.*, 254, 5359–5362.
- 1.121 Amara A., Abudalazeh A. M. A., Rashid Ismail A., Hayati Abd Razak N., Malik Masudi S., Rizal Kasim S. and Arifin Ahmad Z. (2011). Synthesis and Characterization of Porous Biphasic Calcium Phosphate Scaffold from Different Porogens for Possible Bone Tissue Engineering Applications. *Sci. Sinter.*, 43, 183-192.
- 1.122 Le Ray A.-M., Gautier H., Bouler J.-M., Weiss P. and Merle C. (2010). A New Technological Procedure Using Sucrose as Porogen Compound to Manufacture Porous Biphasic Calcium Phosphate Ceramics of Appropriate Micro- and Macro Structure. *Ceram. Int.*, 36(1), 93–101.
- 1.123 Tadic D., Beckmann F., Schwarz K. and Epple M. (2004). A Novel Method to Produce Hydroxyapatite Objects with Interconnecting Porosity that Avoids Sintering. *Biomaterials*, 25, 3335-3340.
- 1.124 Sopyan I., Mel M., Ramesh S. and Khalid K. A. (2007). Porous Hydroxyapatite for Artificial Bone Applications. *Sci. Technol. Adv. Mater*, 8(1), 116-123.
- 1.125 Bártolo P. J., Almeida H. A., Rezende R. A., Laoui T. and Bidanda B. (2008). Advanced Processing to Fabricate Scaffolds for Tissue Engineering, In *Virtual Prototyping and Bio Manufacturing in Medical Applications*. 149-170. Springer US.
- 1.126 Wosek J. (2015). Fabrication of Composite Polyurethane/Hydroxyapatite Scaffolds Using Solvent-Casting Salt Leaching Technique. *Adv. Mater. Sci.*, 15(1), 14-20.
- 1.127 Mehrabnian M. and Mojtaba N-E. (2011). HA/Nylon 6, 6 Porous Scaffolds Fabricated By Salt-Leaching/Solvent Casting Technique: Effect of Nano-Sized Filler Content on Scaffold Properties. *Int. J. Nanomed.*, 6, 1651.
- 1.128 White R. A., Weber J. N. and White, E. W. (1972). Replamineform: A New Process for Preparing Porous Ceramic, Metal and Polymer Prosthetic Materials. *Science*, 176, 922–24.
- 1.129 Ohgushi H., Okumura M., Yoshikawa T., Inoue K., Senpuku N., Tamai S. and Shors E. C. (1992). Bone Formation Process in Porous Calcium Carbonate and Hydroxyapatite. *J. Biomed. Mater. Res.*, 26(7), 885-895.
- 1.130 Weindling S. M., Robinette C. L. and Wesley R. E. (1992). Porous Hydroxyapatite in Orbital Reconstructive Surgery: Radiologic Recognition. *Am. J. Neuroradio.*, 13(1), 239-240.

- 1.131 Nandi S. K., Kundu B., Mukherjee J., Mahato A., Datta S. and Balla V. K. (2015). Converted Marine Coral Hydroxyapatite Implants With Growth Factors: In Vivo Bone Regeneration. *Mat. Sci. and Eng: C*, 49, 816-823.
- 1.132 Arita I. H., Castano V. M. and Wilkinson D. S. (1995). Synthesis and Processing of Hydroxyapatite Ceramic Tapes with Controlled Porosity. *J. Mat Sci.: Mater Med.*, 6(1), 19-23.
- 1.133 Dhara S. and Bhargava P. (2001). Egg White as an Environmentally Friendly Low-Cost Binder for Gelcasting of Ceramics. *J. Am. Ceram. Soc.*, 84(12), 3048-3050.
- 1.134 Itatani, K., Uchino, T. and Okada, I. (2003). Preparation of Porous Hydroxyapatite Ceramics from Hollow Spherical Agglomerates Using a Foaming Agent of H<sub>2</sub>O<sub>2</sub>. *J. Soc. Inorg. Mater. Jap.*, 10(306), 308-315.
- 1.135 Lemos A. F. and Ferreira, J. M. F., (2004). The Valences of Egg White for Designing Smart Porous Bioceramics: as Foaming and Consolidation Agent. *Key Engg Mat.*, 254-256, 1045-1050.
- 1.136 Potoczek M. (2008). Hydroxyapatite Foams Produced by Gel Casting using Agarose. *Mat. Lett.*, 62, 1055–1057.
- 1.137 Fadli, A. and Sopyan, I., (2009). Preparation of Porous Alumina for Biomedical Applications through Protein Foaming Consolidation Method. *Mater. Res. Innov*, 13, 327–329.
- 1.138 Lyckfeldt O., Ferreira J. M. F. (1998). Porous Ceramics by Starch Consolidation. *J. Eur. Ceram. Soc.*, 18, 131-140.
- 1.139 Rodríguez-Lorenzo, L. M. Vallet-Regí, M. and Ferreira, J. M. F. (2002). Fabrication of Porous Hydroxyapatite Bodies by a New Direct Consolidation Method: Starch Consolidation. *J Biomed Mat Res.*, 60(2), 232-240.
- 1.140 Ahmed Y. M. Z., Ewais E. M. M. and El-Sheikh S. M. (2015). Potato Starch Consolidation of Aqueous HA Suspension. *J Asian Ceram Soc*, 3(1), 108-115.
- 1.141 Shuai C., Feng P., Cao C. and Peng, S. (2013). Processing and Characterization of Laser Sintered Hydroxyapatite Scaffold for Tissue Engineering. *Biotechnol Bioprocess Eng*, 18(3), 520-527.
- 1.142 Zhou W. Y., Lee S. H., Wang M., Cheung W. L. and Ip W. Y (2008). Selective Laser Sintering Of Porous Tissue Engineering Scaffolds from Poly (L-Lactide)/Carbonated Hydroxyapatite Nanocomposite Microspheres. *J. Mat. Sci: Mater. Med*, 19(7), 2535-2540.
- 1.143 Zhou W. Y., Wang M., Cheung, W. L. and Ip, W. Y (2010). Selective Laser Sintering of Poly (L-Lactide)/Carbonated Hydroxyapatite Nanocomposite Porous Scaffolds for Bone. *Tissue Eng*. 179-204.
- 1.144 Ma J., Wang C., Peng K.W. (2003). Electrophoretic Deposition of Porous Hydroxyapatite Scaffold. *Biomaterials*, 24, 3505–3510.

- 1.145 Yousefpour M., Afshar A., Chen J. and Zhang X. (2007). Electrophoretic Deposition of Porous Hydroxyapatite Coatings Using Polytetrafluoroethylene Particles as Templates. *Mater. Sci. Eng. C*, 27, 1482–1486.
- 1.146 Farrokhi-Rad M., Loghmani S. K., Shahrabi T. and Khanmohammadi S. (2014). Electrophoretic Deposition of Hydroxyapatite Nanostructured Coatings with Controlled Porosity. *J. Eur. Ceram. Soc.*, 34(1), 97-106.
- 1.147 Schwartzwalder K. and Somers A.V. (1963). Methods of Making Porous Ceramic Articles. US patent, No.3090094.
- 1.148 Saggio-Woyansky, J., Scott, C. E. and Minnear, W. P., (1992). Processing of Porous Ceramics. *Am. Ceram. Soc. Bull.*, 71(11) 1674–82.
- 1.149 Sopyan I. and Kaur J. (2009). Preparation and Characterization of Porous Hydroxyapatite through Polymeric Sponge Method. *Ceram. Int.*, 35, 3161–3168.
- 1.150 Jo I-H., Shin, K-H. Soon, Y-M. Koh, Y-H. Lee, J-H., Kim H-E. (2009). Highly Porous Scaffolds With Elongated Pores Using Stretched Polymeric Sponges as Novel Template. *Mater. Lett.*, 63, 1702–1704.
- 1.151 Ramay H. R. and Zhang, M. (2003). Preparation of Porous Hydroxyapatite Scaffolds by Combination of the Gel-Casting and Polymer Sponge Methods. *Biomaterials*, 24(19), 3293-3302.
- 1.152 Sundaram J., Durance T. D., Wang R. (2008). Porous Scaffold of Gelatin Starch with Nanohydroxyapatite Composite Processed via Novel Microwave Vacuum Drying. *Acta Biomater.* 4(4), 932-942
- 1.153 Feng P., Niu M., Gao C., Peng S. and Shuai, C. (2014). A Novel Two-Step Sintering for Nano-Hydroxyapatite Scaffolds for Bone Tissue Engineering. *Scientific reports* 4.
- 1.154 Brady G. A. and Halloran, J. W. (1997). Stereolithography of Ceramic Suspensions, *Rapid Prototyping J.*, 3, 61–65.
- 1.155 Wilson C., De Bruijn J., Kruijt M., Van Gaalen S., Dhert W., Verbout A. and Van Blitterswijk C. A., Design and Fabrication of Porous Hydroxyapatite Scaffolds for Bone Tissue Engineering Using Rapid Prototyping Techniques. Presented at the 47th Annual Meeting of the Orthopedic Research Society (Feb. 25–28, 2001, San Francisco, CA).
- 1.156 Antonio, A. and Pelzer, R. (2008). Modeling Of Porous Structures for Rapid Prototyping of Tissue Engineering Scaffolds. *Int. J. Adv. Manu. Technol.*, 39(5-6), 501-511.
- 1.157 Kim, J., Lim, D., Kim, Y. H., Young-Hag, K., Lee, M. H., Han, I. (2011). A Comparative Study of The Physical And Mechanical Properties of Porous Hydroxyapatite Scaffolds Fabricated by Solid Freeform Fabrication and Polymer Replication Method. *Int. J. Precis. Eng. Manuf.*, 12(4), 695-701.

## **Chapter-2**

- 2.1. Böhner M. (2010). Resorbable Biomaterials as Bone Graft Substitutes. *Mater Today*, 13(1), 24-30.

- 2.2. Doremus R. H. (1992). Bioceramics. *J. Mat. Sci.*, 27(2), 285-297.
- 2.3. Rahaman M. N., Yao A., Bal B. S., Garino J. P. and Ries M. D. (2007). Ceramics for Prosthetic Hip and Knee Joint Replacement. *J. Am. Ceram. Soc.*, 90(7), 1965-1988.
- 2.4. Langstaff S., Sayer M., Smith, T. J. N. Pugh, S. M. Hesp S. A. M. and Thompson, W. T. (1999). Resorbable Bioceramics Based on Stabilized Calcium Phosphates. Part I: Rational Design, Sample Preparation and Material Characterization. *Biomaterials*, 20(18), 1727-1741.
- 2.5. Rao R. R., Roopa H. N. and Kannan T. S. (1997). Solid State Synthesis and Thermal Stability of HAP And HAP-B-TCP Composite Ceramic Powders. *J. Mat. Sci: Mater Med.*, 8(8), 511-518.
- 2.6. Yang X. and Wang Z. (1998). Synthesis of Biphasic Ceramics of Hydroxyapatite and B-Tricalcium Phosphate with Controlled Phase Content and Porosity. *J. Mater. Chem.*, 8(10), 2233-2237.
- 2.7. Koonawoot R., Saelee C., Thianse, S. and Punyanitya S. Synthesis Control And Characterization Of Hydroxyapatite Ceramic Using A Solid State Reaction. 1st Mae Fah Luang University International Conference 2012
- 2.8. Fahami A., Nasiri-Tabrizi B. and Ebrahimi-Kahrizsangi, R. (2012). Synthesis of Calcium Phosphate-Based Composite Nanopowders by Mechano-chemical Process and Subsequent Thermal Treatment. *Ceram. Int.*, 38(8), 6729-6738.
- 2.9. Yeong K. C. B., Wang J. and Ng S. C. (2001). Mechano-chemical Synthesis of Nanocrystalline Hydroxyapatite from CaO and CaHPO<sub>4</sub>. *Biomaterials*, 22(20), 2705-2712.
- 2.10. Adzila S., Sopyan I. and Hamdi M. (2012). Mechano-chemical Synthesis of Hydroxyapatite Nanopowder: Effects of Rotation Speed and Milling Time on Powder Properties. *Appl. Mech. Mater.*, 110, 3639-3644.
- 2.11. Rhee S. H. (2002). Synthesis of Hydroxyapatite via Mechano-chemical Treatment. *Biomaterials*, 23(4), 1147-1152.
- 2.12. Kao A.M., Aoki H., Kato K. and Sato, A. (1982). Dense Polycrystalline  $\beta$ -Tricalcium Phosphate for Prosthetic Applications. *J. Mater. Sci.*, 17(2), 343-346.
- 2.13. Bouyer E., Gitzhofer F. and Boulos, M. I. (2000). Morphological Study of Hydroxyapatite Nanocrystal Suspension. *J Mater Sci: Mater Med.*, 11(8), 523-531.
- 2.14. Tagai H. and Aoki H. (1987). Preparation of Synthetic Hydro and Sintering of Apatite Ceramics. *Mechanical Properties of Biomaterials*. Eds. G.W. Hastings and D.F Williams New York: John Wiley and Sons, 213-220.
- 2.15. Jarcho, M., Bolen, C. H., Thomas, M. B., Bobick, J., Kay, J. F., and Doremus, R. H. (1976). Hydroxylapatite Synthesis and Characterization in Dense Polycrystalline Form. *J. Mater. Sci.*, 11(11), 2027-2035.
- 2.16. Kivrak N. and Taş A. C. (1998). Synthesis of Calcium Hydroxyapatite-Tricalcium Phosphate (HA-TCP) Composite Bioceramic Powders and Their Sintering Behavior. *J. Am. Ceram. Soc.*, 81(9), 2245-2252.

- 2.17. Cunniffe G. M., Dickson G. R., Partap S., Stanton K. T. and O'Brien F. J. (2010). Development and Characterisation of a Collagen Nano-Hydroxyapatite Composite Scaffold For Bone Tissue Engineering. *J Mater Sci: Mater Med.*, 21(8), 2293-2298
- 2.18. Janačkovića D., Petrović-Prelević I. and Kostić-gvozdenovića L. (2001). Influence of Synthesis Parameters on the Particle Sizes of Nanostructured Calcium-Hydroxyapatite. *Key Eng. Mater.*, (192-195), 203-206.
- 2.19. Manuel C. M., Ferraz, M. P. and Monteiro, F. J. (2002). Synthesis of Hydroxyapatite and Tricalcium Phosphate Nanoparticles—Preliminary Studies. *Key Eng. Mat.*, (240), 555-558.
- 2.20. Masuda Y., Matubara K. and Sakka S. (1990). Synthesis of Hydroxyapatite from Metal Alkoxides through Sol Gel Technique. *J. Ceram. Soc., Jpn.*, (98), 1266- 1277.
- 2.21. LeGeros, R. Z., and LeGeros, J. P. (1993). Dense Hydroxyapatite. In: *An Introduction to Bioceramics*. Hench, L. L. and Wilson, J. (eds.) London : World Scientific : 139-180
- 2.22. Jillavenkatesa A. and Condrate S. (1998). Sol–Gel Processing of Hydroxyapatite. *J. Mater. Sci.*, 33(16), 4111-4119.
- 2.23. Brendel T., Engel A. and Rüssel, C. (1992). Hydroxyapatite Coatings by a Polymeric Route. *J Mater Sci: Mater Med.*, 3(3), 175-179.
- 2.24. Takahashi H., Yashima M., Kakihana M. and Yoshimura M. (1995). Synthesis of Stoichiometric Hydroxyapatite by A Gel Route from the Aqueous Solution of Citric and Phosphonoacetic Acids. *Eur. J. Solid State Inorg. Chem.*, 32(7-8), 829-835.
- 2.25. Qiu H. X., Han Y., Zhuang X., Chen X., Li Y., Jing X. (2007), Preparation of Nano-Hydroxyapatite/Poly(L -Lactide) Biocomposite Microspheres. *J. Nanopart. Res.*, 5(9), 901-908.
- 2.26. Lopatin C. M., Pizziconi V., Alford T. L. and Laursen T. (1998). Hydroxyapatite Powders and Thin Films Prepared By a Sol-Gel Technique. *Thin Solid Films*, 326(1), 227-232
- 2.27. Chai C. S. and Ben-Nissan, B. (1999). Bioactive Nanocrystalline Sol-Gel Hydroxyapatite Coatings. *J Mater Sci: Mater Med.*, 10(8), 465-469.
- 2.28. Weng W., Zhang S., Cheng K., Qu H., Du P., Shen G., Yuan J. and Han G. (2003). Sol–Gel Preparation of Bioactive Apatite Films. *Surf. Coat. Technol*, 167 -292.
- 2.29. Liu D. M., Troczynski T. and Tseng W. J. (2001). Water-Based Sol–Gel Synthesis of Hydroxyapatite: Process Development. *Biomaterials*, 22(13), 1721-1730.
- 2.30. Yoshimura, M. and Suda, H. (1994). Hydrothermal Processing Of Hydroxyapatite: Past, Present, and Future. *Hydroxyapatite and Related Compounds*. Boca Raton (EE. UU.): CRC Press Inc., 45-72.
- 2.31. Neira I. S., Kolen'ko Y. V., Lebedev O. I., Van Tendeloo G., Gupta H. S., Guitián F., and Yoshimura M. (2008). An Effective Morphology Control of Hydroxyapatite Crystals via Hydrothermal Synthesis. *Cryst. Growth Des*, 9(1), 466-474
- 2.32. Suchanek W. L. and Riman, R. E. (2006). Hydrothermal Synthesis of Advanced Ceramic Powders. *Adv. Sci. Technol.*, (45), 184-193.



- 2.33. Neira I. S., Guitián F., Taniguchi T., Watanabe T. and Yoshimura M. (2008). Hydrothermal Synthesis of Hydroxyapatite Whiskers with Sharp Faceted Hexagonal Morphology. *J. Mater. Sci.*, 43(7), 2171-2178.
- 2.34. Loo, S. C. J., Siew, Y. E., Ho, S., Boey, F. Y. C., and Ma, J. (2008). Synthesis and Hydrothermal Treatment of Nanostructured Hydroxyapatite of Controllable Sizes. *J Mater. Sci.: Mater Med.*, 19(3), 1389-1397.
- 2.35. Seo D. S. and Lee J. K. (2008). Synthesis of Hydroxyapatite Whiskers through Dissolution–Reprecipitation Process Using EDTA. *J Cryst Growth*, 310(7), 2162-2167.
- 2.36. Brown P. W., Ten Huizen K. S. and Martin R. I. (2001). U.S. Patent No. 6,201,039. Washington, DC: U.S. Patent and Trademark Office.
- 2.37. Sun Y., Guo G., Tao, D. and Wang, Z. (2007). Reverse Microemulsion-Directed Synthesis of Hydroxyapatite Nanoparticles Under Hydrothermal Conditions. *J. Phys. Chem. Solid*, 68(3), 373-377.
- 2.38. Guo W., Luo G. S. and Wang, Y. J. (2004). A New Emulsion Method to Synthesize Well-Defined Mesoporous Particles. *J Colloid Interface Sci.*, 271(2), 400-406.
- 2.39. Chen J., Wang Y., Chen X., Ren L., Chen Lai, He W., Zhang Q. (2011). A Simple Sol-Gel Technique for Synthesis of Nanostructured Hydroxyapatite, Tricalcium Phosphate and Biphasic Powders. *Mater. Lett.*, (65), 1923-1926.
- 2.40. Sadat-Shojai M., Khorasani M. T., Dinpanah-Khoshdargi E. and Jamshidi A. (2013). Synthesis Methods for Nanosized Hydroxyapatite with Diverse Structures. *Acta Biomater.*, 9(8), 7591-7621.
- 2.41. Ponomareva N. I., Poprygina T. D., Karpov S. I., Lesovoi M. V. and Agapov B. L. (2010). Microemulsion Method for Producing Hydroxyapatite. *Russ. J. Gen. Chem.*, 80(5), 905-908.
- 2.42. Pechini M. P. (1966). U.S. Patent No. 3,231,328. Washington.
- 2.43. Ghosh S. K., Nandi S. K., Kundu B., Datta S., De D. K., Roy S. K. and Basu D. (2008). In Vivo Response of Porous Hydroxyapatite and  $\beta$ -Tricalcium Phosphate Prepared by Aqueous Solution Combustion Method and Comparison with Bioglass Scaffolds. *J. Biomed. Mat. Res. Part B: Appl Biomater*, 86(1), 217-227.
- 2.44. Ghosh S. K., Roy S. K., Kundu B., Datta S. and Basu, D. (2011). Synthesis of Nano-Sized Hydroxyapatite Powders through Solution Combustion Route under Different Reaction Conditions. *Mat. Sci. Engg.: B*, 176(1), 14-21.
- 2.45. Sasikumar S. and Vijayaraghavan R. (2006). Low Temperature Synthesis of Nanocrystalline Hydroxyapatite from Egg Shells by Combustion Method. *Trends Biomater. Artif. Organs*, 19(2), 70-73.
- 2.46. Vadhyathan B, Rao KJ. (1996). Rapid microwave assisted synthesis of hydroxyapatite, *Bull. Mater. Sci.* 19, 1163- 1165.
- 2.47. Tas A. C (2000). Combustion synthesis of calcium phosphate bio ceramic powders, *J. Eur. Ceram. Soc.* 20 2384-2394.

- 2.48. Pratihari S. K., Garg M., Mehra S. and Bhattacharyya S. (2006). Phase Evolution and Sintering Kinetics of Hydroxyapatite Synthesized By Solution Combustion Technique. *J Mat Sci.: Mater Med.*, 17(6), 501-507.
- 2.49. Vallet-Reg M., Gutiérrez-Ros, M. T. Alonso, M. P. De Frutos, M. I. and Nicolopoulos S. (1994). Hydroxyapatite Particles Synthesized By Pyrolysis of an Aerosol. *J. Solid State Chem.*, 112(1), 58-64.
- 2.50. Aizawa M., Hanazawa T., Itatani K., Howell F. S. and Kishioka A. (1999). Characterization of Hydroxyapatite Powders Prepared by Ultrasonic Spray-Pyrolysis Technique. *J. Mat. Sci.*, 34(12), 2865-2873.
- 2.51. Cho, J.S and Kang, Y.C.(2008). Nano-Sized Hydroxyapatite Powders Prepared by Flame Spray Pyrolysis. *J. Alloy. Compd*, 464, 282-287.
- 2.52. An G. H., Wang H. J., Kim B. H., Jeong Y. G. and Choa Y. H. (2007). Fabrication and Characterization of a Hydroxyapatite Nanopowder by Ultrasonic Spray Pyrolysis With Salt-Assisted Decomposition. *Mat. Sci. Engg.: A*, 449, 821-824.
- 2.53. Tas A. C. (2000). Synthesis of Biomimetic Ca-Hydroxyapatite Powders At 37 C In Synthetic Body Fluids. *Biomaterials*, 21(14), 1429-1438.
- 2.54. Wan, Y. Z., Hong, L., Jia, S. R., Huang, Y., Zhu, Y., Wang, Y. L., and Jiang, H. J. (2006). Synthesis and Characterization of Hydroxyapatite–Bacterial Cellulose Nanocomposites. *Compos. Sci. Technol.*, 66(11), 1825-1832..
- 2.55. Kumar Nayak A., Saquib Hasnain M. and Malakar, J. (2013). Development and Optimization of Hydroxyapatite-Ofloxacin Implants for Possible Bone Delivery in Osteomyelitis Treatment. *Current drug delivery*, 10(2), 241-250.
- 2.56. Santos M. H., Oliveira M. D., Souza L. P. D. F., Mansur H. S. and Vasconcelos W. L. (2004). Synthesis Control and Characterization of Hydroxyapatite Prepared By Wet Precipitation Process. *Mater. Res.*, 7(4), 625-630.
- 2.57. Frazer K. A., Ballinger D. G., Cox D. R., Hinds D. A., Stuve L. L., Gibbs R. A., Belmont John W. (2007). A Second Generation Human Haplotype Map of Over 3.1 Million SNPs. *Nature*, 449(7164), 851-861.
- 2.58. Gergely G., Wéber F., Lukács I., Illés, L. Tóth, A. L. Horváth, Z. E (2010). Nano-Hydroxyapatite Preparation from Biogenic Raw Materials. *Cent. Eur. J. Chem.*, 8(2), 375-381.
- 2.59. Boonyang U., Chaopanich P., Wongchaisuwat A., Senthongkaew P. and Siripaisarnpipat, S. (2010). Effect of Phosphate Precursor On The Production Of Hydroxyapatite From Crocodile Eggshells. *J. Biomim Biomater. Tissue Eng.*, 5, 31-37.
- 2.60. Nayak A. K., Bhattacharyya A. and Sen K. K. (2011). In Vivo Ciprofloxacin Release from Hydroxyapatite-Based Bone Implants in Rabbit Tibia: A Preliminary Study. *ISRN Orthopedics*, 2011.
- 2.61. Sinha A., Nayar S., Agrawal A., Bhattacharyya D. and Ramachandrarao, P. (2003). Synthesis Of Nanosized And Microporous Precipitated Hydroxyapatite in Synthetic Polymers and Biopolymers. *J. Am. Ceram. Soc.*, 86(2), 357-359.

- 2.62. Sadat-Shojai M., Khorasani M. T., Dinpanah-Khoshdargi, E. and Jamshidi A. (2013). Synthesis methods for nanosized hydroxyapatite with diverse structures. *Acta Biomater.*, 9(8), 7591-7621.
- 2.63. Engin N. O. and Tas A. C. (1999). Manufacture of Macroporous Calcium Hydroxyapatite Bioceramics. *J. Eur. Ceram. Soc.*, 19(13), 2569-2572.
- 2.64. Li S. H., De Wijn J. R., Layrolle P. and De Groot, K. (2002). Synthesis of Macroporous Hydroxyapatite Scaffolds for Bone Tissue Engineering. *J. Biomed. Mater. Res.*, 61(1), 109-120.
- 2.65. Rodríguez-Lorenzo L. M., Vallet-Regí M. and Ferreira J. M. F. (2002). Fabrication of Porous Hydroxyapatite Bodies by a New Direct Consolidation Method: Starch Consolidation. *J. Biomed. Mater. Res.*, 60(2), 232-240.
- 2.66. Li S., de Wijn J. R., Li J., Layrolle P. and de Groot, K. (2003). Macroporous Biphasic Calcium Phosphate Scaffold with High Permeability/Porosity Ratio. *Tissue Eng.*, 9(3), 535-548.
- 2.67. Li S. H., Wijn J. R., Layrolle P. and Groot, K. (2003). Novel Method to Manufacture Porous Hydroxyapatite by Dual-Phase Mixing. *J. Am. Ceram. Soc.*, 86(1), 65-72.
- 2.68. Peón E., Fuentes G., Delgado J. A., Morejón, L. Almirall A. and García R. (2004). Preparation and Characterization of Porous Blocks of Synthetic Hydroxyapatite. *Lat. Am. Appl. Res.*, 34(4), 225-228.
- 2.69. Lei Yang, Ning Xiao (2005). Preparation of Porous Hydroxyapatite Ceramics with Starch Additive. *Trans Nonferrous Met. Soc. China*, 15(2), 257-260.
- 2.70. Collin I., Lamy B., Gauthier O. and Bouler J. M. (2005). Improvement of Macroporous Biphasic Phosphocalcic Ceramics for the Filling of Bone Defects. *ITBM-RBM*, 26(4), 247-248.
- 2.71. Zhang Y., Xu H. H., Takagi S. and Chow L. C. (2006). In-Situ Hardening Hydroxyapatite-Based Scaffold for Bone Repair. *J Mater Sci: Mater Med.*, 17(5), 437-445.
- 2.72. Klenke F. M., Liu Y., Yuan H., Hunziker E. B., Siebenrock K. A. and Hofstetter W. (2008). Impact of Pore Size on the Vascularization and Osseointegration of Ceramic Bone Substitutes in Vivo. *J Biomed Mater. Res. Part A*, 85(3), 777-786.
- 2.73. Abdurrahim T. and Sopyan I. (2008). Recent Progress on the Development of Porous Bioactive Calcium Phosphate for Biomedical Applications. *Recent Pat. Biomed Eng.* 1(3), 213-229.
- 2.74. Sundaram J., Durance T. D. and Wang R. (2008). Porous Scaffold of Gelatin–Starch with Nanohydroxyapatite Composite Processed via Novel Microwave Vacuum Drying. *Acta Biomater.* 4(4), 932-942.
- 2.75. Tang, Y., Tang, Y., Lv C. and Zhou Z. (2008). Preparation of Uniform Porous Hydroxyapatite Biomaterials by a New Method. *Appl Surf Sci.*, 254(17), 5359-5362.
- 2.76. Swain S. K. and Bhattacharyya S. (2013). Preparation of High Strength Macroporous Hydroxyapatite Scaffold. *Mat. Sci. Eng: C*, 33(1), 67-71.

- 2.77. Yook S. W., Kim H. E., Yoon B. H., Soon, Y. M. and Koh, Y. H. (2009). Improvement of Compressive Strength of Porous Hydroxyapatite Scaffolds By Adding Polystyrene to Camphene-Based Slurries. *Mater Lett.*, 63(11), 955-958
- 2.78. Bakhtiari L., Rezaie H. R., Hosseinalipour S. M. and Shokrgozar M. A. (2010). Investigation of Biphasic Calcium Phosphate/Gelatin Nanocomposite Scaffolds as a Bone Tissue Engineering. *Ceram. Int.*, 36(8), 2421-2426.
- 2.79. Kundu B., Soundrapandian C., Nandi S. K., Mukherjee P., Dandapat N., Roy S., Datta B.K., Mandal T.K., Basu D. and Bhattacharya R. N. (2010). Development of New Localized Drug Delivery System Based on Ceftriaxone-Sulbactam Composite Drug Impregnated Porous Hydroxyapatite: A Systematic Approach For in Vitro And In Vivo Animal Trial. *Pharm Res.*, 27(8), 1659-1676.
- 2.80. Le Ray A. M., Gautier, H. Bouler, J. M. Weiss, P. and Merle C. (2010). A New Technological Procedure using Sucrose as Porogen Compound to Manufacture Porous Biphasic Calcium Phosphate Ceramics of Appropriate Micro-And Macrostructure. *Ceram. Int.*, 36(1), 93-101.
- 2.81. Amara A., Abudalaziz A. M., Ismail R. A., Razak A. H. N., Masudi M. S., Kasim R. S., and Ahmad A. Z. (2011). Synthesis and Characterization of Porous Biphasic Calcium Phosphate Scaffold from Different Porogens for Possible Bone Tissue Engineering Applications. *Sci. Sint.*, 43(2), 183-192.
- 2.82. Madhavi S., Ferraris C. and White T. J. (2005). Synthesis and Crystallization of Macroporous Hydroxyapatite. *J. Solid State Chem.*, 178(9), 2838-2845.
- 2.83. Janney M. A. and Omatete O. O. (1991). U.S. Patent No. 5,028,362. Washington, DC: U.S. Patent and Trademark Office.
- 2.84. Sepulveda P., Binner J. G. P., Rogero S. O., Higa O. Z. and Bressiani J. C. (2000). Production of Porous Hydroxyapatite by the Gel-Casting of Foams and Cytotoxic Evaluation. *J. Biomed. Mater. Res.*, 50(1), 27-34.
- 2.85. Hamplin J., Sambrook R. M. Flowers N. J., Hannon M. J., Sambrook M. R. (2002). Highly Porous Gel-Cast Ceramics in Medical Applications, *Eur. Cell. Mater.*, 4(2), 99.
- 2.86. Jones J. R., Ehrenfried L. M. and Hench, L. L. (2006). Optimising Bioactive Glass Scaffolds for Bone Tissue Engineering. *Biomaterials*, 27(7), 964-973.
- 2.87. Narbat M. K., Orang F., Hashtjin M. S. and Goudarzi A. (2006). Fabrication Of Porous Hydroxyapatite-Gelatin Composite Scaffolds for Bone Tissue Engineering. *Iran Biomed. J*, 10(4), 215-223.
- 2.88. Bundela H. and Bajpai, A. K. (2008). Designing Of Hydroxyapatite-Gelatin Based Porous Matrix as Bone Substitute: Correlation with Biocompatibility Aspects. *eXPRESS Polym. Lett.*, 2, 201-213.
- 2.89. Monmaturapoj N., Soodsawang W. and Thepsuwan W. (2012). Porous Hydroxyapatite Scaffolds Produced by the Combination of the Gel-Casting and Freeze Drying Techniques. *J. Porous Mater.*, 19(4), 441-447.

- 2.90. Aidin S., Angela N. M. H. N and Hazla M. H. (2014). Local Tissue Reaction and Biodegradation of Hydroxyapatite/ Tricalcium Phosphate Composite, *World J Med Sci.* 11 (3): 301-305.
- 2.91. Kim T. W., Ryu S. C., Kim B. K., Yoon S. Y. and Park H. C. (2014). Porous Hydroxyapatite Scaffolds Containing Calcium Phosphate Glass-Ceramics Processed using a Freeze/Gel-Casting Technique. *Met. Mater. Int.*, 20(1), 135-140.
- 2.92. M. Potoczek (2008). Hydroxyapatite Foams Produced by Gel-Casting using Agarose, *Mater. Lett.* 62, 1055–1057.
- 2.93. Ramay H. R. and Zhang, M. (2003). Preparation of Porous Hydroxyapatite Scaffolds by Combination of the Gel-Casting and Polymer Sponge Methods. *Biomaterials*, 24(19), 3293-3302.
- 2.94. Baradararan S., Hamdi M. and Metselaar, I. H. (2012). Biphasic Calcium Phosphate (BCP) Macroporous Scaffold with Different Ratios of HA/B-TCP by Combination of Gel Casting and Polymer Sponge Methods. *Adv. Appl. Ceram.*, 111(7), 367-373.
- 2.95. Li X., Bian W., Li D., Lian Q. and Jin, Z. (2011). Fabrication of Porous Beta-Tricalcium Phosphate with Microchannel and Customized Geometry Based on Gel-Casting and Rapid Prototyping. *Proc. Int. Mech. Eng, Part H: J Eng. Med.*, 225(3), 315-323.
- 2.96. Farhangdoust S., Zamanian A., Yasaei M. and Khorami M. (2013). The Effect of Processing Parameters and Solid Concentration on The Mechanical and Microstructural Properties of Freeze-Casted Macroporous Hydroxyapatite Scaffolds. *Mat. Sci and Engg: C*, 33(1), 453-460.
- 2.97. Deville S., Saiz E. and Tomsia A. P. (2006). Freeze Casting Of Hydroxyapatite Scaffolds for Bone Tissue Engineering. *Biomaterials*, 27(32), 5480-5489.
- 2.98. Wegst U. G., Schecter M., Donius A. E. and Hunger P. M. (2010). Biomaterials by Freeze Casting. *Philos. Trans. R Soc. London A: Mathematical, Physical and Engineering Sciences*, 368(1917), 2099-2121.
- 2.99. Zhao K., Tang Y. F., Qin Y. S. and Wei J. Q. (2011). Porous Hydroxyapatite Ceramics by Ice Templating: Freezing Characteristics and Mechanical Properties. *Ceram. Int.*, 37(2), 635-639.
- 2.100. Fu, Q., Rahaman, M. N., Dogan, F. and Bal, B. S. (2008). Freeze casting of porous hydroxyapatite scaffolds. I. Processing and general microstructure. *J. Biomed. Mater. Res Part B: Appl. Biomaterials*, 86(1), 125-135.
- 2.101. Fu Q., Rahaman M. N., Dogan F. and Bal B. S. (2008). Freeze Casting of Porous Hydroxyapatite Scaffolds. II. Sintering, Microstructure, and Mechanical Behavior. *J Biomed. Mater. Res. Part B: Appl. Biomaterials*, 86(2), 514-522.
- 2.102. Lee E. J., Koh Y. H., Yoon B. H., Kim H. E. and Kim, H. W. (2007). Highly Porous Hydroxyapatite Bioceramics with Interconnected Pore Channels Using Camphene-Based Freeze Casting. *Mater. Lett.*, 61(11), 2270-2273.

- 2.103. Yoon B. H., Koh, Y. H. Park, C. S. and Kim and H. E. (2007). Generation of Large Pore Channels for Bone Tissue Engineering Using Camphene-Based Freeze Casting. *J. Am. Ceram. Soc.*, 90(6), 1744-1752.
- 2.104. White R. A., Weber J. N. and White, E. W. (1972). Replamineform: A New Process for Preparing Porous Ceramic, Metal, and Polymer Prosthetic Materials. *Science*, 176(4037), 922-924.
- 2.105. Ota T., Takahashi M., Hibi T., Ozawa M. Suzuki, S. Hikichi, Y. and Suzuki, H. (1995). Biomimetic Process for Producing SiC "Wood". *J Am Ceram Soc.*, 78(12), 3409-3411.
- 2.106. Schwartzwalder K. and Somers A.V. (1963). Methods of Making Porous Ceramic Articles. US Patent, No.3090094, May 21.
- 2.107. Tian J. and Tian, J. (2001). Preparation of Porous Hydroxyapatite. *J. Mater. Sci.*, 36(12), 3061-3066.
- 2.108. Kim H. W., Knowles J. C. and Kim H. E. (2005). Hydroxyapatite Porous Scaffold Engineered with Biological Polymer Hybrid Coating for Antibiotic Vancomycin Release. *J. Mater Sci.: Mater Med.*, 16(3), 189-195.
- 2.109. Min S. H., Jin H. H., Park H. Y., Park I. M., Park H. C. and Yoon S. Y. (2006). Preparation of Porous Hydroxyapatite Scaffolds for Bone Tissue Engineering. *Mater Sci. Forum*, 510, 754-757.
- 2.110. Saiz E., Gremillard L., Menendez G., Miranda P., Gryn K. and Tomsia A. P. (2007). Preparation of Porous Hydroxyapatite Scaffolds. *Mat. Sci. Engg.: C*, 27(3), 546-550.
- 2.111. Appleford M. R., Oh S., Oh N. and Ong J. L. (2009). In Vivo Study on Hydroxyapatite Scaffolds with Trabecular Architecture for Bone Repair. *J. Biomed. Mater. Res. Part A*, 89(4), 1019-1027.
- 2.112. Bakunova N. V., Komlev V. S., Fedotov A. Y., Fadeeva I. V., Smirnov V. V., Shvorneva L. I., A. N. Gurin, and S. M. Barinov. (2008). A Method of Fabrication of Porous Carbonated Hydroxyapatite Scaffolds For Bone Tissue Engineering. *Powder Met. Prog.*, 8(4), 336.
- 2.113. Oliveira J. M., Rodrigues M. T., Silva S. S., Malafaya P. B., Gomes M. E., Viegas C. A., Dias I. R., Azevedo J. T., Mano J. F. and Reis R.L. (2006). Novel Hydroxyapatite/Chitosan Bilayered Scaffold for Osteochondral Tissue-Engineering Applications: Scaffold Design and its Performance when Seeded with Goat Bone Marrow Stromal Cells. *Biomaterials*, 27(36), 6123-6137.
- 2.114. Jo I. H., Shin K. H., Soon Y. M., Koh Y. H., Lee J. H. and Kim H. E. (2009). Highly Porous Hydroxyapatite Scaffolds with Elongated Pores using Stretched Polymeric Sponges as Novel Template. *Mater Lett.*, 63(20), 1702-1704.
- 2.115. Sopyan I., Mel M., Ramesh S. and Khalid K. A. (2007). Porous Hydroxyapatite for Artificial Bone Applications. *Sci. Technol. Adv. Mater.*, 8(1), 116-123
- 2.116. Swain S. K., S. Bhattacharyya, and D. Sarkar (2011). Preparation of Porous Scaffold from Hydroxyapatite Powders. *Mat. Sci .Engg.: C*, 31(6), 1240-1244.

- 2.117. Gervaso F., Scalera F., Kunjalukkal P.S., Sannino A. and Licciulli A. (2012). High-Performance Hydroxyapatite Scaffolds for Bone Tissue Engineering Applications. *Intl. J. Appl. Ceram. Technol.*, 9(3), 507-516.
- 2.118. Scalera F., Gervaso F., Sanosh K. P., Sannino A. and Licciulli A. (2013). Influence of the Calcination Temperature on Morphological and Mechanical Properties of Highly Porous Hydroxyapatite Scaffolds. *Ceram Int.*, 39(5), 4839-4846.
- 2.119. Roohani-Esfahani S. I., Nouri-Khorasani S., Lu, Z., Appleyard R. and Zreiqat H. (2010). The Influence Hydroxyapatite Nanoparticle Shape and Size on the Properties of Biphasic Calcium Phosphate Scaffolds Coated with Hydroxyapatite–PCL Composites. *Biomaterials*, 31(21), 5498-5509.
- 2.120. Tuck C. and Evans, J. R. G. (1999). Porous Ceramics Prepared From Aqueous Foams. *J Mater Sci Lett.*, 18(13), 1003-1005.
- 2.121. Lindsten G., Brandt J., Carlstrom E. and Kristoffersson, A. (1999). U.S. Patent No. 5,972,284. Washington.
- 2.122. Lyckfeldt O., Brandt J. and Lesca, S. (2000). Protein Forming—A Novel Shaping Technique For Ceramics. *J. Eur. Ceram Soc.*, 20(14), 2551-2559.
- 2.123. Garrn I., Reetz C., Brandes N., Kroh L. W. and Schubert, H. (2004). Clot-Forming: The Use of Proteins as Binders for Producing Ceramic Foams. *J. Eur. Ceram. Soc.*, 24(3), 579-587.
- 2.124. Lomakina K. and Mikova K. (2006). A Study of the Factors Affecting the Foaming Properties of Egg White-A Review. *Czech J. Food Sci*, 24(3), 110-118.
- 2.125. Hanselmann, W., and Mueller, A. (2002). U.S. Patent Application 10/318,205.
- 2.126. Dhara S. and Bhargava P. (2001). Egg White as an Environmentally Friendly Low-Cost Binder for Gelcasting of Ceramics. *J. Am. Ceram. Soc.*, 84(12), 3048-3050.
- 2.127. Sopyan I., Fadli A. and Singh R. (2013). Protein Foaming-Consolidation Method for Fabrication of High Performance Porous Bioceramics. *Adv. Mat. Res.* (Vol. 622, pp. 1759-1763).
- 2.128. Ginebra M. P., Fernández E., Driessens F. and Planell, J. A. (1999). Modeling of the Hydrolysis of  $\alpha$ -Tricalcium Phosphate. *J. Am. Ceram. Soc.*, 82(10), 2808-2812.
- 2.129. Sopyan, I., Fadli, A., and Mel, M. (2012). Porous alumina–hydroxyapatite composites through protein foaming–consolidation method. *J. Mech. Behav Biomed. Mater.*, 8, 86-98.
- 2.130. Sepulveda P., Ortega F. S., Innocentini M. D. and Pandolfelli, V. C. (2000). Properties of Highly Porous Hydroxyapatite obtained by the Gelcasting of Foams. *J. Am. Ceram. Soc.* 83(12), 3021-3024.
- 2.131. Ribeiro C., Goia T. S., Violin K. B., Bressiani J. C. and Bressiani A. H. A. (2011). Osseointegration and Biocompatibility Study of Macroporous Biphasic Calcium Phosphate (BCP) Ceramics Obtained by Consolidation using Albumin. *Adv. Sci. Techno.* 76, 66-71.

- 2.132. Lemos A. F. and Ferreira, J. M. F. (2004). The Valences of Egg White for Designing Smart Porous Bioceramics: as Foaming and Consolidation Agent. *Key Eng. Mater.* 254, 1045-1050.
- 2.133. Lemos A. F. and Ferreira, J. M. F. (2000). Porous Bioactive Calcium Carbonate Implants Processed by Starch Consolidation. *Mat Sci Engg.: C*, 11(1), 35-40.
- 2.134. Woottichaiwat S., Puajindanetr S. and Best S. M. (2011). Fabrication of Porous Hydroxyapatite through Combination of Sacrificial Template and Direct Foaming Techniques. *Eng. J.*, 15(2), 1-16.
- 2.135. Kim Z. K., Oak J. J., Kimura H., Goto T., Inoue A. and Yoon, S. Y. (2009). Achitecture of Porous Hydroxyapatite Scaffolds Using Polymer Foam Process. *J. Biomech. Sci. Eng.*, 4(3), 377-383.
- 2.136. Huang X. and Miao, X. (2007). Novel Porous Hydroxyapatite Prepared By Combining H<sub>2</sub>O<sub>2</sub> Foaming with PU Sponge and Modified with PLGA and Bioactive Glass. *J Biomater. Appln.*, 21(4), 351-374.
- 2.137. Almirall A., Larrecq G., Delgado J. A., Martinez S., Planell J. A., and Ginebra M. P. (2004). Fabrication of Low Temperature Macroporous Hydroxyapatite Scaffolds By Foaming and Hydrolysis of a  $\alpha$ -TCP Paste. *Biomaterials*, 25(17), 3671-3680.
- 2.138. Wilson C., De Bruijn J., Kruijt M., Van Gaalen S., Dhert W., Verbout A. J. and Van Blitterswijk C., Design And Fabrication Of Porous Hydroxyapatite Scaffolds for Bone Tissue Engineering Using Rapid Prototyping Techniques. 47th Annual Meeting, Orthopaedic Research Society, February 25 - 28, 2001, San Francisco, California.
- 2.139. Bose S., Vahabzadeh S. and Bandyopadhyay A. (2013). Bone Tissue Engineering using 3D Printing. *Mater. Today*, 16(12), 496-504.
- 2.140. Woesz A., Rumpler M., Stampfl J., Varga F., Fratzl-Zelman N., Roschger, P., Klaushofer K. and Fratz P. (2005). Towards Bone Replacement Materials from Calcium Phosphates via Rapid Prototyping and Ceramic Gelcasting. *Mater. Sci. Engg.: C*, 25(2), 181-186.
- 2.141. Saiz E., Gremillard L., Menendez G., Miranda, P. Gryn, K. and Tomsia A. P. (2007). Preparation of Porous Hydroxyapatite Scaffolds. *Mat. Sci. Engg.: C*, 27(3), 546-550.
- 2.142. Simon J. L., Michna S., Lewis J. A., Rekow E. D., Thompson V. P., Smay, J. E., Yampolsky A., J. Russell Parsons, and John L. Ricci. (2007). In Vivo Bone Response To 3D Periodic Hydroxyapatite Scaffolds Assembled by Direct Ink Writing. *J. Biomed. Mater. Res. Part A*, 83(3), 747-758.
- 2.143. Kutikov A. B., Gurijala A. and Song, J. (2014). Rapid Prototyping Amphiphilic Polymer/Hydroxyapatite Composite Scaffolds with Hydration-Induced Self-Fixation Behavior. *Tissue Eng. Part C: Methods*, 21(3), 229-241.
- 2.144. Xu H., Han. D., Dong J. S., Shen G. X., Chai G., Yu Z. Y., Lang W. J. and Ai S. T. (2010). Rapid prototyped PGA/PLA scaffolds in the reconstruction of mandibular condyle bone defects. *Int. J Med Robot.* 6(1), 66-72.



- 2.145. Klein C. P. A. T., Driessen A. A. and De Groot, K. (1984). Relationship between the Degradation Behaviour of Calcium Phosphate Ceramics and Their Physical-Chemical Characteristics and Ultrastructural Geometry. *Biomaterials*, 5(3), 157-160.
- 2.146. Klein C. P., de Bleeck-Hogemrst J. M. A., Wolket J. G. C. and De Groot, K. (1990). Studies Of the Solubility of Different Calcium Phosphate Ceramic Particles in Vitro. *Biomaterials*, 11(7), 509-512.
- 2.147. Legeros R. Z. (1993). Biodegradation and Bioresorption of Calcium Phosphate Ceramics. *Clinical Mater.*, 14(1), 65-88.
- 2.148. Cao W. and Hench, L. L. (1996). Bioactive Materials. *Ceram Int.*, 22(6), 493-50
- 2.149. Lin F. H., Liao C. J., Chen K. S., Sun J. S. and Lin, C. P. (2001). Petal-Like Apatite Formed on The Surface of Tricalcium Phosphate Ceramic After Soaking in Distilled Water. *Biomaterials*, 22(22), 2981-2992.
- 2.150. Kwon S. H., Jun Y. K., Hong S. H. and Kim H. E. (2003). Synthesis and Dissolution Behavior of B-TCP and HA/B-TCP Composite Powders. *J. Eur. Ceram. Soc.*, 23(7), 1039-1045.
- 2.151. Kim H. M., Himeno T., Kawashita M., Kokubo T. and Nakamura T. (2004). The Mechanism of Biomineralization of Bone-Like Apatite on Synthetic Hydroxyapatite: An In Vitro Assessment. *J. Royal. Soc. Inter.*, 1(1), 17-22.
- 2.152. Kokubo T., Takadama H. (2006). How useful is SBF in predicting in vivo bone bioactivity? *Biomaterials* 27: 2907–2915.
- 2.153. Sánchez-Salcedo S., Balas, F. Izquierdo-Barba, I. and Vallet-Regí M. (2009). In Vitro Structural Changes in Porous HA/B-TCP Scaffolds in Simulated Body Fluid. *Acta Biomater.*, 5(7), 2738-2751
- 2.154. Liu X., Sun Q., Wang H., Zhang L. and Wang J. Y. (2005). Microspheres of Corn Protein, Zein, For an Ivermectin Drug Delivery System. *Biomaterials*, 26(1), 109-115

#### **Chapter-4**

- 4.1 Haines P. J. (2012). *Thermal Methods of Analysis: Principles, Applications and Problems*. Springer Science and Business Media.
- 4.2 D. Holzmann, D. Holzinger, G. Hesser, T. Schmidt, G. Knor, (2009). Hydroxyapatite Nanoparticles as Novel Low-Refractive Index Additives for the Long-Term UV-Photoprotection of Transparent Composite Materials, *J. Mater.Chem.* (19) 8102-8106
- 4.3 Brunauer S., Emmett P. H. and Teller E. (1938). Adsorption of Gases in Multimolecular Layers. *J. Am. Chem. Soc.*, 60(2), 309-319.
- 4.4 Cullity B. D. and Stock, S. R. (2001). *Elements of X-ray Diffraction* (Vol. 3, p. 15,NJ: Prentice hall.
- 4.5 Greenwood N. N. and Gibb T. C. (1971). *Mössbauer Spectroscopy*. Chapman and Hall, London.
- 4.6 Speyer R. (1993). *Thermal Analysis of Materials*. CRC Press.

- 4.7 Reed J.S., Principles of Ceramic Processing, 2nd edition Wiley, New York (1995), Pages- 367 – 373.
- 4.8 R. Brenzy and Green D. J (1990). The Effect of Cell Size on the Mechanical Behaviour of Cellular Ceramics, *Acta Metall Mater.* Vol 38, (12) 2517-2526 .
- 4.9 E.W. Washburn (1921), The Dynamics Of Capillary Flow, *Phy. Review* 17 273-283.
- 4.10 Kokubo, T., Takadama, H. (2006). How Useful Is SBF In Predicting In Vivo Bone Bioactivity?. *Biomaterials* 27: 2907–2915.
- 4.11 Tas A. C. (2000). Synthesis of Biomimetic Ca-Hydroxyapatite Powders At 37 C in Synthetic Body Fluids. *Biomaterials*, 21(14), 1429-1438.
- 4.12 Mosmann T. (1983). Rapid Colorimetric Assay for Cellular Growth and Survival: Application to Proliferation and Cytotoxicity Assays. *J. immune. Methods*, 65(1), 55-63.

### Chapter-5

- 5.1 Liu C., Huang Y., Shen W. and Cui J. (2001). Kinetics of Hydroxyapatite Precipitation at pH 10 To 11. *Biomaterials*, 22(4), 301-306.
- 5.2 Oliveira M. and Mansur H. S. (2007). Synthetic Tooth Enamel: SEM Characterization of a Fluoride Hydroxyapatite Coating for Dentistry Applications. *Mater. Res.*, 10(2), 115-118.
- 5.3 Zhang S. and Gonsalves K. E. (1997). Preparation and Characterization of Thermally Stable Nanohydroxyapatite. *J. Mater. Sci.: Mater. Med.*, 8(1), 25-28.
- 5.4 Kim W., Zhang Q. and Saito F. (2000). Mechano-chemical Synthesis of Hydroxyapatite from Ca (OH)<sub>2</sub>-P<sub>2</sub>O<sub>5</sub> And CaO-Ca (OH)<sub>2</sub>-P<sub>2</sub>O<sub>5</sub> Mixtures. *J Mat. Sci.*, 35(21), 5401-5405.
- 5.5 Li Z., Wang P. and Wu Z. (2005). Preparation of Nanosized Hydroxyapatite Particles at Low Temperatures. *J Mat. Sci*, 40(24), 6589-6591.
- 5.6 Jarcho M., Bolen C. H., Thomas M. B., Bobick J., Kay J. F. and Doremus R. H. (1976). Hydroxylapatite Synthesis and Characterization in Dense Polycrystalline Form. *J. Mat. Sci.*, 11(11), 2027-2035.
- 5.7 Silva C. C., Pinheiro A. G., Miranda M. A. R., Góes J. C. and Sombra, A. S. B. (2003). Structural Properties of Hydroxyapatite Obtained By Mechano-synthesis. *Solid State Sci.*, 5(4), 553-558.
- 5.8 Fathi M. H., Hanifi A. and Mortazavi, V. (2008). Preparation and Bioactivity Evaluation of Bone-Like Hydroxyapatite Nanopowder. *J. Mater. Proc. Technol.*, 202(1), 536-542.
- 5.9 Arita I. H., Castano V. M. and Wilkinson D. S. (1995). Synthesis and Processing Of Hydroxyapatite Ceramic Tapes with Controlled Porosity. *J. Mater. Sci.: Mater. Med.*, 6(1), 19-23.
- 5.10 Bouyer E., Gitzhofer F. and Boulos M. I. (2000). Morphological Study of Hydroxyapatite Nanocrystal Suspension. *J. Mater. Sci.: Mater. Med.*, 11(8), 523-531.
- 5.11 Liu D. M., Troczynski T. and Tseng W. J. (2001). Water-Based Sol–Gel Synthesis of Hydroxyapatite: Process Development. *Biomaterials*, 22(13), 1721-1730.

- 5.12 Kim I. S. and Kumta, P. N. (2004). Sol–Gel Synthesis and Characterization of Nanostructured Hydroxyapatite Powder. *Mat. Sci. Eng.: B*, 111(2), 232-236.
- 5.13 Ferraz, M. P., Monteiro, F. J., and Manuel, C. M. (2004). Hydroxyapatite Nanoparticles: a Review of Preparation Methodologies. *J. Appl. Biomater. Biomech.* 2(2), 74-80.
- 5.14 Janačkovića D., Petrović-Prelević I. and Kostić-gvozdrenovića L. (2001). Influence of Synthesis Parameters on the Particle Sizes of Nanostructured Calcium-Hydroxyapatite. *Key Eng. Mater.*, (192-195), 203-206.
- 5.15 Kannan S., Ventura J. M. G. and Ferreira J. M. F. (2007). Synthesis and Thermal Stability of Potassium Substituted Hydroxyapatites and Hydroxyapatite/ $\beta$ -Tricalciumphosphate Mixtures. *Ceram. Int.*, 33(8), 1489-1494.
- 5.16 Takahashi H., Yashima M., Kakihana M. and Yoshimura M. (1995). Synthesis of Stoichiometric Hydroxyapatite Solid State Inorg. Chem., 32(7-8), 829-835.
- 5.17 Brendel T., Engel A. and Rüssel C. (1992). Hydroxyapatite Coatings by a Polymeric Route. *J. Mater. Sci.: Mater. Med.*, 3(3), 175-179.
- 5.18 Nayak Y. (2010). Hydroxyapatite–TZP Composites: Processing, Mechanical Properties, Microstructure and in Vitro Bioactivity (Doctoral dissertation). NIT Rourkela.
- 5.19 Gonzales M. G., Cabanelas J. C. and Baselga, J. (2012). Infrared spectroscopy–Material Science, Engineering and Technology, T, 267.
- 5.20 Brown WE, Lehr JR, Smith JP, Frazier AW(1957). Crystallography of octacalcium phosphate. *Journal of the American Chemical Society.* (19):5318-19.
- 5.21 Brown WE, Mathew M, Tung MS.(1981) Crystal chemistry of octacalcium phosphate. *Progress in crystal growth and characterization.*;4(1):59-87.
- 5.22 Betts, Foster, Norman C. Blumenthal, and Aaron S. Posner.(1981) "Bone mineralization." *Journal of crystal growth* 53, 63-73.
- 5.23 Onuma, Kazuo, Atsuo Ito, Tetsuya Tateishi, and Tetsuya Kameyama.(1995). "Growth kinetics of hydroxyapatite crystal revealed by atomic force microscopy." *Journal of crystal growth* 154, no. 1: 118-125.
- 5.24 Onuma, Kazuo, Noriko Kanzaki, Atsuo Ito, and Tetsuya Tateishi.(1998) "Growth kinetics of the hydroxyapatite (0001) face revealed by phase shift interferometry and atomic force microscopy." *The Journal of Physical Chemistry B* 102, no. 40 : 7833-7838.
- 5.25 Viswanath, B., Paromita Kundu, B. Mukherjee, and N. Ravishankar. "Predicting the growth of two-dimensional nanostructures." *Nanotechnology* 19, no. 19 (2008): 195603.
- 5.26 Sun, R., Li, M., Lu, Y., and Wang, A. (2006). Immersion Behavior of Hydroxyapatite (HA) Powders Before and after Sintering. *Mater Charact.* 56(3), 250-254.

## Chapter-6

- 6.1 Yoshikawa H., Myoui A. (2005). Bone Tissue Engineering with Porous Hydroxyapatite Ceramics, *J. Artif. Organs*, 8, 131–136.
- 6.2 Gibson I. R., Best, S. M. Bonfield W. (1999). Chemical Characterization of Silicon-Substituted Hydroxyapatite. *J Biomed Mater Res*, 44, 422–8.

- 6.3 Porter, A.E., Patel, N., Skepper, J.N., Best, S.M., Bonfield W. (2003). Comparison of in vivo Dissolution Processes in Hydroxyapatite and Silicon-Substituted Hydroxyapatite Bioceramics. *Biomaterials*, 24, 4609–4620.
- 6.4 Daculsi G., Legeros R. Z., Mitre D. (1989). Crystal Dissolution of Biological and Ceramic Apatites. *Calcif Tissue Int*, 45, 95–103.
- 6.5 Daculsi G, Kerebel B. (1977). Some Ultrastructural Aspects of Biological Apatite Dissolution and Possible Role of Dislocations. *J. Biol Buccale*, 5, 203–18.
- 6.6 Van Kemenade M., De Bruyn P. L. (1987). A Kinetic Study of Precipitation from Supersaturated Calcium Phosphate Solutions. *J Colloid Interface Sci*, 118, 564–85.
- 6.7 Le Geros R. Z. (1993). Biodegradation and Bioresorption of Calcium Phosphate Ceramics. *Clinical Mater*. 14(1), 65-88.
- 6.8 Kim H., Himeno T., Kokubo T., Nakamura T. (2005). Process and Kinetics of Bonelike Apatite Formation on Sintered Hydroxyapatite in a Simulated Body Fluid, *Electronics*, 26, 4366 – 4373.

### **Chapter-7**

- 7.1 Yang J., Yu J. and Huang Y. (2011). Recent Developments in Gelcasting of Ceramics. *J. Eur. Ceram. Soc.*, 31(14), 2569-2591.
- 7.2 Padilla S., Vallet-Reg M., Ginebra M. P. and Gil, F. J. (2005). Processing and Mechanical Properties of Hydroxyapatite Pieces Obtained by the Gelcasting Method. *J. Eur. Ceram. Soc.*, 25(4), 375-383.
- 7.3 Chen B., Zhang T., Zhang J., Lin Q. and Jiang D. (2008). Microstructure and Mechanical Properties of Hydroxyapatite Obtained by Gel-Casting Process. *Ceram Int.*, 34(2), 359-364.
- 7.4 Omatete O. O., Janney M. A. and Nunn, S. D. (1997). Gelcasting: From Laboratory Development toward Industrial Production. *J. Eur. Ceram. Soc.*, 17(2), 407-413.
- 7.5 Leung W. M., Axelson D. E. and Van Dyke J. D. (1987). Thermal Degradation of Polyacrylamide and Poly (Acrylamide-Co-Acrylate). *J. Polym. Sci. Part A: Polym. Chem.*, 25(7), 1825-1846.
- 7.6 Janney M. A., Omatete O. O., Walls C. A., Nunn S. D., Ogle R. J. and Westmoreland G. (1998). Development of Low-Toxicity Gelcasting Systems. *J. Am. Ceram. Soc.*, 81(3), 581-591.
- 7.7 Yoshikawa H. and Myoui A. (2005). Bone Tissue Engineering with Porous Hydroxyapatite Ceramics. *J. Artif. Org.*, 8(3), 131-136.
- 7.8 Abdurrahim T. and Sopyan I. (2008). Recent Progress on the Development of Porous Bioactive Calcium Phosphate for Biomedical Applications. *Recent Pat. Biomed. Eng.*, 1(3), 213-229.
- 7.9 Sopyan I., Sulaiman N. S., Gustiono D. and Herdianto N. (2005). Porous Hydroxyapatite-Gelatin Composites with Functions of Bone Substitutes and Drug Releasing Agents: A Preliminary Study. *Microelectron MEMS and Nanotech. SPIE*, 60360C-60360C.

- 7.10 Dash S. R., Sarkar R. and Bhattacharyya S. (2015). Gel Casting Of Hydroxyapatite with Naphthalene as Pore Former. *Ceram Int.*, 41(3), 3775-3790.
- 7.11 Ereiba K. M. T., Mostafa A. G., Gamal G. A. and Said A. H. (2013). In Vitro Study of Iron Doped Hydroxyapatite. *J. Biophy. Chem.*, 2013.
- 7.12 Kim H. M., Himeno T., Kokubo T. and Nakamura T. (2005). Process and Kinetics of Bonelike Apatite Formation on Sintered Hydroxyapatite in a Simulated Body Fluid. *Biomaterials*, 26(21), 4366-4373.
- 7.13 Hyakuna, K., Yamamuro, T., Kotoura, Y., Oka, M., Nakamura, T., Kitsugi, T., Kukubo T., Kushitani H. (1990). Surface Reactions of Calcium Phosphate Ceramics to Various Solutions. *J. Biomed. Mater Res.*, 24(4), 471-488.
- 7.14 Combes C. and Rey C. (2002). Adsorption of Proteins and Calcium Phosphate Materials Bioactivity. *Biomaterials*, 23(13), 2817-2823.
- 7.15 Suchanek W. and Yoshimura, M. (1998). Processing and Properties of Hydroxyapatite-Based Biomaterials for Use as Hard Tissue Replacement Implants. *J. Mater. Res.*, 13(01), 94-117.
- 7.16 Thamaraiselvi T. and Rajeswari S. (2004). Biological Evaluation of Bioceramic Materials-A Review. *Carbon*, 24(31), 172.

## Chapter-8

- 8.1 Bloksma A. H. (1990). Dough Structure, Dough Rheology, and Baking Quality. *Cereal Food World (USA)*, 35, 237-244.
- 8.2 Fan J, Mitchell J. R (1999). A Model of Oven Rise of Dough during Baking. *J. Food Eng.*, 41, 69-77.
- 8.3 Dhara S., Pradhan M., Ghosh D and Bhargava P. (2005). Nature Inspired Novel Processing Routes for Ceramic Foams. *Adv. Appl. Ceram*, 104(1), 9-21.
- 8.4 Lyckfeldt O., Brandt J. and Lesca S. (2000). Protein Forming—A Novel Shaping Technique For Ceramics. *J. Euro. Ceram. Soc.*, 20(14), 2551-2559.
- 8.5 Tuck C. and Evans J. R. G. (1999). Porous Ceramics Prepared from Aqueous Foams. *J Mat Sci. Lett.*, 18(13), 1003-1005.
- 8.6 Lindsten G., Brandt J., Carlstrom E. and Kristofferson A. (1999). U.S. Patent No. 5,972,284. Washington.
- 8.7 Tas A. C. (2004). Preparation of Porous Bioceramics by A Simple PVA-Processing Route. *Key Eng. Mat.*, 264, 2079-2082.
- 8.8 Sepulveda P. and Binner J. G. P. (1999). Processing of Cellular Ceramics by Foaming and In Situ Polymerisation of Organic Monomers, *J. Eur. Ceram. Soc.*, 19(12), 2059–66.
- 8.9 Gonzenbach U. T., Studart A. R., Tervoort, E. and Gauckler L. J. (2006). Ultrastable Particle-Stabilized Foams. *Angew. Chemie Int. Ed.*, 45(21), 3526-3530.
- 8.10 Pugh R. J. (2001). Foams and Foaming: Handbook of Applied Surface and Colloid Chemistry, Ed. K. Holmberg. John Wiley and Sons Ltd, West Sussex, 2, 23–43.

- 8.11 Garrn I., Reetz C., Brandes N., Kroh L. W. and Schubert, H. (2004). Clot-Forming: The Use of Proteins as Binders for Producing Ceramic Foams. *J. Eur. Ceram. Soc.*, 24(3), 579-587
- 8.12 Kim H. M., Himeno T., Kawashita M., Kokubo T. and Nakamura T. (2004). The Mechanism of Biomineralization of Bone-Like Apatite on Synthetic Hydroxyapatite: An In Vitro Assessment. *J. R. Soc. Interface*, 1(1), 17-22
- 8.13 Bhattacharyya S. Unpublished work.
- 8.14 Sarangi A. and S. Bhattacharyya, Unpublished work.

## Curriculum Vitae

### **Smruti Rekha Dash**

#57, 5th cross, Hormavu,  
Banaswadi main road, Bangalore  
Email: smrutirekha.dash@gmail.com



**Date of Birth:** 17.07.1984

**Education:** M.Sc. (Chemistry), M.Tech (Ceramic Engg.)

**Research Interest:** Nano material synthesis, Biomaterials, Advanced Ceramics

**Technical Exposure:** Publications: 1, Conference: 6

### **Publications Related to PhD:**

S. R. Dash, R. Sarkar and S. Bhattacharyya “**Gel casting of hydroxyapatite with naphthalene as pore former.**” **Ceramics International 41 (2015) 3775–3790**

### **Conference/Seminars Publications Related to PhD:**

- ◆ National Conference on “Ceramics in Biomedical Applications” (21-22<sup>nd</sup> January 2010) at Department of Ceramic Engineering, NIT Rourkela
- ◆ National Workshop on “Porous Materials: Fabrication and Characterization” (30-31<sup>st</sup> March) at Department of Biotechnology and Medical Engineering, NIT Rourkela.
- ◆ Young Scientist Training Workshop “BIOMAT 12” (6-8<sup>th</sup> Dec 2012) at Indian Institute of Science, Bangalore
- ◆ International conference on Design of Biomaterials “BIND 12” (9-11<sup>th</sup> Dec 2012) at Indian Institute of Science, Bangalore
- ◆ International Symposium for Research Scholar on Metallurgy, Material Science and Engineering “ISRS 2012” (13-15<sup>th</sup> Dec 2012) at IIT Madras, Chennai, India.
- ◆ 3rd National Conference on Processing and Characterization of Materials “NCPCM 2013”(6-7<sup>th</sup> Dec-2013) Department of Metallurgical and Materials Engineering, NIT Rourkela.